Network Modelling of Bioactive Porous Media

Andrew Krause
St Anne's College
University of Oxford

A thesis submitted for the degree of
Doctor of Philosophy

June 2017

Acknowledgements

I am impossibly grateful for the love, support, and friendship of countless people throughout my time as a DPhil student. I am thankful to my fellow graduate students Ferran Brosa Planella, Nabil Fadai, Micky Gomez, Jake Taylor-King, Ousman Kodio, James Kwiecinski, Ben Sloman, and Zach Wilmott, all of whom put up with my technical and esoteric banter, and were endlessly kind to me. I am tremendously grateful to the support staff, and especially Sandy Patel, for guiding me through the complexity of existence as an international student.

My supervisors have all been essential in the writing of this thesis, but more importantly in inspiring me beyond the DPhil, and providing the criticism needed for me to improve myself and my abilities to thrive as a researcher. Dmitry showed me a passion and clearness for deep mathematics that has rekindled a love within me for the subject. I am thankful for the hours we spent discussing beautiful things, even if only a taste of that has made it into the present work. Robert was essential in setting me down the right path several times as I stumbled through my research, and his friendship is something that I cherish. I am deeply grateful to Sarah for being so eager to accept me as a student. I am equally indebted to her for the pages and pages of work that she poured through to help me improve myself. I cannot understate how important each of these people were to the creation of this thesis, and to my future endeavours within mathematics, although I will claim any errors herein as mine alone.

My parents, Albert and Vickie Krause, and my brother Al Krause, have provided me with inspiration and constant encouragement that I needed far more than they may know. I am very blessed to have a family who have been there for me in innumerable ways, even at great cost to themselves. My wife, Sarah, has been a source of support and encouragement throughout my time here. I am beyond fortunate to have met Sarah when I needed her most, and would have never dreamed of travelling to Oxford without someone like her to guide me.

There are many others who have been crucial to any successes I have had while at Oxford, especially members of OCIAM and the WCMB. Ivan Avramidi, Lorie Liebrock, Philip Maini, Phil Spomer, Snezna Rogelj, John Starrett, Bill Stone, Lucas Uecker, and Bixiang Wang are others without whom I would not be where I am today.

Abstract

In this thesis we consider several approaches to modelling interactions between fluid flow and cell proliferation in a bioactive porous medium. This is motivated by models of cell growth within tissue engineering scaffolds placed in perfusion bioreactors. These scaffolds are porous materials used to facilitate nutrient transport to cells placed within them. Recent modelling efforts have sought to understand the influence that cells have on the effective permeability of these tissue scaffolds, and hence on the capacity of the porous medium to facilitate fluid and nutrient transport, which enhances the overall growth of tissue within a scaffold. Contemporary experimental and theoretical studies have emphasized the importance of mechanical forcing on cells due to their environment. We therefore consider simple models of cell growth that assume cells are affected by the fluid itself, either via shear stress, hydrostatic pressure, or local flow rate, and that cell growth influences the local permeability of the scaffold at higher cell densities via pore-blocking. Hence, we are interested in the feedback between cell growth and fluid flow within a bioactive porous medium. It is within this simplified context of fluid-growth interaction that we explore different approaches to modelling the spatial structure of the pore network, and the influence that this has on the cell density distribution throughout the scaffold.

Models in the literature are often spatially homogeneous (ODE) or spatially continuous (PDE), only implicitly accounting for the discrete pore network of the medium. The pore and scaffold length scales in typical experiments with perfusion bioreactors can lead to scaffolds with relatively few pores, and it is unclear that macroscopic spatially averaged (homogenized) continuous models will capture features present in small pore networks. We propose a suite of spatially continuous models, modified from existing PDE approaches in the literature, and compare these to discrete lattice (ODE) systems in order to elucidate differences between

these modelling paradigms. We also use the structure of the lattice model to explore stochastic analogues that are computationally and theoretically amenable to analysis. We explore behaviours of these models via numerical simulations, bifurcation analyses, and asymptotic reductions to simpler systems.

Our lattice modelling approach provides a 'mesoscopic' perspective, where the effective equations governing the cell growth and fluid flow are prescribed as ODEs at each pore. These capture the microscale dynamics at the pore scale, as opposed to homogenization approaches where the microscale is explicitly related to macroscale equations. This also allows us to use tools from dynamical systems theory which are substantially more tractable in the finite dimensional setting of ODEs (with algebraic conditions for the fluid flow), as opposed to the infinite dimensional setting of PDEs (consisting of coupled elliptic and parabolic equations). Additionally, we do not have to worry about issues of numerical convergence or existence of solutions that are important in the spatially continuous setting. Our emphasis on mesoscopic governing equations makes this network-based approach somewhat unique in the tissue engineering community.

We demonstrate qualitative and quantitative differences between these continuum and network paradigms, and in particular show behaviours captured by explicitly accounting for the discrete pore network that are not captured in spatially continuous models. For each kind of fluid-cell interaction, we classify behaviours depending on nondimensional model parameters in order to elucidate in what regimes discrete models may provide useful insights into bioactive porous materials. We also discuss computational considerations for analyzing these kinds of models, and in particular suggest that stochastic and discrete models may be easier to simulate in some parameter regimes compared to typical spatially continuous models. Our results suggest several novel approaches to pursue in accounting for the finite discrete nature of bioactive porous media, and we highlight several useful further directions.

Contents

Chapter 1

Introduction

Tissue engineering is a rapidly growing field which applies techniques from a variety of disciplines to create tissues and organs *de novo* [96, 183]. There is increased need for these technologies as the most successful surgical approaches for many major illnesses involve the implantation of tissue grafts or entire replacement organs taken from suitable donors, and the supply of donor tissue is much smaller than the need for these surgeries. Patient transplant lists continue to grow, especially due to increased longevity [14, 17, 54, 131], driving a large need for providing alternatives to donated organs and tissues. In addition to meeting this need, engineered tissues with the correct *in vivo* properties have applications in toxicology screening and drug testing [56, 75, 123]. While therapeutic tissue engineering has tremendous potential to address this donor tissue shortage, there is much left to do before serious clinical applications become a reality. Tissue growth is exceedingly complex, being regulated by an enormous variety of processes, from intracellular transduction pathways to tissue-level mechanics and issues of biocompatibility and *in vivo* implantation. Understanding these mechanisms is crucial to the development of reliable methods for engineering viable replacement tissues and organs.

A major challenge in the successful engineering of artificial tissue is to understand and exploit processes that occur on very different spatial and temporal scales [73, 103, 109, 125, 138, 141, 157, 167, 182, 188, 197]. Mathematical modelling has been increasingly used to understand these complex physical and biological processes, and hence underpins experimental work in tissue engineering [57]. Despite significant progress in recent years, there is still a need to better understand the basic biological and physical aspects underpinning the engineering of artificially constructed tissues and organs in order to achieve widespread clinical success [183]. In addition to providing conceptual understanding, quantitative mathematical models can be used

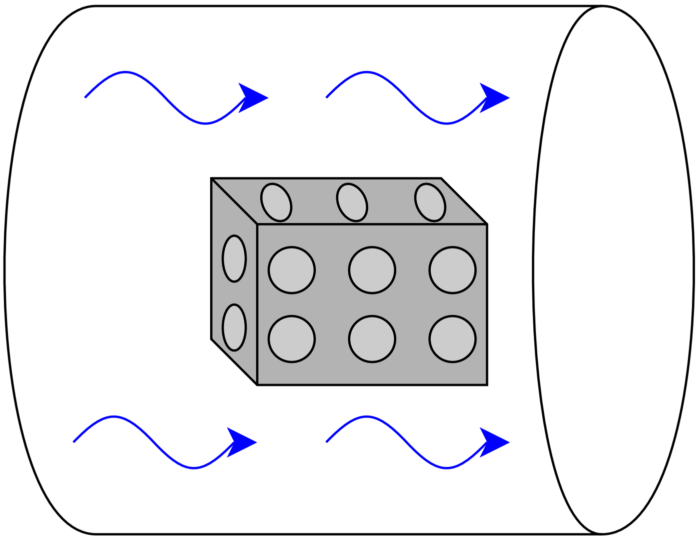

Figure 1.1: A diagram of a porous tissue scaffold within a cylindrical perfusion bioreactor. Flow moves from the left to the right of the bioreactor, and passes through the porous scaffold carrying nutrient-rich culture medium.

to predict and optimize experimental operating regimes which saves on costly and time-consuming experimental trials [30, 124, 135].

A contemporary strategy for *in vitro* tissue engineering is to seed cells onto a porous biomaterial scaffold which is placed inside a bioreactor where it is perfused with nutrient-rich culture medium [35, 63, 87, 153]. A diagram of this set-up is shown in Figure 1.1. This procedure helps overcome diffusion-limited nutrient transport which is an obstruction to the development of larger clinically-relevant 3-D tissue constructs [103, 107]. There is large variation between cell types, scaffolds, and bioreactor geometries used to grow artificial tissues [96, 109, 182]. Some cell types are mechano-sensitive and can be induced to proliferate, differentiate, or die in response to properties of the local cellular mechanical environment, such as local fluid shear stress [9, 45, 48, 80, 98, 156, 162, 203] or hydrostatic pressure [105]. Some cells produce an extracellular matrix (ECM) that is sufficiently dense to substantially affect the flow of culture medium through individual pores [76]. Understanding these fluid flow and cell growth interactions, and what roles they have in a tissue engineering experiment, is an important challenge.

Mathematical modelling plays a key role in underpinning experimental design, optimizing operating regimes, and predicting experimental outcomes [124]. Mathematical models have also been used in lieu of costly and time-consuming experimental trials. There is a growing literature of models used to understand the interactions between fluid mechanical forces exerted on mechano-sensitive cells, and the effect that cell growth has on the flow via blocking of scaffold pores. The simplest of these are spatially homogeneous models where ODEs are used to model the evolution of each phase, such as in [99]. However, the spatial structure of a scaffold can have profound effects on the growth of the tissue, due to the transport of cells and nutrients, as well as variations in the mechanical stress experienced by cells throughout the scaffold [96, 128]. Determining the spatial distribution of cells within a porous tissue scaffold, and the nature of their local biomechano-chemical environment, is a key challenge that mathematical modelling can address [115, 175]. Understanding the time-dependent coupling between cell growth and fluid flow is currently an active area of modelling and experimental investigation in tissue engineering and related fields [57]. Accounting for spatial variation beyond homogeneous or compartmental models, however, leads to several alternative model formulations. Broadly these fall into two categories: spatially continuous models, and spatially discrete (network) models. Hybrid models which couple spatially continuous and discrete components are also well-studied. The main emphasis of the present Thesis is to investigate discrete and continuum models of tissue engineering scaffolds, with the aim of elucidating differences between these alternative modelling frameworks.

1.1 Spatial Models of Bioactive Porous Media

The pore and scaffold length scales in typical experiments with perfusion bioreactors can lead to scaffolds with relatively few pores, and it is unclear that macroscopic spatially averaged (homogenized) continuous models will capture features present in small pore networks. See Figure 6 of [39] for an example of a porous scaffold with very few pores, and [103] and [182] for general discussions of pore size, scaffold geometry, and transport phenomena in porous tissue scaffolds. We summarize coarse ranges of these scales in Table 1.1 taken from experimental and theoretical literature, and truncated to order-of-magnitude estimates. It is clear from these data that there are a wide range of fundamental parameters characterizing an *in vitro* tissue engineering experiment, and determining ideal parameters within these ranges is a nontrivial problem. This difficulty is compounded by the spatial structure of the tissue scaffold, as growing cells rarely follow simple uniform growth patterns and instead will be influenced by spatial properties of the scaffold and the perfused flow [115].

There are a large variety of spatially continuous models in tissue engineering which consider various aspects of cell proliferation, nutrient transport, and mechanical processes within a tissue scaffold [124]. While there are network models of porous media

Parameter	Range
Cell volume[1278]	$10^{-18} - 10^{-15}\mathrm{m}^3/\mathrm{cell}$
Maximum cell density[2]	$10^{15} - 10^{18}\mathrm{cell}/\mathrm{m}^3$
Scaffold length[125]	$10^{-3} - 10^{-2}\mathrm{m}$
Pore length scale[258]	$10^{-5} - 10^{-3}\mathrm{m}$
Cell proliferation timescale[127]	$10^{4} - 10^{6}\mathrm{s}$
Viscosity[2]	$10^{-4} - 10^{-3}\mathrm{kg}/(\mathrm{ms})$
Cell-free scaffold porosity[24]	40-97%
Pump flow rate[25]	$10^{-5} - 10^{-3}\mathrm{m}^2/\mathrm{s}$
Cell diffusion rate[12]	$10^{-12} - 10^{-11}\mathrm{m}^2/\mathrm{s}$

Table 1.1: Order of magnitude estimates for some key parameters in the tissue engineering literature. [1] [182], [2] [166], [3] [109], [4] [179], [5] [63], [7] [52], [8] [189].

in the literature, and in particular some approaches within tissue engineering and related fields, the impact of the discrete spatial structure of porous tissue scaffolds on tissue growth has not been fully explored. In particular, there have not been thorough comparisons between spatially continuous and spatially discrete models in the context of a bioactive medium within tissue engineering, and it is chiefly this comparison that we will address in this thesis. Within mathematical oncology and other fields involving tissue dynamics, comparisons between discrete and continuous models have been carried out which give great insight into the importance of discrete structures, such as vascular networks. These comparisons indicate when such structures should be accounted for directly as discrete components of a model, or when they can be coarse-grained as a term or variable in a continuum setting [22]. We first give a broad overview of existing spatial models in tissue engineering and related areas, before outlining the approach we take throughout the rest of the thesis.

1.1.1 Spatially Continuous Models

To describe the spatial evolution of artificial tissue growth, many macroscale continuum models for bioactive porous media have been proposed [124]. These approaches are computationally much cheaper than a full simulation of flow within the pores and do not require detailed knowledge of the microstructure. Due to the complexity of growing tissue *in vitro*, and the wealth of biochemical and biophysical processes involved over a range of spatial and temporal scales, many different theoretical models exist in the literature [59]. These models result in partial differential equations for the dependent variables, such as cell density and fluid velocity, with constitutive assumptions describing the interactions between these variables. We make a distinction between two broad classes of models: multiphase models which explicitly capture the mass and momentum transfer between phases, and those which accommodate these physical laws implicitly via suitable constitutive relationships.

Multiphase models account for multiple phases explicitly (e.g. fluid, scaffold, cells, etc). The governing equations are derived from conservation of mass and momentum for each phase, and interactions between the phases are captured via the specification of appropriate constitutive laws [126, 133]. Alternatively, many models include the effect of cell growth on the fluid flow implicitly, by considering a cell density equation based on conservation of mass, and then prescribing the scaffold porosity to be a function of cell density [36, 145, 146, 166]. We will refer to these as implicit models, in comparison to multiphase models which explicitly account for interactions between phases in terms of physical forces. The flow of fluid through the porous scaffold is then governed by a relationship involving this permeability, such as Darcy's law. In all of these macroscale approaches, constitutive assumptions relate microscale processes, such as cell growth, to macroscale parameters. In both multiphase and implicit models, equations have been derived that account for the influence of shear stress on cell growth. Additionally, homogenization techniques have been proposed to precisely capture the relationship between macroscopic parameters in these models, such as porosity and growth, and the fluid flow at the pore scale [32, 125, 167]. We briefly give examples of each of these kinds of approaches below.

After being seeded with cells, tissue engineering scaffolds are a composite medium composed of numerous interacting constituents, from different types of cells and ECM, to culture medium, and the scaffold itself. Multiphase approaches (sometimes called mixture theory) provide a natural spatially continuous framework within which each of these constituent components may be represented by spatially continuous variables, such as volume fraction, density, velocity, pressure, etc. The governing equations are determined by mass and momentum conservation for each phase together with suitable constitutive relationships that capture the material properties of each phase as well as interactions between phases. These fields which constitute each phase vary in time and space due to mitosis and apoptosis of cells, production of ECM, degradation of the scaffold, etc.

The basis of these multiphase models is a set of conservation laws which relate the volume fraction of the ith phase, θ_i, the density, ρ_i, velocity $\boldsymbol{u}_i$, and stress tensor σ_i. Typically the culture medium is very viscous and the flow velocity is small enough so that inertial terms can be neglected, although some models will include inertial terms in some subdomain of the model where the local velocity may be large.

For a system of n incompressible phases, neglecting any body forces, these conservation laws can be written as [124],

$$\rho_i \left(\frac{\partial \theta_i}{\partial t} + \nabla \cdot (\theta_i \boldsymbol{u}_i) = S_i \right), \tag{1.1}$$

$$\nabla \cdot (\theta_i \boldsymbol{\sigma}_i) + \sum_{j \neq i} \boldsymbol{F}_{ij} = \boldsymbol{0}, \tag{1.2}$$

where t denotes time, S_i is the net rate of mass transfer into the ith phase, $\boldsymbol{F}_{ij}$ denotes the force on phase i due to interactions with phase j, and the symbols ∇ and $\nabla\cdot$ are the spatial gradient and divergence operators respectively. Equations (1.1)-(1.2) represent conservation of mass and momentum respectively. In some parameter regimes, such as when the total flow rate is large, inertial terms must be retained in Equation (1.2). Equations (1.2)-(1.1) are augmented with constitutive relationships which describe how the stress tensor σ_i, as well as the interphase forces $\boldsymbol{F}_{ij}$, depend on the volume fraction and density of each phase. These constitutive relationships depend on the type of tissue being studied, the properties of the scaffold, and the flow regime under consideration [100, 149]. Finally, appropriate boundary and initial conditions are specified to close the system. We now review some of the relevant tissue engineering literature which has employed this kind of framework to determine governing equations to model tissue scaffolds. Such models can be used to explore nutrient transport, cell proliferation, and the cell density distribution within a tissue engineering scaffold.

Pearson et al [133, 134, 135, 136] employed a multiphase approach to model culture medium fluid, scaffold, and cell phases within a hollow fibre bioreactor. This bioreactor design consists of parallel hollow permeable tubes which facilitate nutrient transport to the cells seeded in the extracapillary space surrounding the fibres. The small aspect ratio of the bioreactor was used to simplify these models by transforming a 3-D model to one with a 1-D geometry, and the reduced systems of governing equations were then solved numerically to gain insight into how to stimulate uniform cell growth throughout the scaffold. O'Dea et al [126] developed a model of cells, culture medium, and tissue scaffold with the aim of understanding the role of cell-cell and cell-scaffold interactions on tissue growth in a perfusion bioreactor. The focus was on mechanotransduction effects, such as the influence of fluid shear stress on the cell growth. Their analytical and simulation results gave insight into using experimental data to determine the dominant mechanical regulatory mechanisms within a cell population. There is also a very large literature on the use of multiphase models in cancer biology and wound healing, but for brevity we do not review it here; see

[23, 24, 149] as examples and [2, 147, 148, 155, 158] for reviews of vascular and avascular tumour modelling. Multiphase models also appear in other areas of bioactive porous material, such as in the development and growth of biofilms [6, 49, 89].

We now discuss the class of implicit models. While these models typically account for multiple constituent phases within a bioreactor (e.g. cell, nutrient, scaffold) using mass and momentum conservation laws, these are not employed for every phase as in Equations (1.2)-(1.1). Rather, these models include the effect of cell growth on the fluid flow implicitly, by considering a cell density equation based only on conservation of mass, and then prescribing the scaffold porosity to be a function of cell density. As an example, the model presented in [166] considers a fluid modelled via Darcy's law, and reaction-diffusion equations describing the evolution of the nutrient and cell/ECM phases. These equations can be written in a general form as

$$\boldsymbol{u} = \frac{k(N)}{\mu}\nabla p, \quad \nabla \cdot \boldsymbol{u} = 0, \tag{1.3}$$

$$\frac{\partial N}{\partial t} = F(N, c, \sigma) + \nabla \cdot \left(D_N(N)\nabla N\right), \tag{1.4}$$

$$\frac{\partial c}{\partial t} + \boldsymbol{u} \cdot \nabla c = G(N, c, \sigma) + D_c \nabla^2 c, \tag{1.5}$$

where $\boldsymbol{u}$ is the fluid velocity, μ is the viscosity, N is the density of the cell phase, c is the concentration of the nutrient, $k(N)$ is the cell-density dependent permeability, σ is the fluid shear stress, D_N and D_c are diffusion rates of the cells and nutrient respectively, and F and G are cell growth and nutrient uptake relationships respectively. Note that the cell diffusion is given as a (generally nonlinear) function of the cell density N, in order to capture density-dependent dispersal of cells within a porous medium [124, 182]. Constitutive laws for this system are used to determine appropriate forms for the permeability $k(N)$ and the fluid shear stress σ which is related to the Darcy velocity $\boldsymbol{u}$ as well as the cell-dependent permeability. Finally, we remark that Equations (1.3)-(1.5) are a system of coupled elliptic and parabolic equations, as the fluid flow is quasi-static and hence slave to the temporal evolution of the cell density distributions, which themselves depend on the distribution of nutrients throughout the scaffold. We now review some examples of models of this type in the tissue engineering literature.

Coletti et al [36] proposed a model of nutrient transport, fluid flow, and nutrient-limited cell growth in a tissue-engineering bioreactor which was used to investigate the effect of experimental protocols employed to overcome diffusion-limited transport, and to study adverse conditions that are observed experimentally, such as flow channelling along bioreactor walls. Accounting for both cell-density-dependent permeability and mechanotransduction of shear stress by cells, Shakeel et al [166] investigated a model of nutrient transport and cell growth in a porous scaffold within a perfusion bioreactor. Cell proliferation and ECM deposition were assumed to decrease the local porosity, and hence permeability of the scaffold, while moderate values of the shear stress were assumed to enhance both cell growth and uptake of a generic nutrient by the cells. Although it was suggested that cell death would occur at higher values of shear stress (corresponding to higher flow rates into the scaffold), this was not explored. Pohlmeyer et al [145, 146] used a similar approach to [166] to model other aspects of cell growth in perfusion bioreactors, including growth-factor driven haptotaxis. Using comparable implicit modelling approaches, Nava et al [119] considered a nutrient and shear stress-dependent moving boundary problem to model cell growth in a multi-compartment computational model. Their results included development of computational approaches for coupling sub-models with 2 and 3 dimensional spatial regions. Hossain et al [76] considered the coupling of fluid shear stress, cell growth, and the fluid flow in a scaffold-free perfusion bioreactor.

Mathematical homogenization approaches have been proposed to upscale microscale features of the scaffold. These approaches begin by considering cell proliferation, fluid flow, and nutrient transport within a small microscale region (typically a single pore or a periodic ‘cell’ of a few pores). Exploiting the disparity between the lengthscale at this microscale and the overall lengthscale of the tissue scaffold or other porous medium, effective macroscopic equations can be derived using several similar approaches such as formal multiscale asymptotics or volume averaging [41]. Effective macroscale equations often take the form of either the multiphase models described by Equations (1.1)-(1.2), or the implicit models given by Equations (1.3)-(1.5), depending on how the equations governing the dynamics at the microscale are determined. Two major advantages to homogenization approaches are that they provide a justification or derivation for effective equations at the macroscale, and that they allow parameters in macroscale models to be directly related to microscale features under consideration, such as accretion of cell biomass in pores, or different pore geometries. We now consider some examples of this approach in tissue engineering and related literature.

Shipley et al [167] developed a model for fluid, glucose, and lactate transport in a microstructured porous medium. In this study, the variation of the effective permeability of the scaffold due to cell growth was not considered. O’Dea et al [125] considered the advection of a generic diffusible nutrient through a porous medium and derived macroscale equations accounting for microscale accretion of biomass at the pore surface due to nutrient uptake. Homogenisation has also been used to upscale fluid flow and elastic deformation in a fibre-reinforced hydrogel scaffold for cartilage tissue engineering [32]. Outside of tissue engineering, several other homogenisation approaches have been developed to upscale tissue growth processes. Irons et al [79] developed a model of biomass accretion in a porous medium aimed at understanding vascular tumour growth. Penta et al [139] derived a macroscopic model of a porous linearly elastic medium that accounted for mass exchange at the microscale between the phases due to accretion of the solid phase at the pore surface. Collis et al [37] determined effective equations for a poroelastic medium where microscale elastic stresses and deformations were homogenized alongside growth and solute transport. All of the above homogenization results are typically valid for specific parameter regimes, such as when the elastic and growth time scales are strongly separated.

1.1.2 Spatially Discrete, Network Structured, and Hybrid Models

In contrast to the spatially continuous models described above, network models have been used increasingly to describe porous media [160, 161]. These are 'mesoscopic' models, whereby the porous medium is discretized as a graph with nodes and edges linking them. Fluid flow can then be described by assigning a pressure to each node, and determining the flow rate between nodes, including any sources or sinks of fluid into the network.

To give some idea of the kind of structures these network models incorporate, we describe flow in an arbitrary network as done in [111, 112, 176] and many others. We consider an arbitrary graph described by an adjacency matrix A_{ij} such that $A_{ij} = 1$ if nodes i and j are connected by an edge, and $A_{ij} = 0$ otherwise. We consider a pressure, p_i, at each node i, and prescribe a flow between each node. For instance, it is common to assume Poiseuille flow between each node, so that

$$q_{ij} = \frac{\pi (R_{ij})^4}{8 l \mu}(p_i - p_j), \tag{1.6}$$

where q_{ij} is the volumetric flow rate ($\mathrm{m^3 s^{-1}}$) from node i to node j, R_{ij} is the effective radius of an idealized 'pipe' between these nodes, l is the length of the edge, and μ is the viscosity of the fluid. Assuming the fluid is incompressible, we can write conservation of mass at each node as

$$\sum_{j=1}^{n^2} A_{ij} q_{ij} = f_i, \tag{1.7}$$

where f_i are the volumetric flow rates into the nodes due to sources (e.g. at boundaries of the network). Other processes, such as cell growth and network remodelling, are assumed to occur on a longer timescale so that equations (1.6)-(1.7) are used to determine the flow through the network quasi-statically.

Network models of flow through porous media explicitly describing the pore structure have not, to the best of our knowledge, been used in the context of tissue engineering scaffolds. However, network approaches have been used to model flow in geological and geochemical porous media, such as the growth of biofilms in soils or mass accretion in pores due to solid forming reactions, as well as in angiogenesis and its applications to cancer modelling and wound healing [4, 113, 176, 180]. We now review some of these models as motivation for our network modelling approach. We also mention that Mely et al [116] and Barbotteau et al [11] used percolation theory to model random cell growth in a lattice to determine effective properties of bone tissue engineering scaffolds, although we note that the effect of flow on the growth process was not explicitly modelled, and biomechanical effects such as shear stress were therefore not included.

Biofilms growing in porous media have been modelled using a dynamic (e.g. time-dependent) pore network with coupling between the growth of the biofilm and flow throughout the network. Thullner and Baveye [176] proposed a lattice model of a porous medium, where growing biofilms clogged pores. Nutrients were carried by the fluid, affecting the biofilm growth throughout the porous medium. Different constitutive assumptions relating pressure differences to flow rates in pore throats were explored and resulted in global changes in hydraulic conductivity throughout the entire network. Gharasoo et al [60] and Rosenzweig et al [159] extended this approach to consider the influence of pore heterogeneity, as well as different kinds of reactions, within the network. Tsimpanogiannis and Lichtner [180] also considered a reactive transport model utilizing networks in a geochemical setting with solid formation leading to pore blocking, which resulted in changes in the flow throughout the network.

Returning to biological phenomena, network modelling has been used extensively in the study of angiogenesis, which is the formation of new blood vessels from existing ones. Alongside vascular network remodelling, angiogenesis plays a major role in cancer biology, wound healing, and developmental biology; see [129, 163, 198] for contemporary reviews of these fields. The discrete structure of microvessels has motivated a long history of using network models to understand their formation, and associated fluid and mass transport. Anderson and Chaplain [4] considered continuum and discrete models of endothelial-cell (tip cell) led vessel sprouting, and specifically derived the (probabilistic) movement of discrete cells via a finite-difference discretization of the corresponding continuum description. Capillaries then form behind these tip cells, growing the vascular network. Extending this approach, McDougall et al [112, 113] developed a network model for angiogenesis induced by a nearby tumour, and investigated fluid flow through the resulting network structure. Their results suggested that topological properties of the network, such as the number of anastomoses (loops), were key factors in determining the flow through the resulting network, which impacts the effectiveness of drug delivery via the vasculature. Reviews of some of the earlier theoretical literature utilizing these approaches can be found in [27, 29]. More recent network remodelling frameworks have been developed and applied to vascular tumours [150, 155, 164, 187] whereby vascular remodelling occurs due to lack of flow or tumour angiogenic factors being produced by cells due to hypoxia.

Many recent models of cancer growth and treatment, including many of the network models above, adopt an individual-cell-based modelling approach for some components of the overall tumour model, such as discrete cells. Individual-based models track the local microenvironment around a cell, composed of mechanical stresses and chemical concentrations, in order to capture biophysical interactions between cells and between cells and the surrounding environment [22, 53]. These models can either treat the cells as discrete cellular-automata confined to a spatial lattice [58], use off-lattice models of cells as points [44], or use cellular-Potts models which specify intracellular and environmental interactions via a Hamiltonian [62]. Similar discrete modelling approaches have also been employed in vasculogenesis [140]. Intracellular processes can be described by systems of ordinary differential equations which model processes in the cytoplasm and nucleus associated with each individual cell. Simulations of many individual cells are then used to gain insight into tissue-level behaviour [147].

Comparisons between individual-based and continuum models of growing cell populations have suggested certain parameter regimes where the approaches agree and disagree, which has implications for applicability and computational tractability of each kind of model [22, 127, 142]. Hybrid discrete and continuum models of vascular tumours have also been studied, where the vasculature itself has a discrete structure, but transport of nutrients, cell migration, and cell/ECM growth throughout the tumour is modelled as spatially continuous [50, 97, 106, 130, 137, 187, 190, 191, 196]. These hybrid models offer the advantage of describing the discrete structure of the vasculature, but can be efficiently simulated computationally [42]. Other multiscale frameworks linking vasculature, cell cycle dynamics, and other effects have also been pursued in the context of infectious diseases and tissue dynamics in general [34, 201], which combine spatially continuous and spatially discrete submodels.

Finally, we also mention analogous approaches to those used in angiogenesis applied to wound healing; these consist of similar continuum, discrete, and hybrid modelling approaches. McDougall et al [110] develops a hybrid discrete and continuum model of angiogenesis in retinal wound healing, using many of the same ideas of discrete tip cell migration as in [4]. Flegg et al [51] reviews the current state of reaction-transport models, in particular considering angiogenesis in the context of dermal wounds that heal via replenishment of granulation tissue and ECM. In a larger context, Jorgensen and Sanders [82] reviews models of wound healing and closure, differentiating between models based on the phase of the healing process (e.g. hemostasis, inflammation, proliferation, remodelling), concluding that many models emphasize contraction and proliferation, but that wound closure has been less well-studied. We particularly note the use of discrete models that characterize vasculature, as in the tumour literature discussed above, coupled to continuum models for reaction and transport of cells and nutrients [28, 171].

1.1.3 Prototypical Bioactive Scaffold in a Perfusion Bioreactor

Having reviewed some of the network and hybrid modelling literature, we return to the discussion of a tissue engineering scaffold as an active porous medium. The pore and scaffold length scales in typical experiments with perfusion bioreactors can lead to scaffolds with relatively few pores, and it is unclear that macroscopic spatially continuous models will capture features present in small networks of pores. Again referring to [103, 182] for general discussions of pore size, scaffold geometry, and transport phenomena in porous tissue scaffolds, we remark that the number of pores, channel lengths, and porosity in a typical tissue scaffold varies widely. This variety of scaffolds exists alongside large variations in the types of cells seeded onto these scaffolds (and the ECM that they produce), leading to a massive range of parameters only partly summarized by Table 1.1. Motivated by concerns with these spatially continuous modelling approaches, we propose a novel lattice model of a bioactive porous medium. We compare this to a typical continuum model, modified from [166], to elucidate the different kinds of behaviour displayed by each modelling paradigm.

We consider the following biological system that captures many of the features encountered when engineering artificial tissues. We model a cell phase, which incorporates the ECM produced by the cells, and a fluid phase modelling the culture medium, which together saturate a two-dimensional porous scaffold. We consider model behaviours on the timescale of cell proliferation, focusing in particular on the role of fluid mechanical stimuli on proliferation. On this timescale, we assume the scaffold remains rigid, and that cell growth and ECM production can influence the local permeability of the scaffold by, e.g., blocking pores. The models we develop are generic, so while we broadly parameterize and think of them in terms of the biological and physical characteristics shown in Table 1.1, we do not specialize to a particular cell type or scaffold. Rather, we demonstrate differences in model predictions that should hold even if the models were specialized to a particular tissue engineering setting. While we present general modelling frameworks which could be used to model many of the experiments cited at the beginning of this Chapter, changes to specific features of the models would be necessary to account for features of some experimental systems. For example, in the case of very large pores that are no longer well-approximated by cylindrical pipes, the constitutive relationship describing fluid flow between pores (Poiseuille flow) should be replaced by one representing the microscale flow more accurately.

A large variety of tissue scaffolds and cell types are used to grow artificial tissue within perfusion bioreactors [96]. We now discuss the kinds of scaffolds and cells that we envision within a perfusion bioreactor for which our models would be appropriate. We consider cells which are mechano-sensitive (e.g. to fluid shear stress [45, 48, 80]) so that it is sensible to think of cell proliferation and death as being strongly influenced by fluid-mechanical forcing. Examples of such cells include osteoblasts and endothelial cells, for which mechano-transduction of fluid-mechanical forces plays a key role in differentiation and proliferation. We also consider cells which, together with ECM, decrease the local permeability of the scaffold via pore-blocking as they proliferate [76, 182]. There are numerous techniques to produce tissue scaffolds, such as 3-D printing of porous hydroxyapatite and poly(vinyl)alcohol composites [39], and fabrication of collagen sponges via pepsin-digested bovine skin [63], among many others [78]. These scaffolds have a large range of pore sizes and channel geometries, as shown in Table 1.1, leading to a variety of scaffold porosities. Reviews such as [152, 154] report porosities from 40-98%, although more viable scaffolds tend to have higher porosities. Perfusion bioreactors often use scaffolds that are highly porous with porosities ranging from 70%-90%, and pore diameters typically in the range of 250μm-600μm [87].

In [166] and [30] it was assumed that moderate levels of shear stress would enhance cell proliferation, but the detrimental effects of large shear stress were not considered. Several studies have shown detrimental effects of high shear on renal epithelial cells [45] and pancreatic endothelial cells [162]. The influence of shear stress on cell adhesion and 'wash-out' has been studied for human fibroblast cells [91, 104]. We are interested in the effects of high levels of shear stress not explored in previously-mentioned models [30, 126, 166], and assume that cells die if the local shear stress exceeds a certain threshold, either due to specific mechano-transduction mechanisms for apoptosis, or due to detachment induced by the flow which has been investigated in the tissue engineering literature [109, 192]. Under this latter mechanism, our models assume that cells do not reattach to the scaffold downstream after detachment, which is appropriate for some cell types under high velocity viscous flows [168]. High levels of shear-stress were assumed to induced cell death and detachment in [31], where nutrient limitations and other biomechanical stimuli were considered in a hollow-fibre bioreactor. We assume that the culture medium is pumped into the scaffold at a fixed flow rate, and that local increases in cell density decrease the local permeability of the scaffold. For the sake of simplicity, we will first assume that the cells are in a nutrient-rich environment and hence we do not explicitly model a nutrient phase; we instead emphasize qualitative differences between lattice and continuum models with cell growth mediated only by a single function of the fluid flow (e.g. shear stress). Focusing on a single stimulus allows us to elucidate paradigmatic differences between spatially continuous and spatially discrete models in a simple setting. Additionally, we can think of death due to high levels of shear stress as corresponding to the degradation of nutrient modelled in [166]. In later Chapters we will modify the mechanical force of the fluid on the cells to consider variations on this approach, including using the local fluid flow rate as a proxy for nutrient transport in Chapter 4. This allows us to relax our assumption on the cells being in a nutrient-rich environment, while still focusing on a single stimulus model.

We note that the lattice model we derive has a similar discrete network structure to many models found in the angiogenesis literature, many of which originated in [4]. However, our model differs in two key ways from the majority of discrete and hybrid models in the tumour, wound healing, and biofilm modelling literature discussed above. Firstly, the underlying lattice topology is intended to represent the pore space of the tissue scaffold, and is a static network, rather than an evolving dynamic network. Secondly, we do not track individual cells with random motility, but instead consider nodal cell densities which diffuse via a continuous-time deterministic process.

The active aspect in our models consists of cells changing the local pore size, but not growing or remodelling the network as is considered in the angiogenesis literature.

This lattice modelling approach provides a 'mesoscopic' perspective, where the effective equations are ODEs at each node intended to capture the microscale dynamics at the pore scale, as opposed to homogenization approaches where the microscale is explicitly related to macroscale equations. As fluid and cell phases are described in this spatially discrete framework, there is no need to use a hybrid discrete-continuum approach to account for the pore network. This also allows us to use tools from dynamical systems theory which are substantially more tractable in the finite dimensional setting of ODEs (with algebraic conditions for the fluid flow), as opposed to the infinite dimensional setting of PDEs (consisting of coupled elliptic and parabolic equations). Additionally, issues of numerical convergence and existence of solutions that are important in the spatially continuous setting are much simpler in the finite-dimensional setting of ODEs. While this lattice model can be viewed as a method-of-lines discretization of a corresponding system of PDEs, the number of nodes is not a parameter which determines convergence to the solution of PDEs, but instead is a fixed physical parameter corresponding to the number of pores in a tissue scaffold. Additionally, the lattice model can be augmented with different constitutive laws capturing pore-scale geometrical details. In the limit of infinitely many pores, these constitutive differences could lead to a different continuum limit. Our emphasis on mesoscopic governing equations makes this network-based approach somewhat unique in the tissue engineering community, and could serve as an alternative to typical homogenized models.

1.2 Thesis Outline

Given the present state of the tissue engineering modelling literature, we believe there is a gap between spatially continuous and spatially homogeneous modelling approaches corresponding to experimental regimes where spatially discrete models are more appropriate. Motivated by these deficiencies, we propose several novel lattice models of a bioactive porous medium. We compare these to typical continuum models, modified from [36, 166, 193] and others cited therein, in order to elucidate the different kinds of behaviour displayed by each modelling paradigm. We emphasize qualitative differences between solutions to these continuum and discrete models. We describe the biological implications for the quantitative predictions from the spatially continuous and spatially discrete models. We explore relatively simple models to facilitate comparisons between these distinct approaches. The qualitative differences we demonstrate in the lattice model cannot easily be reconciled with the continuum approach, as the dynamics are fundamentally different. We also discuss these classes of models in terms of computational efficiency.

A major theme of the thesis is to thoroughly understand these differences between lattice and continuum models of bioactive porous media. For simplicity, we consider models that only account for fluid throughout the medium, and a cell phase. We do not separately consider the ECM produced by the cells, but use a single cell phase to account for both cells and ECM. We assume this cell phase blocks pores as cells proliferate, and hence this proliferation reduces the local conductivity of the porous medium. We also assume the cells are affected by the fluid flow via simple interaction terms motivated by models of mechanotransduction and mechanically-induced cell death. We do not consider nutrient transport, solid mechanical forces (e.g. we consider only rigid tissue scaffolds), or more complicated cellular physiology or motility beyond simple feedback mechanisms between fluid flow and cell proliferation and death. We also allow the cells to diffuse throughout the scaffold.

In Chapter 2 we describe the physical idealization of a bioactive porous medium that we use throughout the thesis, and then proceed to derive lattice and continuum models involving shear induced cell death at high values of the local shear stress. We nondimensionalize these models, highlighting the key parameters that remain and their physical interpretation. We then numerically simulate the models, demonstrating a variety of lattice-size-dependent patterning behaviours of the cell density throughout the scaffold. We discuss the onset and degree of heterogeneity of this patterning with respect to the nondimensional parameters. We show in particular that the cell density distributions between lattice and continuum models is typically very different, with more heterogeneous cell density distributions found in the lattice models. We include a term accounting for nonlinear cell diffusion, due to the porous structure of a tissue scaffold, and analyze the impact that this nonlinearity has compared to linear cell diffusion which we use in all of our subsequent analysis. We also observe oscillations in cell density only in the lattice model, which motivates studying a mathematically simpler variant of this model in Chapter 3. Most of the material in Chapter 2 can also be found in the paper [94].

In Chapter 3 we use the same modelling framework as before, but consider pressure-induced cell death at high local pressure instead. This leads to non-uniform patterning of a simpler nature, where typical solutions are horizontal gradients of cell density across the scaffold. We use regular asymptotic expansions in the diffusion parameter to show that the behaviour of cell density distributions in the large diffusion limit tends to a uniform spatial equilibrium. Away from this asymptotic regime, we observe vertically-symmetric and asymmetric oscillations in cell density for both continuum and lattice models, and describe a nonlocal mechanism that induces these oscillations. We use these results to simulate lattice and continuum models at sample points in a bounded region of parameter space in order to classify solution behaviours in terms of boundary conditions and dimensionality. We also show numerical continuation of low-dimensional lattice solutions, which allows us to elucidate properties of these different oscillations, and relate them back to those found in Chapter 2. In particular we find Hopf and pitchfork bifurcations in small lattices, and suggest why these bifurcations lead to asymmetric behaviours in solutions of the lattice model, whereas the behaviours of the continuum model are typically simpler. Most of the material from this Chapter is also contained in [93].

In Chapter 4 we present a third variation on this modelling framework, considering cell death due to values of the local fluid flow rate being too high or too low. Fluid flow is taken as a proxy for nutrient transport, and so low flow rates are assumed to induce cell death via starvation, whereas high flow rates are assumed to kill cells as they are washed away in a high flow regime. We demonstrate comparable patterning results to those of Chapter 2, but also find differences in the kinds of patterning due to starvation, especially between the lattice and continuum cases. Finally, we show that non-equilibrium dynamics are possible by revealing a time-varying pattern that is not a simple oscillation, as well as demonstrating chaotic dynamics in some parameter regimes. While we do not claim that these behaviours are physically meaningful, they do suggest some complicated spatio-temporal behaviours not found in our other models. These results suggest several directions for further work, in terms of both modelling fluid-growth coupling in biological media, and understanding discrete and continuum dynamical systems.

Chapter 5 contains a final variation on the preceding types of models involving a stochastic growth process which we describe algorithmically. We only consider dynamics on lattice domains, and simulate these stochastic processes for the shear, pressure, and fluid flow rate models described in the previous Chapters. We compare these simulations to deterministic simulations with random initial conditions. We find a variety of interesting behaviours for these models including cases where the random process settles into a simple stationary distribution corresponding to a specific cell density distribution, and other cases where the stochastic process settles into a time-dependent random behaviour. We demonstrate evidence for a concentration of measure that occurs for larger lattices such that some observables (e.g. the spatial mean cell density) become less sensitive to initial conditions for both stochastic and deterministic models, as the lattice size increases. This concentration of measure also applies to the randomness inherent in the growth process, so that the standard deviation between spatial mean cell density between different random realizations decreases as the lattice size increases. This suggests that for large lattices, the long-time behaviour is determined purely by parameters in the model and not by initial cell densities or random fluctuations. Finally we show how computationally efficient the stochastic algorithms are compared to their deterministic counterparts.

We conclude in Chapter 6 with an overview of our results and their implications for modelling bioactive porous media. We specifically review our findings about lattice versus continuum models, and suggest experimental regimes where accounting for the discrete pore network directly may influence model behaviours substantially. We highlight several outstanding questions, as well as promising directions for further work in understanding these kinds of active media. In particular, while our primary motivation throughout this work is on modelling a bioactive tissue engineering scaffold, we believe that our results are widely applicable to active porous media in general. For example, modifications of our models could be useful in understanding the mechanical interactions of fluid flow and biofilms in porous media [46, 143]. As many of the results in this thesis are obtained by numerically integrating ordinary and partial differential equations, we review basic numerical analysis concepts and demonstrate convergence checks for our simulations in Appendix A.

Chapter 2

Modelling of a Bioactive Porous Tissue Scaffold with Shear-Stress Induced Cell Death

A contemporary procedure to grow artificial tissue is to seed cells onto a porous biomaterial scaffold and culture it within a perfusion bioreactor to facilitate the transport of nutrients to growing cells. Typical models of cell growth for tissue engineering applications make use of spatially homogeneous or spatially continuous equations to model cell growth, flow of culture medium, nutrient transport, and their interactions. The network structure of the physical porous scaffold is often incorporated through parameters in these models, either phenomenologically or through techniques like mathematical homogenization. We derive a model on a square grid lattice to demonstrate the importance of explicitly modelling the network structure of the porous scaffold, and compare results from this model with those from a modified continuum model from the literature. We capture two-way coupling between cell growth and fluid flow by allowing cells to block pores, and by allowing the shear stress of the fluid to affect cell growth and death. We explore a range of parameters for both models, and demonstrate quantitative and qualitative differences between predictions from each of these approaches, including spatial pattern formation and local oscillations in cell density present only in the lattice model. These differences suggest that for some parameter regimes, corresponding to specific cell types and scaffold geometries, the lattice model gives qualitatively different model predictions than typical continuum models. Our results inform model selection for bioactive porous tissue scaffolds, aiding in the development of successful tissue engineering experiments and eventually clinically successful technologies.

The main novel contributions of this Chapter consist of the development and analysis of a lattice model of coupled cell growth and fluid flow in a bioactive porous medium, as well as an exploration of fluid shear stress induced cell death, which has received little attention in the theoretical modelling literature. Additionally, we relate our lattice model to an analogous continuum model, and discuss differences between these alternative modelling approaches. We demonstrate novel phenomena exhibited by the lattice framework, including oscillations in cell density not found in the spatially continuous model. These differences between lattice and continuum models become more pronounced as the size of the lattice decreases. While discrete and continuum models have been compared in the literature (e.g. in [22]), our lattice modelling approach differs from these as described in Section 1.1.3.

In this Chapter, we consider the following biological system that captures many of the features encountered when engineering artificial tissues. We model a cell phase, which incorporates the ECM produced by the cells, and a fluid phase modelling the culture medium, which together saturate a two-dimensional porous scaffold. We consider model behaviours on the timescale of cell proliferation, focusing in particular on the role of shear stress on cell proliferation. In [166] and [30] it was assumed that moderate levels of shear stress would enhance cell proliferation, but the detrimental effects of large shear stress were not considered. Several studies have shown detrimental effects of high shear on renal epithelial cells [45], pancreatic endothelial cells [162], and the influence of shear stress on cell adhesion and 'wash-out' has been studied for human fibroblast cells [91, 104]. We are interested in the effects of high levels of shear stress not explored in previously-mentioned models, and assume that cells die if the local shear stress exceeds a certain threshold, either due to specific mechano-transduction mechanisms for apoptosis, or due to detachment induced by the flow [109, 192]. Under this latter mechanism, our model assumes that cells do not reattach to the scaffold downstream after detachment, which is appropriate for some mechanical environments and cell types [168]. High levels of shear-stress were assumed to induce cell death and detachment in [31], where nutrient limitations and other biomechanical stimuli were considered in a hollow-fibre bioreactor. We assume that the culture medium is pumped into the scaffold at a fixed flow rate, and that local increases in cell density decrease the local permeability of the scaffold. For the sake of simplicity, we do not explicitly model a nutrient phase but instead emphasize qualitative differences between lattice and continuum models that appear to be generic independent of nutrient model used. Additionally, we can think of death due to high levels of shear stress as being related to the degradation of nutrient explored in [166].

While spatially discrete models of active porous media exist in other contexts, as discussed in Section 1.1.2, the model developed in this Chapter is the first such model in tissue engineering that the authors are aware of. Similarly, shear stress induced cell death was accounted for in [31], but exploring this effect was not the chief goal of their work, and so our results here are the first to present the impact of shear-stress induced cell death in a bioactive porous medium. Additionally, we emphasize results on the spatial patterning of the cell density distribution and how this distribution depends on both the modelling paradigm and parameter values in the models. The key insight of this Chapter is that the development of the cell density distribution heavily depends on the density of pores within the tissue scaffold, as well as how large the effect of cell diffusion is, as this is the primary factor which determines how much heterogeneity the cell density distribution develops over time.

In Section 2.1 we present our continuum and lattice modelling approaches, and discuss the physical and biological parameters. In Section 2.2 we compare results from these two models, primarily using numerical simulations. Finally in Section 2.3 we discuss the implications of our study for the successful modelling of porous media in tissue engineering applications.

2.1 Motivation and Modelling Frameworks

We consider a two dimensional rigid porous medium as a model of the tissue scaffold. For simplicity, we consider a square domain with side length L. The culture medium is an incompressible viscous Newtonian fluid, with dynamic viscosity μ. We assume that fluid is pumped at a constant flow rate Q_c ($\mathrm{m}^2\mathrm{s}^{-1}$) into the left side of the domain, and exits through the right side. We assume no fluid enters or leaves through the horizontal boundaries of the domain. See Figure 2.1(a) for a visualization of the domain. We assume that cells grow logistically, diffuse within the scaffold, and cannot leave the domain. We assume that cells will stop growing and will die if the shear stress exceeds a threshold value. The timescale of interest is that of cell proliferation. Finally, we neglect advection of the cells by the fluid, as we assume cells which are detached from the scaffold do not reattach downstream.

2.1.1 Continuum Model of a Bioactive Porous Medium

We describe the square domain as spatially continuous with Cartesian coordinates $\boldsymbol{x}^* = (x^*, y^*) \in [0, L]^2$ (we use asterisks throughout to denote dimensional variables).

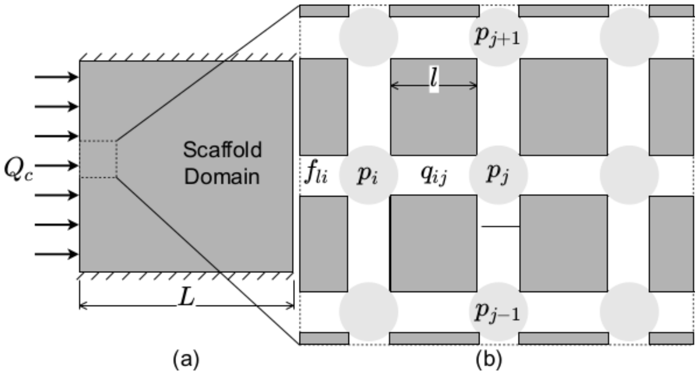

Figure 2.1: A diagram of the scaffold domain (a) where fluid enters at a prescribed flow rate, Q_c, from the left and exits on the right side of the scaffold. The horizontal boundaries are impermeable. Enlarged (b) is the lattice structure of the scaffold, with fluid entering node i from the left boundary at a volumetric flow rate f_{li}. L denotes the size of the scaffold, l the length of an internal 'pipe,' p_i the pressure at node i, and q_{ij} the volumetric flow rate from node i to node j. Fluid is present in the white and light gray regions (denoting nodes in the lattice model), and the dark gray regions are impermeable.

We assume that the pore Reynolds number is small and neglect fluid inertia. We use Darcy's Law to model flow through the scaffold [13], so that

$$\boldsymbol{u}^* = -\frac{k^*(x^*, y^*, N^*)}{\mu}\nabla^* p^* \quad \text{and} \quad \nabla^* \cdot \boldsymbol{u}^* = 0, \tag{2.1}$$

where $\boldsymbol{u}^*$ is the Darcy velocity of the fluid, p^* is the fluid pressure, and $k^*(x^*, y^*, N^*)$ is the permeability of the scaffold which depends on the cell density N^*.

For ease of computation, we prescribe a pressure drop across the domain so that, along with no flux conditions at the horizontal boundaries, we impose

$$\boldsymbol{n} \cdot \boldsymbol{u}^* = 0 \ \text{ at } \ y^* = 0, L, \ \ 0 \leq x^* \leq L, \tag{2.2}$$

$$p^* = p_0 \ \text{ at } \ x^* = 0, \ \ 0 \leq y^* \leq L, \quad \text{and} \quad p^* = p_1 \ \text{ at } \ x^* = L, \ \ 0 \leq y^* \leq L, \tag{2.3}$$

where p_0 is the upstream pressure, p_1 is the downstream pressure, and $\boldsymbol{n}$ is the outward unit normal.

We use the linearity between pressure and the Darcy velocity to rescale the fluid variables to match the prescribed fluid flow rate through the scaffold. The total flow rate through the boundary at $x^* = 0$ is

$$Q_0^* = \int_0^L -\frac{k^*(0, y^*, N^*)}{\mu}\frac{\partial p^*}{\partial x^*} dy^*. \tag{2.4}$$

We define the rescaled Darcy velocity to be,

$$\boldsymbol{u_r^*} = \frac{Q_c}{Q_0^*}\boldsymbol{u}^*. \tag{2.5}$$

The cell density N^* is governed by the reaction-diffusion equation,

$$\frac{\partial N^*}{\partial t^*} = \beta\left(F_1(\sigma^*)N^*\left(1 - \frac{N^*}{N_c}\right) - F_2(\sigma^*)N^*\right) + \nabla^* \cdot (D^*(N^*)\nabla^* N^*), \tag{2.6}$$

where t^* is time, N_c is the maximum cell density, β is the cell proliferation rate, D^* is a nonlinear cell diffusion coefficient, σ^* is the fluid shear stress, and the dimensionless functions $F_1(\sigma^*)$ and $F_2(\sigma^*)$ capture the effect of fluid shear stress on growth and death respectively. The terms on the right hand side correspond to logistic growth, cell death, and cell diffusion respectively. For simplicity we assume that β also quantifies the death rate due to high shear, and F_1 and F_2 are dimensionless functions of the shear stress that vary between 0 and 1 (see 2.12).

The no flux conditions for the cell density are,

$$\boldsymbol{n} \cdot \nabla N^* = 0 \text{ for } \boldsymbol{x} \in \partial[0, L]^2, \tag{2.7}$$

where $\partial[0, L]^2$ denotes the boundaries of the square domain. Finally we impose the following initial condition for cell density,

$$N^*(x^*, y^*, 0) = N_0^*(x^*, y^*), \tag{2.8}$$

where $N_0^*(x^*, y^*)$ is the initial scaffold seeding density.

We now specify how the scaffold permeability k^* appearing in Equation (2.1) depends on the cell density N^*. Following [36], we write the porosity as

$$\hat{\phi}(N^*) = \phi_0(1 - \nu N^*), \tag{2.9}$$

where ϕ_0 is the volume fraction of pore space in the scaffold without cells, and ν is the volume of pore space occupied by an individual cell. We require that $\nu N_c \leq 1$ so that under the bounded dynamics of Equation (2.6), $0 \leq \hat{\phi}(N^*) \leq \phi_0$ for all $N^* \leq N_c$.

We follow [166] and relate the cell-dependent porosity to the scaffold permeability via

$$k^*(N^*) = k_0\hat{\phi}(N^*)^3, \tag{2.10}$$

where k_0 is the permeability of the cell-free scaffold.

We require an expression for the shear stress σ^* in Equation (2.6). We follow [193] and [166] and write,

$$\sigma^* = \frac{4\mu\tau}{R_0}\frac{\|\boldsymbol{u_r^*}\|}{\hat{\phi}(N^*)}, \tag{2.11}$$

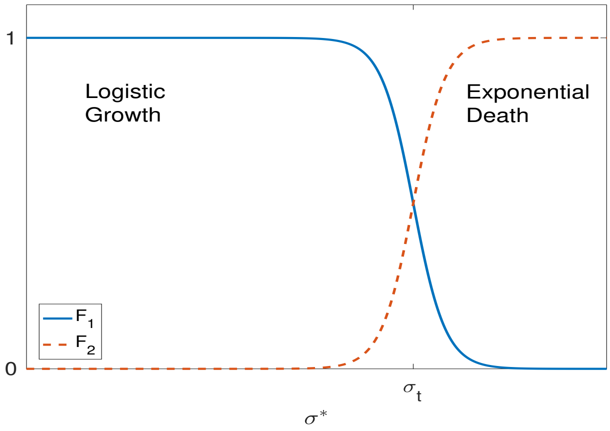

Figure 2.2: Plots of the shear stress functions, $F_1(\sigma^*)$ and $F_2(\sigma^*)$. For $\sigma^* < \sigma_t$, cells grow logistically, whereas for $\sigma^* > \sigma_t$, cells die. These effects are local in space as the value of the shear stress depends on the position in the scaffold, and the overall profile of the flow.

as the shear stress experienced by cells at the pore scale in terms of the Darcy velocity, where R_0 is the typical radius of a pore and τ is the tortuousity of a typical fluid path. As in [193] and [166], we neglect the influence that cells have on the tortuousity τ and treat it as a nondimensional constant corresponding to the average ratio of streamline lengths to the straight-line distance between two points. The more tortuous the scaffold, the faster the interstitial fluid has to be to travel longer paths in the same time.

Finally we specify the functions $F_1(\sigma^*)$ and $F_2(\sigma^*)$ to be

$$F_1(\sigma^*) = 1 - \left(\frac{1}{2}\right)(\tanh[g(\sigma^* - \sigma_t)] + 1), \text{ and } F_2(\sigma^*) = \left(\frac{1}{2}\right)(\tanh[g(\sigma^* - \sigma_t)] + 1), \tag{2.12}$$

where g and σ_t are sharpness and threshold parameters. Caricatures of these functions are plotted in Figure 2.2. These functions model smoothed step-function behaviour and are commonly used in the literature [36, 166]. These functions capture logistic growth for small and moderate shear stress, and cell death at large values of shear stress.

We nondimensionalise as follows

$$(x^*, y^*) = L(x, y), \quad \nabla^* = \frac{1}{L}\nabla, \quad (N^*, N_0^*) = N_c(N, N_0), \quad \hat{\phi}(N^*) = \phi_0\phi(N),$$

$$k^*(N^*) = k_0\phi_0^3 k(N), \quad p^* = (p_0 - p_1)p + p_1, \quad \boldsymbol{u}^* = \frac{k_0\phi_0^3(p_0 - p_1)}{\mu L}\boldsymbol{u}, \quad \boldsymbol{u}_{\boldsymbol{r}}^* = \frac{Q_c}{L}\boldsymbol{u}_{\boldsymbol{r}},$$

$$D^*(N^*) = D_n D(N),\ \ Q_0^* = \frac{k_0 \phi_0^3 (p_0 - p_1)}{\mu} Q_0,\ \ \sigma^* = \frac{4\mu\tau Q_c}{L R_0 \phi_0}\sigma,\ \ t^* = \frac{t}{\beta}, \tag{2.13}$$

leading to the following nondimensional system of equations,

$$\boldsymbol{u} = -k(N)\nabla p,\ \ \nabla \cdot \boldsymbol{u} = 0, \tag{2.14a,b}$$

$$\frac{\partial N}{\partial t} = F_1(\sigma) N (1 - N) - F_2(\sigma) N + \delta \nabla \cdot \left(D(N) \nabla N \right), \tag{2.14c}$$

$$Q_0 = \int_0^1 -k(N(0, \hat{y}, t)) \frac{\partial p}{\partial x}(0, \hat{y}) d\hat{y},\ \ \boldsymbol{u_r} = \frac{\boldsymbol{u}}{Q_0}, \tag{2.14d,e}$$

$$\phi(N) = (1 - \rho N),\ \ k(N) = \phi(N)^3,\ \ \sigma = \frac{\|\boldsymbol{u_r}\|}{\phi(N)}, \tag{2.14f,g,h}$$

$$F_1(\sigma) = 1 - \left(\frac{1}{2}\right)(\tanh[g_c(\sigma - \sigma_c)] + 1),\ \ F_2(\sigma) = \left(\frac{1}{2}\right)(\tanh[g_c(\sigma - \sigma_c)] + 1), \tag{2.14i,j}$$

where $\rho = \nu N_c$ is the maximum available fraction of the pore space the cells can occupy, $\delta = D_n/\beta L^2$ is the ratio of proliferation and diffusion timescales, $g_c = (4\mu\tau Q_c)/(L R_0 \phi_0) g$ is a sharpness parameter, and $\sigma_c = (L R_0 \phi_0)/(4\mu\tau Q_c)\sigma_t$ is the threshold parameter.

The nondimensional boundary conditions are

$$\boldsymbol{u} \cdot \boldsymbol{n} = 0 \ \text{ at } \ y = 0, 1,\ \ 0 \leq x \leq 1, \tag{2.15}$$

$$p = 1 \ \text{ at } \ x = 0,\ \ 0 \leq y \leq 1, \quad \text{and} \quad p = 0 \ \text{ at } \ x = 1,\ \ 0 \leq y \leq 1, \tag{2.16}$$

$$\boldsymbol{n} \cdot \nabla N = 0 \ \text{ for } \boldsymbol{x} \in \partial[0, 1]^2, \tag{2.17}$$

with the initial data

$$N(x, y, 0) = N_0(x, y). \tag{2.18}$$

Equations (2.14)-(2.18) are a modified form of those used by [166], where we have neglected nutrient transport and nonlinear cell diffusion, but included a mechanism for cell death induced by high shear stress.

2.1.2 Lattice Model

We idealize the scaffold domain of length L as an n by n square lattice representing the connectivity between pores. At each node we specify the local cell density together with fluid pressures which we use to define volumetric flow rates along the edges between nodes. We assume these edges represent pipes of length $l = L/n$. See Figure 2.1 for a diagram of this idealization.

We prescribe a constitutive law relating the pressure p_i at each node i with the volumetric flow rate between the nodes, where $1 \leq i \leq n^2$. The particular form of this relationship depends on the microstructure of the scaffold under consideration, but for simplicity we assume Poiseuille flow between each node, so that

$$q_{ij}^* = \frac{\pi (R_{ij}^*)^4}{8 l \mu}(p_i^* - p_j^*), \tag{2.19}$$

where q_{ij}^* is the volumetric flow rate ($\mathrm{m}^3\mathrm{s}^{-1}$) from node i to node j, and R_{ij}^* is the effective radius of the pipe between these nodes, which will depend on the cell density at the nearby nodes (see Equation (2.26)).

Due to incompressibility, we can write conservation of mass at each node as

$$\sum_{j=1}^{n^2} A_{ij} q_{ij}^* = \begin{cases} f_{li}, & 1 \leq i \leq n, \\ 0, & n < i \leq n^2 - n, \\ -f_{ir}, & n^2 - n < i \leq n^2, \end{cases} \tag{2.20}$$

where A_{ij} is the unweighted undirected adjacency matrix of the lattice representing the connectivity of nodes, and f_{li} and f_{ir} are the volumetric flow rates into the nodes at the left and the right side of the scaffold respectively, which will be used to prescribe the total volumetric flow rate into the scaffold. We have that $A_{ij} = 1$ if there is an edge between node i and node j, and otherwise $A_{ij} = 0$. While we only consider a square lattice here, this formulation is general and any pore network topology can be accounted for by providing a different adjacency structure.

As in Section 2.1.1 we prescribe a pressure drop across the domain. We fix the pressure upstream of the left boundary as p_0, and the pressure downstream of the right boundary as p_1. Then the volumetric flow rate of fluid entering each node at the left is given by $f_{li} = (\pi R_0^4 (p_0 - p_i^*))/(8 l \mu)$ for $1 \leq i \leq n$, and the volumetric flow rate of fluid leaving each node along the right by $f_{ir} = (\pi R_0^4 (p_i^* - p_1))/(8 l \mu)$ for $n^2 - n < i \leq n^2$, where R_0 is the radius of pipes entering and exiting the scaffold.

We combine equations (2.19) and (2.20) together with the expressions for the boundary volumetric flow rates f_{li} and f_{ir}, to find that for all nodes i,

$$\sum_{j=1}^{n^2} A_{ij} (R_{ij}^*)^4 (p_i^* - p_j^*) = \begin{cases} R_0^4 (p_0 - p_i^*), & 1 \leq i \leq n, \\ 0, & n < i \leq n^2 - n, \\ -R_0^4 (p_i^* - p_1), & n^2 - n < i \leq n^2. \end{cases} \tag{2.21}$$

Equations (2.21) represent an algebraic system of n^2 equations for the nodal pressures, p_i^*. As before, the physically relevant boundary condition is a constant volumetric flow rate into the scaffold. We exploit the linearity of the fluid problem above to rescale the fluid variables to match this condition. The total volumetric flow rate into the pipes along the left boundary is

$$Q^* = \sum_{i=1}^{n} \frac{\pi R_0^4}{8l\mu}(p_0 - p_i^*). \tag{2.22}$$

We rescale the volumetric flow rates q_{ij}^* by,

$$q_{ij}^{r*} = q_{ij}^* \frac{Q_l}{Q^*}, \tag{2.23}$$

where Q_l is the volumetric flow rate into the scaffold. Note that Q_l has dimensions of $\mathrm{m}^3\mathrm{s}^{-1}$, whereas for the 2-D spatially continuous model, the flow rate Q_c had dimensions of $\mathrm{m}^2\mathrm{s}^{-1}$. If we assume that the mean fluid velocity (not the Darcy velocity) into the pore space of the scaffold along the left boundary is the same between the two models, we must have $Q_c/(L\phi_0) = Q_l/(n\pi R_0^2)$ where the factor of πR_0^2 is the cross-sectional area of each pipe, and n accounts for the number of pipes along the leftmost boundary. Hence $Q_l = (n\pi R_0^2 Q_c)/(L\phi_0)$, and we use this relationship in the remainder of the Chapter.

Again assuming that cells grow logistically, die, and diffuse to neighbouring nodes, the evolution equation for the cell density N_i^* at node i is

$$\frac{dN_i^*}{dt^*} = \beta\left(F_1^l(\sigma_i^*)N_i^*\left(1 - \frac{N_i^*}{N_c}\right) - F_2^l(\sigma_i^*)N_i^*\right) + \sum_{j=1}^{n^2} A_{ij}D^*(N_i^*, N_j^*)(N_j^* - N_i^*), \quad i = 1\ldots n^2, \tag{2.24}$$

where $D^*(N_i^*, N_j^*)$ is the local nonlinear cell diffusion rate to move between neighboring nodes, σ_i^* is a local average of the shear stress defined in Equation (2.29), and the functions F_1^l and F_2^l model the effect of shear stress on cell growth and death. Equations (2.24) are analogous to Equation (2.6). In particular, the cell proliferation rate β and maximum cell density N_c have the same meaning as in Equation (2.6). The cell diffusion rate between nodes can be related to cell diffusion on the length scale of the scaffold D_n by $D_l = D_n/l^2 = n^2 D_n/L^2$. We specify an initial condition at each node as

$$N_i^*(0) = N_{i0}^*. \tag{2.25}$$

We model the effect of cell growth on the fluid flow by taking the effective radius of a pipe to depend on the nearby cell densities as

$$R_{ij}^* = R_0\left(1 - \frac{\nu}{2}(N_i^* + N_j^*)\right), \tag{2.26}$$

where again ν represents cell volume. Equation (2.26) models pipes with radii that linearly decrease as the cell density increases at nearby nodes. Note that we must have $\nu N_c \leq 1$ for this radius to be non-negative for all feasible cell densities. This relationship is analogous to the porosity relationship given in Equation (2.9).

We compute the shear stress in each pipe under the assumption of Poiseuille flow made in Equation (2.19). The local velocity profile in the pipe R_{ij}^* is

$$u_{ij}^*(r^*) = -2\left(\frac{(R_{ij}^*)^2 - (r^*)^2}{\pi(R_{ij}^*)^4}\right) q_{ij}^{r*}, \tag{2.27}$$

where $0 \leq r^* \leq R_{ij}^*$ is the radial coordinate. The magnitude of the shear stress at the wall of each pipe is then

$$\sigma_{ij}^* = \mu\left|\frac{\partial u_{ij}^*}{\partial r^*}\left(R_{ij}^*\right)\right| = \frac{4\mu}{\pi(R_{ij}^*)^3}\left|q_{ij}^{r*}\right|. \tag{2.28}$$

As cell densities are defined at the nodes, we must relate the shear stress in each idealized pipe to an average shear stress σ_i^* at each node. We note that adding the shear stresses from the four neighboring nodes accounts for the total volumetric flow rate twice, so we sum the shear stress in each pipe connected to node i and divide by 2 to obtain

$$\sigma_i^* = \frac{1}{2}\sum_{j=1}^{n^2} A_{ij}\sigma_{ij}^* = \sum_{j=1}^{n^2} A_{ij}\frac{2\mu}{\pi(R_{ij}^*)^3}\left|q_{ij}^{r*}\right|. \tag{2.29}$$

We model the influence of this averaged shear stress on cell proliferation and death as before by

$$F_1^l(\sigma_i^*) = 1-\left(\frac{1}{2}\right)(\tanh[g(\sigma_i^*-\sigma_t)]+1), \quad F_2^l(\sigma_i^*) = \left(\frac{1}{2}\right)(\tanh[g(\sigma_i^*-\sigma_t)]+1). \tag{2.30}$$

These functions have the same form as those in Equations (2.12); see Figure 2.2 for a visualization.

For each $1 \leq i, j \leq n^2$ we nondimensionalize by taking

$$p_i^* = (p_0 - p_1)p_i + p_1, \quad Q^* = \frac{\pi R_0^4(p_0 - p_1)}{8l\mu}Q, \quad (N_i^*, N_{i0}^*) = N_c(N_i, N_{i0}),$$

$$D^*(N_i^*, N_j^*) = D_l D(N_i, N_j), \quad q_{ij}^{r*} = \frac{n\pi R_0^2 Q_c}{L\phi_0}q_{ij}^r,$$

$$q_{ij}^* = \frac{\pi R_0^4(p_0 - p_1)}{8l\mu}q_{ij}, \quad \sigma_i^* = \frac{2\mu Q_c}{L\phi_0 R_0}\sigma_i, \quad t^* = \frac{t}{\beta}, \quad R_{ij}^* = R_0 R_{ij}, \tag{2.31}$$

from which we obtain

$$q_{ij} = R^4(N_i, N_j)(p_i - p_j), \tag{2.32a}$$

$$\sum_{j=1}^{n^2} A_{ij} q_{ij} = \begin{cases} 1 - p_i, & 1 \le i \le n, \\ 0, & n < i \le n^2 - n, \\ -p_i, & n^2 - n < i \le n^2, \end{cases} \tag{2.32b}$$

$$\frac{dN_i}{dt} = F_1^l(\sigma_i) N_i (1 - N_i) - F_2^l(\sigma_i) N_i + \delta n^2 \sum_{j=1}^{n^2} A_{ij} D(N_i, N_j)(N_j - N_i), \tag{2.32c}$$

$$Q = \sum_{i=1}^{n} 1 - p_i, \;\; q_{ij}^r = q_{ij} \frac{1}{Q}, \;\; R_{ij} = 1 - \frac{\rho}{2}(N_i + N_j), \;\; \sigma_i = n \sum_{j=1}^{n^2} A_{ij} R_{ij} \left| q_{ij}^r \right|, \tag{2.32d,e,f,g}$$

$$F_1^l(\sigma_i) = 1 - \left(\frac{1}{2}\right)(\tanh[g_l(\sigma_i - \sigma_l)] + 1), \;\; F_2^l(\sigma_i) = \left(\frac{1}{2}\right)(\tanh[g_l(\sigma_i - \sigma_l)] + 1), \tag{2.32h}$$

where $i = 1 \dots n^2$, $\delta = (D_n)/(L^2 \beta)$ is the ratio of proliferation and diffusion timescales, $\rho = \nu N_c$ is the maximum available fraction of pore radius cells can occupy, $g_l = (2\mu Q_c g)/(L R_0 \phi_0)$ is a sharpness parameter, and $\sigma_l = (L R_0 \phi_0 \sigma_t)/(2\mu Q_c)$ is the shear stress threshold parameter. Note that ρ and δ are identical parameters between the lattice and continuum models. The parameters g_l and σ_l are analogous to g_c and σ_c but may have different values for a particular experimental system. The number of pores, n, does not explicitly appear in the cell density equation (except to scale diffusion) or the constitutive law for its relationship to pipe radii as we have accounted for issues of lengthscale in thinking of N_i as the nondimensional density of cells, rather than a cell number. The effects of size constraints on cell growth are hence captured by the parameters ν and N_c which we have nondimensionalized into the parameter ρ which will in practice vary with the scaffold size L, pore lengthscale l and pore radius R_0, but we have left this relationship unspecified for generality in order to model different geometric pore structures. We also have the initial data

$$N_i(0) = N_{i0}, \quad 1 \le i \le n^2. \tag{2.33}$$

In addition to fundamental differences between a spatial continuum and a discrete lattice, there are two significant constitutive differences between our models. The exponents in the relationships between the Darcy velocity, $\boldsymbol{u_r}$, or volumetric flow rates, q_{ij}, which play analogous roles, and the cell density are not the same between the two models. To see this, we write Equation (2.14a) using the permeability k and porosity ϕ in Equations (2.14f,g) as

$$\boldsymbol{u} = -\left(1 - \rho N\right)^3 \nabla p, \tag{2.34}$$

and similarly rewrite (2.32a) using the effective pipe radii from Equation (2.32f) to find,

$$q_{ij} = \left(1 - \frac{\rho}{2}\left(N_i + N_j\right)\right)^4 (p_i - p_j). \tag{2.35}$$

These relationships show that for a given local pressure drop, the local Darcy velocity in the PDE is larger in regions of high cell density than the corresponding volumetric flow rate in the lattice.

There are also differences in the nondimensional expressions for the shear stress in each model (see Equation (2.14h) and Equation (2.32g)). To visualize how these constitutive differences lead to quantitatively different predictions, consider a uniform cell density in both models. Let $N(x, y, t) = \hat{N}(t)$ for all (x, y) in the domain and $N_i(t) = \hat{N}(t)$ for $1 \le i \le n^2$. For a uniform cell density, the fluid flow is uniform so $\|\boldsymbol{u_r}\| = 1$ and $q^r_{ij} = 1/n$ for all i, j. This can be seen from solving Equations (2.14a,b) and (2.14d-h) for the PDE, or Equations (2.32a,b), and (2.32d-g) for the lattice. Note that in the lattice, we have nondimensionalized such that the total volumetric flow rate into the scaffold from the left boundary is 1, leading to the flow in each horizontal pipe being $1/n$ as there are n pipes along the boundary. We can then compute the (spatially uniform) shear stress for the PDE model as,

$$\sigma = \frac{\|\boldsymbol{u_r}\|}{\phi(N)} = \frac{1}{1 - \rho\hat{N}}, \tag{2.36}$$

and for the lattice model as,

$$\sigma_i = n \sum_{j=1}^{n^2} A_{ij} R_{ij} \left|q^r_{ij}\right| = \frac{2}{(1 - \rho\hat{N})^3}. \tag{2.37}$$

We plot these shear stresses as functions of $\hat{N}$ in the interval $[0, 1]$ in Figure 2.3. For large cell densities, the shear stress experienced by the cells in the continuum and lattice models differs by two orders of magnitude. These differences between Equations (2.36) and (2.37) prevent quantitative agreement between our models; we emphasize qualitative differences between the model predictions by exploring ranges of parameters in the following discussion.

Various forms of nonlinear cell diffusion have been used to model the movement of cells within porous media. For simplicity, we primarily consider only linear cell diffusion ($D(N) = D(N_i, N_j) = 1$), so that both models have linear cell diffusion at a rate δ. In Section 2.2.5 we demonstrate that the linear diffusion regime still accurately captures the main features we are trying to illustrate.

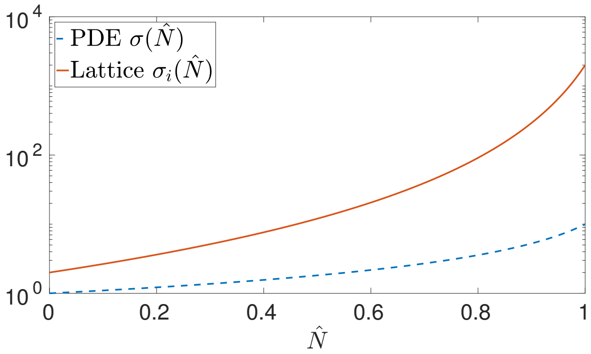

Figure 2.3: Plots of the uniform shear stress for a uniform cell density distribution $\hat{N}$, for $\rho = 0.9$. Note that the vertical axis is scaled logarithmically.

Parameter	Expression	Values
Cell volume[7]	ν	$4.2 \times 10^3 - 1.7 \times 10^4 \mu\text{m}^3/\text{cell}$
Maximum cell density [1] [2] [7]	N_c	$10^{13} - 10^{14}\text{cell/m}^3$
Scaffold length[7]	L	$2 - 10\text{mm}$
Pore length scale[3]	l, R_0	$85 - 325\mu\text{m}$
Cell proliferation timescale[1] [2]	$1/\beta$	$6.59 \times 10^4\text{s}$
Viscosity[7]	μ	0.7mPs
Cell-free scaffold porosity[2] [4]	ϕ_0	40-97%
Pump flow rate[3] [5]	Q_c	$5.2 - 6.24\text{mm}^2/\text{s}$
Cell diffusion rate[1] [2]	D_n	$10^{-12} - 10^{-11}\text{m}^2/\text{s}$
Tortuosity[6] [8] [9]	τ	1.15
Ratio of timescales	$\delta = D_n/L^2\beta$	$10^{-4} - 10^1$
Maximum cell volume fraction	$\rho = \nu N_c$	$10^{-2} - 1$
Pores per lattice side	$n = L/l$	$10 - 10^3$

Table 2.1: Parameters used in the models. [1] [182], [2] [166], [3] [109], [4] [179], [5] [63],[6] [193], [7] [189], [8] [90], [9] [92], .

2.1.3 Model Paremeters

The continuum and lattice models contain a number of parameters that can vary significantly between tissue engineering experiments. As we are primarily interested in informing model selection, rather than constructing quantitatively accurate models, we focus on the orders of magnitude over which these parameters vary. Table 2.1 lists typical parameter values found in the literature. Using these values we estimate the ranges of the two nondimensional parameters, ρ and δ, that appear in both models, and estimate the number of pores per side of the square lattice n.

The shear stress threshold σ_t and the sharpness parameter g are not readily available in the literature. We treat the nondimensional thresholds σ_l and σ_c as model parameters and demonstrate model behaviours as they vary. Motivated by existing theoretical models in which the function F_1 approximated a step function [166], we set $g_l = g_c = 60$. In our simulations we fix $\rho = 0.9$ so that cell growth significantly affects the effective permeability of the scaffold.

The nondimensional parameters ρ and n can readily be determined from the properties of a specific porous scaffold microstructure and cell type. We can use the values in Table 2.1 to estimate that the number of pores in a typical scaffold ranges from approximately 10^2 to 10^6. Similarly, given the values of the cell volume ν and pore radii R_0, we compute that the number of cells required to fill a pore can vary in the range of $10^2 - 10^4$. We now simulate our models in order to explore behaviours as these nondimensional parameters vary.

2.1.4 Numerical Simulations

The lattice size n and diffusion to proliferation rate δ are varied to demonstrate the range of qualitative behaviours displayed by these models. Specifically we take $n = 25, 50, 75$, and 100 for the lattice simulations, and $\delta = 10^{-4}, 10^{-3}, 10^{-2}$, and 10^{-1} for both models. We take values of both lattice and PDE thresholds to be $\sigma_c = \sigma_l = 2.5, 5, 7.5, 10, 100$, and 1000.

The continuum model given by Equations (2.14)-(2.18) was simulated using the finite element solver Comsol with 24,912 triangular elements. Time and space refinements were carried out to ensure that the numerical approach converged. Additionally, the results found via Comsol were consistent with those found from a finite-difference scheme implemented to solve the same model. The lattice model given by Equations (2.32)-(2.33) was solved using an explicit adaptive Runge-Kutta method in Matlab. To ensure accuracy of our simulations with respect to the bifurcation behaviour discussed in Section 2.2.3, we constrain the maximum Runge-Kutta time step to be 10^{-3} [33]. Specific simulations were also undertaken with a fixed time step Runge-Kutta scheme with refinements in the size of the time step to ensure convergence.

We consider our initial condition to be a perturbed uniform cell density. On a lattice with $n = 100$ nodes per side, we set $N_i(0) = 0.1 + h\xi_i$ where $\xi_i \sim \mathcal{N}(0, 1)$ is a normally distributed noise term, and we use three values of the variance, $h = 10^{-2}, 10^{-3}$, and 10^{-4}. Each realization of this perturbed uniform state is then interpolated on the smaller lattices, or onto the triangular elements of the continuum model, so that all simulations have approximately consistent initial conditions. We compute mean cell densities as,

$$\hat{N}(t) = \left(\frac{\sum_{i=1}^{n^2} N_i(t)}{n^2} \right), \tag{2.38}$$

for the lattice and

$$\hat{N}(t) = \int_0^1 \int_0^1 N(x, y, t) dx dy, \tag{2.39}$$

for the PDE (computed numerically using the triangular elements from the finite element scheme). For each set of parameters simulated, and each value of the variance h, we repeat the simulation 100 times using different random seeds in order to investigate how robust each result is to different initial cell densities.

2.2 Results and Discussion

In Section 2.2.1 we discuss how the cell density changes from uniform logistic growth to death in local regions of the scaffold, leading to spatial heterogeneity in cell density which is observed over long timescales. In Section 2.2.2 we discuss the onset time of this spatial patterning. In Section 2.2.3 we discuss oscillations in cell density that are observed only in simulations of the lattice model. In Section 2.2.4, we compare the model predictions for the final cell densities. Finally, in Section 2.2.5, we compare the results of a linear cell diffusion model with those of a model with nonlinear cell diffusion.

2.2.1 Spatial Heterogeneity

Over long timescales (nondimensional times of $t > 10$) all of our simulations exhibit significant spatial heterogeneity in cell density and shear stress. In some regions of the scaffold the cell density is close to the nondimensional carrying capacity, and there is reduced fluid flow and low shear stress in these areas. There are also regions of high fluid flow and associated shear, and low cell density. The spatial structure of the cell density distributions depends heavily on the parameter δ.

For large values of the parameter ($\delta \geq 10^{-3}$), a single region or channel develops with low cell density, and through which the majority of fluid passes. In the remainder of the domain, there is little fluid flow and the cell density is high; see Figure 2.4. The location of the large fluid channel, corresponding to regions of low cell density, depends on the initial data and parameter values, but we always observe a single channel for $\delta \geq 10^{-3}$. For brevity we plot only the cell density distributions in the scaffold, as the associated shear stress can be inferred from these plots (the fluid flow

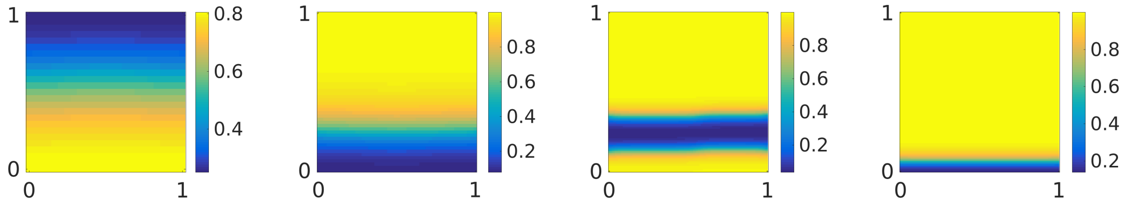

(a) $n = 25$, $\delta = 10^{-1}$ (b) $n = 50$, $\delta = 10^{-2}$ (c) $n = 100$, $\delta = 10^{-3}$ (d) PDE, $\delta = 10^{-3}$

Figure 2.4: Plots of the cell density with $t = 30$ and $\sigma_c = \sigma_l = 10$ demonstrating simple spatial patterning at various values of diffusion, $\delta \geq 10^{-3}$. The size of these channels is consistent for all 300 realizations of different random initial conditions, although the location of the channels does change.

is always low in regions of high cell density and vice versa). For $\delta = 10^{-4}$, we find significantly more spatial structure in the final cell density distributions. Figure 2.5 shows plots of the cell density at various times for lattice sizes $n = 25, 50$ and 100, with threshold parameter $\sigma_l = 2.5$ (for one realization of the initial cell density). After a period of growth, the initial uniform state rapidly breaks up into several aggregates of high cell density (e.g. $N_i > 0.8$, typically close to 1) surrounded by regions of low cell density (e.g. $N_i < 0.2$, typically close to 0), which then evolve slowly due to diffusion and shear stress mediated cell growth and death. For the smallest lattice size ($n = 25$), this process stabilizes quickly leading to a steady state cell density within the first $t = 10$ time units (compare the cell density distributions for $n = 25$ and $t = 10, 15,$ and 30 in Figure 2.5). For $n = 100$, many interior clusters slowly shrink as the cell aggregates along the top and bottom boundaries of the scaffold continue to grow over a longer timescale. Figure 2.6 shows cell density distribution plots for $\sigma_l = 7.5$. Note that for each n and t, the total area of high cell density is larger in Figure 2.6 than in 2.5. For both $\sigma_l = 2.5$ and $\sigma_l = 7.5$, the number of clusters of high cell density is initially greater in the $n = 100$ case after the onset of non-uniform growth, but there is a coarsening over time which reduces the number of distinct fluid channels and disconnected regions of high cell density. In comparison, the number of disconnected regions of high cell density is larger in the smaller lattices by the end of the simulation time in both Figures 2.5 and 2.6 (compare the $t = 30$ plots for $n = 25$ and $n = 100$ in both Figures). This difference in the number of disconnected regions of high cell density between small and large lattices is robust across multiple realizations.

Note that in Figure 2.5 the coarsening for the $n = 100$ lattice involves small clusters of high cell density disappearing, while for Figure 2.6 it is primarily channels of low cell density that disappear over time. This difference in long-time behaviour

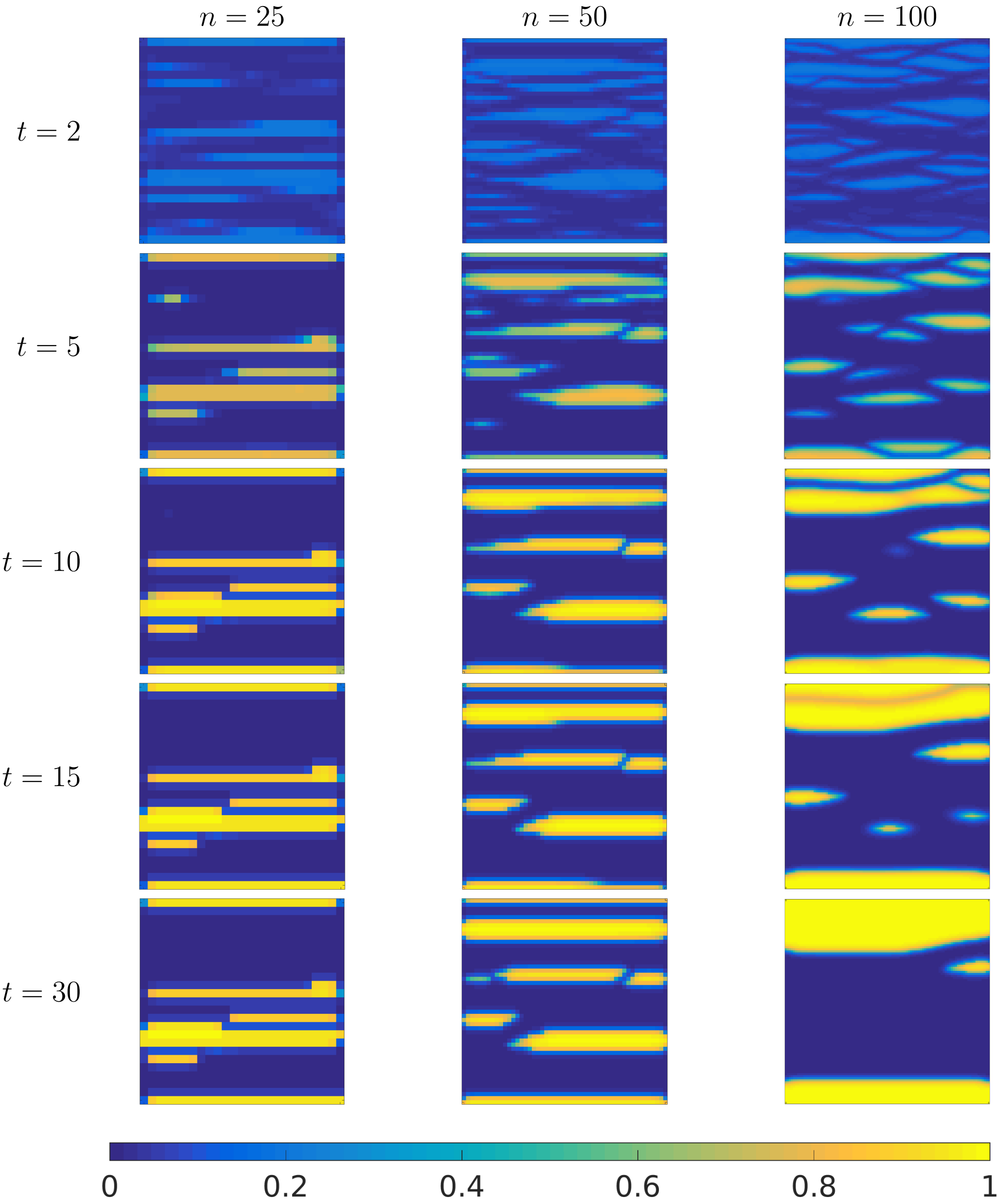

Figure 2.5: Cell density plots with $\delta = 10^{-4}$, $\sigma_l = 2.5$ for three lattice sizes at different points in time for one realization of the initial cell density.

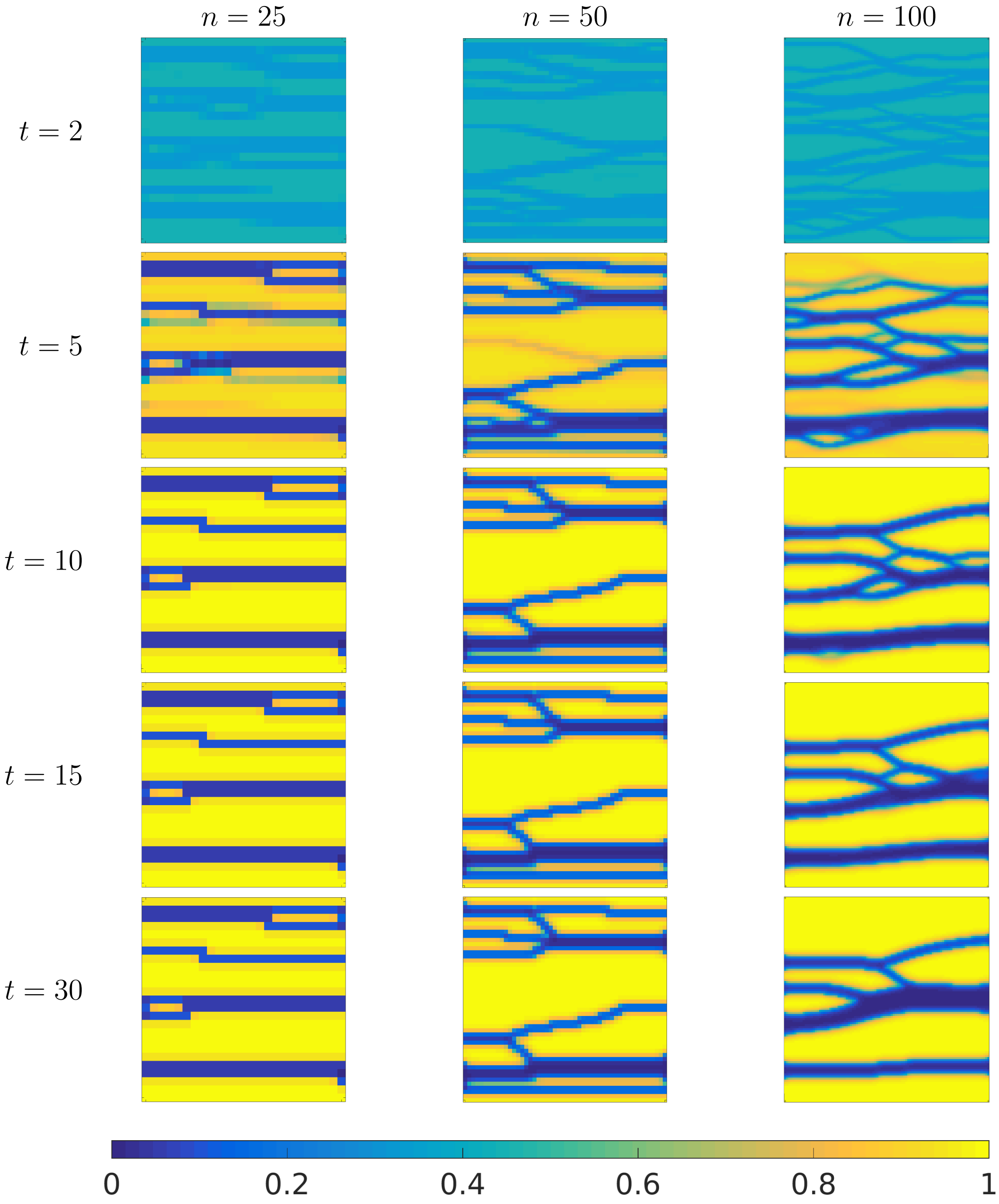

Figure 2.6: Cell density plots with $\delta = 10^{-4}$, $\sigma_l = 7.5$ for three lattice sizes at different points in time for one realization of the initial cell density.

can be understood via the threshold parameter σ_l. When $\sigma_l = 2.5$, cells die at relatively low values of shear stress and the overall cell density is low so cells recede away from regions of high fluid flow. For $\sigma_l = 7.5$ cells can withstand much more shear and grow over a much larger proportion of the scaffold, filling in small channels of fluid flow over time.

These results demonstrate a diverse range of behaviour for the lattice models. Figure 2.7 illustrates predictions from the PDE model for the cell density distribution over the spatial domain at various times and for four values of the threshold parameter σ_c for one realization of the initial cell density. This model also exhibits transient dynamics where clusters of high cell density form, and then coarsen into larger regions of high cell density as in the $n = 100$ lattice shown in Figures 2.5 and 2.6. Overall there are more regions of high cell density in the PDE model compared to the lattice simulations, which is consistent with the shear stress predictions given in Figure 2.3 (for the same cell density, this plot shows lower predicted shear stress values for the PDE model compared to the lattice model).

In Figure 2.8, we plot time series of mean cell densities, $\hat{N}(t)$, for lattice simulations with $n = 25, 50$, and 100, as well as for the PDE for the same realization of the initial cell densities used in Figures 2.5-2.7. The $n = 25$ lattice quickly equilibrium for each σ_l, whereas the larger $n = 100$ simulations show growth and death processes over a longer timescale, and in some cases these have not reached an equilibrium value at the end of the simulations at $t = 30$ (compare the long time behaviour in Figures 2.8a and 2.8c). We truncate the numerical experiments here partly because temporal variations in mean cell density beyond this point for all simulations were small, and partly because this period of time would exceed most *in vitro* tissue engineering experiments as $t = 30$ would typically be on the order of months. All simulations shown in Figure 2.8 grow logistically at the same rate until some region of the scaffold reaches the shear stress threshold σ_l or σ_c leading to non-uniform growth, and eventually to differences in final mean cell densities.

We observe less spatial structure in the PDE simulations than in the lattice simulations (compare Figures 2.5 and 2.6 with Figure 2.7). We quantify spatial variation in cell density with a heterogeneity function. For simplicity we choose

$$E(N_1, \ldots, N_{n^2}) = \frac{1}{n} \sum_{j=1}^{n^2} \sum_{i=1}^{n^2} A_{ij} \left| N_i - N_j \right|, \tag{2.40}$$

which is the total absolute difference in cell density between adjacent nodes throughout the lattice. The function satisfies $E \geq 0$ with $E = 0$ only for a homogeneous cell

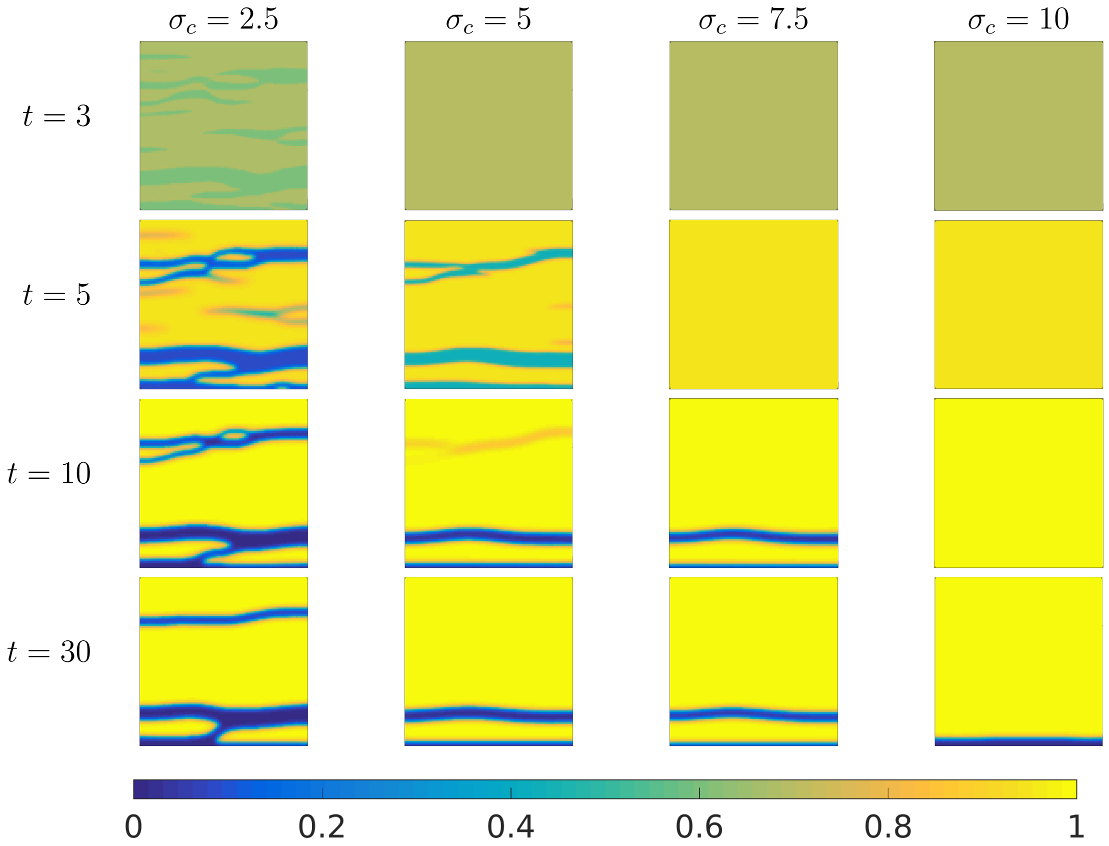

Figure 2.7: Cell density plots with $\delta = 10^{-4}$, organized with $\sigma_c = 2.5, 5, 7.5$, and 10 from left to right, and at times $t = 2, 5, 10, 15$, and 30 from top to bottom for one realization of the initial cell density.

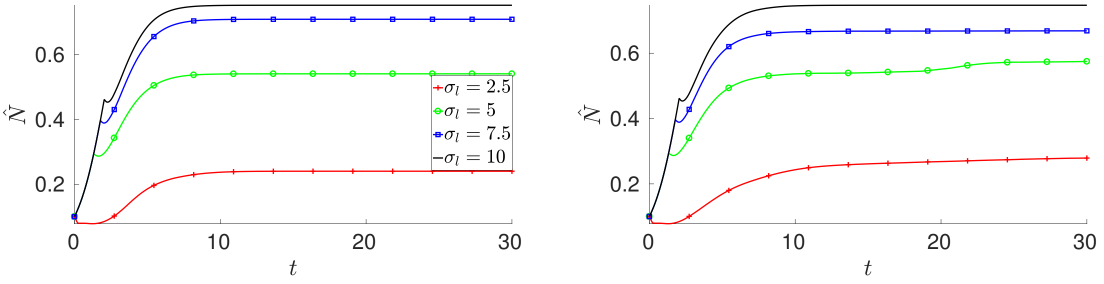

(a) $n = 25$ (b) $n = 50$

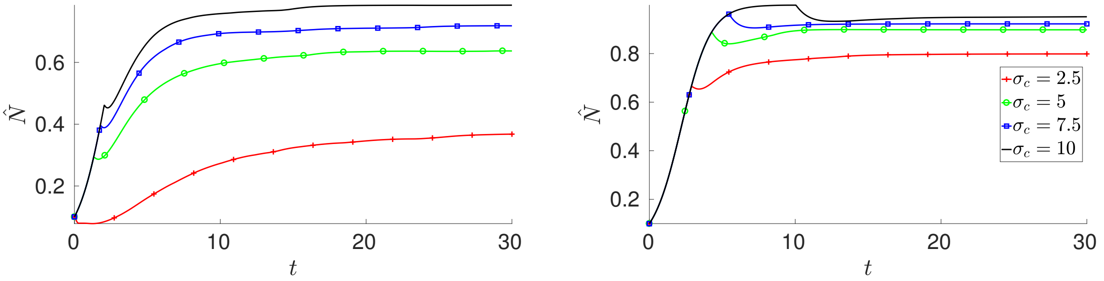

(c) $n = 100$ (d) PDE

Figure 2.8: Mean cell density plots over time for $\delta = 10^{-4}$ for lattice and PDE simulations for the same realization of the initial cell densities used in Figures 2.5-2.7.

density distribution. The PDE solutions were interpolated onto a square grid with a size of 100 by 100, so the function defined by (2.40) can be seen as a discretization of the functional $\int_0^1 \int_0^1 |\partial_x N(x, y)| + |\partial_y N(x, y)|\, dxdx$ which is a measure of anisotropic total variation [184]. This heterogeneity function allows for a quantitative visualization of the coarsening behaviour described earlier that was qualitatively observed in Figures 2.5-2.6.

In Figure 2.9 we plot values of this function for the simulated cell densities at $t = 30$ averaged over 300 realizations of the initial cell densities. For the majority of parameter combinations simulated, the value of the heterogeneity given by (2.40) was lower for the PDE simulations than for any of the lattice simulations with the same parameters. Larger values of diffusion show significantly smaller values of spatial heterogeneity, and for most combinations of the parameters the larger lattice of size $n = 100$ has a lower value of E than the other two lattice sizes. Figure 2.10 shows a time series of this function for one choice of parameters for the lattice simulations and for a corresponding PDE simulation. For $n = 25, 50$, and for the PDE, the difference between the final heterogeneity and its maximal value is small, while for $n = 100$ the maximum value of E occurs around $t \approx 4$, and then slowly falls over time to a value

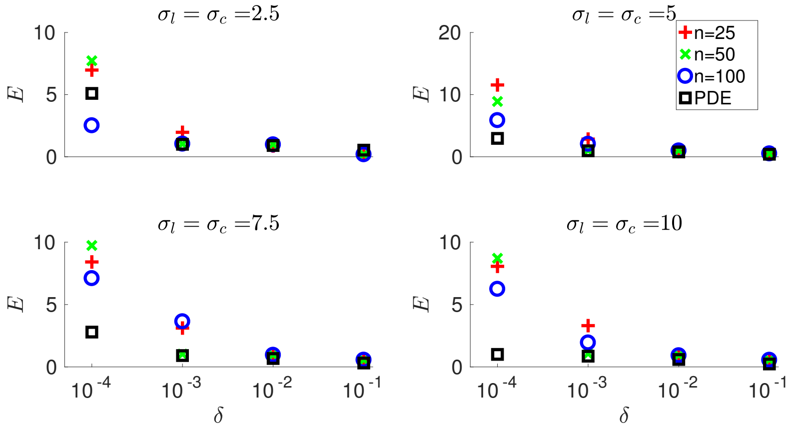

Figure 2.9: Plots of the heterogeneity of cell density defined by (2.40) over the four values of δ for several parameter combinations for the PDE and lattice models at $t = 30$. Note the variation in the ranges of the heterogeneity function E. The standard deviation of E between 300 realizations is, in each case, less than 1% of the reported mean value across all realizations.

that is significantly smaller (compare this to Figure 2.6 for $n = 100$ and $t \geq 5$).

There is less spatial heterogeneity in the final cell densities of the PDE simulations than in the corresponding lattice model for all values of n and all values of σ_l and σ_c except for $\sigma_l = \sigma_c = 2.5$, where we note that for the cell density distributions in Figure 2.5 the cells have aggregated to the sides for $n = 100$ and $t = 30$ and hence created a single large channel in the center of the scaffold, whereas several small channels remain in Figure 2.7. We note that in Figure 2.10, there is a specific time at which spatial heterogeneity emerges (e.g. E is no longer 0), which corresponds to the onset of cell death in some regions of the scaffold.

2.2.2 Onset of Non-Uniform Patterning Due to Shear-Induced Cell Death

As the initial data are approximately uniform, the evolution of the cell density can be determined analytically up to the time that cell death occurs. For $\sigma \lesssim \sigma_c$, the cell growth is purely logistic. This bound is sharp in the limit of $g \to \infty$ where F_1 and F_2 become step-functions, but it is approximately obeyed for $g = 60$ so that for shear stress values below σ_c, cells will grow logistically. Hence, for a constant initial condition $N_0 \in [0,1]$, we have

$$N(\boldsymbol{x},t) = N_0 \frac{\exp(t)}{1 + N_0(\exp(t) - 1)}, \quad \boldsymbol{x} \in [0,1]^2, \quad t < t_s, \tag{2.41}$$

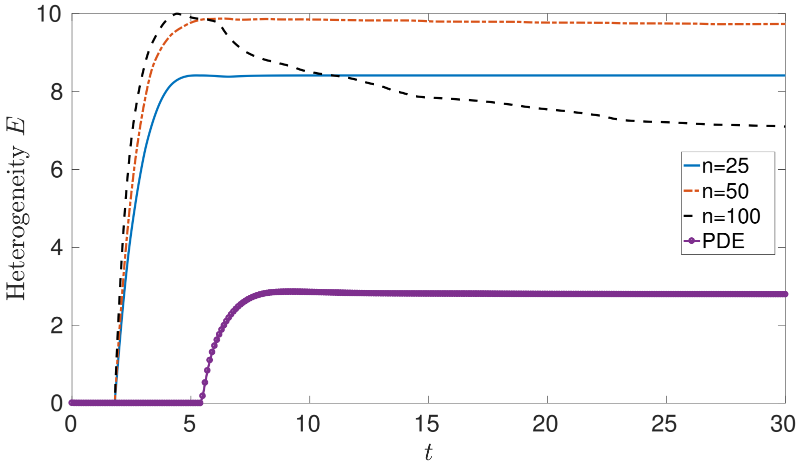

Figure 2.10: Plots of the heterogeneity of cell density defined by (2.40) over the simulation time for $\delta = 10^{-4}$ and $\sigma_l = \sigma_c = 7.5$ for one realization of the initial condition. Qualitatively similar behaviour occurred in other realizations.

where t_s is the time that it takes for the shear stress to become approximately equal to the threshold parameter, and hence for the cells to no longer undergo uniform logistic growth everywhere.

From Equation (2.36) we see that t_s may be defined implicitly by

$$\sigma_c \approx \sigma(t_s) = \frac{1}{1 - \rho N(t_s)}. \tag{2.42}$$

Substituting (2.41) into (2.42) gives

$$t_s = \ln\left(\frac{(\sigma_c - 1)(1 - N_0)}{N_0\,(1 - \sigma_c\,(1 - \rho))}\right). \tag{2.43}$$

Analogously for the lattice model, for $\sigma_i \lesssim \sigma_l$, the cell growth is purely logistic at each node. So for a constant initial condition $N_{i0} = N_0 \in [0, 1]$ for each i, we have

$$N_i(t) = N_0 \frac{\exp(t)}{1 + N_0(\exp(t) - 1)}, \quad 1 \leq i \leq n^2, \quad t < t_s, \tag{2.44}$$

t_s again being the time for the shear stress at some node to become comparable to the shear threshold. From Equation (2.37) we approximate t_s by

$$\sigma_l \approx \sigma_i(t_s) = \frac{2}{(1 - \rho N_i(t_s))^3}. \tag{2.45}$$

We substitute (2.44) into (2.45) to find

$$t_s = \ln\left(\frac{\left(2^{\frac{2}{3}}\sigma_l^{\frac{1}{3}} - 2\right)(1 - N_0)}{N_0\left(2 - 2^{\frac{2}{3}}\sigma_l^{\frac{1}{3}}\,(1 - \rho)\right)}\right). \tag{2.46}$$

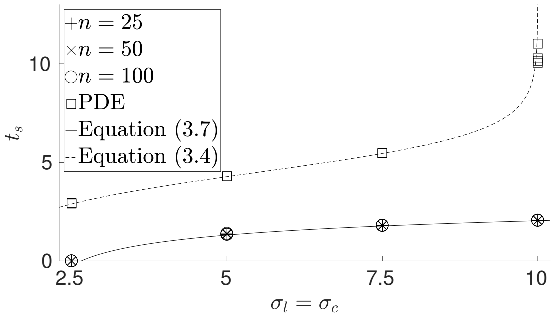

Figure 2.11: Plots of the numerical values of t_s for all parameter combinations of $\delta = 10^{-1}, 10^{-2}, 10^{-3}, 10^{-4}$ and $\sigma_c = \sigma_l = 2.5, 5, 7.5$, and 10 for the PDE and lattice models over 300 realizations. The symbols $+$, x, the circle and the square are for the numerical solutions for lattice sizes $n = 25, 50, 100$ and the PDE respectively. The continuous lines are plots of the analytical approximations from (2.43) and (2.46). The standard deviation of t_s between 300 realizations is, in each case, less than 1% of the reported mean value across all realizations.

We compare Equations (2.43) and (2.46) to the numerically computed values of t_s which correspond to $t_s \equiv \min_t \left(\max_x \left(\sigma(\boldsymbol{x}, t)\right) > \sigma_c\right)$ for the PDE simulations, and $t_s = \min_t \left(\max_i(\sigma_i(t)) > \sigma_l\right)$ for the lattice simulations. In Figure 2.11 we plot values of t_s for all lattice and PDE simulations with varying δ, σ_c, and σ_l. We see excellent agreement between the analytical and numerical predictions for both the lattice and the PDE. We see that t_s does not depend on the lattice size n or the parameter δ except for the PDE simulation at $\sigma_c = 10$. We note that $\sigma_c = 10$ is a limiting case as Equation (2.43) indicates that $t_s \to \infty$ as $\sigma_c \to 10$ if the initial cell density distribution was exactly uniform.

The time t_s can be seen in Figure 2.8 where the form of the time series changes from a logistic curve, and for all values of σ_l and σ_c the mean cell density begins decreasing at this time. In most cases this period of decreasing mean cell density is short relative to the simulation timescale. The time t_s can also be seen in Figure 2.10 as the point where the heterogeneity increases sharply from $E = 0$, due to the onset of non-uniform growth.

2.2.3 Lattice Oscillations

A particularly interesting behaviour we observe in some lattice simulations are oscillations in cell density. Such oscillations are not found the PDE model. Figure 2.12 shows a time series plot of the cell density at every lattice node for $n = 10$ and $n = 25$ in (a)-(b), and corresponding plots of nodal values of the shear stress in (c)-(d). After

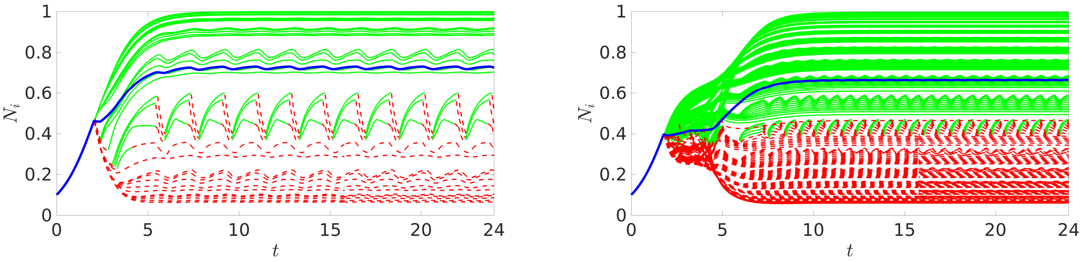

(a) $\sigma_l = 10$, $n = 10$, $\delta = 0.01$ (b) $\sigma_l = 7.5$, $n = 25$, $\delta = 0.014$

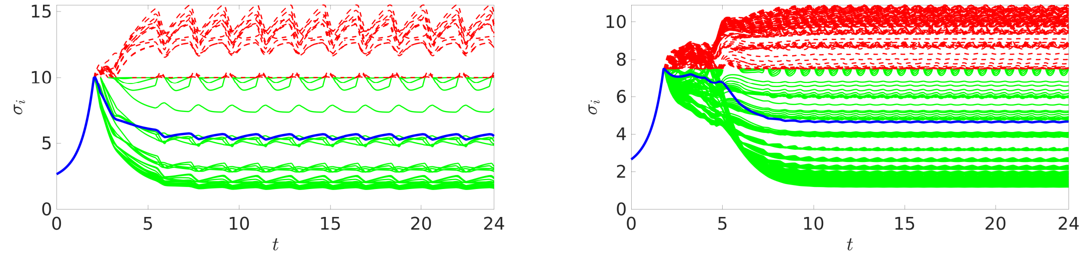

(c) $\sigma_l = 10$, $n = 10$, $\delta = 0.01$ (d) $\sigma_l = 7.5$, $n = 25$, $\delta = 0.014$

Figure 2.12: Plots of the cell density at every node for different parameter combinations in (a)-(b), and shear stress at every node in (c)-(d) for one realization of the initial cell densities. Green solid lines correspond to the cells at that node growing logistically ($\sigma_i < \sigma_l$), and red dashed lines correspond to exponential death ($\sigma_i > \sigma_l$). The blue line shows the spatial mean cell density in (a)-(b), and the spatial mean shear stress in (c)-(d).

a period of transient behaviour, the nodal cell densities and nodal values of the shear stress oscillate in phase. Nodes that are growing ($\sigma_i < \sigma_l$) are green solid lines, and nodes that are dying ($\sigma_i > \sigma_l$) are red dashed lines. The spatial mean cell density and shear stress are plotted in blue, which is also oscillating but with a small amplitude. Thus the overall effect of the lattice oscillations on the mean cell density is small. The particular time-series shown in Figure 2.12 will have different transient behaviour for different realizations of the initial data, but due to the simple spatial behaviour at large diffusion parameter (e.g. Figure 2.4), the amplitude and frequency of the oscillations for long times is the same for each realization we simulated.

In regions of the scaffold where the local shear stress exceeds the threshold σ_l, cells are (exponentially) dying due to high shear stress. These nodes all have relatively low cell density and hence more fluid passes through them, maintaining this high value of shear stress. In other regions of the scaffold with low shear stress, cells grow logistically. Diffusion acts to move cells from regions of high density to low density, and so cells move from regions with low shear stress to regions of high shear stress. In certain parameter regimes, this process finds an equilibrium value where these regions separate, as in Figures 2.5 and 2.6, where between regions of growth and death there are some nodes of intermediate cell density. However, for certain values of n, σ_l, and δ, the movement and growth of cells gives rise to a different behaviour from this equilibrium as the growth of cells in regions of high cell density substantially affects fluid flow and shear stress throughout the entire scaffold. As seen in Figure 2.12, diffusion from growing regions can cause regions that are dying to increase in total cell density, and similarly, regions that are growing logistically can decrease in cell density due to diffusion.

We plot bifurcation diagrams of the maximal nodal oscillation amplitudes in Figures 2.13a-2.13b for several lattice sizes and two values of the threshold parameter, over a range of the parameter δ. After enough time has passed to ensure we are no longer observing transient dynamics, we compute the maximum nodal amplitude as $N_{osc} = \max_i\{\max_t\{N_i(t)\} - \min_t\{N_i(t)\}\}$ to capture the largest oscillation. We plot the frequency ω_N of these nodal oscillations computed with the Fast Fourier Transform in Figures 2.13c-2.13d. We note that the frequency is the same for every node in the lattice.

These bifurcation diagrams show that for each n and σ_l, the one-dimensional parameter space over δ is composed of disconnected regions where oscillations are permitted (see behaviour illustrated in Figure 2.12), and regions where cell densities tend to steady states (see Figure 2.8). Further simulations within each of these regions (using different realizations of the perturbations of the initial data, for instance) have consistent behaviour, and we conjecture that that these behaviours are generic within each region in parameter space demarcated by the bifurcation between steady state behaviour and oscillations. In Figure 2.13 we see that the number of disconnected regions in δ-space with oscillatory behaviour increases as n increases, and the maximal amplitudes decrease with increasing n. We note that for $n = 100$, there are many disconnected bifurcation regions for very small δ, but these all have correspondingly small magnitudes in oscillation and so they are not visible in Figure 2.13. For larger values of n, the oscillation amplitudes become so small that they are comparable to numerical truncation and rounding errors, and we conjecture that these oscillations play no role for larger lattices. There is a trend of increasing oscillation frequency and decreasing nodal amplitude for larger values of δ for a given lattice size. The larger lattices have significantly smaller variations in mean cell density of the scaffold due to these oscillations. This is due to only a small subset of the nodes switching between growth and death behaviours during an oscillation. These oscillations do not occur in any of our PDE simulations. For large n, our simulations show that the

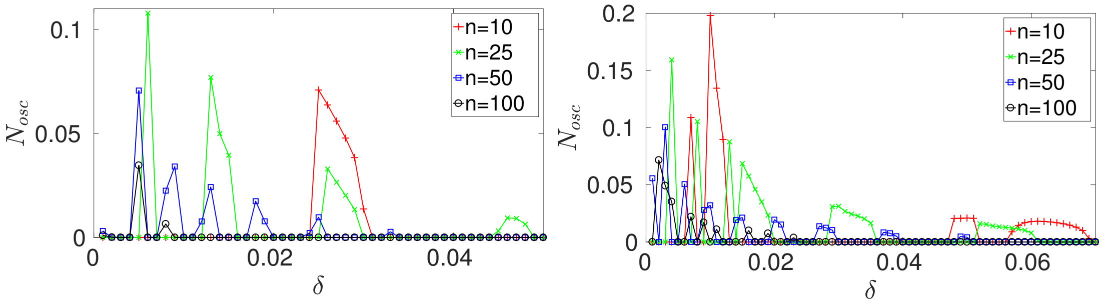

(a) $\sigma_l = 7.5$ (b) $\sigma_l = 10$

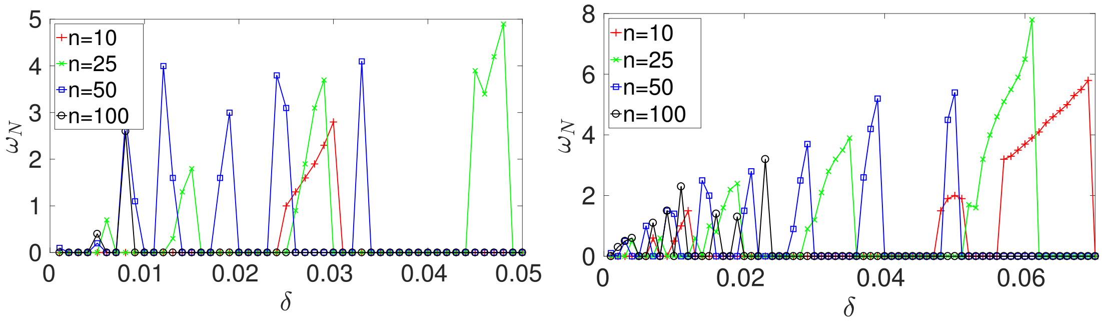

(c) $\sigma_l = 7.5$ (d) $\sigma_l = 10$

Figure 2.13: Plots (a)-(b) are bifurcation diagrams showing the maximum magnitude of nodal oscillation in the lattice for different lattice sizes. This is plotted in steps of 0.001 in δ. Plots (c)-(d) are corresponding frequencies for these nodal oscillations. We only show results corresponding to one realization of the initial cell densities, but further simulations had quantitatively identical behaviour.

amplitudes of oscillation in mean cell density decreases, as shown by the blue lines in Figure 2.12, and that the proportion of nodes switching between growth and death behaviours also decreases. Similarly, nodal shear stress oscillations also decrease in amplitude as the lattice size increases. In the other direction, for lattices of size $n = 5$ and smaller, no oscillations were observed. We refer to Chapter 3 for a discussion of Hopf bifurcations in a similar lattice system, where cells die due to high fluid pressure rather than shear stress. There we argue that the oscillations observed in this model are due to a combination of nonlocal effects from the quasi-static fluid equations, coupled with symmetry-breaking bifurcations in the lattice models.

2.2.4 Mean Cell Density Predictions

We can broadly understand the global behaviour of the numerical simulations by comparing their final mean cell densities computed via Equations (2.38) and (2.39). Figure 2.14 is a plot of the spatial mean of the cell density after 30 nondimensional units of time. For any given shear stress threshold and δ, the PDE model has a higher

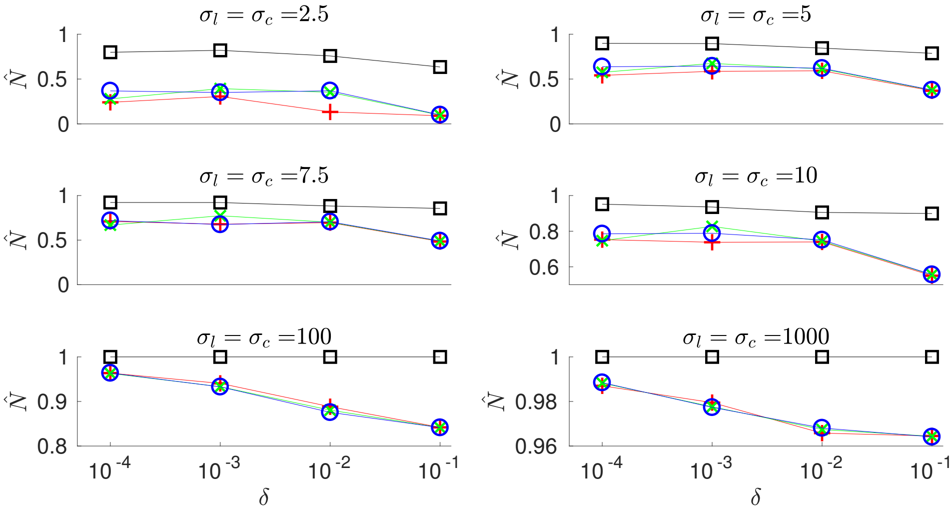

Figure 2.14: Plots of the mean cell density $\hat{N}$ at the final time $t = 30$ over the four values of δ for all parameter combinations for the PDE and lattice models. The symbols $+$, $\times$, $\circ$ and $\Box$ are for the lattice sizes $n = 25, 50, 100$ and the PDE respectively. Note the variation in the ranges of the mean cell density $\hat{N}$ (y-axis). The standard deviation of this spatial mean between 300 realizations is, in each case, less than 1% of the reported mean value across all realizations.

mean cell density. This is expected due to the differences between the constitutive assumptions for shear stress in each model (see Figure 2.3).

The value of the parameter δ has a non-monotonic effect for some lattice simulations. In particular, for $\sigma_c, \sigma_l \leq 10$, the maximum mean cell density for the $n = 50$ lattice occurs for the intermediate value of the diffusion parameter $\delta = 10^{-3}$. For the large value of $\delta = 10^{-1}$ in each plot, the lattice size is insignificant in determining the mean cell density. Similarly, for the large shear stress thresholds $\sigma_l = 100$, and 1000 shown in the bottom two plots, cell death occurs only in a very small region of the domain, so the lattice size is almost inconsequential in determining the final mean cell density. For $\sigma_l \leq 10$ and $\delta \leq 10^{-2}$, however, there are differences between the final mean cell density for different lattice sizes. This suggests that for applications where the ratio of proliferation to diffusion timescales is small, and where cells are very sensitive to high shear stress, the topology of the underlying pore network plays a role in determining the final mean cell density.

2.2.5 Nonlinear Cell Diffusion

Here we consider the effect of nonlinear cell diffusion. We follow [166] and use the following (nondimensionalized) functional forms for the diffusion coefficient,

$$D\left(N\right) = \delta \exp\left(\gamma\left(N-1\right)\right), \quad D\left(N_i, N_j\right) = \delta \exp\left(\gamma\left(\frac{N_i+N_j}{2}-1\right)\right), \qquad (2.47)$$

for the continuum and lattice models respectively. For values of cell density near the carrying capacity (dimensionless value of 1), diffusion given by (2.47) approximates the linear case with the same nondimensional parameter δ. For small values of cell density, the effective diffusion of cells throughout the porous medium is smaller than the corresponding linear value (δ) for all n. The dimensionless parameter γ determines the strength of this nonlinear effect; [166] used $\gamma = 2$ to ensure a sufficiently nonlinear behaviour while remaining within a parameter regime where the speed of a proliferating front of cells could be computed. Here we carry out several simulations for varying values of γ in the interval $(0, 5]$. For small nonlinearity ($\gamma \lesssim 10^{-2}$), nonlinear cell diffusion simulations have identical mean cell density and oscillatory behaviours as linear cell diffusion simulations. For moderate nonlinearity ($10^{-2} \lesssim \gamma \lesssim 3$), qualitative features such as cell density aggregation and oscillations are retained, but quantitative differences in cell density distributions and oscillation frequency appear. For larger values of γ, we no longer observe oscillations in cell density.

We first consider the spatial cell density distributions with nonlinear cell diffusion. We take $\gamma = 2$ in Equations (2.47) and repeat the simulations (using the same realization of the initial data) from Figure 2.6, and display these in Figure 2.15. While the steady state cell density distributions have changed, the organization of cells into high density aggregates occurs in both the linear and nonlinear cell diffusion simulations. Additional simulations (with different realizations of the initial cell density, and different values of σ_l) show qualitatively similar coarsening behaviour in the $n = 100$ simulations with nonlinear cell diffusion compared to the linear case (see Figures 2.5-2.6). Similarly, $n = 25$ simulations including nonlinear cell diffusion quickly settle into a steady state as in the linear case. Quantitatively, the change in the spatial mean cell density for $\gamma \leq 1$ is less than 5% in each case shown in Figure 2.14. Larger values of the nonlinearity parameter γ leads to larger changes to the spatial mean cell densities reported in Figure 2.14 for linear cell diffusion, but we leave further quantification of this to future work.

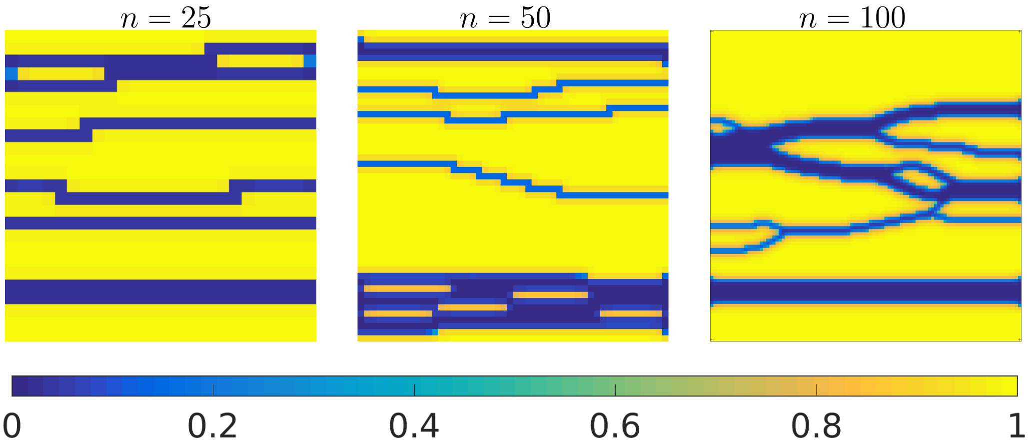

Figure 2.15: Cell density plots with $\delta = 10^{-4}$, $\gamma = 2$, and $\sigma_c = 7.5$, for $n = 25, 50,$ and 100 at $t = 30$ with the same realization of the initial data as used in Figure 2.6.

Next we consider the effect of nonlinear cell diffusion on the oscillations in cell density found in Section 2.2.3. For small values of the nonlinearity, e.g. $\gamma \leq 10^{-2}$, the oscillatory behaviour of solutions is quantitatively the same up to a slight phase shift due to differences in transient dynamics. We plot two example time series in Figure 2.16 that use the same parameter sets as those in Figure 2.12, but now including nonlinear cell diffusion with $\gamma = 0.1$ and 1. We see that the period of the oscillation has approximately doubled in both cases compared with the linear diffusion simulations shown in Figure 2.12. For increasing values of γ, many of the regions (in δ) of oscillatory behaviour shown in Figure 2.13 become smaller, and completely disappear for $\gamma \geq 3$. We conclude that large values of nonlinear diffusion can be stabilizing in that oscillatory regions of parameter space shrink in size, and all oscillatory behaviour disappears for large enough values of γ. As before, we do not observe any oscillatory behaviour in the continuum model with nonlinear cell diffusion.

2.3 Conclusions

In this Chapter we have explored complementary lattice and continuum models for a bioactive porous tissue scaffold, and demonstrated several important differences in model behaviours. The lattice simulations show that considering finite pore networks when modelling cell growth within a porous scaffold will lead to qualitative differences compared with PDE models. Varying degrees of spatial heterogeneity in the cell density distribution are displayed in the lattice model, whereas for most of the pa-

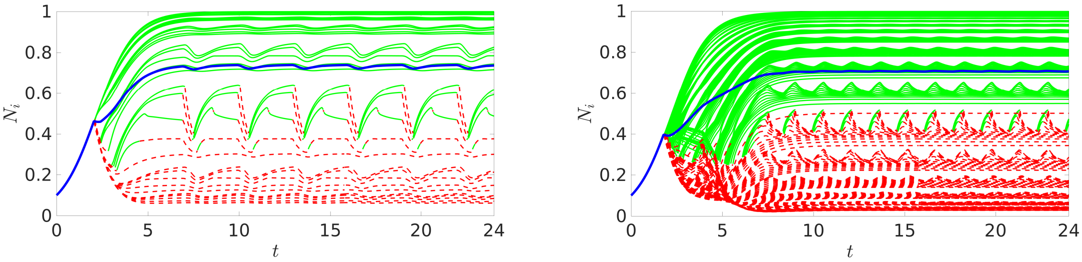

(a) $\sigma_l = 10$, $n = 10$, $\delta = 0.01$,$\gamma = 0.1$ (b) $\sigma_l = 7.5$, $n = 25$, $\delta = 0.014$, $\gamma = 1$

Figure 2.16: Plots of the cell density of every node for the same parameter combinations shown in Figure 2.12 with nonlinear cell diffusion given by (2.47). Green solid lines correspond to the cells at that node growing logistically ($\sigma_i < \sigma_l$), and red dashed lines correspond to exponential death ($\sigma_i > \sigma_l$). The blue line shows the spatial mean cell density.

rameter space the PDE solutions exhibit simpler spatial structures, such as one or two horizontal channels. The significant variation between different lattice sizes indicates that considering the spatial network explicitly has a nontrivial impact on pattern formation. The smoothing behaviour observed in both the PDE and large n lattice models is reminiscent of models of coarsening in condensed matter physics, where initial spatial irregularities evolve into larger spatial structures. That this coarsening occurs at different timescales and to different degrees due to the size of the lattice is an unexpected result. We conjecture that, modulo constitutive differences, a PDE and a very large lattice (e.g. $n > 100$) should have comparable behaviour, but for smaller pore networks the finite structure of the lattice becomes important to the overall growth process within the scaffold.

We observe small amplitude oscillations in cell density exclusively in the lattice model. While the effects of these oscillations on the total mean cell density of the scaffold are small, and would likely not be physically observed given experimental noise, their presence is an interesting effect of finite lattice size. Additionally, the larger variations in nodal values of shear stress (see Figure 2.12(c)-(d)) has important implications for shear-stress mediated tissue growth. In particular, shear-stress can play a role in both cell proliferation and cell differentiation [80]. These spatiotemporal oscillations in shear stress could potentially lead to the formation of heterogeneity in the cell populations within the scaffold, and hence influence the integrity and uniformity of artificial tissue [200].

Nonlinear interactions could amplify these oscillations. For instance, some tissue scaffolds are cyclically loaded to facilitate cell growth via mechano-transduction [5, 120, 145]. In certain parameter regimes, this oscillatory forcing could interact in non-trivial ways with these lattice induced oscillations, for instance inducing resonance in the cell density oscillations. This is especially true given that small amplitude oscillations in cell density give rise to larger shear stress variations, which suggests feedback between cell proliferation and shear stress. We leave the investigation of such possibilities to future work.

Some strategies for quantifying experimental cell distributions have been proposed which could validate the steady-state distributions of cell density we demonstrate in Figures 2.5-2.7 [175], though we note that these approaches involve sacrificing tissue scaffolds after cells have stopped proliferating. Observing oscillations in cell density experiments would be difficult given the small oscillation amplitude, and the difficulty in producing temporal datasets from tissue scaffolds due, e.g., to requiring the scaffolds to be sacrificed in order to ascertain cell density. Models can also be validated by comparing other key outputs, such as the mean cell densities given in Figure 2.14, against experimentally accessible data [124]. While validating these models is difficult, once validated such theoretical models provide predictions for the spatiotemporal evolution of important quantities (e.g. shear stress and cell density) throughout the scaffold, without the need for large numbers of costly and time-consuming experiments.

While we observed quantitative differences between these paradigms (see Figure 2.14), we attribute most of these differences to the constitutive assumptions as shown in Equations (2.36)-(2.37), and these constitutive assumptions can vary between particular applications of these models. We note that there are differences in mean cell density between lattices of different sizes, which suggests that the size of the network does play a role in determining the mean cell density of the scaffold. We have explored simulations using different functional forms of ϕ, k, and R_{ij}, as well as different values of ρ. These preliminary simulations were consistent with the qualitative differences reported here between lattice and continuum models. The constitutive choices we have made in this Chapter do give results that are consistent with [119] in that our 2-D fluid model in the PDE over-predicts cell density compared with the 3-D fluid ('tube') model of the lattice. We also note that despite the simplicity of our models, the qualitative differences between lattice and continuum formulations exist even when we introduce nonlinear diffusion into the model. We conjecture that these differences are inherent to the forms of the models used here suggesting that discrete spatial geometry should be carefully incorporated into macroscopic tissue engineering models. This is in line with the study of discrete and continuum cell monolayers [22], where insights from individual and lattice cellular-automata models were necessary to inform the continuum formulation.

These differences in the type of behaviours displayed by continuum and lattice models exist even though the network geometry studied here, a square grid lattice, is simple. More complicated hexagonal and face centred cubic lattices [190], off-lattice models [187], and other complex microscale models have been used in hybrid discrete-continuum settings. In addition to a more complex network geometry, there are many components that could be included in this lattice model, such as a model of nutrient transport, or a more detailed microscale relationship between cell density and fluid flow. Nevertheless, these simple models give insight into the kinds of differences one can expect from each modelling paradigm.

For experiments involving small pore sizes or large constructs, the pore network is relatively dense and we expect continuum and lattice models to be comparable in terms of predicting cell proliferation and global fluid properties, such as scaffold permeability. For small scaffolds or scaffolds with large pores, however, we expect lattice models to significantly differ from continuum models in their predictions. The variations between the lattices of different size implies that a good model of the finite network geometry of a scaffold is important in understanding the tissue growth process for such scaffolds. Given a realistic description of the evolution of cells and fluid flow at the pore scale, our approach gives an alternative to continuum approaches such as mathematical homogenization in upscaling these microscale processes. Numerical solution of the lattice model is no more difficult than an equivalent discretization of a continuum model, and so the only practical disadvantage of using a lattice model would be the requirement of specifying the network topology, and determining appropriate fluid and cell properties at the scale of nodes in the network. We believe that pursuing these kinds of models can lead to novel insights in understanding the growth of artificial tissue, and eventually in developing clinically successful technologies.

Chapter 3

Analysis of Bioactive Porous Media with Pressure-Induced Cell Death

In Chapter 2 we introduced two models of a two-dimensional porous tissue scaffold within a perfusion bioreactor. These models incorporated interactions between a viscous fluid phase representing a culture medium, and a cell phase modelling the biomass of proliferating cells and their extracellular matrix. Cells were assumed to die if the local fluid shear stress became too large, and cell proliferation was assumed to block pores, reducing the local permeability of the scaffold. We modelled this system using a continuum approach involving a system of PDEs, and a lattice approach involving a spatially embedded network of ODEs, and discussed quantitative and qualitative differences between the modelling predictions arising from these approaches. Here we consider a variant of the lattice model, as well as a spatially continuous analogue, where cells are affected by fluid pressure, rather than shear stress. While these models are physically interesting in their own right, they are primarily chosen as they are more amenable to mathematical analysis. The understanding gained from analyzing these simpler models provides insights into the behaviour of the shear-stress models discussed in Chapter 2.

Novel contributions of this Chapter include an analysis of lattice and continuum models of a bioactive porous medium where the only biomechanical forcing of the fluid on the cells is cell death mediated through the local hydrostatic pressure. While hydrostatic pressure has been used to model cell proliferation in tissue engineering scaffolds (e.g. in [120]), it has not been modelled as a mechanism to induce cell death. Additionally, in analyzing our models asymptotically and numerically, we elucidate several kinds of solution behaviours which are interesting from a purely mathematical point of view.

We analyze these models from a dynamical systems perspective emphasizing qualitative changes in model behaviour as parameters are varied. Depending on the size of the underlying network, we find that long-time oscillations and steady states in cell density are observed in both models. These behaviours can be classified as either vertically symmetric or vertically asymmetric. Steady state behaviour can be described in large cell diffusion regimes via asymptotic expansions in the diffusion parameter. We numerically continue steady state solutions into intermediate diffusion regimes, where we observe symmetry-breaking bifurcations to both oscillatory and steady state behaviours that can be explained via local bifurcations, as well as symmetry-preserving oscillations that do not bifurcate from steady states. The spatially continuous analogue of the model only exhibits vertically symmetric steady states and oscillatory solutions, and we conjecture that it is the finite lattice that gives rise to the more complicated symmetry-breaking bifurcations. We suggest that the origin of both types of oscillations is a nonlocal reaction-diffusion mechanism mediated by quasi-static fluid flow. Finally, we relate these results back to the original modelling question of how network topology influences tissue growth in a bioactive porous tissue scaffold.

Continuum models for fluid flow in porous media can be justified for pore networks with many pores, corresponding either to large porous materials such as oil reservoirs, or to materials with densely connected pore structures such as sponges [13]. Many current tissue scaffolds used experimentally, however, have pore sizes and scaffold geometries such that the number of pores is $O(10^3)$ or less [39, 59, 103, 182]. These experimental considerations motivate our study of finite lattice models. While lattice approaches exist in related biological literature [11, 113, 176], there is still much work needed to understand the impact of finite pore networks on porous media undergoing structural changes due to cell growth.

In this Chapter we modify the models presented in Chapter 2 by assuming that cells are sensitive to high pressures, rather than fluid shear stress. This is motivated in part by computational modelling of cell death due to hydrostatic pressure [120], and by experimental work demonstrating cell death due to pressure [105]. Additionally, these modified models are more amenable to mathematical and numerical investigations due to the simpler coupling between the flow and growth processes. The number and structure of steady states is much smaller, allowing for a (spatial) dimensional reduction of the model that captures many salient features of the dynamics. In the models presented in Chapter 2, oscillatory solutions were only present for the lattice model, and were more pronounced for smaller pore networks. In contrast, here we will show the existence of oscillatory behaviour in both lattice and continuum models. Insights gained from analyzing these simpler models carry over to Chapter 2 as a basis for understanding the mathematical mechanisms leading to oscillatory behaviour in the shear stress models.

We remark that others have considered pressure-driven cell growth and death. Byrne and Drasdo [22] considered high levels of pressure to prevent proliferation due to contact-inhibition. This model was partly motivated by previous work on cell motion in tumours due to pressure [23]. The authors in [22] showed that cell growth can lead to high-pressure cores in some cell monolayers, and within such high-pressure cores cells cease to proliferate. Similarly, [120] modelled bone tissue engineering scaffolds subject to time-dependent forcing due to hydrostatic pressure, and demonstrated that cell memory was an important feature to consider in order to optimize construct mineralization. In our model, we will similarly assume cells do not proliferate when the pressure exceeds a given threshold, but we will also assume cells die at high levels of hydrostatic pressure, which does not appear in the preceding models, but has been shown to occur at some values of hydrostatic pressure for *Escherichia coli* [105].

In Section 3.1, we present our lattice and continuum models, and briefly discuss the underlying modelling assumptions and components. We also present one-dimensional (1-D) reduced models of the full two-dimensional (2-D) equations. One benefit of doing this is that in 1-D, the fluid flow component of each model can be explicitly expressed as a function of the cell density. In Section 3.2, we present numerical solutions of the lattice and continuum models, demonstrating typical solution behaviours. In Section 3.3, we derive asymptotic solutions appropriate for large values of the diffusion parameter, and show that these always tend to a steady spatially uniform state. We use these solutions to bound the region in parameter space where we anticipate non-equilibrium dynamics (e.g. oscillations). In Section 3.4, we describe the more complicated dynamics outside of this asymptotic parameter regime. We do this by presenting numerical bifurcation diagrams over two parameters for large and small lattices alongside the continuum model. Using these diagrams we broadly characterize the steady states and long-time oscillatory states by their symmetry properties. We present continuation results showing the existence of Hopf and pitchfork bifurcations that break the vertical symmetry of steady state solutions. Additionally, we reveal that a different kind of oscillation exists, which preserves vertical symmetry and is not due to a local bifurcation from a steady state. Finally, we give an overview of these results in Section 3.5, and discuss implications for modelling of porous scaffolds used in tissue engineering.

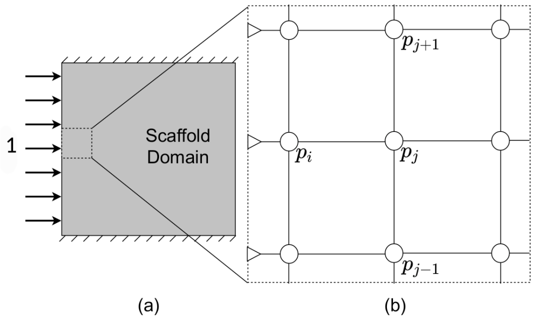

Figure 3.1: A representation of the scaffold domain in (a), and a lattice representation of a small part of it in (b). Fluid enters the domain at unit flow rate on the left side, and leaves along the right side of the lattice. The horizontal boundaries are impermeable.

3.1 Description of the Models

We consider a square lattice of n nodes per side, and at each node define a pressure p_i and a cell density N_i for $1 \leq i \leq n^2$. See Figure 3.1 for a representation of this lattice. We label nodal variables with single indices, counting from the bottom-left upwards so that p_1 is the pressure at the bottom-left node, and p_{n^2} is the pressure at the top-right node. We define the adjacency matrix A by $A_{ij} = A_{ji} = 1$ if nodes i and j are connected, and $A_{ij} = 0$ otherwise. We write the graph Laplacian as the matrix L such that $\sum_j A_{ij}(v_i - v_j) = \sum_j L_{ij} v_j$. See [121] (and references therein) for a discussion of networks in general and properties of the matrices A and L.

We assume the fluid is viscous, Newtonian, and incompressible. We model the flow rate between nodes i and j via Poiseuille flow in a pipe of radius R_{ij}, and assume that R_{ij} depends on the cell density at nodes i and j. We assume that a constant fluid flow enters the domain from the left and leaves the domain along the right side of the lattice, where we impose a (nondimensional) fluid flow rate of 1. We assume impermeable horizontal boundaries. To solve this problem, we prescribe a unit pressure drop across the scaffold which will have an associated fluid flow rate Q into the domain. We use a pressure rescaling procedure described in Chapter 2 to ensure that a unit flow rate enters the domain. We assume that there is a critical pressure p_l so that cells at node i grow logistically for values of the pressure $p_i < p_l$, and die for values of $p_i > p_l$. We also assume that cells can diffuse between nodes. Our system of non-dimensional equations is then

$$\sum_{j=1}^{n^2} A_{ij} R_{ij}^4 (\tilde{p}_i - \tilde{p}_j) = \begin{cases} 1 - \tilde{p}_i, & 1 \leq i \leq n, \\ 0, & n < i \leq n^2 - n, \\ -\tilde{p}_i, & n^2 - n < i \leq n^2, \end{cases} \tag{3.1}$$

$$\frac{dN_i}{dt} = F_1(p_i)N_i(1 - N_i) - F_2(p_i)N_i + \delta n^2 \sum_{j=1}^{n^2} A_{ij}(N_j - N_i), \quad 1 \leq i \leq n^2, \tag{3.2}$$

$$R_{ij} \equiv R(N_i, N_j) = 1 - \frac{\rho}{2}(N_i + N_j), \qquad p_i = \tilde{p}_i \frac{1}{Q}, \qquad Q = \sum_{i=1}^{n} 1 - \tilde{p}_i, \quad \text{(3.3a,b,c)}$$

$$F_1(p_i) = 1 - \left(\frac{1}{2}\right)(\tanh[g(p_i - p_l)] + 1), \, F_2(p_i) = \left(\frac{1}{2}\right)(\tanh[g(p_i - p_l)] + 1), \quad \text{(3.4a,b)}$$

where the parameter δ represents cell diffusion, ρ determines the effect of cell density on the pipe radius and hence the local fluid flow, and g is a smoothing parameter. Equations (3.1) represent conservation of mass enforced at each node, with a unit pressure drop imposed across the square domain. Equations (3.2) describe logistic cell growth and death modulated by the functions F_1 and F_2 of the pressure at that node, along with cell diffusion between nodes. Equation (3.3a) describes how the presence of cells influences the pipe radii, and Equations (3.3b)-(3.3b) rescale the pressures to match the total fluid flow into the domain. Equations (3.4) describe functions of the pressure chosen to model a 'proliferation' and a 'death' response of the cells to low and high values of fluid pressure respectively. The use of hyperbolic tangent functions is a modelling choice following [166], although similar choices such as step functions and mollified step functions have been used elsewhere [36]. Note that the physical fluid flow rate into the domain has been scaled to unity, but it is captured by the nondimensional threshold parameter p_l. See Section 2.1.1 for further details.

The analogous dimensionless continuum model is

$$\boldsymbol{u} = -k(N)\nabla\tilde{p}, \qquad \nabla \cdot \boldsymbol{u} = 0, \quad \text{(3.5a,b)}$$

$$\frac{\partial N}{\partial t} = F_1(p)N(1 - N) - F_2(p)N + \delta\nabla^2 N, \tag{3.6}$$

$$Q_c = \int_0^1 -k(N(0, \hat{y}, t))\frac{\partial p}{\partial x}(0, \hat{y})d\hat{y}, \quad p = \frac{\tilde{p}}{Q_c}, \qquad k(N) = (1 - \rho N)^3, \quad \text{(3.7a,b,c)}$$

$$F_1(p) = 1 - \left(\frac{1}{2}\right)(\tanh[g(p-p_c)]+1),\ F_2(p) = \left(\frac{1}{2}\right)(\tanh[g(p-p_c)]+1), \quad \text{(3.8a,b)}$$

where δ, ρ, g are positive constants with the same meaning as before, p_c is analogous to p_l, and Q_c is analogous to Q. We prescribe the boundary and initial conditions

$$\boldsymbol{u} \cdot \boldsymbol{n} = 0 \text{ at } y = 0, 1,\ 0 \leq x \leq 1, \tag{3.9}$$

$$\tilde{p} = 1 \text{ at } x = 0,\ 0 \leq y \leq 1,\ \tilde{p} = 0 \text{ at } x = 1,\ 0 \leq y \leq 1, \tag{3.10}$$

$$\boldsymbol{n} \cdot \nabla N = 0 \text{ for } \boldsymbol{x} \in \partial[0,1]^2,\ N(x, y, 0) = N_0(x, y). \tag{3.11}$$

Both models have no-flux or Neumann conditions on all boundaries for the cell density, and on the horizontal boundaries for the fluid. To describe solutions with certain symmetries, we also consider spatially 1-D models without horizontal boundaries, as well as periodic conditions on both cell density and fluid flux along the horizontal boundaries. For the lattice, these conditions are encoded in the adjacency matrix A_{ij}.

We now consider simplifications of the models available when there is a vertical symmetry - that is, when the cell density distribution (and hence the pressure) is vertically symmetric. This is motivated by the presence of this symmetry in some numerical solutions from Section 3.2, and will provide a basis for understanding some mathematical aspects of these models.

3.1.1 1-D Lattice Model

We first simplify the lattice equations by eliminating the rescaling of the pressure. Substituting Equation (3.3b) into Equation (3.1) we have

$$\sum_{j=1}^{n^2} A_{ij} R_{ij}^4 (p_i - p_j) = \begin{cases} \frac{1}{Q} - p_i, & 1 \leq i \leq n, \\ 0, & n < i \leq n^2 - n, \\ -p_i, & n^2 - n < i \leq n^2, \end{cases} \tag{3.12}$$

where we solve for Q in terms of p_i from Equation (3.3b) to find

$$Q = \frac{n}{1 + \sum_{j=1}^{n} p_j}.$$

Using this expression for Q, our system of fluid equations (3.12) becomes

$$\sum_{j=1}^{n^2} A_{ij} R_{ij}^4 (p_i - p_j) = \begin{cases} \frac{1}{n}\left(1 + \sum_{j=1}^{n} p_j\right) - p_i, & 1 \leq i \leq n, \\ 0, & n < i \leq n^2 - n, \\ -p_i, & n^2 - n < i \leq n^2. \end{cases} \tag{3.13}$$

We solve the pressure equations when the solutions are vertically symmetric. We label the value at a representative node by $p_i \equiv \hat{p}_k$ where $k = \left\lceil \frac{i-1}{n} \right\rceil$, where $\lceil a \rceil$ is the smallest integer greater than a. So the first n variables have the value $\hat{p}_1$, the next n have the value $\hat{p}_2$, etc. We analogously denote the cell densities as $N_i = \hat{N}_k$. We rewrite Equation (3.13) using these variables as

$$\sum_{j=1}^{n} \hat{A}_{ij} R^4(\hat{N}_i, \hat{N}_j)(\hat{p}_i - \hat{p}_j) = \begin{cases} \frac{1}{n}, & i = 1, \\ 0, & 1 < i < n, \\ -\hat{p}_n, & i = n, \end{cases} \tag{3.14}$$

where we have used the simplification $(1 + \sum_{j=1}^{n} p_j)/n - p_i = (1 + n\hat{p}_1)/n - \hat{p}_1 = 1/n$. The adjacency matrix $\hat{A}_{ij}$ represents the path graph on n vertices, so that $\hat{A}_{ij} = 1$ if $i = j \pm 1$ or $\hat{A}_{ij} = 0$ otherwise. Adding all n equations in (3.14) we find that $\hat{p}_n = 1/n$, where we have used the symmetry of the function R. For $1 \leq i < n$ we can iteratively solve these equations to find

$$\hat{p}_i = \frac{1}{n}\left(1 + \sum_{k=i}^{n-1} R^{-4}(\hat{N}_k, \hat{N}_{k+1})\right).^{1} \tag{3.15}$$

Hence in the 1-D model, we obtain the following system of n coupled equations for the cell density,

$$\frac{d\hat{N}_i}{dt} = F_1(\hat{p}_i)\hat{N}_i(1 - \hat{N}_i) - F_2(\hat{p}_i)\hat{N}_i + \delta n^2 \sum_{j=1}^{n} \hat{A}_{ij}(\hat{N}_j - \hat{N}_i), \quad 1 \leq i \leq n, \tag{3.16}$$

with $\hat{p}_i$ given by (3.15).

3.1.2 1-D PDE Model

We assume that the cell density varies only in the x direction, so that the permeability $k = k(N(x))$ also only varies in this direction. We then have by Equations (3.5) and (3.9)-(3.10) that $\tilde{p} = \tilde{p}(x)$, so the governing flow equations become

$$\text{(3.17a,b,c)} \qquad 0 = \partial_x(k(x)\partial_x\tilde{p}), \;\; Q_c = -k(N(0))\frac{\partial\tilde{p}}{\partial x}(0), \quad p = \frac{\tilde{p}}{Q_c}.$$

Integrating Equation (3.17a) subject to the boundary conditions (3.10) we find

$$\tilde{p}(x) = \frac{\displaystyle\int_x^1 \frac{1}{k(N(\alpha))} d\alpha}{\displaystyle\int_0^1 \frac{1}{k(N(\alpha))} d\alpha}. \tag{3.18}$$

---

[1] This is equivalent to saying that resistance in serial circuits is additive, where this pressure variable is playing the role of voltage and $R^{-4}(\hat{N}_k, \hat{N}_{k+1})$ is the resistance between nodes k and $k + 1$.

Substituting (3.18) into (3.17b) we compute Q_c, and from (3.17c) we find

$$p(x) = \int_x^1 \frac{1}{k(N(\alpha))} d\alpha. \tag{3.19}$$

Substituting (3.19) into Equation (3.6) we obtain a single equation for the cell density,

$$\frac{\partial N}{\partial t} = F_1 \left(\int_x^1 \frac{1}{k(N(\alpha))} d\alpha \right) N(1-N) - F_2 \left(\int_x^1 \frac{1}{k(N(\alpha))} d\alpha \right) N + \delta \partial_x^2 N. \tag{3.20}$$

Equation (3.20) is a spatially nonlocal scalar reaction-diffusion equation for the cell density N.

3.1.3 Bounded Dynamics

We now comment on the boundedness of solutions to both models, in the full 2-D setting, in order to deduce reasonable ranges of model parameters that we explore in Sections 3.2 and 3.4. We first show that solutions to the Equations (3.1)-(3.4) are bounded within the region $[0,1]^{n^2}$. We note that for all $p \in \mathbb{R}$, the functions in Equations (3.4) satisfy $0 \leq F_1(p) \leq 1$ and $0 \leq F_2(p) \leq 1$. Now we assume that for some t^*, $N_i(t^*) \in [0,1]$ for all i, and $N_k(t^*) = 1$ for at least one k. We then have that

$$\frac{dN_k}{dt} = -F_2(p_k) + \delta n^2 \sum_{j=1}^{n^2} A_{kj}(N_j - 1) \leq 0, \tag{3.21}$$

Hence continuously differentiable (C^1) solutions to Equations (3.2) are bounded above.

Similarly, assume that for some t^*, $N_i(t^*) \in [0,1]$ for all i, and that $N_m(t^*) = 0$ for at least one m. We then have that,

$$\frac{dN_m}{dt} = \delta n^2 \sum_{j=1}^{n^2} A_{mj}(N_j) \geq 0, \tag{3.22}$$

and so continuously differentiable solutions are also bounded below. Note that these bounds are independent of the pressures p_i. So we have that $N_i(t) \in [0,1]$ for all i and for all $t \geq 0$.

While we are not aware of a formal comparison principle applicable to Equations (3.5)-(3.11), the above argument gives a heuristic bound on the behaviour of solutions for these equations as well. The existence of spatiotemporal oscillations, which we show in Section 3.2, suggests that a general comparison principle does not hold for this system. Hence a rigorous treatment of Equations (3.5)-(3.11) would be needed in order to formally extend this argument. Nevertheless, we will assume that PDE solutions are similarly bounded, and our numerical solutions confirm this.

3.2 Numerical Exploration of Solution Behaviours

In this section we present numerical solutions for the 2-D lattice equations (3.1)-(3.4) as well as the PDE system given by (3.5)-(3.11). We fix $\rho = 0.9$ so that cell growth significantly affects the effective permeability of the medium. To capture sufficiently sharp behaviour in the pressure functions, we set $g = 60$. The remaining parameters are varied to demonstrate the range of solution behaviours.

The PDE model was simulated using the finite element software COMSOL with 24,912 triangular elements, as well as a finite difference scheme to verify the results obtained from the COMSOL implementation. The lattice model was solved using an explicit adaptive Runge-Kutta method, 'ode45' in MATLAB, with a maximal time step of 10^{-3}. The restriction of the maximal time step was to ensure a good approximation of bifurcation phenomena [33]. Convergence checks were carried out in the time step in the numerical schemes for both models, and in the number of elements for the PDE.

From Section 3.1.3 and the monotonicity of Equations (3.15) and (3.19), we can compute the maximum and minimum possible pressures throughout the domain in each (1-D) model. We then deduce the ranges of the pressure threshold parameters p_l and p_c that lie between maximum and minimum pressures in the scaffold.. This allows us to explore dynamics that are not the trivial states of either uniform cell death or logistic cell growth to a uniform carrying capacity. To compute these extremal pressures, we set the cell densities $N_i = 0$ or $N_i = 1$ for all i. Using (3.15), we vary p_l as

$$\frac{1}{n} < p_l < \frac{1 + (n-1)(1-\rho)^{-4}}{n} \approx 10^4, \tag{3.23}$$

for the lattice and using (3.19) we use

$$0 < p_c < (1-\rho)^{-3} = 10^3, \tag{3.24}$$

for the PDE. Note the difference in the orders of magnitude between these two ranges, which is due to the constitutive difference between Poiseuille flow and cubic permeability in Darcy's law. See Chapter 2 for a discussion of why these constitutive exponents differ between the models. Changing the exponent in the permeability, Equation (3.7b), from 3 to 4 gives quantitatively similar behaviour for the PDE and very large lattices.

For most initial cell densities simulated, and for all small initial cell densities, the lattice and PDE models are both insensitive to perturbations in initial conditions. For all of our simulations, we set the initial data to be a perturbed uniform state

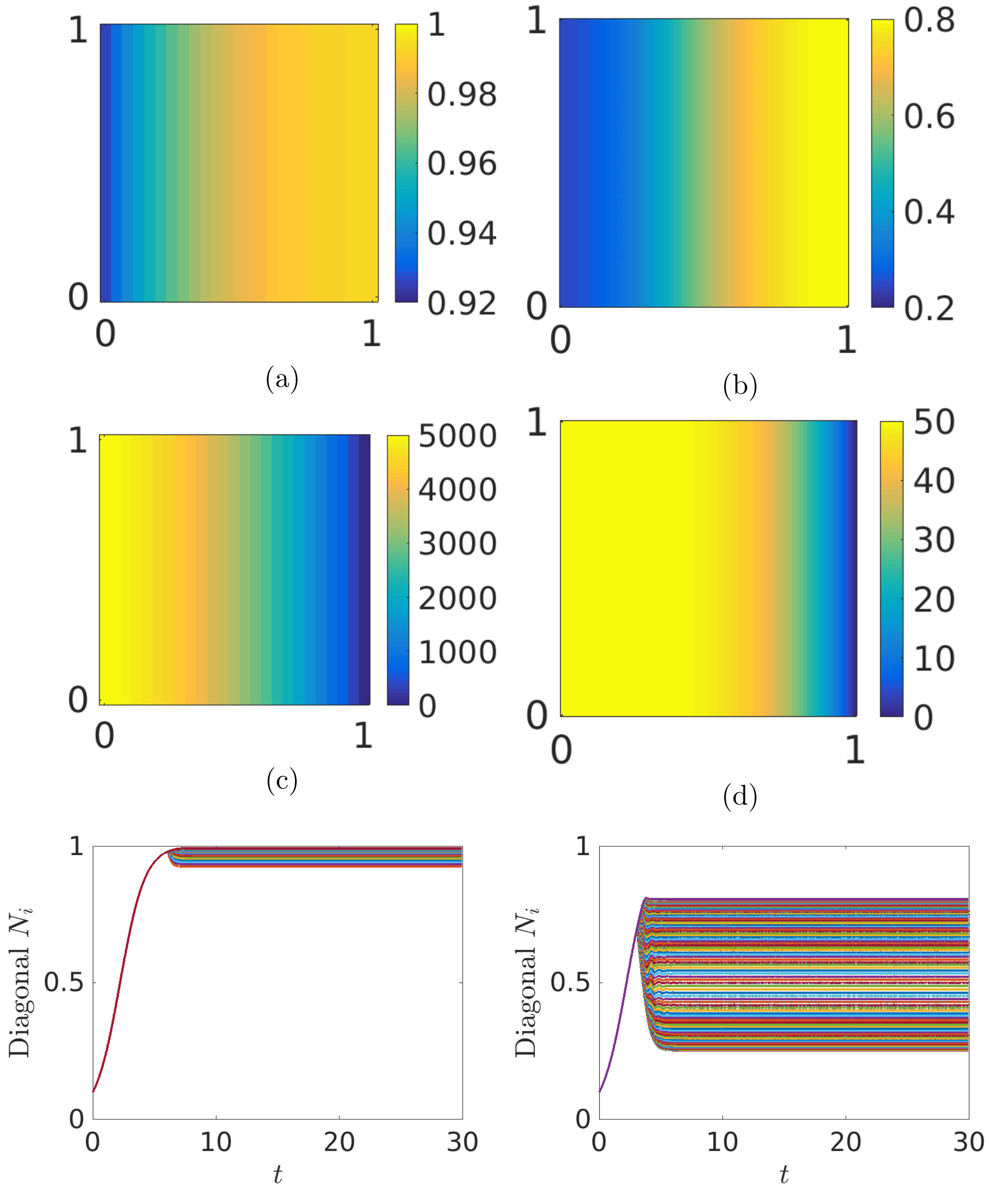

(a) (b) (c) (d) (e) (f)

Figure 3.2: Cell density plots in (a)-(b), pressure plots in (c)-(d) at $t = 30$ for $\delta = 10^{-1}$, and time series showing the evolution from uniform growth to these stationary patterns in (e)-(f). Plots (a), (c) and (e) correspond to simulations with $p_l = 5000$, with $n = 25$ and plots (b), (d), and (f) correspond to simulations with $p_l = 50$ with $n = 100$.

so that $N_0(x, y) \approx 0.1$ and $N_i(0) \approx 0.1$. The cell densities grow uniformly until the pressure at some point of the domain reaches the threshold p_c for the PDE or p_l for the lattice, where some regions then experience cell death due to high pressure. The simulations then tend to a spatial horizontal gradient in cell density with low cell density on the left side of the lattice (where the pressure is highest) and high cell density on the right side of the lattice (where the pressure is lowest). We observe one of three different long time behaviours: a stable steady state, a vertically symmetric 'pulsating' oscillation, or a vertically asymmetric oscillation. The steady states we observe are either vertically symmetric or asymmetric. The latter is only seen in lattice simulations with $n \lessapprox 50$.

At large values of δ (e.g. $\sim O(1)$), or large values of the threshold parameters p_l or p_c, all simulations tend to a similar steady state with a gradual horizontal gradient in cell density. We conjecture that these solutions are vertically symmetric. In Figure 3.2 we plot two example cell density distributions alongside corresponding plots of pressure.Note that here, $\delta = 10^{-1}$ is sufficiently large to see very little variation in cell density for some values of the threshold p_l - consider the colour ranges in Figure 3.2a. We also plot time series of the nodal evolution along the diagonals of the scaffold, i.e. all nodes along the lines $x = y$ and $x = 1 - y$, in Figures 3.2e-3.2f. For large δ, there is a non-negligible cell density present in the region of high pressure despite the local cell density being governed by exponential death. The pressure does not vary significantly in this region of lower cell density near the left side of the scaffold, as the effective permeability changes little at low cell densities. In these parameter ranges, the 1-D reduction described in Section 3.1.1 is a quantitatively accurate approximation to the cell density along any row of the lattice.

For smaller values of the diffusion we observe a different long-time behaviour. In some cases, the cell density throughout the scaffold oscillates with a 'pulsing' between the right and the left side of the domain, maintaining a vertical symmetry throughout the oscillations. In Figure 3.3 we show the cell densities across diagonal nodes for two cases, a lattice of size $n = 100$ in Figure 3.3a and the PDE in Figure 3.3b, and observe stable oscillations at each node throughout the domain. For this parameter choice, the lattice simulation in Figure 3.3a has the largest oscillations in cell density for nodes at the far left of the lattice, and these values never get close to the zero. In comparison, the PDE simulation in Figure 3.3b has its largest oscillations in the middle of the domain, and the far leftmost part of the domain exhibits very small cell densities. In Figure 3.4 we plot the cell density at three different points in time throughout half of an oscillation period for the same simulations as in 3.3. In Figure 3.4a, we

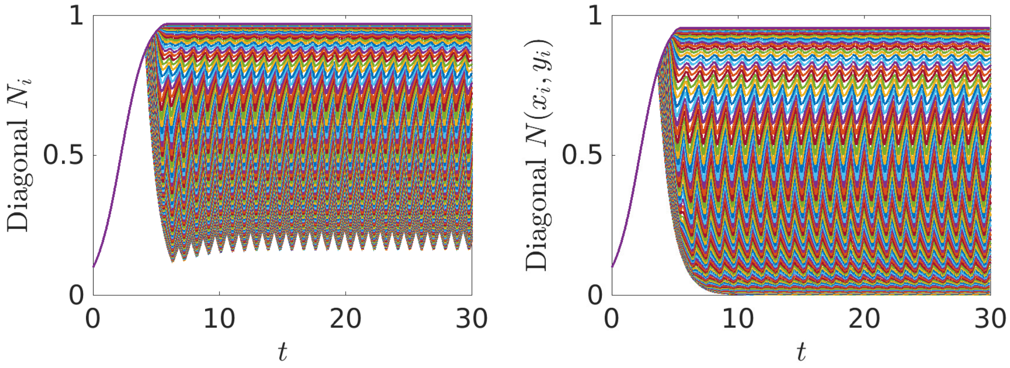

(a) (b)

Figure 3.3: Time series of nodal values of the cell density for a lattice of size $n = 100$, $\delta = 10^{-2}$, $p_l = 500$ in (a), and along 200 corresponding diagonal interpolants of the PDE system with $\delta = 10^{-2}$, $p_c = 50$ in (b).

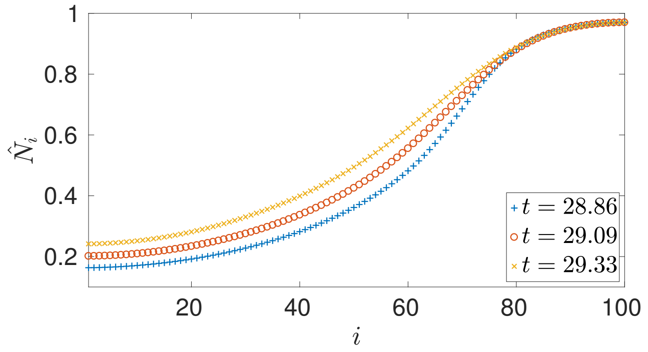

(a)

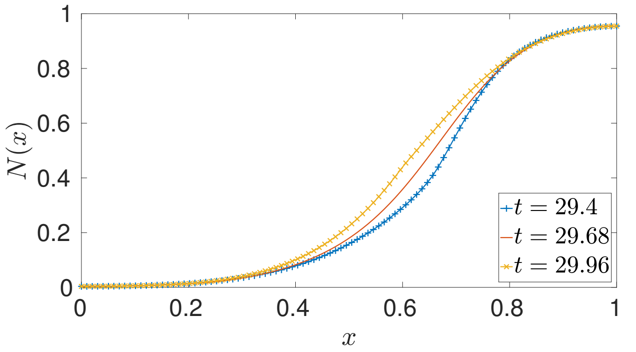

(b)

Figure 3.4: Plots (a) are of cell density for a lattice of size $n = 100$, $\delta = 10^{-2}$, $p_l = 500$ at three times during one oscillation. Plots (b) are of cell density for the PDE with $\delta = 10^{-2}$, $p_c = 50$ at three times during one oscillation. Note that we have simulated the 2-D models but averaged over any vertical variation in cell density in both cases.

plot just the 1-D values of the column-averaged cell density as these oscillations are vertically symmetric, and similarly we plot vertically-averaged cell densities for the PDE in Figure 3.4b. The oscillations move between the yellow and blue curves with a period of $t \approx 0.94$ in Figure 3.4a and $t \approx 1.12$ in Figure 3.4b. These large oscillations persist in the 1-D reductions of both models, as well as when the horizontal boundary conditions for cells and fluid flow are changed from Neumann to periodic conditions. This suggests that these oscillations are inherently a 1-D phenomenon.

The above kinds of behaviours - vertically symmetric steady states and oscillations - appear in the PDE and in large lattices (e.g. for $n = 100$), and appear to be generic behaviours. In addition to these behaviours, qualitatively different steady states and oscillations exist in the smaller lattices. In many of the smaller lattice simulations, we observe a complicated breaking of the vertical symmetry. In Figure 3.5 we give an example of these vertically asymmetric oscillations. The cell density oscillates vertically between the two impermeable horizontal boundaries. Note that the time series in Figure 3.5e separates into 'bands.' These correspond to columns in the lattice (shown in Figures 3.5a-3.5d). The largest of these bands that changes between a growing and a dying state (shown in red and green in Figure 3.5e) corresponds to the third column from the right boundary in the lattice. The bands which are always green (locally growing logistically) correspond to nodes on the right of this column, and those that are always red correspond to nodes on the left of this column. These oscillations are more complicated than the vertically symmetric behaviours discussed previously, as their existence depends on the number of nodes n of the lattice in addition to the boundary conditions. We note that the spatial mean cell density during an oscillation, plotted in Figure 3.5f, has many turning points despite being simply periodic. For this particular parameter set, changing the horizontal boundary conditions from no-flux on the fluid and cells to periodic conditions eliminated the oscillations. Similarly, the 1-D model did not display oscillating behaviour for these parameters.

In Figure 3.6a we demonstrate vertically asymmetric oscillations in an $n = 25$ lattice. We plot the cell density at every node and demonstrate a similar oscillation as in Figure 3.5. We also show the effect of changing the domain on the behaviour shown in Figure 3.6a. We show plots of cell density for periodic horizontal boundary conditions for both the fluid and the cell density in Figure 3.6b, and for the 1-D model in Figure 3.6c. The periodic conditions in Figure 3.6b change how the oscillation interacts with the boundary, and hence the bands do not display the same structure as in Figure 3.6a. The 1-D model in Figure 3.6c does not oscillate and instead reaches

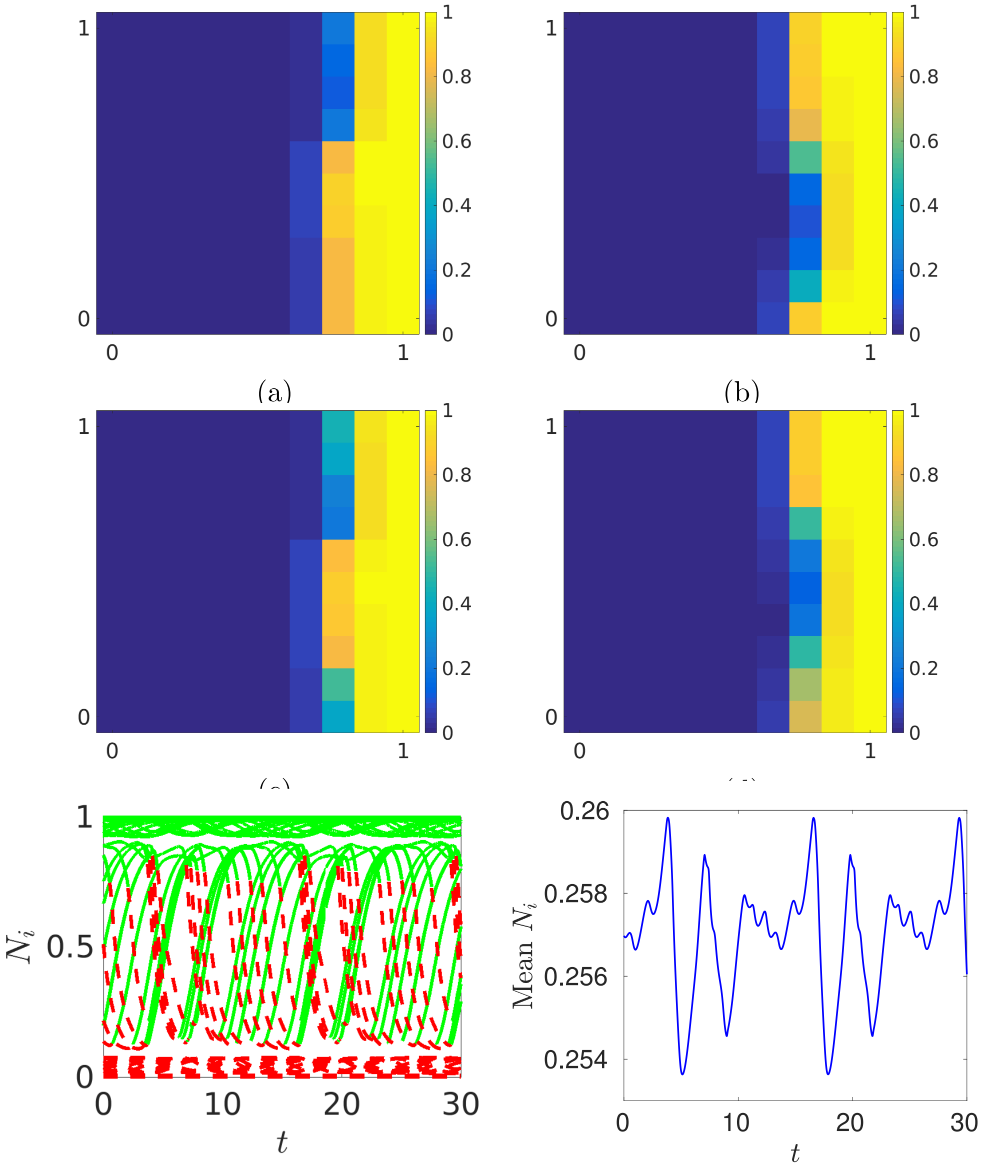

(a) (b)

(c) (d)

(e) (f)

Figure 3.5: Plots of cell density for a lattice of size $n = 10$, $\delta = 10^{-3}$, $p_l = 500$ at times $t = 15$, $t = 20$, $t = 25$, and $t = 30$ in (a)-(d) respectively. We plot the nodal values of the cell density at every node in the lattice in (e) where the line is coloured green if $p_i < p_l$ and red if $p_i > p_l$. In (f) we plot the spatial mean cell density during the oscillations. Note that we have only shown time series for latter time periods after the cell densities have settled into oscillations.

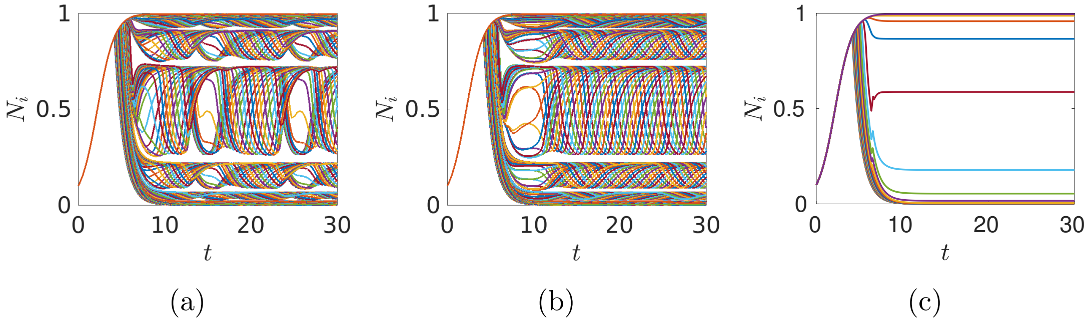

Figure 3.6: Nodal plots of cell densities for a lattice of size $n = 25$, $\delta = 10^{-3}$, $p_l = 500$ with (a) no-flux conditions on the horizontal boundaries, (b) periodic conditions on these boundaries, and (c) the 1-D model.

a steady state. The periods of the vertically asymmetric oscillations in Figures 3.5 and 3.6 are much larger than the vertically symmetric oscillations in Figure 3.3. In addition to the absence of asymmetric oscillations in the 1-D models, this change in oscillation frequency is how we differentiate these two kinds of oscillatory behaviours.

We also observe combinations of both kinds of oscillations. In Figure 3.7 we compare 1-D and 2-D simulations of a lattice of size $n = 25$ with $p_l = 750$ for different values of δ. In 3.7b we observe asymmetric oscillations in a 2-D lattice in combination with smaller amplitude and higher frequency oscillations for some nodes. In 3.7d we instead observe fast oscillations with a slow variation indicative of two kinds of oscillatory behaviours. Figures 3.7a and 3.7c are the 1-D versions of Figures 3.7b and 3.7d respectively, and indicate the strength of the underlying pulsing oscillation in the 2-D simulations. Figure 3.7c shows more nodes oscillating with larger amplitudes compared to Figure 3.7a, which suggests why the oscillations in Figure 3.7d are qualitatively different from those in Figure 3.7b. Note that the frequencies of the fast oscillations in the 2-D simulations correspond to the frequencies of the 1-D oscillations, and hence the underlying vertically symmetric behaviour. We also find parameters where a pulsing oscillation in 1-D exists along with a vertically asymmetric steady state in the 2-D model, leading to a vertically asymmetric oscillation that is at the frequency of the vertically symmetric 1-D oscillation, but it is not vertically symmetric due to the underlying cell density distribution (steady state). In Section 3.4 we explore the parameter space in the 1-D and 2-D models, and demonstrate that regions with large amplitudes at some nodes in the 1-D model will correspond to pulsing oscillations in the 2-D model, so that these more exotic behaviours exist only when the 1-D model has smaller amplitude oscillations.

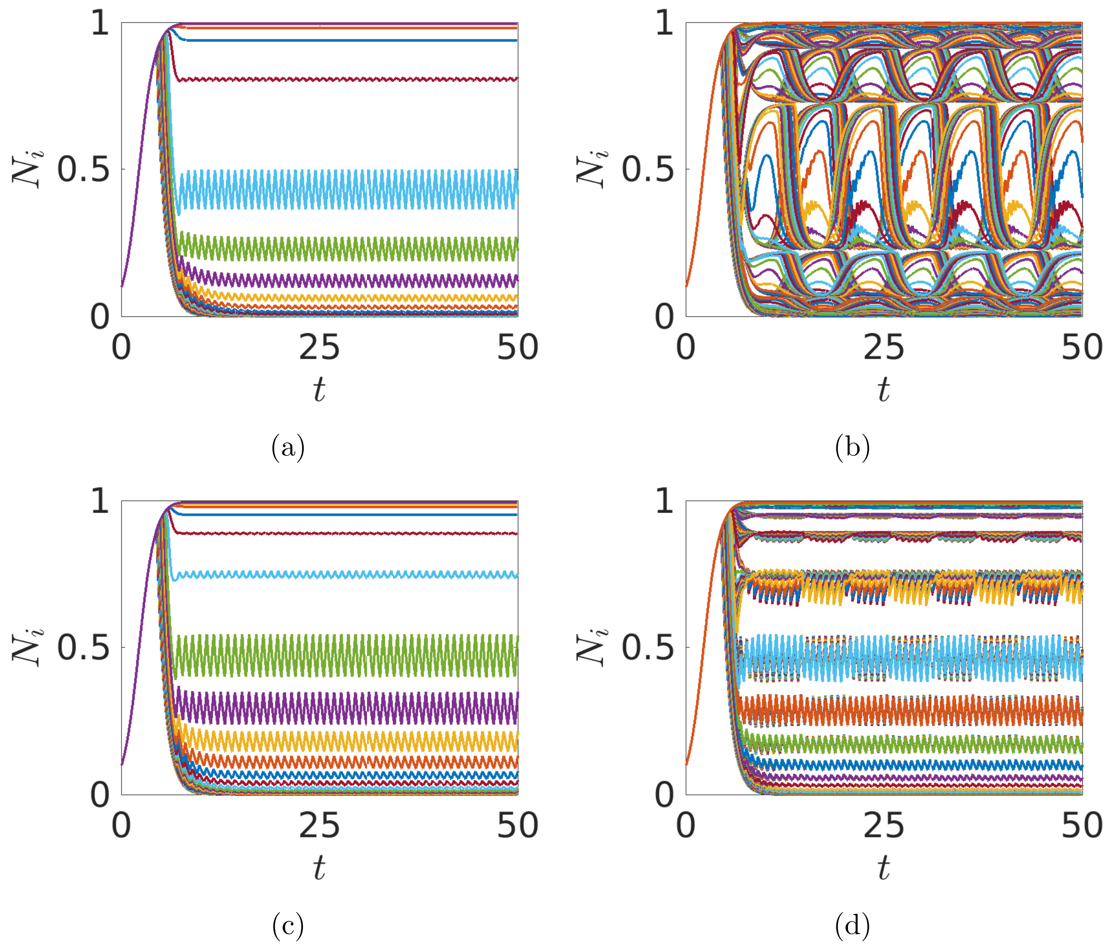

(a) (b)

(c) (d)

Figure 3.7: Plots of the cell density at each node for $n = 25$, $p_l = 750$, with $\delta = 10^{-3}$ in (a) and (b) and $\delta = 2 \times 10^{-3}$ in (c) and (d). The 1-D model is plotted in (a) and (c), and the 2-D in (b) and (d).

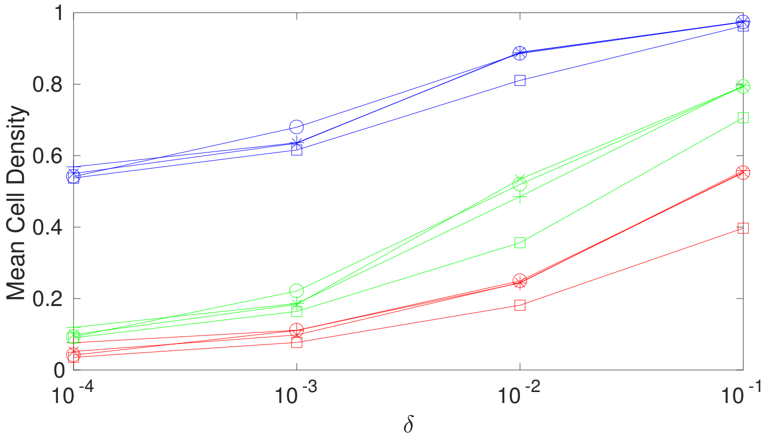

Figure 3.8: Mean cell density across several simulations of the lattice and the PDE models over four values of δ averaged over the time from $t = 20$ to $t = 30$ and across space (nodes in the lattice, (x, y) in the PDE). The symbols $+$, $\times$, $\circ$, and $\square$ are for the lattice sizes $n = 25, 50, 100$, and the PDE respectively. The colours red, green, and blue correspond to $p_l =$ 50, 500, and 5000, respectively, and $p_c = p_l/10$.

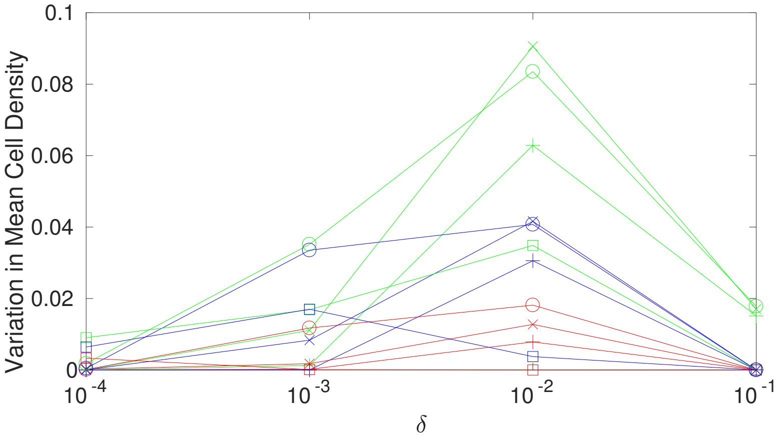

Figure 3.9: Variation in the spatial mean cell density across several simulations of the lattice and the PDE models over four values of δ averaged over the time from $t = 20$ to $t = 30$. The symbols $+$, $\times$, $\circ$, and $\square$ are for the lattice sizes $n = 25, 50, 100$, and the PDE respectively. The colours red, green, and blue correspond to $p_l =$ 50, 500, and 5000, respectively, and $p_c = p_l/10$.

We quantitatively compare some of these lattice and PDE simulations in terms of their spatial mean cell density. We assume that after $t = 20$ time units that the cell density is close to its long-time behaviour (either a steady state or an oscillation). To account for variations due to oscillatory behaviour, we average over 10 time units (after the transient 20 time unit period) and plot the spatial mean of the cell density for each simulation in Figure 3.8. The colours correspond to the thresholds $p_c = p_l/10$, and the symbols to the various lattice sizes and the PDE. We note that the diffusion δ and the pressure threshold largely determine the mean cell density. For $\delta \leq 10^{-2}$ in particular, the lattice size plays a significant role in determining this mean cell density for some values of p_l. We approximate the spatial mean cell densities for $\delta \gtrapprox 10^{-1}$ in Section 3.3 asymptotically.

We also consider how the oscillations affect the spatial mean cell density. We compute the maximum and minimum values that the spatial mean cell density takes in 10 time units (again after a period of $t = 20$ time units). We plot the difference between these values in Figure 3.9, using the same symbols and colours to denote the simulations as in Figure 3.8. This difference gives a measure of the quantitative effect these oscillations have on experimental observables, such as permeability and total cell density. We observe some interesting variations in the amplitude of these oscillations, such as a non-monotonic dependence on both δ and the pressure thresholds for different models. All of the simulations with large oscillations in spatial mean cell density in this plot (e.g. above the value of 0.03) correspond to vertically symmetric oscillations, and were quantitatively comparable to their 1-D counterparts. The vertically asymmetric oscillations have only a small effect on changes in spatial mean cell density.

Some simulations exhibit excitable dynamics. In Figure 3.10a we first show the evolution of cell density for a small ($n = 10$) lattice to steady state. Then in Figures 3.10b through 3.10d we add increasing perturbations to the cell density at a single node at the top-right of the lattice. We observe small excursions from the equilibrium for very small perturbations (Figure 3.10b), larger excursions from equilibrium for larger perturbations (Figure 3.10c), and finally a sufficiently large perturbation induces a pulsing oscillation in Figure 3.10d. This excitability is due to the nonlocal nature of the quasi-static fluid coupling, in that an increase in cell density at one node in the lattice affects the overall flow through the scaffold instantaneously and hence the pressure at every other node. This is particularly true for nodes that have high cell density as the nonlinearity in Equations (3.1) and (3.3a) amplifies the effect of large cell densities. Note in particular that we only perturb one node in Figures

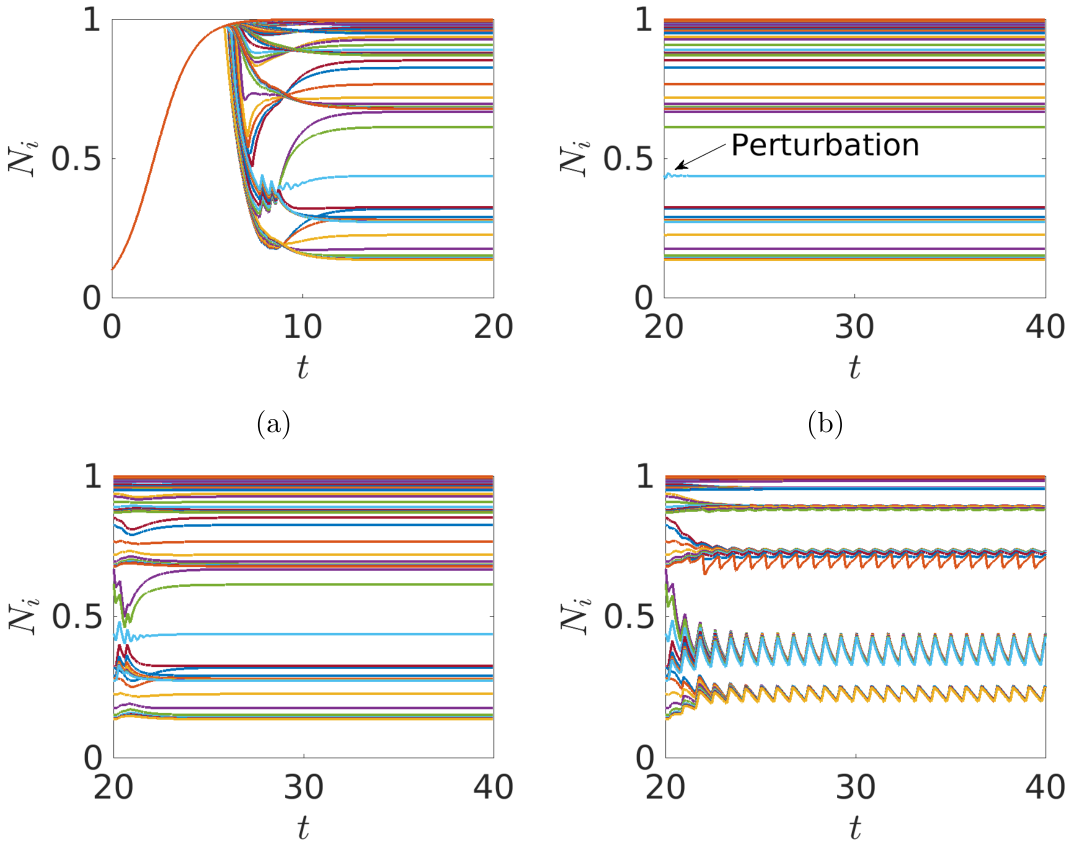

(a) (b)

(c) (d)

Figure 3.10: Excitable dynamics with $n = 10$, $p_l = 4000$, $\delta = 10^{-2}$. In (a) we show the trajectory from a uniform state to a nonuniform equilibrium at each node. In (b)-(d) we show the final state from (a) evolves after a perturbation of the cell density at a single node. These perturbations are to node N_{91} at the bottom right of the lattice, and of sizes 10^{-5} in (b), 3×10^{-4} in (c) and 4×10^{-4} in (d).

3.10b-3.10d, yet several nodes grow or die rapidly at $t = 20$ due to this nonlocal effect. In Section 3.4, we use numerical continuation to show the coexistence of locally stable steady states and pulsing oscillations for large regions of parameter space. A sufficiently large perturbation can move the state of the system between basins of attraction of these different long-time behaviours.

The smoothing parameter g plays only a marginal role in these oscillations. The behaviours found in all of the simulations we performed are qualitatively and quantitatively the same in the limit of $g \to \infty$ (we replaced the functions F_1 and F_2 in Equations (3.4) with Heaviside step-functions, and obtained quantitatively comparable results). In the other direction, we set $g = 1$ and repeated the simulation in Figure 3.3a, and the results displayed only small differences in the initial transient leading up to the oscillation, and otherwise the same behaviour. In contrast, the oscillations in Figures 3.5 and 3.6 were not present if $g = 1$ for any parameters simulated, and instead steady state behaviour was obtained. This indicates that these vertically asymmetric oscillations are related to sharp transitions between cell growth and death due to pressure.

We can modify our model to account for quiescent cell states, without growth or death, induced by high pressure that is not high enough to kill the cells. We plot an example of this in Figure 3.11. These figures are generated by adding a term z to the threshold inside of the function F_2 from Equations (3.4), so that $F_2(p_i) = \left(\frac{1}{2}\right)(\tanh[g(p_i + z - p_l)] + 1)$. For small values of z relative to p_l the dynamics are broadly similar; compare Figures 3.11a and 3.11b. For increasing values of z, the form of the oscillation changes, with increasing period as z increases, and eventually the oscillation is damped out due to diffusion for a large enough quiescent regime, as in Figure 3.11f. Depending on the parameters we have found that the period of the oscillation can be extended from ≈ 1 time unit to greater than 3000 time units. Our numerical results suggest that capturing quiescent behaviour may have a comparable effect to smoothing the pressure forcing on the cells (e.g. decreasing the value of g) in terms of asymptotic dynamics for small z, whereas large z tends to regularize the dynamics leading toward more steady state behaviours. We do not explore these variations further here.

Modulo differences in the constitutive relations, the behaviour of the PDE model and larger lattices is similar. This is expected due to the similarities between the lattice equations and a method-of-lines discretization of the PDE. In this Section we have illustrated typical solution behaviours displayed by lattice and PDE models. In Section 3.4.2 we use simulations from a large subset of the feasible parameter space

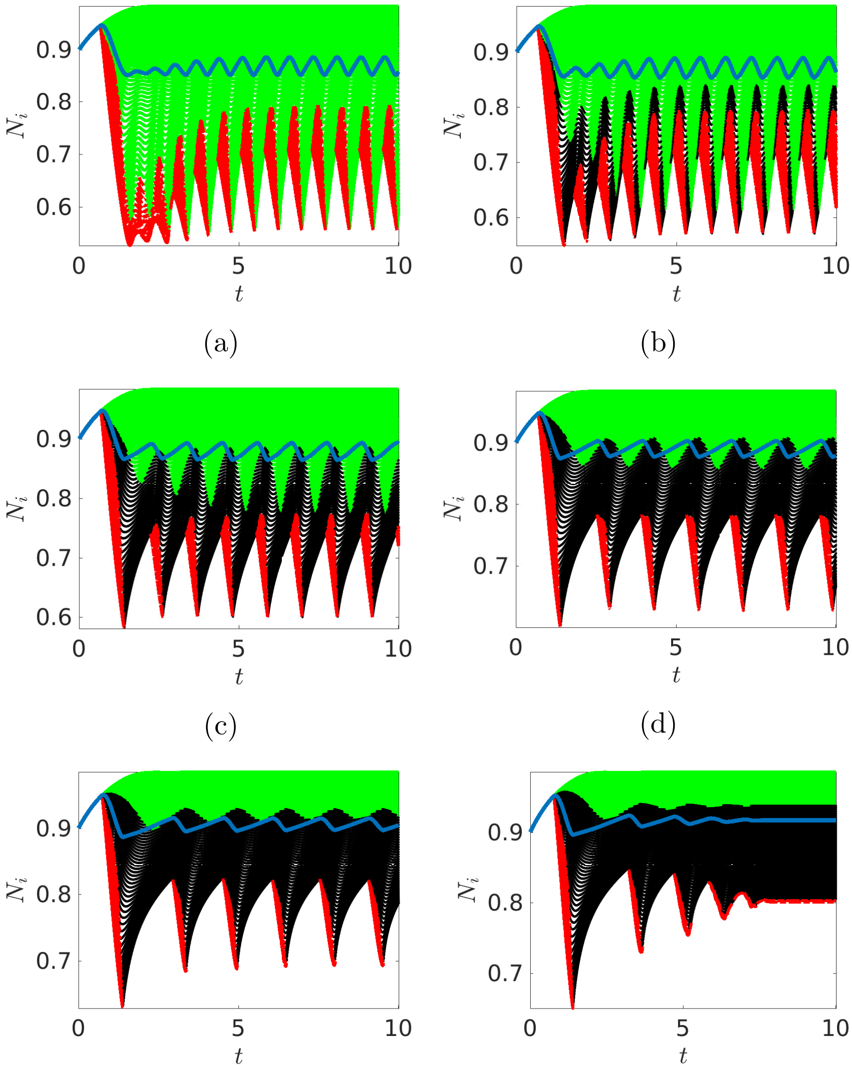

(a) (b)

(c) (d)

(e) (f)

Figure 3.11: Time series of nodal values of the cell density for a 1-D lattice of size $n = 100$, with $\delta = 0.05$ and $p_l = 2000$. In (a) we have no quiescent regime (e.g. cells go from growing to dying immediately as pressure is varied). We then increase the threshold in the function F_2 by $z = 10, 50, 100, 200$, and 300 in each subsequent plot (b)-(f). Green nodes are growing ($p_i < p_l$), red nodes are dying ($p_i > p_l + z$) and black nodes are quiescent, only changing value due to diffusion ($p_l < p_i < p_l + z$). We overlay the mean cell density in blue in each plot.

(n, δ, p_l, and p_c) to understand where in parameter space these behaviours arise. In particular, we provide evidence that smaller lattices exhibit more complicated dynamics. Before demonstrating these results, we describe some asymptotic approaches that allow us to restrict our numerical efforts to specific parameter regimes.

3.3 Asymptotic Solutions in the Large Diffusion Limit

For larger values of the diffusion parameter δ, the numerical solutions approach an equilibrium with little variation between nodal values (see Figures 3.2a and 3.2e where $\delta = 10^{-1}$ is sufficient to observe very little spatial variation). We pursue an asymptotic solution for both models in the limit where $1/\delta \ll 1$. This asymptotic solution allows us to quantitatively predict the solution structure for large values of δ. In particular, large-δ values give rise to simple steady state solutions, so that when we exhaustively explore a subset of the parameter space in Section 3.4.2, we only consider small values of δ, namely $\delta \leq 10^{-1}$.

To make analytical progress we simplify the pressure forcing terms throughout the rest of this Section. Letting $g \to \infty$ our pressure functions become $F_1(p_i) = H(p_l - p_i)$ and $F_2(p_i) = H(p_i - p_l)$, where H is the Heaviside step function. For convenience, we take H to be continuous on the right, so that $\lim_{\varepsilon \to 0^+} H(\varepsilon) = H(0) \equiv 1$.

3.3.1 Lattice Asymptotics

We first consider solutions in the large diffusion limit for the lattice. We rewrite Equation (3.2) as,

$$\delta^{-1}\frac{dN_i}{dt} = \delta^{-1}(H(p_l - p_i)N_i(1 - N_i) - H(p_i - p_l)N_i) - n^2 \sum_{j=1}^{n^2} L_{ij}N_j, \quad 1 \leq i \leq n^2. \tag{3.25}$$

We expand our variables as $N_i = N_{0,i} + \delta^{-1}N_{1,i} + O(\delta^{-2})$ and $p_i = p_{0,i} + \delta^{-1}p_{1,i} + O(\delta^{-2})$. Substituting these expansions into Equation (3.25) and formally equating powers of δ, we find that the leading-order equation for the cell density, $N_{0,i}$, is

$$0 = -n^2 \sum_{j=1}^{n^2} L_{ij}N_{0,j}, \quad 1 \leq i \leq n^2. \tag{3.26}$$

The graph Laplacian L has one zero eigenvalue with the corresponding eigenvector $v = (1, 1, , \ldots, 1)^T$ [121]. Therefore the leading-order cell densities are all equal; that is $N_{0,i} = N_0$ for some N_0, for all i.

To compute N_0 we consider the next-order problem,

$$\frac{dN_0}{dt} = (H(p_l - p_{0,i})N_0(1 - N_0) - H(p_{0,i} - p_l)N_0) - n^2 \sum_{j=1}^{n^2} L_{ij} N_{1,j}, \quad 1 \le i \le n^2. \tag{3.27}$$

Equations (3.1) do not explicitly depend on δ and so the pressures $p_{0,i}$ satisfy Equations (3.1) with the uniform cell density N_0. As a spatially-constant cell density N_0 is vertically symmetric, we can use Equation (3.15) to determine the pressures $p_{0,i}$. In order to eliminate the $N_{1,j}$ terms, we sum Equation (3.27) over i and note that $\sum_{i=1}^{n^2} L_{ij} = 0$ for all j, to find

$$n\frac{dN_0}{dt} = \sum_{i=1}^{n} (H(p_l - \hat{p}_{0,i})N_0(1 - N_0) - H(\hat{p}_{0,i} - p_l)N_0), \tag{3.28}$$

where we have relabelled the pressures to reflect the 1-D symmetry, and divided both sides by n.

The pressures $\hat{p}_{0,i}$ are monotonically decreasing in i with $\hat{p}_{0,n} = 1/n$. Excluding cases corresponding to p_l outside of the ranges given by (3.23), there exists an $m = m(N_0)$ such that for all $j \le m$ and $k > m$, $\hat{p}_{0,j} \ge p_l$ and $\hat{p}_{0,k} < p_l$. Thinking of m as an integer, we have that solutions of Equation (3.28) satisfy,

$$n\frac{dN_0}{dt} = (n - m(N_0))N_0(1 - N_0) - m(N_0)N_0. \tag{3.29}$$

We now approximate $m(N_0)$ as a real variable, rather than an integer, in order to make analytical progress and avoid many tedious details. We will justify this approximation later by observing how well the solution matches numerical solutions of the full problem. By setting the left hand side of Equation (3.15) equal to p_l, we find $m(N_0)$ to be

$$m(N_0) = [n - R^4(N_0, N_0)(p_l n - 1)]^+ = [n - (1 - \rho N_0)^4 (p_l n - 1)]^+, \tag{3.30}$$

where $[f]^+ = \max(f, 0)$ is the positive part of the function f. It is necessary to define m using the notation $[f]^+$ as for small N_0, corresponding to $p_i < p_l$ for all i, the value of $m(N_0)$ is negative. Equations (3.29) and (3.30) represent a single scalar first-order ordinary differential equation, compared with the original n^2 differential equations (3.2) and n^2 algebraic equations (3.1), although our scalar equation is not smooth (e.g. not differentiable) due to the function $m(N_0)$.

We now look for a steady state solutions, $N_0^* \ge 0$, to Equation (3.29). If $m(N_0^*) = 0$, then $N_0^* = 0$ or $N_0^* = 1$ are the only solutions to Equation (3.29), and we will show that they cannot be stable steady states within the parameters we consider. Assuming that $m(N_0^*) > 0$, we substitute (3.30) into Equation (3.29), and find that N_0^* satisfies the quintic polynomial

$$0 = R^4(N_0^*, N_0^*)(p_l n - 1)(2 - N_0^*) - n = (1 - \rho N_0^*)^4 (p_l n - 1)(2 - N_0^*) - n. \quad (3.31)$$

We will first argue that any root of Equation (3.31) must be unique within the interval $(0, 1)$, and then show the existence and global stability of $N_0^* \in (0, 1)$.

Let $\tilde{N} = R(N_0^*, N_0^*) = 1 - \rho N_0^*$. Since $0 < \rho < 1$, all roots $N_0^* \in (0, 1)$ of Equation (3.31) must be associated to roots $\tilde{N} \in (0, 1 - \rho)$ of

$$0 = \tilde{N}^4(p_l n - 1)\left(2 - \frac{1}{\rho} + \frac{\tilde{N}}{\rho}\right) - n = \tilde{N}^5 \frac{(p_l n - 1)}{\rho} + \tilde{N}^4(p_l n - 1)\left(2 - \frac{1}{\rho}\right) - n, \quad (3.32)$$

and vice versa. Equation (3.32) has only one sign change in its coefficients (as $p_l > 1/n$ by (3.23)). By Descartes' rule of signs, Equation (3.32) has at most one positive root, implying that there cannot be more than one root in the interval $0 \leq \tilde{N} \leq 1 - \rho$. Hence any root of equation (3.31) in $(0, 1)$ must be unique.

We now argue by monotonicity that this root exists and is globally attractive for initial data in the full interval $[0, 1]$. We will use this root to construct solutions to equation (3.29). The function $m(N_0)$ given by (3.30) is monotonically increasing in N_0, and for $1 + 1/n < p_l < (1 + (n - 1)(1 - \rho)^{-4})/n$ we have that $m(0) = 0$ and $m(1) > 0$. So there is a unique value $\hat{N}_0$ such that $m(\hat{N}_0) = 0$ and for all $N > \hat{N}_0$, $m(N) > 0$. From Equation (3.30) we compute that

$$\hat{N}_0 = \frac{1 - \left(\dfrac{n}{p_l n - 1}\right)^{\frac{1}{4}}}{\rho}, \quad (3.33)$$

which is within the interval $[0, 1]$.

By monotonicity, we have that $m(N_0) \geq 0$ for all $N_0 \in [\hat{N}_0, 1]$. Since $m(0) = 0$ and $m(1) > 1$, we have that $N_0 = 0$ is an unstable steady state and $N_0 = 1$ is not a steady state solution to Equation (3.29) for these parameters. From Equation (3.29) we have that $N_0'(t) < 0$ when $N_0 = 1$ and $N_0'(t) > 0$ when $N_0 = 0$. This implies that continuous solutions to Equation (3.29) do not leave the interval $[0, 1]$, which is consistent with the boundedness of solutions to the full system shown in Section 3.1.3. We note that for $m(N_0) = 0$, the right side of (3.29) is positive, so $N_0(t)$ grows in time and approaches $\hat{N}_0$. Similarly, for $N_0 = \hat{N}_0$, the right side of (3.29) is positive as $1 - \hat{N}_0 > 0$. So the region $(\hat{N}_0, 1)$ absorbs solutions with initial data $N_0(0) \in (0, 1]$, and hence we must have that there exists a steady state solution $N_0^* \in (\hat{N}_0, 1)$ to (3.29). Both existence and global attractivity of this steady state follows from the fact that Equation (3.29) is just a scalar first-order ODE within the region $N_0^* \in (\hat{N}_0, 1)$.

We can solve equation (3.29) by considering the cases when $N_0(0) < \hat{N}_0$ and $N_0(0) > \hat{N}_0$ separately. We first assume that $N_0(0) \in (0, \hat{N}_0)$. By the monotonicity of m, and the fact that $N'(t) > 0$ as long as $m(N) = 0$, there exists some t_s such that $N_0(t_s) = \hat{N}_0$. So substituting (3.30) into (3.29) we have

$$\frac{dN_0}{dt} = \begin{cases} N_0(1 - N_0), & t \leq t_s, \\ (1 - \rho N_0)^4 \left(p_l - \dfrac{1}{n}\right) N_0(2 - N_0) - N_0, & t > t_s. \end{cases} \tag{3.34}$$

The solution to equation (3.34) for $t \leq t_s$ is a logistic function,

$$N_0(t) = \frac{N_0(0)e^t}{N_0(0)(e^t - 1) + 1}, \quad t \leq t_s, \tag{3.35}$$

which we use to compute t_s. We set $N_0(t_s) = \hat{N}_0$ and use equations (3.33) and (3.35) to find

$$t_s = \ln \left(\frac{(1 - N_0(0)) \left(1 - \left(\dfrac{n}{np_l - 1}\right)^{\frac{1}{4}}\right)}{N_0(0) \left(\left(\dfrac{n}{np_l - 1}\right)^{\frac{1}{4}} + \rho - 1\right)} \right). \tag{3.36}$$

We consider equation (3.34) for $t > t_s$. This equation has a sixth-order polynomial nonlinearity, and we are not aware of a method to explicitly integrate it. We know by the boundedness of $N_0(t)$, however, that $N_0(t_s)$ is nearby in a nondimensional sense to our equilibrium value N_0^* for any initial mean cell density $N_0(0)$. So we expect approximately exponential convergence to N_0^* for $t > t_s$. We substitute the ansatz

$$N_0(t) = N_0^* + Ae^{-r(t - t_s)}, \quad t > t_s, \tag{3.37}$$

for $|A| \ll 1$ into equation (3.34), and take the Taylor series of the right hand side about $A = 0$ to find

$$\begin{aligned} &- rAe^{-r(t-t_s)} = (1 - \rho N_0^*)^4 \left(p_l - \frac{1}{n}\right) N_0^*(2 - N_0^*) - N_0^* \\ &+ \left\{ \left(p_l - \frac{1}{n}\right) \big(2(1 - \rho N_0^*)^4 (1 - 1N_0^*) - 4(1 - \rho N_0^*)^3 N_0^* (2 - N_0^*)\rho\big) - 1 \right\} Ae^{-r(t-t_s)} + O(A^2). \end{aligned} \tag{3.38}$$

The $O(1)$ term on the right hand side of equation (3.38) is zero, as N_0^* is the solution to equation (3.31), which is obtained numerically. Comparing $O(A)$ terms we have

$$r \sim \left(p_l - \frac{1}{n}\right)\left(4(1-\rho N_0^*)^3 N_0^*(2-N_0^*)\rho - 2(1-\rho N_0^*)^4(1-N_0^*)\right) + 1. \tag{3.39}$$

In order to make the solution (3.37) continuous with our solution for $t \leq t_s$, we take $A = N_0(t_s) - N_0^*$ (which for our dynamics satisfies $|N_0(t_s) - N_0^*| \leq 1$) where $N_0(t_s)$ is the solution from equation (3.35) evaluated at $t = t_s$. Our asymptotic solution can then be written as

$$N_0(t) = \begin{cases} \dfrac{N_0(0)e^t}{N_0(0)(e^t-1)+1}, & t \leq t_s, \\ N_0^* + \left(\dfrac{N_0(0)e^{t_s}}{N_0(0)(e^{t_s}-1)+1} - N_0^*\right)e^{-r(t-t_s)}, & t > t_s, \end{cases} \tag{3.40}$$

where t_s is defined by equation (3.36) and r by equation (3.39).

Next we consider the case that $N_0(0) > \hat{N}_0$. We have that $m(N_0(0)) > 0$, and so we can use the method above to find an exponential solution of the form given by equation (3.37) as before. The value of A is again determined by forcing the solution to continuously approach the initial data, which gives that $A = N_0(0) - N_0^*$. So the solution in this case is

$$N_0(t) = N_0^* + (N_0(0) - N_0^*)e^{-rt}, \tag{3.41}$$

with r given by equation (3.39).

The solution given by equation (3.40) describes a period of logistic cell growth, followed by an exponentially fast convergence to a steady state, and depends on the initial mean cell density $N_0(0)$, p_l, ρ and n. If the initial mean cell density is high enough to immediately cause cells to die due to pressure, there is no logistic growth phase and Equation (3.41) describes the exponential convergence to a steady state. These analytical solutions also match numerical solutions of (3.29) extremely well; see Figure 3.12. In the worst case of $N_0(0) = 0.9$ and $p_l = 10$, where there is no logistic growth, we note that the analytical solution is still quite close to the numerical solution despite the value of $A = 0.45$, which is not asymptotically small. We suspect that this close agreement is due in part to solutions being bounded in $[0,1]$, so that we always have $|A| < 1$, along with the existence of a unique stable steady state to equation (3.29).

We compare the asymptotic solution (3.40) for the cell density, N_0, against the (spatial) mean cell density for the full two-dimensional problem (3.1)-(3.4) for various

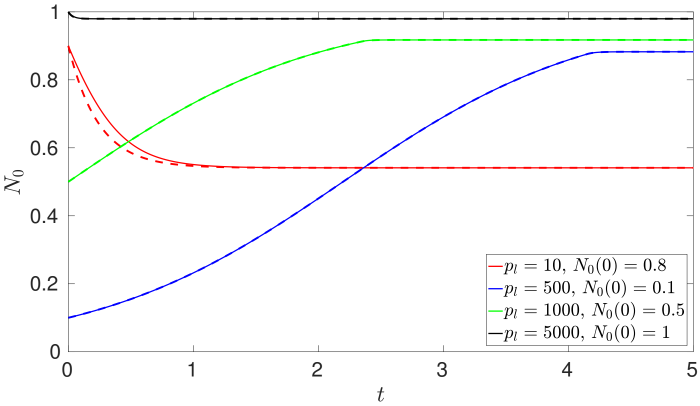

Figure 3.12: Plots of $N_0(t)$ computed from simulations of equations (3.29)-(3.30) as solid lines, as well as the asymptotic solutions (3.40)-(3.41) as dashed lines, for $n = 10$ and different initial mean cell densities $N_0(0)$ and thresholds p_l.

values of δ in Figure 3.13. For small values of δ, the oscillations in nodal cell densities have an overall effect on the spatial mean cell density such that our asymptotic solution over-predicts the mean cell density of oscillatory solutions. Increasing δ, we see a relatively fast convergence to the asymptotic solution for the spatial mean cell density N_0. Comparable results hold for different values of p_l and n, and for the solution given by equation (3.41).

In Figure 3.14 we plot values of (spatial) mean cell densities for simulated solutions of equations (3.1)-(3.4) for a lattice with $n = 10$, along with corresponding N_0^* computed from Equation (3.31). In both cases we plot the steady state behaviour, so if the simulations of the full problem were oscillatory, we averaged over some period of time as in Figure 3.8. The large δ steady state N_0^* accurately predicts the long-time spatial mean cell density for $\delta \approx 1$ for all values of p_l, and for smaller values of δ for larger values of p_l. For smaller values of δ, the variation from the asymptotic solution is partly due to significant spatial variation in the cell density N_i. The jagged regions in the plots are due to changes in the number of grid points that are growing or dying, rather than coarse plotting. The convergence in δ being faster for larger values of p_l explains why in Figure 3.2a the cell density is very close to uniform, whereas in Figure 3.2b there is a substantial deviation from uniformity.

We remark that the above asymptotic solutions are not comparable to any asymptotic limit involving the parameter n. For n sufficiently large, the behaviour of the lattice should approach the behaviour of a continuum model, as it can be viewed as a method-of-lines discretization of such a model; the term in Equations (3.2) involving the Laplacian matrix L_{ij} will tend to the continuum Laplacian in the limit of $n \to \infty$.

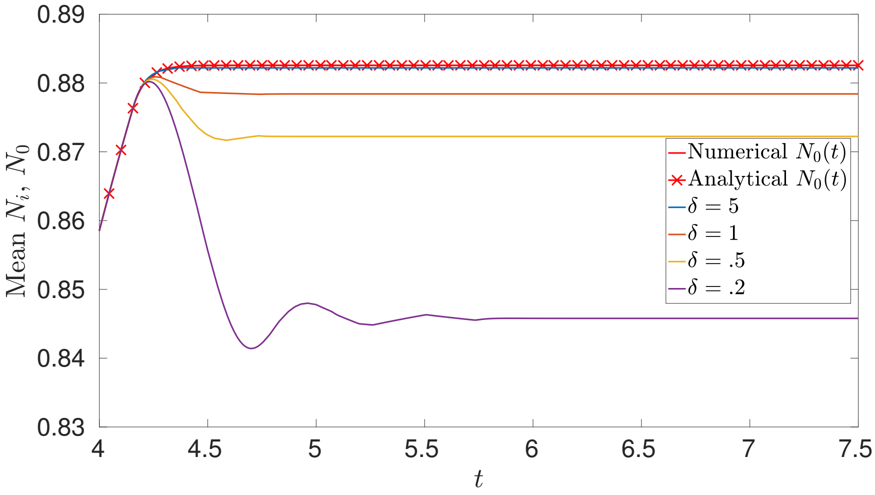

Figure 3.13: Plots of the asymptotic cell density, N_0, computed from numerical solutions of equations (3.29)-(3.30), analytical solutions given by (3.40), and simulations of the full two-dimensional model (3.1)-(3.4) for $n = 100$, $p_l = 500$, and $\delta = 0.1, 0.5, 1,$ and 5.

Such a limiting continuum model will only differ from the continuum model presented in this Chapter in the use of different constitutive relationships; the original continuum model uses $\phi = (1 - \rho N)^3$ whereas the continuum limit of the lattice will involve a porosity of the form $\phi = (1 - \rho N)^4$. Asymptotics involving large but finite values of n could be pursued to reveal the nature of finite-size effects, but we leave exploration of this limit as future work.

3.3.2 PDE Asymptotics

We expand our variables as $N = N_0 + \delta^{-1} N_1 + O(\delta^{-2})$ and $p = p_0 + \delta^{-1} p_1 + O(\delta^{-2})$. Substituting these into Equation (3.6), we find the leading-order equation for cell density,

$$\nabla^2 N_0 = 0, \tag{3.42}$$

which, along with the boundary condition in equations (3.11), shows that N_0 is constant throughout the domain (e.g. by the Maximum Principle). To find N_0 we consider the next order problem,

$$\frac{dN_0}{dt} = H(p_c - p_0) N_0 (1 - N_0) - H(p_0 - p_c) N_0 + \nabla^2 N_1. \tag{3.43}$$

We now eliminate the dependence on N_1 using the divergence theorem. Integrating equation (3.43) over the domain, along with the boundary conditions in (3.11), we

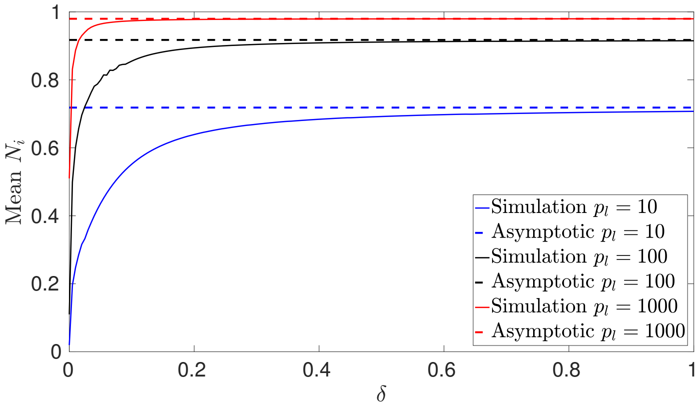

Figure 3.14: Plots of steady state spatial mean cell density for lattice simulations with $n = 10$ at three different values of the threshold p_l against the predicted steady state solution from equation (3.31).

find

$$\frac{dN_0}{dt} = \int_0^1 H(p_c - p_0(x))N_0(1 - N_0) - H(p_0(x) - p_c)N_0 dx, \tag{3.44}$$

where $p_0(x)$ is a function of x only due to the leading-order cell density N_0 being constant.

From equation (3.19) we have that $p_0(x) = (1 - x)/k(N_0)$ which is monotonically decreasing in x. Given the bound from (3.24), which implies that we will see neither uniform logistic growth or uniform cell death, there must exist a point $x^*(N_0)$ such that for all $x \leq x^*(N_0)$, $p_0(x) \geq p_c$, and for all $x > x^*(N_0)$, $p_0(x) < p_c$. From Equation (3.44) we then have,

$$\frac{dN_0}{dt} = (1 - x^*(N_0))N_0(1 - N_0) - x^*(N_0)N_0, \tag{3.45}$$

where $x^*(N_0) = [1 - p_c k(N_0)]^+ = [1 - p_c(1 - \rho N_0)^3]^+$, where again the positive part must be taken to avoid a negative value of $x^*(N_0)$ for small N_0. We have reduced a system of two partial differential equations in equations (3.5)-(3.6) to equation (3.45) which is an ordinary differential equation, although $x^*(N_0)$ is not everywhere-differentiable. At steady state, the solution N_0^* must satisfy,

$$0 = p_c k(N_0^*)(2 - N_0^*) - 1 = p_c(1 - \rho N_0^*)^3(2 - N_0^*) - 1, \tag{3.46}$$

where we are neglecting the unstable steady state $N_0^* = 0$. This is a quartic equation for N_0^* which can be solved numerically. Up to constitutive differences giving different exponents between $k(N_0)$ and $R^{-4}(N_0)$, it can also be seen as the limit of equation (3.31) as $n \to \infty$.

As in equation (3.31), equation (3.46) can be shown to have at most one solution in the interval $(0, 1)$ as follows. Let $\tilde{N} = 1 - \rho N_0^*$. Then for $N_0^* \in (0, 1]$ we have $0 < \tilde{N} \leq 1 - \rho$ and $\tilde{N}^4 + (2\rho - 1)\tilde{N}^3 - \rho/p_c = 0$, whose coefficients can have at most one sign change, and hence there is a maximum of one positive root of $\tilde{N}$ by Descartes' Rule of Signs. A similar global stability argument as in Section 3.3.1 shows that there exists such a unique root and that it attracts all initial data $N_0(0) \in (0, 1]$.

We can follow the same procedure that was employed in Section 3.3.1 to derive Equations (3.40) and (3.41) to solve equation (3.45). We again consider a period of logistic growth (assuming the initial cell density is not too large), wherein the solution can be found analytically. As the cell density becomes large enough to induce non-uniform death (e.g. $x^*(N_0 > 0)$, we exploit the fact that the difference between $N_0(t)$ and the equilibrium solution given by Equation (3.46) is small to find the solution for all time t. We define $\hat{N}_0$ to be the value of cell density such that $x^*(\hat{N}_0) = 0$ and for all $N_0 > \hat{N}_0$, $x^*(N_0) > 0$. If we assume that $N_0(0) < \hat{N}_0$, then the solution takes the form

$$N_0(t) = \begin{cases} \dfrac{N_0(0)e^t}{N_0(0)(e^t - 1) + 1}, & t \leq t_c, \\ N_0^* + \left(\dfrac{N_0(0)e^{t_c}}{N_0(0)(e^{t_c} - 1) + 1} - N_0^* \right) e^{-r_c(t - t_c)}, & t > t_c, \end{cases} \tag{3.47}$$

where $N_0(0)$ is the initial mean cell density, N_0^* is the unique root of equation (3.46), the switching time t_c is given by

$$t_c = \ln \left(\frac{(1 - N_0(0)) \left(1 - \left(p_c^{\frac{1}{3}} - 1\right)\right)}{N_0(0)(1 - (1 - \rho)\, p_c^{\frac{1}{3}}} \right), \tag{3.48}$$

and r_c is given by

$$r_c = p_c(3(1 - \rho N_0^*)^2 N_0^*(2 - N_0^*)\rho - 2(1 - \rho N_0^*)^3(1 - N_0^*)) + 1. \tag{3.49}$$

Similarly, if we assume that the initial cell density satisfies $N_0(0) > \hat{N}_0$, then the solution is

$$N_0(t) = N_0^* + (N_0(0) - N_0^*)e^{-r_c t}. \tag{3.50}$$

Solutions (3.47) and (3.50) are analogous to the lattice solutions (3.40) and (3.41). In Figure (3.15) we compare the analytical and numerical solutions to equation (3.45). The worst case behaviour, shown in red, corresponds to the asymptotic parameter $N_0^* - N_0(t_c) = 0.5$, and it is not surprising that there is a transient discrepancy between the numerical and analytical solutions in this case.

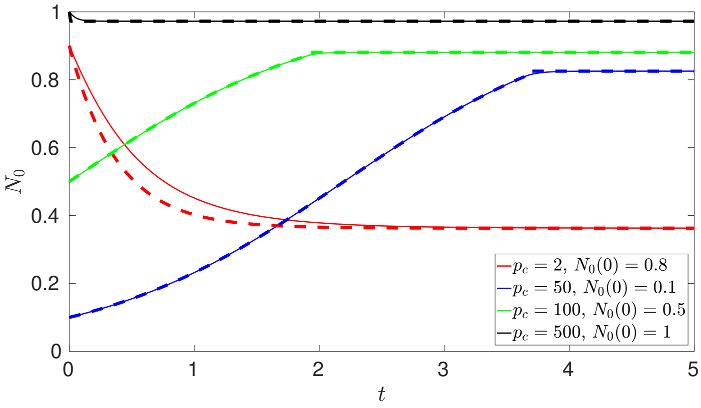

Figure 3.15: Plots of $N_0(t)$ computed from simulations of equation (3.45) as solid lines, as well as the asymptotic solutions, (3.47) for increasing curves and (3.50) for decreasing curves, as dashed lines for different initial mean cell densities $N_0(0)$ and thresholds p_c.

We compare this solution for the cell density N_0 against the spatial mean cell density for the full 2-D problem (3.5)-(3.11) for various values of δ in Figure 3.16. For small values of δ, as in the lattice case, there is some discrepancy between the numerical and asymptotic solutions due to spatial structure. As we increase δ, however, we see a relatively fast convergence to the asymptotic solution for N_0. Comparable results hold for different values of p_c. We note that the asymptotic solution converges more quickly to the equilibrium value N_0^* than the numerical solution of Equation (3.45).

In this Section we have shown that there exist parameter regimes with relatively simple dynamics for large values of δ, or moderate δ and large values of p_l or p_c (see Figure 3.14; the PDE behaviour is qualitatively similar). In these regimes, the transient and long-time dynamics of both the lattice and PDE models can be captured by a simple scalar ODE with a unique attracting steady state. We anticipate that the oscillatory solutions observed in Section 3.2 can be confined to regions of the parameter space where either δ is small, or the threshold p_l or p_c is small. We also note that other simulations show that the dimensionality (e.g. 1-D or 2-D) or the nature of the boundary conditions of the model (e.g. periodic) does not play a role in solution behaviour within this asymptotic regime, whereas it does play a role in the nature of oscillations and steady states observed outside of it (see Figure 3.6).

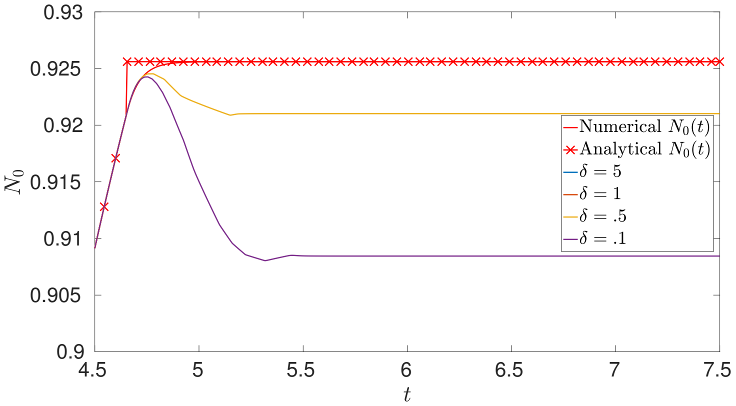

Figure 3.16: Plots of$N_0(t)$ computed from numerical solutions of equations (3.45), analytical solutions given by (3.47), and simulations of the full two-dimensional model (3.5)-(3.11) for $p_c = 200$, and $\delta = 0.1, 0.5, 1$, and 5.

3.4 Bifurcations in Small and Large Lattices

We now consider the behaviours observed in Section 3.2 from the perspective of how solution behaviours change as parameters are varied. We begin by demonstrating the existence of Hopf and pitchfork bifurcations from steady states in an $n = 4$ lattice as δ varies, and describe how the size of the lattice affects the existence of these bifurcations. Finally we classify behaviours observed in simulations throughout a bounded subset of the parameter space of δ and p_l (or p_c) for larger lattices and the PDE.

3.4.1 Existence of Symmetry-Breaking Bifurcations

We examine a low-dimensional ($n = 4$) lattice model, and numerically continue steady state solutions over a range of δ with $p_l = 15$. We track the local stability of these steady state solutions to small amplitude perturbations by evaluating the Jacobian of the system and its eigenvalues. We use natural parameter continuation and manually switch between solution branches by continuing solutions in δ from any stable equilibria found by solving Equations (3.2). That is, we take our equilibrium solution for a specific value of δ, $N_i^*(\delta)$, then solve the algebraic steady state Equations (3.2) using the MATLAB function ‘fsolve’ with $N_i^*(\delta)$ as an initial guess for the solution at a new value of the parameter $\delta' = \delta \pm \epsilon$ for some small ϵ. We choose $\epsilon = 10^{-4}$, and continue solutions forward and backward for all $\delta \in [0, 2]$.

Equations (3.1) can be viewed as a weighted graph Laplace equation, and can be inverted numerically to find the pressures as functions of the cell density. We consider the $n^2 \times n^2$ matrix corresponding to the Jacobian of equations (3.2) with p_i a function of $N_1, \ldots, N_{n^2}$ for all i. We denote the *ith* eigenvalue of the Jacobian evaluated along a branch of steady states by σ_i. See [165] for discussion of continuation procedures in general.

In Figure 3.17, we plot the value of the cell density at the bottom-left node, N_1, corresponding to different steady state solution branches, for varying δ found from the above procedure. The solid lines denote steady states with all eigenvalues having negative real part, $\max_i\{\Re(\sigma_i)\} < 0$, and hence are locally linearly stable. The dashed lines have at least one eigenvalue with positive real part, and so are linearly unstable. The black line corresponds to a vertically symmetric equilibrium (which remains vertically symmetric for all δ), and the red and blue lines to vertically asymmetric equilibria (see the insets of Figure 3.17 which show cell density distributions for these equilibria at $\delta = 0.5$).

Around $\delta \approx 0.08$ (point A), the vertically symmetric steady state loses stability. Beyond point A there is an oscillating solution that attracts solutions perturbed from the now unstable vertically symmetric solution. This oscillating solution is of the vertically asymmetric kind plotted in Figure 3.5. We plot the envelope of the oscillation that N_1 undergoes during a period. We plot the two eigenvalues with largest real part in Figure 3.18, and show that at the point where the vertically symmetric steady state loses stability, the eigenvalues cross the imaginary axis in a conjugate pair (e.g. $\Im(\sigma_i) \neq 0$ for the two complex conjugate σ_i with $\Re(\sigma_i) = 0$). Since the oscillatory solution immediately beyond this loss of stability is numerically stable and its amplitude is small for δ near the bifurcation point, this indicates a supercritical Hopf bifurcation giving rise to the stable limit cycle that we observe for $\delta \gtrapprox 0.08$ in Figure 3.17.

For $\delta \approx 1.5$ (point D), two solution branches emerge from the vertically symmetric branch as it loses stability (for decreasing δ). These vertically asymmetric solutions are reflected copies of one another, as is typical in a pitchfork bifurcation. We plot the eigenvalues of these continued branches in Figure 3.19 showing evidence that this is a pitchfork bifurcation. The eigenvalues touch the imaginary axis with zero imaginary part at D in Figure 3.19 then return to the left hand side of the plane, whereas in Figure 3.18 the eigenvalues cross the imaginary axis as the vertically symmetric solution loses stability. We plot cell densities at every lattice node in the insets of Figure 3.17 of all three steady state branches at the point $\delta = 0.5$. Note that the symmetric branch is unstable for this value of δ. The asymmetric branches both lose stability at $\delta \approx 0.46$ (point C), again satisfying the criteria for a Hopf bifurcation, as

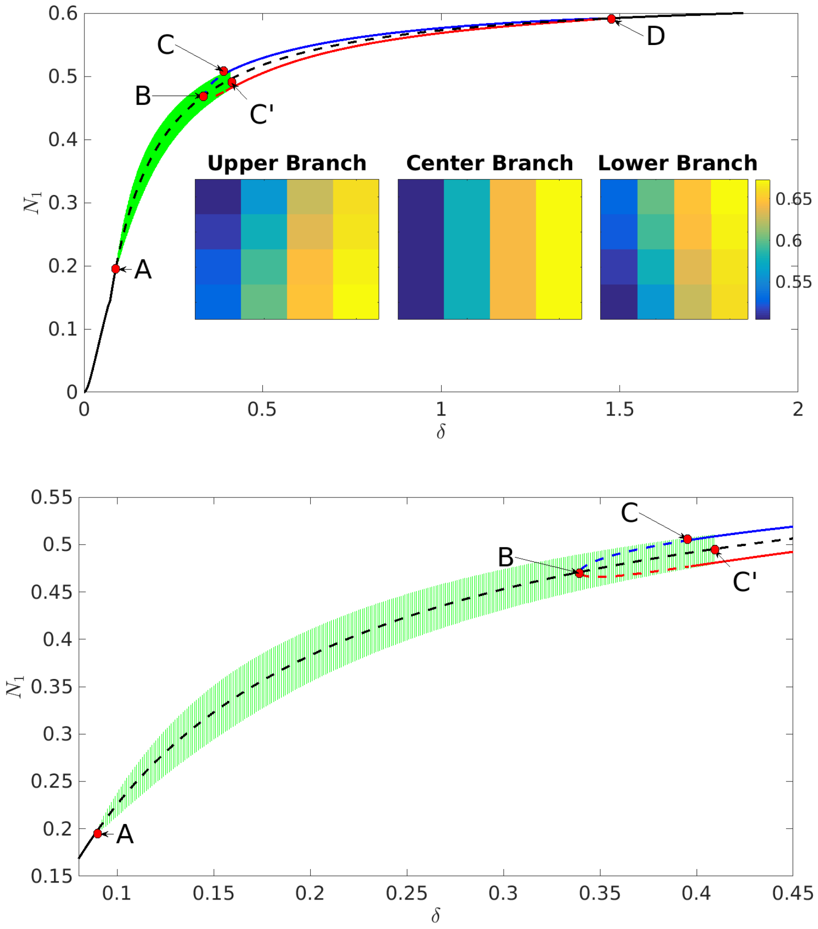

(b)

Figure 3.17: In (a) we plot the cell density N_1 at the bottom-left of the lattice corresponding to three steady state branches found via numerical continuation. Solid lines correspond to locally stable steady states, dashed lines to unstable steady states, and the green lines represent an envelope of oscillations about the steady state solutions. The insets show cell density plots across the lattice at $\delta = 0.5$. Note that only the Center Branch (black line) solution is vertically symmetric, whereas the other two are not. The letters correspond to different bifurcations described in the text. For this case, $n = 4$, $p_l = 15$ and $\rho = 0.9$. The plot in (b) is a closer look at the oscillatory regime.

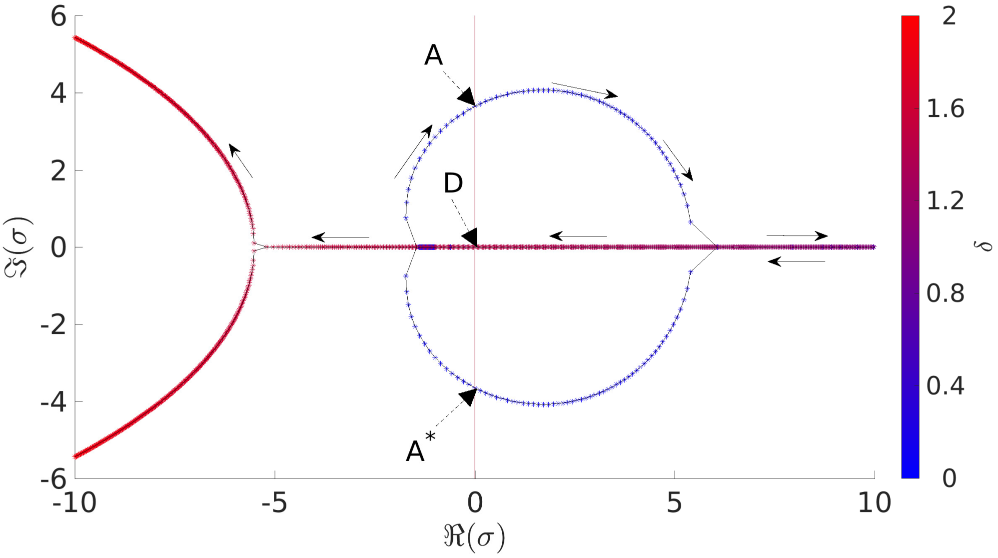

Figure 3.18: Plots of the two eigenvalues σ_i with largest real part of the Jacobian evaluated at the vertically symmetric branch, coloured according to the value of δ. The arrows denote the direction of increasing δ. The first crossing of the imaginary axis $\Re(\sigma_i) = 0$, at A and its complex conjugate A*, corresponds to a Hopf bifurcation. The second crossing of the imaginary axis, at point D, corresponds to a pitchfork bifurcation where the center branch again gains stability.

the eigenvalues with the largest real part again cross the imaginary axis in Figure 3.19 (but here for decreasing δ). In this case, however, we do not find a small amplitude *stable* limit cycle, and instead solutions are attracted to the limit cycle previously generated, which has a large amplitude at this point. This shows that there is a subcritical Hopf bifurcation for both of the asymmetric equilibria at C, which leads to the creation of an unstable limit cycle.

For larger values of diffusion the limit cycle is no longer observable and we suspect it becomes unstable around $\delta \approx 0.47$ (point C’). We know that an unstable limit cycle exists to the right of C, between C and C’, and that this may lead to the loss of stability for the stable limit cycle at C’, but we do not pursue these claims here. Lastly, we see that around $\delta \approx 0.4$ (point B) the three steady state solution branches merge, and the eigenvalues shown in Figure 3.19 have the same structure for the rest of the continued solution. Note that near B all branches have large real eigenvalues ($\sigma_i \approx 20$), and so there is no exchange of stability. While we have only shown plots for N_1, plots for all N_i show that these behaviours are qualitatively consistent across all states, and hence these branches, their stability, and the merging of branches are faithfully captured by Figure 3.17.

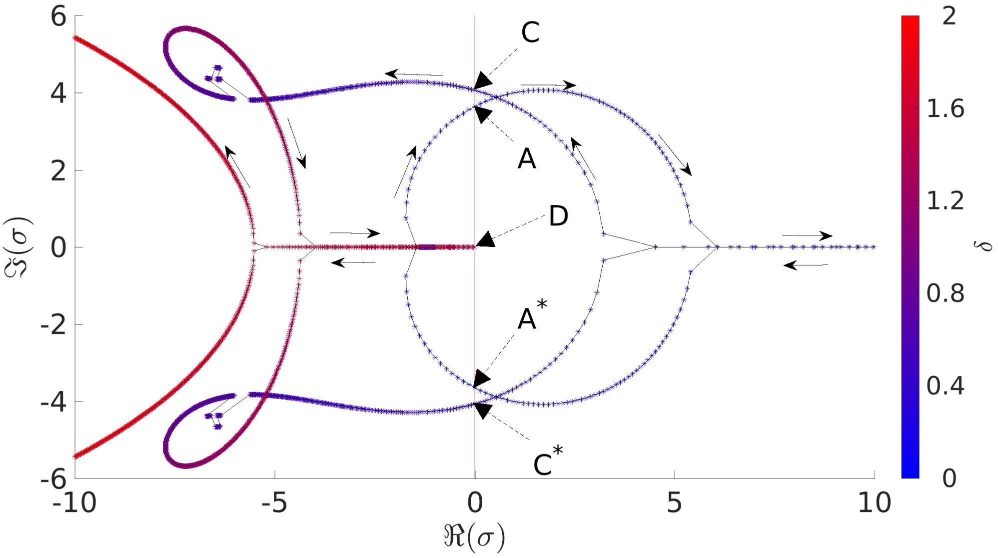

Figure 3.19: Plots of the two eigenvalues σ_i with largest real part of the Jacobian evaluated at the upper branch, coloured according to the value of δ. The arrows denote the direction of increasing δ. Note that the eigenvalues along the lower branch are precisely the same for small δ. For $\delta \lessapprox 0.4$ the eigenvalues follow the same trajectory as in Figure 3.18, undergoing a Hopf Bifurcation at A (with complex conjugate A*), but rather than returning along the real axis they develop a complex conjugate pair, and cross the imaginary axis in a pair at C and C*. They approach the origin along the real axis at D, but remain in the left hand side of the plane, as this solution branch merges with the vertically symmetric branch which gains stability at this point.

The results in Figures 3.17-3.19 suggest the existence of Hopf and pitchfork bifurcations, alongside multiple steady states, and oscillatory behaviour in the 2-D lattice with $n = 4$. We did not observe any pulsing oscillations of the type shown in Figure 3.4. We briefly summarize results for other values of n. For $n = 2$ and $n = 3$ we only observed steady states for a large region of parameter space. Similar behaviours to $n = 4$ (vertically asymmetric and symmetric steady states and asymmetric oscillations) were observed for $n = 5, 6$. For $n = 7$, the 2-D lattice had both vertically symmetric pulsing oscillations, as in Figure 3.4 and vertically asymmetric oscillations, in addition to steady state behaviour. For the 1-D model given by Equations (3.16), we only observed steady state behaviour for $n \leq 6$, and oscillations and steady states for $n \geq 7$.

For parameter values where a pulsing oscillation exists but a vertically asymmetric oscillation does not, the vertically symmetric steady state remains locally stable. The 1-D model exhibits a locally stable steady state solution for every parameter combination we simulated. These facts together suggest that it is only these asymmetric oscillations or steady states that can induce instability in vertically symmetric 2-D steady states, as these vertically symmetric steady states correspond to steady states in the 1-D model which are always (locally) stable. The multiple stability of steady states and oscillations (e.g. between point C and C' in Figure 3.17) observed also provides an explanation for the excitable behaviour in Figure 3.10, as the perturbations need to be sufficiently large to move out of the basin of attraction of the locally stable steady state.

These results suggest that the vertically asymmetric oscillations in the smaller lattices are due to local symmetry-breaking bifurcations of Hopf type. For general differential-algebraic systems, codimension-1 bifurcations can also be due to a singularity in the algebraic subsystem, or due to saddle-node bifurcations [185]. By the regularity of the graph Laplacian in (3.1), we conjecture that no singularity-induced bifurcations can occur. While we are unable to rule out saddle-node bifurcations, we do not observe them in any of our continuation studies. The vertically symmetric pulsing oscillations are not, as far as we can detect numerically, created via a Hopf or other local bifurcation from a steady state.

3.4.2 Classification of the Parameter Space

Even for small lattices, a complete classification of the parameter space is not tractable. Instead we now consider lattices of varying size and classify behaviours broadly as oscillatory or steady-state, and record properties of solutions. Namely, we record the

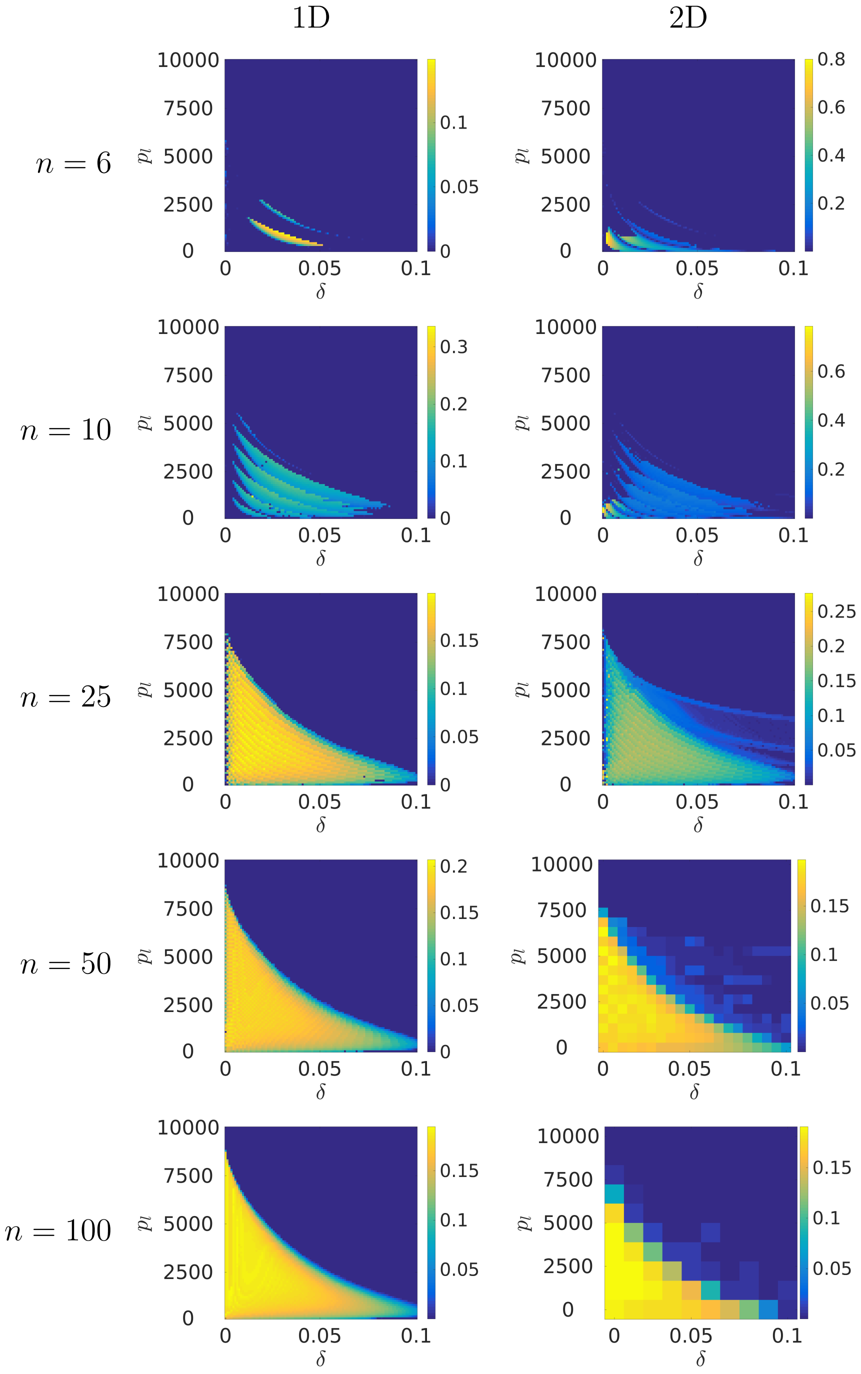

Figure 3.20: Amplitude of the maximal nodal oscillation after $t = 40$ time units for different lattice sizes and dimensions over δ and p_l.

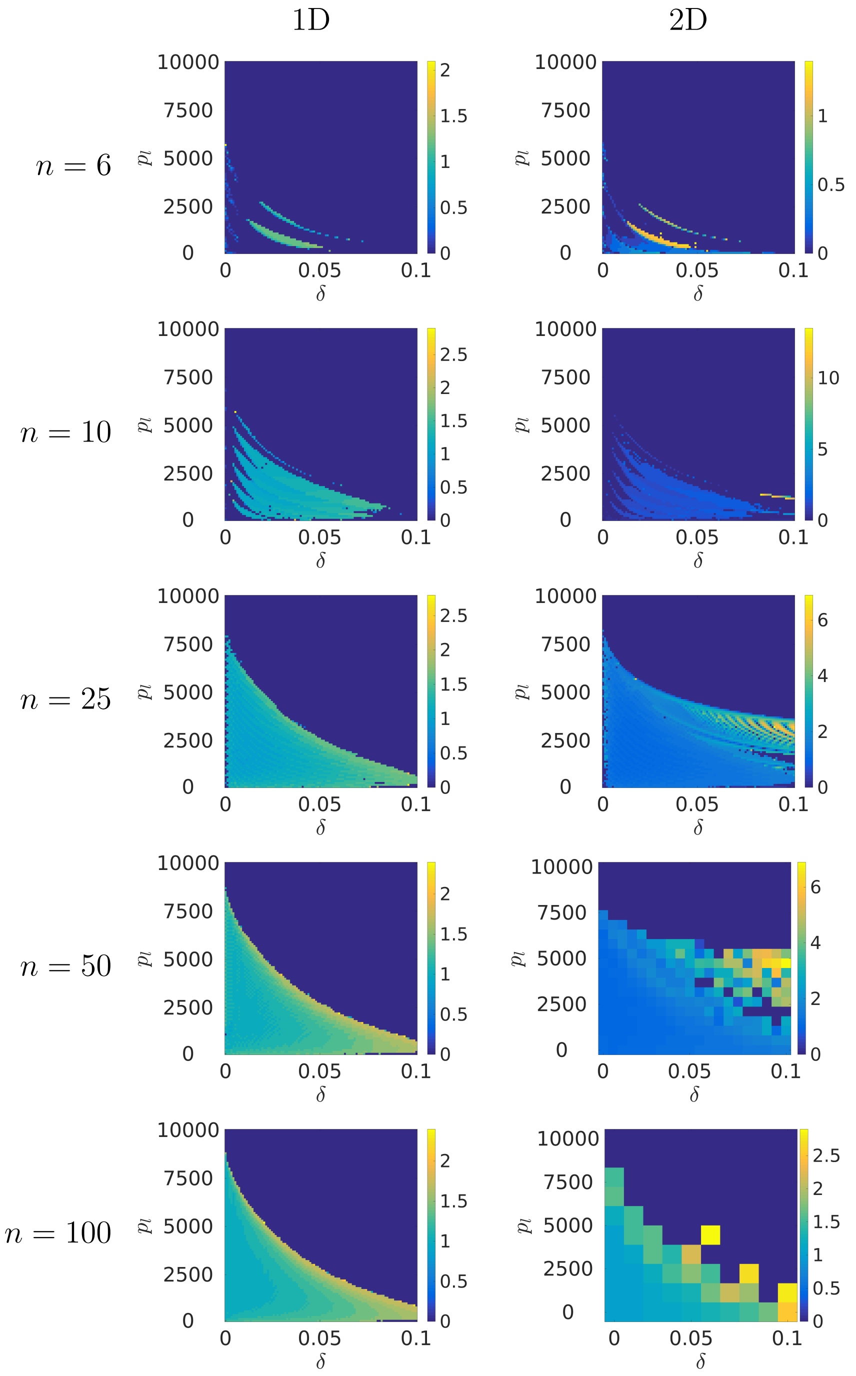

Figure 3.21: Frequency of the nodal oscillation after $t = 40$ time units for different lattice sizes and dimensions over δ and p_l.

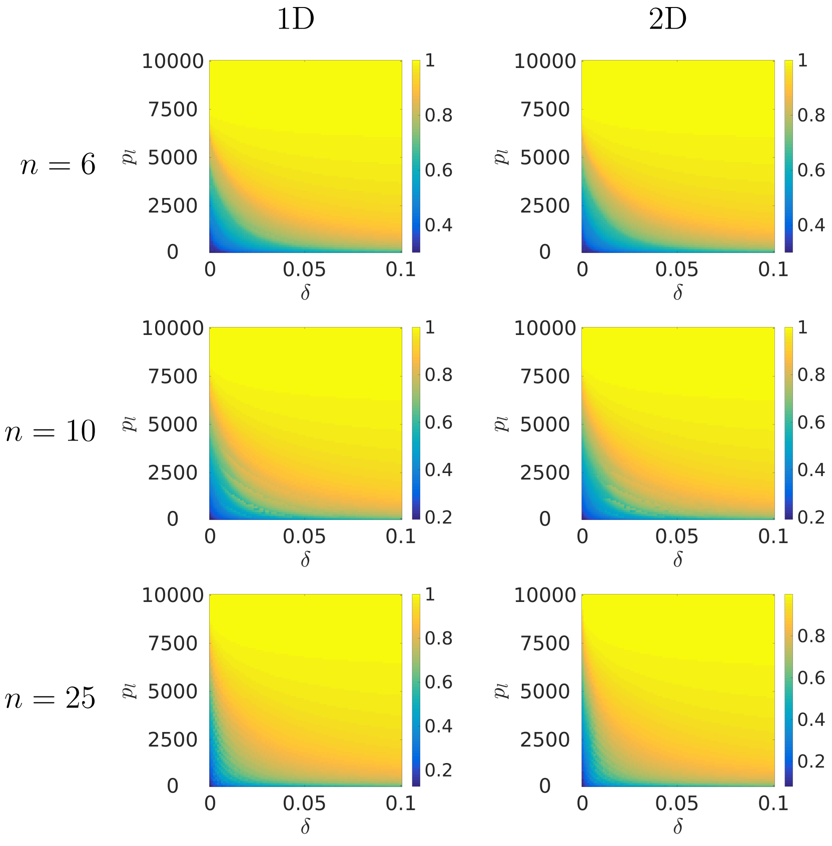

Figure 3.22: Mean cell density after $t = 40$ time units for different lattice sizes and dimensions over δ and p_l. The mean is computed over all nodes, and over the last 10 time units as described in the text. The $n = 50$ and $n = 100$ plots are visually identical to the $n = 25$ and so are omitted.

amplitude of oscillations, spatial mean cell density, and frequency of oscillations. The results from Section 3.3 suggest that for large values of diffusion the cell density is approximated accurately by a spatially constant solution. For this reason we choose to do parameter sweeps between $\delta = 0.001$ and $\delta = 0.1$, and variations in the threshold parameters within the bounds given by (3.23)-(3.24). We compute bifurcation plots in (δ, p_l) and (δ, p_c) in the following way. We first discretize the parameter space, and numerically simulate the governing equations at each discrete point for a sufficiently long period of time (we set this time to be $t = 40$, and use identical initial conditions described at the start of Section 3.2). We then truncate our simulation to analyze only the last 10 units of time. For each node, or in the case of the PDE for each interpolated discretized element, we compute the largest and smallest values this node takes in the truncated time series to compute a nodal oscillation amplitude.

In Figure 3.20 we plot the maximal (over all nodes) amplitude of these nodal

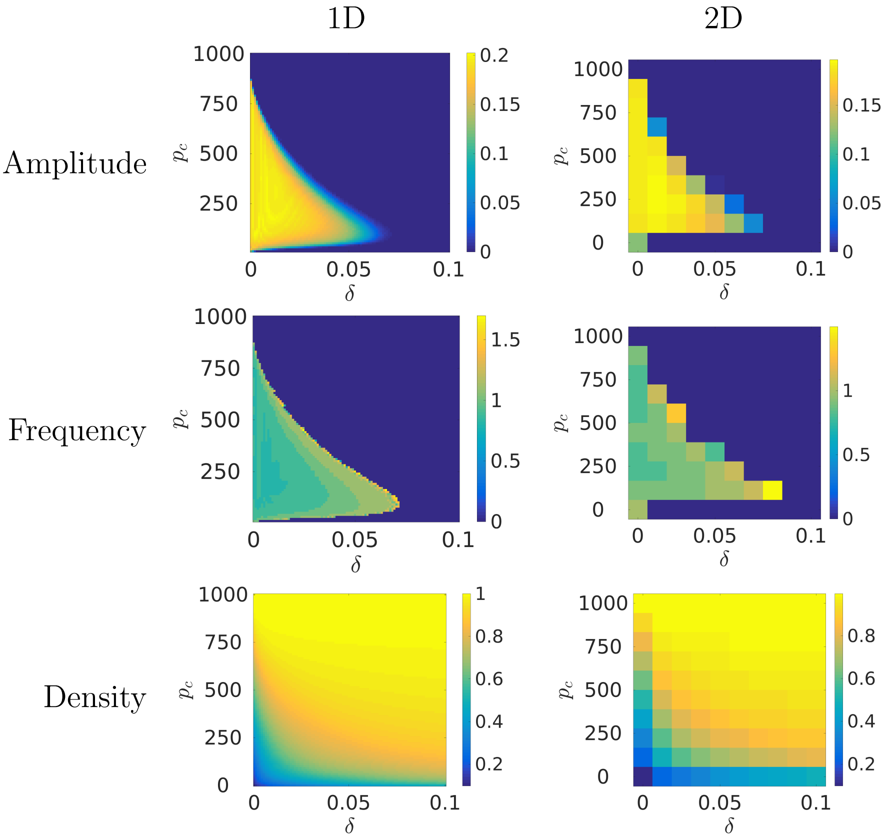

Figure 3.23: Bifurcation diagrams for the PDE in 1-D and 2-D over δ and p_c. Plotted in the first row is the amplitude, and the second the frequency of the maximal nodal oscillation after $t = 40$ time units. The third row is the spatial mean cell density over the domain and over the last 10 time units as in Figure 3.22.

oscillations in the lattice. In Figure 3.21 we plot the frequency of nodal oscillations computed using the Fast-Fourier Transform of these truncated time series, and in Figure 3.22 we plot the mean cell density, where the mean is both in space and over the last 10 time units. We plot corresponding PDE bifurcation diagrams in Figure 3.23. Additionally, for the majority of these simulations we took the diffusion to vary in steps of 0.001. For most of the lattice simulations we took the threshold parameter from $p_l = 100$ to $p_l = 10000$ in increments of 100. For the 1-D PDE simulations we took the threshold parameter from $p_c = 10$ to $p_c = 1000$ in increments of 10. Finally, for the 2-D $n = 50$ bifurcation plot we used coarser sampling taking steps of 0.005 in δ and 500 in p_l, and for the 2-D PDE and $n = 100$ lattice we took steps of 0.01 in δ, 100 in p_c, and 1000 in p_l respectively.

The larger lattices in Figure 3.20 and the PDE in Figure 3.23 appear to have an oscillatory region for small δ or small p_l. The 2-D lattices have more complicated regions not present in the 1-D models where vertically asymmetric oscillations are present (compare the left and right columns of Figure 3.20, especially for $n \geq 25$). The magnitude of the nodal oscillations away from the pulsing regime (bottom-right region of each plot in the right column of Figure 3.20) decreases as n increases, whereas the pulsing oscillations maintain a comparable amplitude for $n \geq 25$. Regions with large (nodal) amplitudes in the 1-D model correspond to pulsing oscillations in the 2-D model. The mixed oscillation (vertically symmetric and asymmetric) behaviours shown in Figure 3.7 exist only when the 1-D model has smaller amplitude oscillations, and hence along the boundaries of the oscillatory regions in the plots along the left of Figure 3.20. Note too that for $n = 6$ and $n = 10$ both the 1-D and 2-D oscillation regions are much more disconnected than the corresponding regions for larger lattices. For $n \geq 25$ the region where oscillatory behaviour is observed appears to become simply connected in the 1-D models, but it is unclear that this happens in the 2-D case for large n.

The frequency of oscillations away from the small δ or p_l regime increases with δ (see Figure 3.21). The oscillation frequency is substantially larger for oscillations present in the 2-D lattices that are not present in their 1-D counterparts; compare the colour ranges in Figure 3.21. The PDE behaviours shown in Figure 3.23 have no appreciable difference between the 1-D and 2-D model behaviours. This suggests that the symmetry-breaking oscillations of the smaller lattices disappear in the limit of $n \to \infty$.

The oscillatory region in Figure 3.20 for small δ or p_l corresponds to where the mean cell density is significantly below the carrying capacity (see Figure 3.22), and

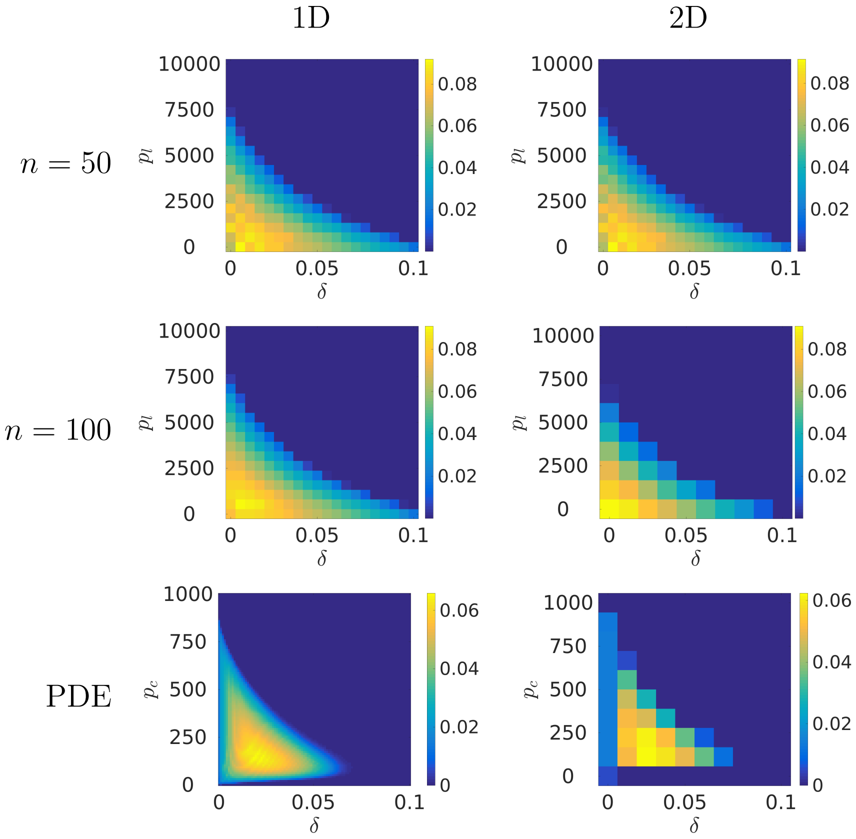

Figure 3.24: Amplitude of oscillations in the spatial mean cell density after $t = 40$ time units for different lattice sizes and dimensions over δ and p_l.

we conjecture that this allows for oscillatory behaviour. Note that for $n = 10$, the mean cell density in this (bottom-left) region of Figure 3.22 appears to reflect the disconnected structure of the oscillatory regions in Figure 3.20 for these small lattices. Compare, for instance, the $n = 10$ 1-D model for both Figures 3.22 and 3.20.

We can also consider the amplitudes of oscillations in the spatial mean cell density over the entire lattice in Figure 3.24, in comparison to the maximal nodal oscillations plotted in Figure 3.20. We see no qualitative difference between the solutions of the 1-D and 2-D models, suggesting that for large n, the asymmetric oscillations become less influential on the spatial mean cell density.

3.5 Discussion

In this paper we have presented and analyzed a pair of new models based on those we proposed in Chapter 2 that describe an active porous medium with interactions between cell growth and fluid flow. We have demonstrated several notable differences between the lattice models of various sizes, as well as between the lattice models and the spatially continuous model.

In Section 3.1 we presented the lattice and continuum models, and demonstrated a reduction to a 1-D model available for vertically symmetric cell density distributions. In Section 3.2, we solved the (1-D and 2-D) systems numerically to demonstrate the existence of steady state solutions and oscillations, either preserving or breaking vertical symmetry. Vertically symmetric solutions were robust to changing the boundary conditions and dimension of the models, as well as the size of the lattice above a minimum threshold. Asymmetric solutions appeared in smaller lattices. In Section 3.3 we derived large δ asymptotic solutions for cell density in both the continuum and lattice models. In Section 3.4 we exhibited Hopf bifurcations from steady states to vertically asymmetric oscillations. The vertically symmetric oscillations, on the other hand, do not appear to be created from local bifurcations from steady states that we observed. The asymptotic solutions from Section 3.3 allowed us to confine parameter sweeps in Section 3.4 to ranges of the model parameters where variation in spatial and temporal structure may be found, and we characterized model behaviours across these parameter ranges. We found that there is a region of parameter space for small δ or small pressure thresholds where oscillations are observed. This region appears simply connected for large lattices, and for the continuum model, but for smaller lattices the parameter space consists of disconnected regions corresponding to oscillatory behaviour. Smaller lattices also exhibit both vertically symmetric and asymmetric oscillations.

Results in Sections 3.2-3.4 demonstrate an important role played by vertically symmetric steady states and oscillatory solutions to these models. Our numerical explorations show that in various limits, notably the large lattice limit of $n \to \infty$, these two solutions are the only stable long-time behaviours of the models, at least within the parameter regimes we explored. For smaller lattices we have shown the existence of Hopf and pitchfork bifurcations that break the symmetry of the vertically symmetric steady state solutions and give rise to asymmetric steady states, and asymmetric oscillating solutions. The phase space and the parameter space for medium-sized lattices ($10 \lessapprox n \lessapprox 100$) is difficult to analyze as it admits all of the various solutions, alongside what are complicated combinations of them (as demonstrated in Figure 3.7).

We can interpret our results in terms of solution symmetry and nonlocal reaction-diffusion mechanisms. Due to results from [26, 108], and others (see [169] for a more thorough review), it is known that *local* scalar reaction-diffusion equations with Neumann data on a bounded domain have relatively simple asymptotic behaviour - namely, all bounded solutions converge to spatially uniform equilibria. Equation (3.20) is a simplification of our model that still admits spatially-structured and oscillatory solutions despite being a scalar reaction-diffusion equation, and hence this nonlocality is a necessary component for both the spatially structured steady states and oscillatory behaviours. Simpler models of this kind of nonlocal reaction-diffusion have been considered in [16, 68, 72, 101], and the references therein, where oscillations and non-uniform equilibria are found and analyzed. We note that these models are qualitatively similar to Equation (3.20) with different nonlinearities, both in the reaction kinetics and the integral kernel.

We conjecture that it is this inherently nonlocal structure, driven by the long-range quasi-static pressure forcing, that gives rise to the oscillatory behaviours we observe. For smaller lattices, the vertically asymmetric steady states and oscillations are related to the discrete structure of these finite-size lattices, as these are not present in the continuum analogue. We conjecture that this discrete structure leads to symmetry-breaking effects due, for example, to the anisotropic nature of discrete diffusion on a lattice [25]. We conclude that the vertically asymmetric oscillations are then an interplay of this symmetry breaking with the nonlocal mechanism described before.

Our observations about vertically asymmetric oscillations are consistent with the oscillations observed in Chapter 2, where a similar model captured cell death due to high values of shear stress. While we did not explore 1-D reductions in Chapter 2, the models there satisfied the same fluid equations and hence must also have a nonlocal coupling between cell growth and fluid pressure as demonstrated in Sections 3.1.1 and 3.1.2. The decreasing amplitudes of oscillations for larger lattice sizes, and the absence of oscillations in the continuum analogue, suggests that these oscillations are analogous to the vertically asymmetric oscillations in the pressure-forced model, as these are also a finite-size effect observed in smaller lattices.

Solutions of the shear-stress model in Chapter 2 do not oscillate in the continuum setting, whereas solutions to the pressure-forced model given by Equations (3.5)-(3.11) do oscillate in a vertically symmetric way. In the shear-stress model, the amplitude of oscillations decreased with the size of the lattice, and oscillations were not observed in the spatially continuous analogue. This may be due to a localization of the nonlocal pressure as the shear-stress in those models is a function of gradients in pressure. This is in contrast to the models presented in Section 3.1, as the pressure itself is forcing the cell growth problem, and hence oscillations are observed in both lattice and continuum models.

The use of fluid pressure as a cell stimulus in this Chapter allows for other simplified model behaviours not possible in the shear stress model of Chapter 2. For example, we did not consider vertically symmetric solutions in the case of shear stress, as these were not observed numerically. We argue that such a 1-D model would lead to spatially uniform cell densities as follows. The shear stress in the continuum model depends on the fluid flow rate and porosity as $\sigma = \|\boldsymbol{u_r}\|/\phi(N)$. We note that the 1-D model gives the same value of the fluid flow rate at all nodes. This implies that the only spatial deviations in shear stress across a 1-D scaffold will be due to differences in the cell density, as the shear is inversely proportional to the porosity, $\sigma \propto \phi(N)^{-1}$. We also have that the porosity decreases with increasing cell density. Hence, the shear stress will increase for increasing cell density, and decrease for decreasing cell density. Overall, this will lead to a steady state of a spatially uniform cell density. While this argument is in terms of the continuum model, an analogous argument holds for the lattice model, replacing porosity by local pipe radii.

In the context of bioactive porous media, the models presented in this Chapter demonstrate several interesting effects due to the finite pore network captured in our lattice model. In the limit of very large lattices, we suspect that spatially continuous models are good approximations to these kinds of pore networks, at least for the simple topology considered here [186]. For smaller networks, we have demonstrated nontrivial effects due to the discrete symmetries inherent in the finite-scale lattice that cannot, as far as we are aware, be captured in continuous analogues [25]. We suspect that more realistic (and hence more complicated) pore networks may exhibit other behaviours due to the presence or lack of symmetries in the topology of the pore network. The tissue engineering literature, for instance, emphasizes macroscopic and microscopic properties of porous scaffolds, such as permeability and pore size respectively, but does not seem to consider as much the importance of the discrete structure of pore networks [78, 81, 197]. Further explorations of network models of bioactive porous media, such as those studied here, will be both quantitatively useful for applications, and provide a number of interesting mathematical questions to pursue.

Chapter 4

Flow Rate Mediated Proliferation and Death

In this Chapter we propose another variant of the models introduced in Chapter 2, and consider cell death due to high rates of fluid flow, as well as cell death due to lack of flow. Fluid flow is used as a proxy for nutrient transport, and low flow rates are assumed to induce cell death via starvation, whereas high flow rates are assumed to kill cells. Mechanistically, cell death at high flow rates is either due to cells being washed away, or mechanically-induced apoptosis. We demonstrate various patterning results similar to those of Chapter 2, but also show differences in the patterning due to starvation effects, which demonstrate differences between the lattice and continuum model solutions. In particular, we observe diagonal ridges of high cell density in the lattice simulations that are absent from the continuum model solutions. We also observe non-equilibrium dynamics in the lattice model such as a time-varying pattern that is not a simple oscillation, as well as a different simulation exhibiting chaotic dynamics. While these non-equilibrium behaviours may not be seen in experimental conditions, they are interesting effects that are only present in the lattice model.

As far as we are aware, the simple modelling approach taken to relate nutrient transport to fluid flux in this Chapter has not been considered in the literature before. We demonstrate new qualitative differences between lattice and continuum models in terms of cell density aggregation and patterning, as well as non-equilibrium solution behaviours that have not, to our knowledge, been observed in simple models of tissue engineering scaffolds.

Cell death due to lack of flow can be seen as a proxy for nutrient transport being insufficient to sustain cell proliferation, whereas death due to high flow can be seen as cells (and extracellular matrix) being washed away or destroyed. This is different in two ways from the model using shear stress presented in Chapter 2. In this Chapter, the fluid flow rate has a different constitutive relationship between the local cell density and the pressure compared to the shear stress in Chapter 2. Additionally, the inclusion of a starvation effect was not present in the previous models. Insufficient fluid flow is a crucial problem in tissue engineering, as it tends to lead to necrotic cores in large tissue constructs [96, 103, 107, 183]. While shear stress has been implicated in cell death via apoptosis [48, 80, 98, 156, 203], there are only a few studies on the impact of fluid flow directly leading to cell death, although it does play a role in some tissues [7, 10]. As far as we are aware, there are no comparable theoretical models that consider either cell death due to high fluid flow rates, or use low flow rates as a proxy for nutrient transport, although there are many models that include nutrient transport (e.g. [1, 36, 125, 126, 133, 166, 167, 199]). We are unaware of similar phenomenological approaches in the literature, and so while this model is very simple and may not be suitable for quantitative predictions, it provides a novel approach to capturing multiple effects that fluid flow can have on cell growth in a bioactive porous medium.

In Section 4.1 we present the lattice and continuum model variants, modified from the models derived in Section 2.1. In Section 4.2 we show numerical results that demonstrate non-uniform patterning comparable to that found in Chapter 2, and also demonstrate how cell starvation leads to different kinds of patterning. In Section 4.2.1 we present non-equilibrium results that demonstrate the existence of quasi-periodic or chaotic solutions. While these are likely not physically relevant, as they occur in unrealistic parameter ranges, they are mathematically interesting, and we give an example that can be shown (numerically) to be chaotic. We give a concluding discussion in Section 4.3.

4.1 Flow Rate Nutrient Transport Model

We use the same fluid and cell growth models as in Chapters 2 and 3, modifying only the functions F_1 and F_2 that couple the fluid flow to the cell evolution equation. We first consider the lattice model presented in Section 2.1.2 and discussed further in Section 3.1. We model the local fluid flow rate by averaging the total amount of fluid passing through each node. We define Q_i as the fluid flow rate through node i as follows: we consider magnitudes of fluid flowing through a node by taking absolute values, and sum the resulting flow rate magnitudes over the nearby pipes. After a suitable nondimensionalization and summation of Equation (2.19), we have,

$$Q_i = n \sum_{j=1}^{n^2} A_{ij} \left| q_{ij} \right| = n \sum_{j=1}^{n^2} A_{ij} R^4(N_i, N_j) \left| p_i - p_j \right|. \tag{4.1}$$

At the left and right boundaries we double this value to match the flow rates in the interior, as interior values account for both fluid leaving and entering nodes. We then define

$$F_1(Q_i) = \left(\frac{1}{2}\right)(\tanh[g(Q_i - Q_G)] + 1) - \left(\frac{1}{2}\right)(\tanh[g(Q_i - Q_D)] + 1), \tag{4.2}$$

$$F_2(Q_i) = \left(\frac{1}{2}\right)(\tanh[g(Q_G - Q_i)] + 1) + \left(\frac{1}{2}\right)(\tanh[g(Q_i - Q_D)] + 1), \tag{4.3}$$

where Q_G is the threshold flow rate above which cells have enough nutrient to proliferate and not starve, and Q_D is the threshold flow rate above which cells die. As in Section 2.1, we note that the particular forms of these functions are not important. These functions are plotted in Figure 4.1. Some specific limits of Equations (4.2) are useful to consider. One notable simplification is the limit $Q_G \to -\infty$ which corresponds to the cells being well-fed independent of the local fluid flow rate. Similarly, for a fixed Q_G, the limit $Q_D \to \infty$ models cell death due to starvation, but does not consider cell death due to high fluid flow. The full model is defined by coupling Equations (2.32a-f) with the functions F_1 and F_2 replaced by those defined by Equations (4.1)-(4.2).

To define the continuous analogue, we use the Darcy velocity defined by Equation (2.5) as a proxy for the local flow rate through the pores in the continuous domain. We can relate the magnitude of the local flow rate to the Darcy velocity as we did with Equations (2.11) and (2.29) in the shear stress model; see, in particular, Equation (2.27). We then have the following nondimensional form of the local fluid flow rate in a pore,

$$Q_p = \|\boldsymbol{u_r}\|. \tag{4.4}$$

We model the influence of this flow rate on the cells in an analogous way to the lattice model,

$$F_1(Q_p) = \left(\frac{1}{2}\right)(\tanh[g^c(Q_p - Q_G^c)] + 1) - \left(\frac{1}{2}\right)(\tanh[g^c(Q_p - Q_D^c)] + 1), \tag{4.5}$$

$$F_2(Q_p) = \left(\frac{1}{2}\right)(\tanh[g^c(Q_G^c - Q_p)] + 1) + \left(\frac{1}{2}\right)(\tanh[g^c(Q_p - Q_D^c)] + 1), \tag{4.6}$$

where g^c, Q_G^c, and Q_D^c are sharpness and threshold values for the PDE model. The full model is defined by coupling Equations (2.14a-g) with the functions F_1 and F_2 replaced by those defined by Equations (4.4)-(4.5).

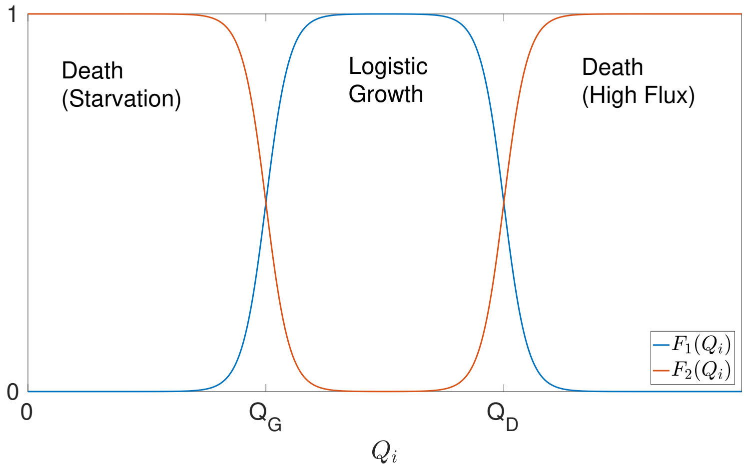

Figure 4.1: For low values of the fluid flow rate $Q < Q_G$, cells will die due to lack of nutrients. For values of Q above the threshold Q_D, cells will die due to being washed away by high flow. Between these two regimes, $Q_G < Q < Q_D$, cells will grow logistically.

Due to the nondimensionalization and the form of Equation (4.1), a uniform flow from the left to the right side of the scaffold would lead to a uniform value of $Q_i = 2$ for all i, as fluid flow rate enters each node, and leaves each node with a unit value. Likewise, a uniform flow in the PDE model would lead to a uniform value of $Q_p = 1$. As with the shear stress model, this nondimensionalization does not correspond to an exact matching between the PDE and the lattice models. We can relate the threshold parameters, taking $Q_D = 2Q_D^c$ and $Q_G = 2Q_G^c$. Likewise, we again take $g^c = g = 60$. For simplicity, we set $Q_D = 2$ in all of our simulations so that cells die when the local flow rate equals the flow rate for uniform cell density distributions. Taking $Q_D \lessapprox 2$ is a necessary condition for the uniform cell density distribution to become non-uniform, as uniform cell density growth does not change the local value of Q_i as it did p_i or σ_i before. We vary the other parameter with values of $Q_G \to -\infty$ to represent no death due to cells lacking nutrients, $Q_G = 0.1$ modelling cells requiring a small amount of fluid flow to stay alive (5% of the amount required to kill them due to high flow rate), and $Q_G = 1$ representing cells requiring a substantial amount of fluid flow (50% of the high flow rate threshold).

We motivate the functional forms of F_1 and F_2 by considering the two regimes of low and high flow, which are both assumed to induce cell death, separately. We again recall that we assume cells are either growing logistically, or dying exponentially, and this can be seen from the fact that $F_2 = 1 - F_1$. Firstly, there is experimental evidence that cells subject to high flow regimes can detach from substrates they reside on, and that cells and ECM can be washed away within experimental perfusion bioreactor systems [91, 104, 109, 192]. While we do not provide a detailed model of any particular detachment mechanism, we capture these experimental results by assuming that $F_2 \approx 1$ when the flow rate is sufficiently high (and hence $F_1 \approx 0$).

Secondly, we motivate using the local fluid flow rate as a proxy for nutrient transport by analyzing a typical (continuum) nutrient transport equation. Under suitable assumptions on the flow rate and nutrient uptake, we show that the nutrient concentration remains high in regions of high fluid flow rate. We consider the reaction-advection-diffusion model given in [166]. In nondimensional form this equation is,

$$\frac{\partial S}{\partial t} + \boldsymbol{u_r} \cdot \nabla S = D_S \nabla^2 S - R_S G(N, S, \sigma), \tag{4.7}$$

where S is the concentration of the nutrient, D_S is the inverse Péclet number, R_S is the rate of nutrient consumption relative to advection, and G represents the uptake of the nutrient by the cells, which was modulated by the shear stress σ in [166]. We note that the nutrient uptake function should satisfy $G \geq 0$, and hence cells will decrease the local nutrient concentration via uptake of the nutrient S. A variety of boundary conditions have been employed for nutrient transport models such as Equation (4.7), but for simplicity, [166] considered no-flux conditions on the vertical boundaries, and Dirichlet conditions on the inlet and outlet of the domain. Specifically, we can write $S(t, 0, y) = 1$ and $S(t, 1, y) = 0$, where we have nondimensionalized the nutrient concentration by the upstream concentration.

Equation (4.7) can give rise to a variety of distributions of the nutrient field S. In addition to the functional form of the nutrient uptake and the cell density distribution, the nondimensional parameters D_S and R_S determine the transport of nutrients throughout the scaffold. As shown in [40], an advection-dominated flow will lead to nutrient concentrations which are constant along streamlines. Specifically, in the regime where $D_S \ll 1$ and $R_S \ll 1$, we have that the nutrient transport at steady state satisfies $\boldsymbol{u_r} \cdot \nabla S = 0$. Hence, if the magnitude of the local fluid flow rate is high, and if nutrient uptake by cells can be neglected, then the nutrient concentration will remain approximately the same as the inlet concentration anywhere the fluid flow is dominated by advection (e.g. where the Péclet number is large). This suggests that in regions where transport is dominated by advection, cells will remain in a nutrient-rich environment due to advective transport from the inlet source of nutrients. Regions where the flow has stagnated will then lead to low concentration of nutrients, and hence cell starvation.

In summary we have that for very low flow rates, nutrient transport will be limited, and hence starvation will lead to cell death. For very high flow rates, cells will detach from the scaffold and be washed away, effectively leading to cell death. In intermediate flow regimes where the flow rate is sufficiently large to facilitate nutrient transport, but not too large to lead to detachment, we expect cells to proliferate. While these assumptions are not valid in general, for reasonably small tissue constructs and sufficiently large perfusion regimes, we anticipate the phenomenological models shown in Figure 4.1 to be a reasonable qualitative approximation to the influence of the fluid flow on the evolution of the cell density.

4.2 Numerical Results

We demonstrate numerical results for this model variant, and compare the results to the shear stress model of Chapter 2. As with the shear stress model, there is a dependence of the final state on the initial condition, and on the parameter values used. In contrast to the previous two models, the uniform growth becomes immediately non-uniform due to the value of Q_D, rather than growing logistically and uniformly for some time. In these simulations we use the same initial data and numerical methods as described in Section 2.1.4. For most of our simulations in the parameter ranges described above, we observe only steady state behaviour. In all cases we consider, however, the steady states exhibit spatial patterning.

As with the previous models, the behaviours for most simulations with $\delta \geq 10^{-3}$ are spatially simple, with the cell density becoming high in a distinct region of the scaffold, and low in one or two regions as the fluid flow rate increases locally. In Figure 4.2 we plot several cell density distributions to illustrate this. Patterns with a single fluid channel are more common than the two fluid channel case illustrated in Figure 4.2b, but this is a numerically stable steady state when perturbed slightly. As can be seen by the variation in the colorbars, the value of δ and Q_G play a role in determining the cell density in the high-density region, and the steepness of the gradient between the growing and dying regions. As the cell density is composed of two or three vertically symmetric regions, the fluid flow is primarily unidirectional from the left side of the scaffold to the right. So regions with higher cell density necessarily have a lower local fluid flow rate, and can only grow to a certain cell density before the local fluid flow rate in a this region becomes too high (e.g. reaches Q_D).

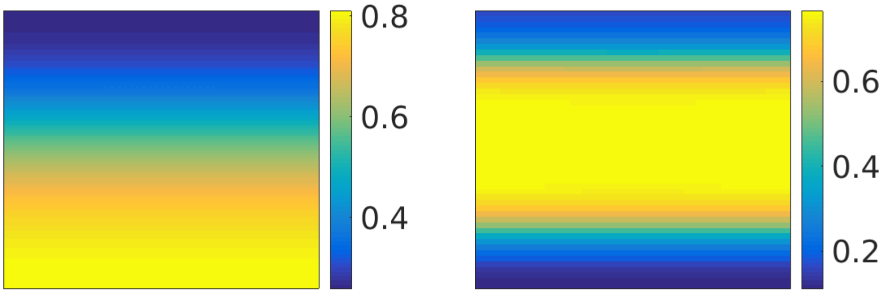

(a) $n = 100$, $\delta = 10^{-1}$, $Q_G \to -\infty$ (b) $n = 50$, $\delta = 10^{-2}$, $Q_G = 0.1$

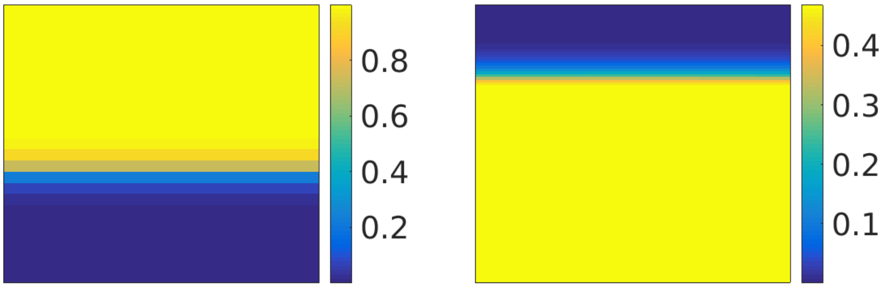

(c) $n = 25$, $\delta = 10^{-3}$, $Q_G \to -\infty$ (d) PDE, $\delta = 10^{-2}$, $Q_G = 1$

Figure 4.2: Plots of the cell density corresponding to $t = 30$ and $Q_D = 2$ demonstrating simple spatial patterning at various values of diffusion, $\delta \geq 10^{-3}$.

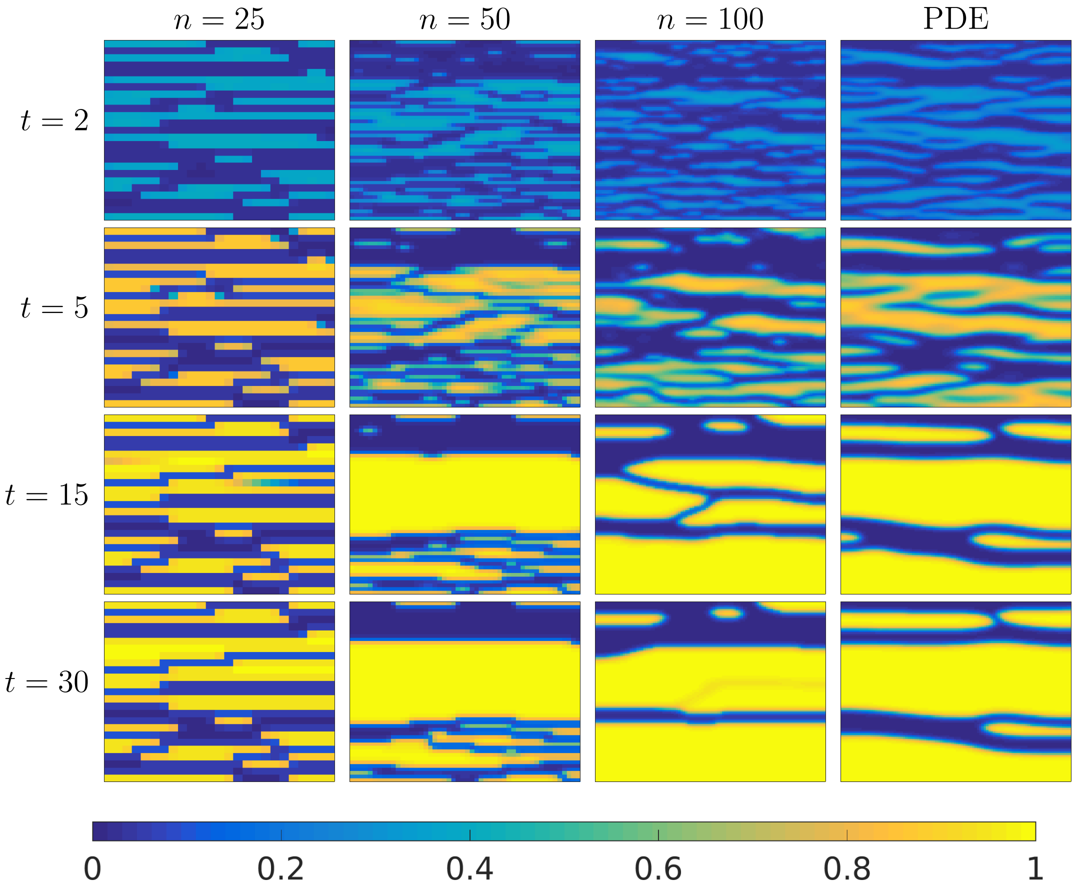

Figure 4.3: Cell density plots with $\delta = 10^{-4}$, $Q_D = 2$, $Q_G \to -\infty$ for three lattice sizes at different points in time alongside simulations of the PDE model.

More complicated spatial patterning is observed for $\delta = 10^{-4}$. Neglecting the need for nutrients and considering cells to die due solely to high fluid flow, we plot cell density distributions over time in Figure 4.3. We see very similar behaviour to simulations of the shear stress model discussed before in Figures 2.5 and 2.6. Although in the simulations shown in Figure 4.3, the PDE maintains a comparable level of heterogeneity, and the $n = 25$ lattice takes longer to settle into a final steady state compared with the shear stress model simulations in Figure 2.5 and 2.6. Despite using the same initial data as in these shear stress simulations (the same realization of the random initial data from Section 2.1.4), the solutions in Figure 4.3 do have different cell density distributions with qualitatively different features (e.g. locations of fluid channels and high cell density regions). This is due to the difference between the flow rate forcing Q_i here, as opposed to the shear stress σ_i in Chapter 2.

We now introduce starvation into the model by setting $Q_G = 0.1$ so that there must be sufficient fluid flowing in the scaffold through each region to support cell

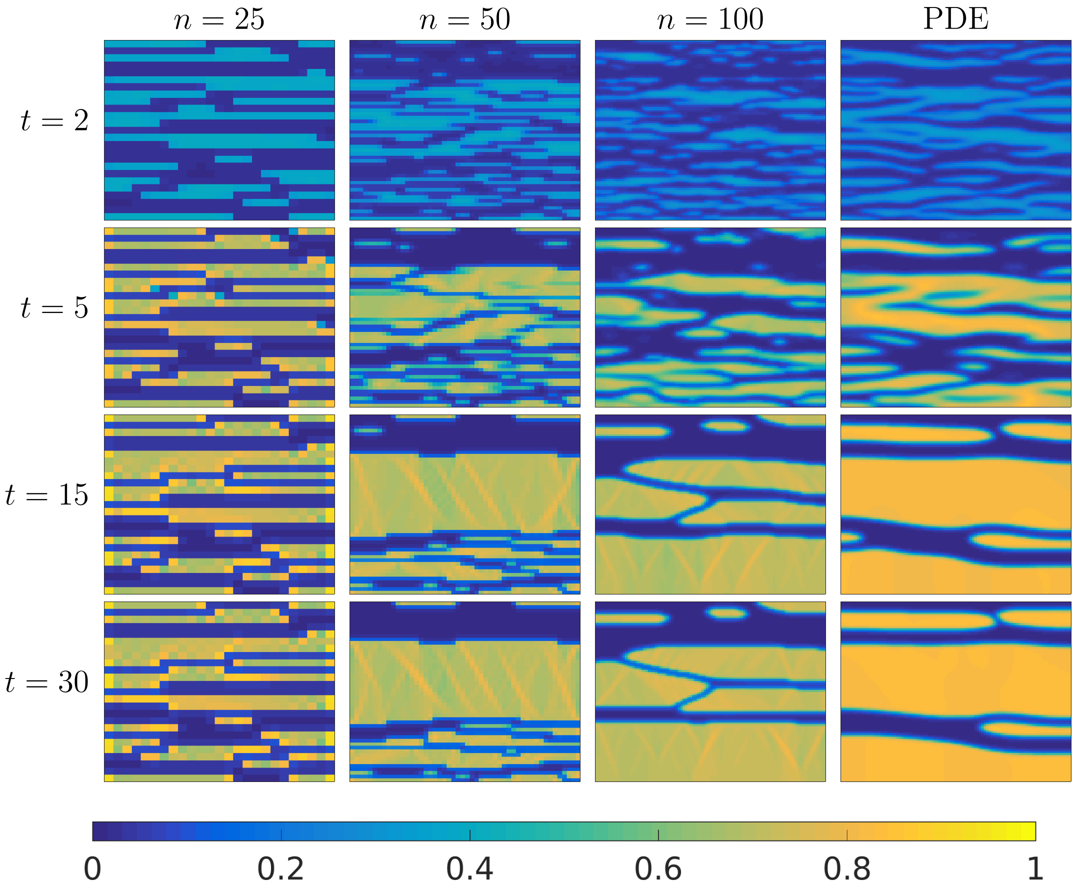

Figure 4.4: Cell density plots corresponding to $\delta = 10^{-4}$, $Q_D = 2$, $Q_G = 0.1$ for three lattice sizes at different points in time alongside simulations of the PDE model.

growth. We plot simulations of various lattice sizes and the PDE in Figure 4.4. We see that the final cell densities (at $t = 30$) are similar in coarse structure to those in Figure 4.3, but that each large cell aggregate has regions of lower cell density. That is, unlike Figure 4.3, the $t = 30$ plots of Figure 4.4 have multiple channels of low cell density rather than one or two large channels. For the three lattices, we also observe higher cell densities in diagonal ‘stripes’ throughout these regions of high cell density. We conjecture that this is a finite size effect due to the boundaries of these cell aggregates, likely due to the anisotropy of the flow in the finite lattice. In particular, the corner of a region of high cell density is more likely to have fluid flowing through it than a ‘flat’ boundary with respect to the direction of the flow. We note that this heterogeneity within an aggregate of high cell density in Figure 4.4 at $t = 30$ is absent from the PDE model, which simply has a lower cell density throughout each aggregate compared to the spatially structured interiors of the aggregates in each lattice simulation.

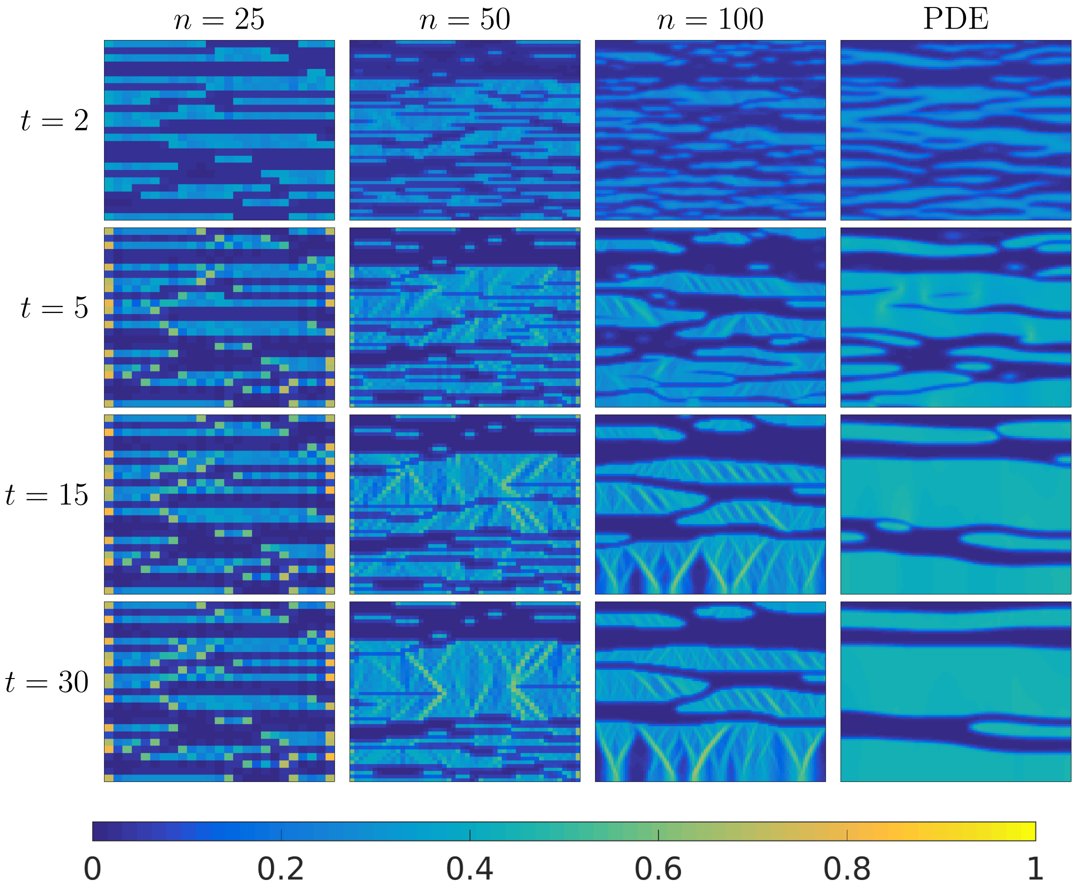

Figure 4.5: Cell density plots corresponding to $\delta = 10^{-4}$, $Q_D = 2$, $Q_G = 1$ for three lattice sizes at different points in time alongside simulations of the PDE model.

We can look at a more extreme starvation scenario by considering $Q_G = 1$, so that cells require a substantial portion of the total fluid flow through the scaffold to grow. We plot these cell densities over time in Figure 4.5. Again we note a similar coarse structure to Figures 4.3 and 4.4, but a much more pronounced effect on the 'internal' structure of cell aggregates. The diagonal bands of high cell density are much more evident, and in some cases appear to affect the flow enough to lead to cell death in some regions of the scaffold (see the bottom-left portion of Figure 4.5 for $t = 30$ and $n = 100$ compared to the same region in the previous simulations). Again, the clusters of high cell density in the PDE are reduced in density, but are essentially uniform internally, without the banded structure found in the lattice solutions.

We compare these simulations broadly by considering the spatial mean cell densities as a function of the parameters. We plot the mean cell density at $t = 30$ in Figure 4.6. We notice that for large values of the diffusion parameter ($\delta = 10^{-1}$) there is only a small variation, except between $Q_G = 1$ and the other threshold values. For

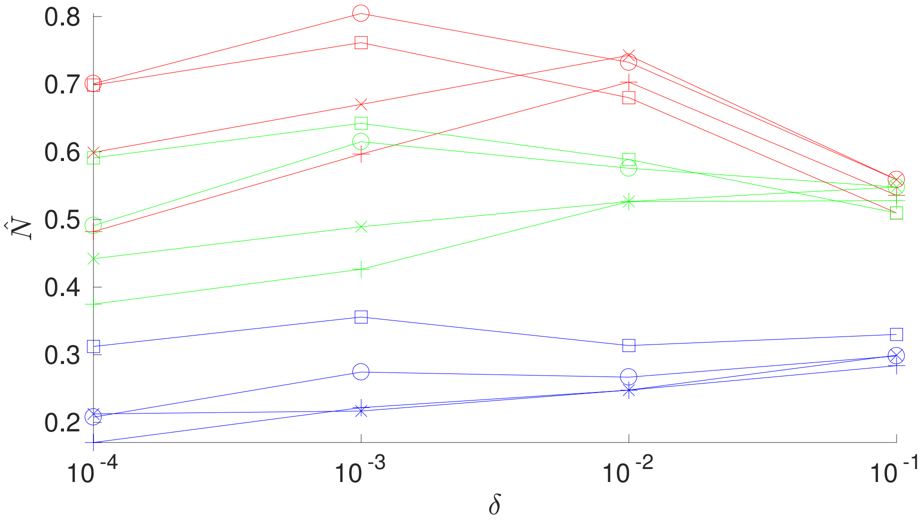

Figure 4.6: Plots of the spatial mean cell density for all parameter combinations for the PDE and lattice models at $t = 30$. The symbols $+$, $*$, $\bigcirc$, and $\square$ are for the lattice sizes $n = 25, 50, 100$ and the PDE respectively. The colors red, green, and blue are for $Q_G \to -\infty, 0.5$, and 1 respectively.

smaller values of the diffusion parameter, both the variation between lattice size and threshold parameters become much more significant. We observe non-monotonic behaviour for most cases in terms of the diffusion, and the lattice size also appears to have a non-monotonic effect in some cases. It is particularly interesting that for the values of $\delta = 10^{-3}$ and 10^{-4}, the size of the lattice (or the PDE model) appears to have a larger effect than the order of magnitude change in diffusion.

We conjecture that the bands observed in the lattice simulations in Figures 4.4 and 4.5 are due to finite-size effects. In particular, the effective radius of each pipe is determined by averaging the cell density at nearby pores. Recall that the pipe radius corresponding to each edge is defined by,

$$R_{ij} = \left(1 - \rho \frac{N_i + N_j}{2}\right), \tag{4.8}$$

where $\rho = 0.9$ throughout our simulations. For a flow which is primarily unidrectional, and in particular flowing in one of the directions parallel to one set of edges, the overall effect of high cell density nodes crucially depends on how they are arranged. See Figure 4.7 for an example of three different cell density distributions with the same spatial mean cell density in an $n = 3$ lattice. High cell density nodes placed along a unidirectional flow will have a large effect on (locally) decreasing the flow rate, as the effective permeability is much smaller. High cell density nodes that are

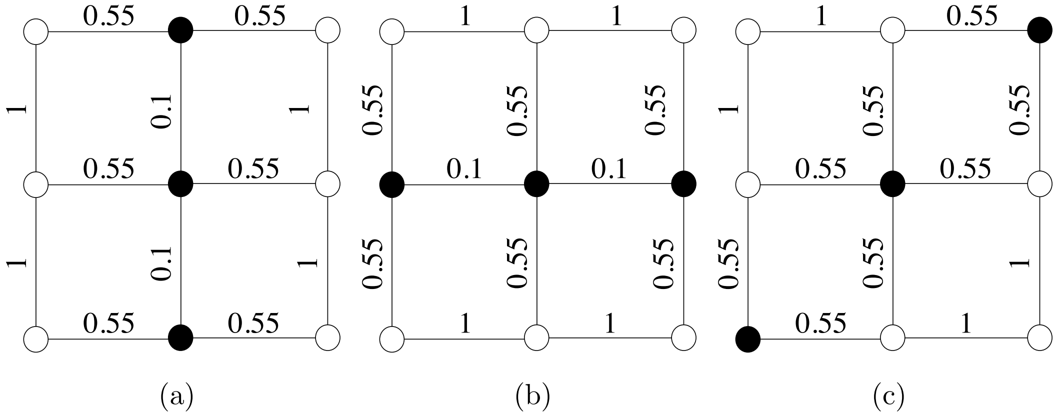

Figure 4.7: Three cell density distributions with a white node i corresponding to $N_i = 0$, and a black node corresponding to $N_i = 1$. The pipe radii from Equation (4.8) are shown alongside each edge.

orthogonal to the primary flow direction will have a much smaller effect on the local permeability, and hence the structure of the flow (See Figure 2.3 for the rational-function dependence of σ_i on the average cell density in nearby pipes). Typically flow will move from left to right, and at a flow rate proportional to R_{ij}^4. So for a given pressure drop, the cell density distribution in Figure 4.7c will accommodate more flow than either of those in Figures 4.7a or 4.7b.

We remark that other settings beyond a regular fixed lattice will not necessarily exhibit this behaviour, but may have analogous patterning due to the constraints of a regular lattice channelling flow around active pipes. More complicated hexagonal and face centred cubic lattices [190], off-lattice models [187], and other complex microscale models have been used in hybrid discrete-continuum settings. Off-lattice models for vasculature [150, 164] show a variety of interesting network structures, but these may not be appropriate for modelling flow in a printed tissue engineering scaffold as such a pore network is static, rather than dynamically created. Random networks, however, are possible models for some kinds of tissue scaffolds [132]. We leave investigation of such models to future work, but remark that the patterning mechanism shown in Figure 4.7 does clearly depend on the topology of the network. We note that this arrangement of cells does not lead to flow rates that are either too high or too low precisely because of the local topological structure of the network. These bands of high cell density also give rise to more complicated time-dependent behaviours which we now explore.

4.2.1 Non-Equilibrium Dynamics

All simulations with $Q_G \to \infty$ or 0.1 are approximately at steady state by $t = 30$ (e.g. simulating for $t = 30$ more units of time changed the cell density at each node by less than 5%, and the mean cell density by much less). The same is true of all PDE simulations above, and all simulations for the lattice with $n = 25$. The $n = 50$ and $n = 100$ simulations with $Q_G = 1$, however, exhibited non-steady state dynamics over arbitrarily long periods of time. Here we demonstrate that there are interactions between the 'bands' of high cell density observed in Figure 4.5 for $n = 50$ and $n = 100$ around $t = 30$, and suggest that these interactions are what induce the non-equilibrium behaviour.

We plot cell density distributions over time, as well as time series for particular nodes, in Figure 4.8. We begin with smoothed initial data near the top of the scaffold in Figure 4.8a, and observe these bands interacting for $t \geq 500$ units (although for brevity we only plot the first 50 time units). We see bands forming and interacting, in ways akin to scroll and spiral waves [71, 85, 117, 118]. The bottom half of the scaffold domain remains near 0 cell density, as the flow rate there is prohibitively high. The growth and death phases in the upper half of the domain are entirely due to interactions between the cells blocking fluid flow, and the cells starving due to too little flow (that is, for all i in the top part of the domain, we have $Q_i < Q_D$, so it is only the lower threshold Q_G that induces cell death).

In Figure 4.8g we plot time series for 5 nodes within the interacting region, and note that they appear quite irregular (e.g. not obviously periodic or quasi-periodic). We computed these simulations using varying maximal time steps from $\Delta t = 0.05$ to $\Delta t = 0.001$, and consistently found the same qualitative behaviours. It is unclear if this behaviour is chaotic or simply quasi-periodic [173]. One typical method for determining this distinction is to compute the maximal Lyapunov exponent along a trajectory of the system, which measures how quickly nearby trajectories separate (or converge in the case of asymptotically stable trajectories) [84, 195]. We note that in order to compute the (time-dependent) Lyapunov exponents, one must solve a much larger system of equations alongside the lattice model. Additionally, due to numerical error, determining the sign of the maximal Lyapunov exponent can be difficult (as on chaotic trajectories, some of these can cluster near zero). In lieu of computing these exponents, we opt to use the zero-one test for chaos proposed and described in [65, 67] to determine if these simulations are in fact chaotic. This test uses results from Ergodic Theory to determine if a time series originates from sampling trajectories on a chaotic attractor. Briefly, the time series is mapped to a set of random translation

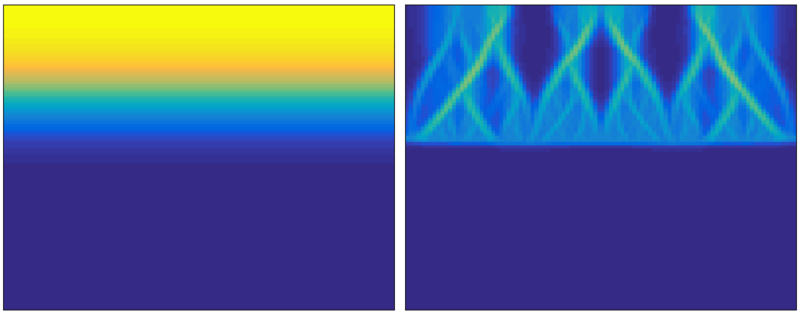

(a) $t = 0$ (b) $t = 10$

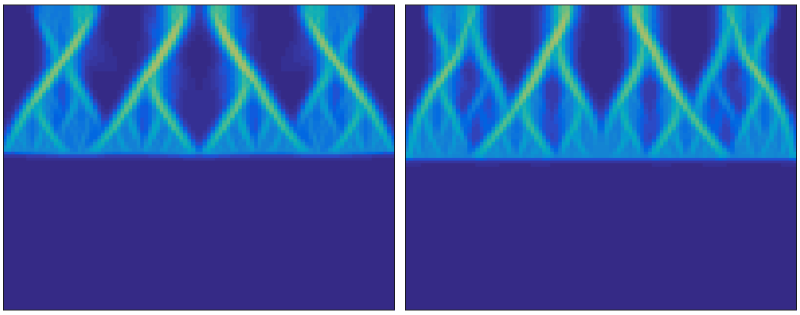

(c) $t = 20$ (d) $t = 30$

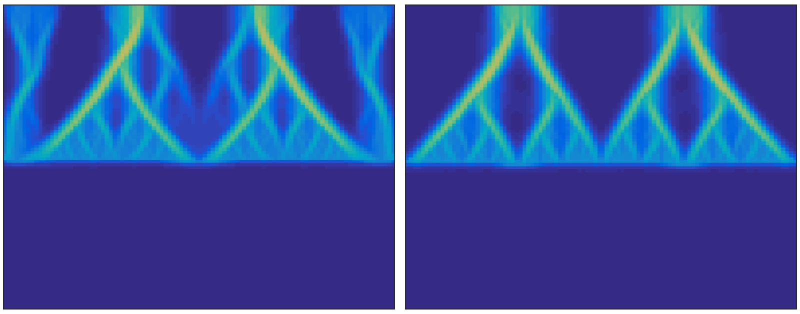

(e) $t = 40$ (f) $t = 50$

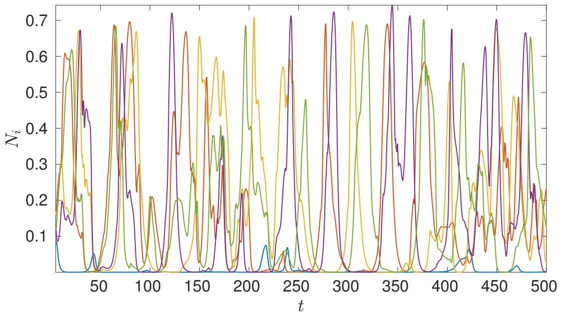

(g) $t = 50$

Figure 4.8: Plots of the cell density distribution corresponding to $\delta = 10^{-4}$, $Q_D = 2$ and $Q_G = 1$ for $n = 100$ in (a)-(f) at various times, and time series for 5 nodes ($i = 10, 30, 50, 70$, and 90) in (g).

variables. For non-chaotic dynamics, these variables will always be bounded functions along the time series, whereas for chaotic trajectories the mean squared displacement of the translation variables will grow linearly in time. The algorithm then samples many such translation variables, and after some statistical machinery, returns values close to 0 for non-chaotic time series and values close to 1 for chaotic time series; we refer to [66] for details.

After truncating to the last 400 time units, this algorithm was applied to each nodal time series (where the time series were individually subsampled as described in [66] to avoid oversampling issues). Most of these returned values close to 0, although for at least 4 nodes, values above 0.6 were reported. We suspect that a much longer time series would be needed to determine if this behaviour is chaotic, or if instead it is quasi-periodic with a high embedding dimension. In either case, it is a more complicated behaviour than anything else we have observed in this model or in those from Chapters 2 and 3.

We also mention a purely non-physical parameter regime where chaotic solutions were observed. If we take $\delta = 10^{-4}$, $Q_D \to \infty$ and $Q_G = 2$ for $n \geq 25$ we observe chaotic trajectories that can be verified as chaotic via the zero-one test mentioned above (all 625 nodal values reported were above 0.8 after truncating and subsampling). We plot time series for the case $n = 25$ in Figure 4.9 for all nodes. We note that the two regions in these time series (for later times $t \geq 10$) correspond to interior nodes, which fluctuate about a cell density of 0.7, and vertical boundary nodes which fluctuate around 0.3. This case is non-physical as it requires cells to receive above-average amounts of fluid flow through every node in order to not starve. As we are fixing the total flow rate into the scaffold, and cells decrease the local permeability of the scaffold as they grow, these parameters do not correspond to a meaningful physical experiment that we are aware of.

4.3 Discussion

In this Chapter we have explored an alternative model to the shear-stress model from Chapter 2, and the pressure model from Chapter 3. The primary motivation for doing this is as a way of including a starvation mechanism, using the local fluid flow as a proxy for nutrient transport. While we have proposed this as a phenomenological model, one could consider a nutrient transport model where the nutrient is carried by the fluid via advection, as in Equation (4.7). When diffusion and uptake of nutrient

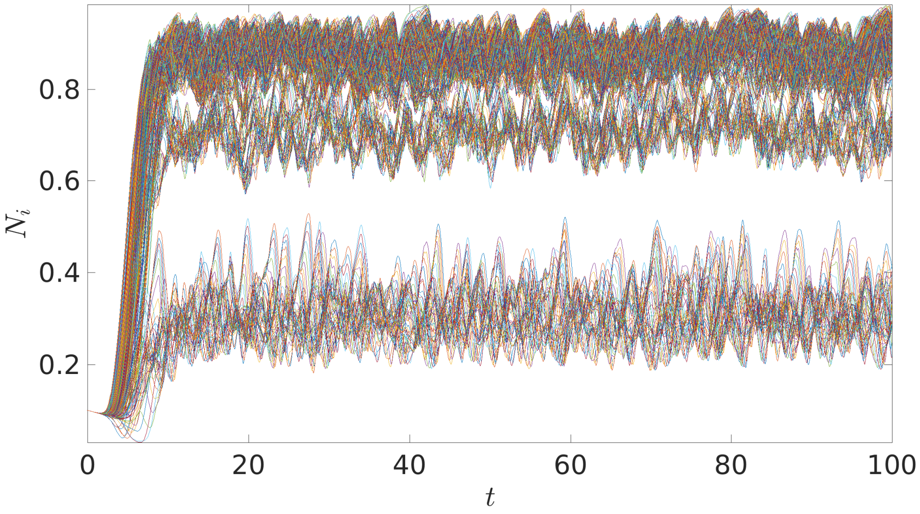

Figure 4.9: Chaotic time series of nodal values for a simulation corresponding to $\delta = 10^{-4}$, $Q_D = \infty$ and $Q_G = 2$ for $n = 25$.

by the cells are both negligible, demonstrated in a simple setting that the local concentration of nutrient pumped into a scaffold will be primarily determined by the flow rate in that part of the scaffold. This comparison can be explored more rigorously in order to elucidate differences between models incorporating nutrient transport, and our phenomenological flow model.

We emphasize that this model is a caricature, and likely does not recapitulate many aspects of real fluid-growth coupling in a tissue engineering scaffold quantitatively, especially as the threshold parameters Q_G and Q_D are difficult to determine. Nevertheless, the phenomenological models developed in this Chapter can give important biological and mathematical insight. Both lattice and continuum models exhibit aggregation of cells in regions of high cell density, as in Chapter 2. Increasing the fluid flux sensitivity threshold threshold Q_G decreases the mean density of these aggregates in both models, but also leads to spatial structures appearing within the aggregates only in the lattice models. In particular, Figures 4.4 and 4.5 show the profound influence of the network structure of the lattice model on the resulting cell density distributions, which is completely absent in the continuum model. Finally, the complicated spatiotemporal chaos exhibited by this model suggests an underlying complexity to the class of models being investigated. While this behaviour is likely not one which corresponds to a biological reality, it is indicative of some of the difficulties involved in analyzing models of bioactive porous media due to the nonlocal nature of fluid-growth coupling.

Despite the simplicity of this alternative approach, we have shown a variety of different behaviours that suggest directions for further work using similar ideas. In particular, validating the assumption of fluid flow rate as a proxy for nutrient transport could lead to model simplification throughout the literature. Additionally, compared with the shear stress and pressure forced models of previous Chapters, this model shows the greatest differences in qualitative behaviour between the spatially continuous and lattice models. These differences are particularly apparent in the internal patterning observed in Figures 4.5, and the non-equilibrium behaviours demonstrated in Section 4.2.1. We suspect that these differences are more pronounced due to the inherently more complex competing mechanisms of cell death for high and low values of fluid flow rate. This model then provides a fruitful framework for further investigation in mathematical and biological directions.

Chapter 5

Stochastic Lattice Models of a Bioactive Medium

In this Chapter we consider a third paradigm to model bioactive porous media: stochastic growth models. Specifically, we modify the growth process on a lattice described in Chapters 2-4, so that cells evolve randomly in a discrete manner, rather than deterministically in a continuous state. We explore simulations of these stochastic models with deterministic simulations using identical random initial conditions in both models. We find several different behaviours such as the stochastic model settling into a stationary time-independent configuration, or fluctuating indefinitely in time. We demonstrate that observables like the spatial mean cell density become less sensitive to initial conditions, for both stochastic and deterministic models, as the lattice size increases. We finally discuss these algorithms in terms of their computational efficiency compared to numerical simulations of the systems of ordinary differential equations defining the cell growth and death process in the deterministic lattice models.

The stochastic lattice models presented in this Chapter are novel approaches to modelling fluid-cell interactions in a bioactive porous tissue scaffold. In particular, while stochastic models for tissue growth processes exist, we are unaware of any which have coupled fluid flow with a stochastic cell evolution determined by a single quasi-static flow stimulus (e.g. shear stress, pressure, or fluid flux). Additionally, we provide numerical evidence for aspects of universal behaviour (in other words, insensitivity to some model details) in both deterministic and stochastic lattice models. This leads to an insensitivity to initial conditions found in these models, if the number of nodes is sufficiently large.

We motivate this stochastic approach in two ways. Firstly, stochastic models in mathematical biology are increasingly employed due to the complexity and uncertainty in biological processes; see [47, 64, 114] and references therein. Secondly, treating the cells in a discrete way (either present or not at each lattice site) allows for a simple update rule lending itself to a computationally efficient algorithm to simulate the growth process. Many such stochastic models exist for growth, migration, invasion, and other interactions in areas ranging from cancer biology to population dynamics [38, 102, 132, 170, 177, 181, 194].

In addition, this stochastic perspective gives insight into several aspects of our deterministic lattice-based models. We demonstrate a heuristic for why sensitivity to initial conditions may decrease as the size of the lattice is increased, due to relationships that the stochastic model has to simpler 'universal' stochastic lattice models [12]. This is motivated in large part by simpler stochastic processes on lattices, such as percolation discussed, for instance, in [70, 122, 161]. This universality shows an insensitivity of the final cell density in the scaffold to the initial seeding strategy, as long as the lattice is sufficiently large. We note that several models in tissue growth have made comparable observations, although for models where a dynamic network has formed due to multiscale processes [97, 106, 130]. Our models will differ from these in the ways described at the end of Section 1.1.3, as we are modelling the proliferation and diffusion of cells in a static network.

In Section 5.1 we present our stochastic model, and describe some approaches to simulate it and how these approaches compare. We also compare simulations of the model with the deterministic lattice simulations presented in previous Chapters. In Section 5.3 we discuss this model in terms of criticality and universality (detail-independence) in simple stochastic models, and aspects of these general phenomena that are present within our specific model. In particular, this gives some heuristic information about the behaviour of large lattices that is useful for lattice and continuum models of bioactive media. Finally in Section 5.4 we discuss some computational considerations of this approach, and in particular how the stochastic model lends itself to much faster simulation than the deterministic models presented before. Alongside the results about universal behaviour, this gives a particularly efficient way to generate simulations corresponding to large lattices.

5.1 A Stochastic Model of a Porous Tissue Scaffold

As in Chapters 2-4, we consider an n by n square lattice, and denote nodal pressures as $\boldsymbol{p} = (p_1, \ldots, p_{n^2})$ and cell densities as $\boldsymbol{N} = (N_1, \ldots, N_{n^2})$. We use the same formulation for the fluid flow problem, so the pressures satisfy Equations (2.32a,b) which can be written (from Section 3.1.1) as

$$\sum_{j=1}^{n^2} A_{ij}\left(1-\frac{\rho}{2}(N_i+N_j)\right)^4 (p_i-p_j) = \begin{cases} \dfrac{1}{n}\left(1+\displaystyle\sum_{j=1}^{n} p_j\right) - p_i, & 1 \leq i \leq n, \\ 0, & n < i \leq n^2-n, \\ -p_i, & n^2-n < i \leq n^2. \end{cases} \tag{5.1}$$

We model the influence of the flow on cell growth using the functions $F_1(\boldsymbol{p})$ and $F_2(\boldsymbol{p})$ defined by either Equations (2.32h), (3.4), or (4.2), depending on if we are considering shear, pressure, or fluid flow rate effects on cell growth and death. We write the nodal values of the shear functions $F_1^i = \eta F_1(\sigma_i)$ and $F_2^i = \eta F_2(\sigma_i)$,where η is a constant that determines the time scale, and we use similar expressions for the pressure and flow rate models. We discretize the cell densities, so that $N_i \in \{0,1\}$ for all i. Alternative state-space descriptions (e.g. finer discretizations or continuum descriptions) of the cell density can be considered, but this binary classification leads to a simple stochastic model of growth throughout the lattice which we adopt for conceptual and computational amenability. While we think of N_i as a cell density at node i, an alternative perspective is to think of it as a value determining if cells are present or not in the lattice at node i.

We define our process over a small time step $\Delta t \ll 1$, and construct our stochastic model in the following way. If there are cells at node i at time t, that is $N_i(t) = 1$, then the probability of cells dying at node i in the interval $(t, t+\Delta t)$, or equivalently $N_i(t+\Delta t) = 0$, is $F_2^i \Delta t$. A similar growth rule involving F_1^i could be used to determine which nodes gain new cells, but in order to account for local diffusion we will use the adjacency matrix of the graph A_{ij} describing nodal connectivity. This is to avoid spontaneous growth far away from where cells currently reside. If $N_i(t) = 0$, then the probability of $N_i(t+\Delta t) = 1$ is $\sum_{j=1}^{n^2} A_{ij} F_1^i N_j \Delta t$. We will now describe two algorithms to simulate this process.

5.1.1 Uniform Time-Stepping Algorithm

We fix a time step Δt, and for each time t we solve Equations (5.1) and use the functions F_1^i and F_2^i to determine the cell density distribution at the next time step, $\boldsymbol{N}(t+\Delta t)$. For each lattice site i we generate a random number r_i uniformly distributed in $(0,1)$. If $N_i(t) = 1$ and $r_i < \Delta t F_2^i$, then the cells in that node die (e.g. due to pressure, shear, or flow rate) so we set $N_i(t+\Delta t) = 0$. If $r_i > \Delta t F_2^i$, then we keep the same value of $N_i(t + \Delta t) = 1$. If the fluid property (shear stress, pressure, fluid flux) is above the threshold to induce death, then $F_2^i \approx \eta$ and this rule samples the probability of a cell at site i dying under this flow regime ($\eta \Delta t$) in one time step. Similarly, if the fluid property is in the growth regime, then $F_2^i \approx 0$, and the probability of a uniform random variable r_i satisfying $r_i < \Delta t F_2^i$ is arbitrarily small, and in practice equal to 0 for the forms of these functions we are considering here.

Similarly, if $N_i(t) = 0$ and $r_i < \Delta t \sum_{j=1}^{n^2} A_{ij} F_1^i N_j$, then we set $N_i(t+\Delta t) = 1$. This gives the probability of growth within time Δt (when the flow variable F_1^i permits it) to be $\eta \Delta t \sum_{j=1}^{n^2} A_{ij} N_j$, so that cells can only grow when there are cells nearby, and are more likely to grow when many adjacent nodes have cells present. We then iterate this procedure from $t = 0$ until $t = T$ for some fixed end time T. We give pseudo-code for this process in Algorithm 1.

Algorithm 1 Stochastic cell growth Algorithm with synchronous updating.

```
$t := 0$
while $t < T$ do
    Solve (5.1) and Compute $F_1^i$ and $F_2^i$ for all $i$
    Generate $r_i \sim \mathcal{U}(0,1)$ for all $i$
    for all $1 \le i \le n^2$ do
        if $N_i = 1$ & $r_i < \Delta t F_2^i$ then
            $N_i := 0$
        else if $N_i = 0$ & $r_i < \Delta t \sum_{j=1}^{n^2} A_{ij} F_1^i N_j$ then
            $N_i := 1$
        end if
    end for
    $t := t + \Delta t$
end while
```

5.1.2 Gillespie-Like Algorithm

Another way to understand and simulate this model is in terms of exponentially distributed growth and death times. Using ideas originally popularized by Doob and Gillespie [47, 61], we can compute a waiting time for each node until an 'event' occurs, where cells either grow or die at a particular node. Let $A(\boldsymbol{N}(t))ds$ be the probability of an event (cell growth or death at a node) occurring in the time interval $[t, t + ds)$. Denote by $f(A(\boldsymbol{N}(t)), s)ds$ the probability that an event occurs in the interval $[t + s, t + s + ds)$, where ds is an infinitesimally small time. We follow [47] to derive an expression for f which will allow us to understand how these probabilities change over the time interval $[t, t + s)$.

Denote the probability that no events occur in the interval $[t, t+s)$ by $g(A(\boldsymbol{N}(t)), s)$. We then have that

$$f(A(\boldsymbol{N}(t)), s)ds = g(A(\boldsymbol{N}(t)), s)A(\boldsymbol{N}(t+s))ds. \tag{5.2}$$

To compute g, we consider an arbitrary $\sigma > 0$ and write the probability that no events occur in the interval $[t, t+\sigma+d\sigma)$ for an infinitesimal $d\sigma$ as,

$$g(A(\boldsymbol{N}(t)), \sigma+d\sigma) = g(A(\boldsymbol{N}(t)), \sigma)(1-A(\boldsymbol{N}(t+\sigma))d\sigma) = g(A(\boldsymbol{N}(t)), \sigma)(1-A(\boldsymbol{N}(t))d\sigma), \tag{5.3}$$

where we have used the fact that assuming no events have occurred in the interval $[t, t+\sigma)$, we have that $A(\boldsymbol{N}(t+\sigma)) = A(\boldsymbol{N}(t))$. Rearranging Equation (5.3) and taking the limit $d\sigma \to 0$ we have that,

$$\frac{dg(A(\boldsymbol{N}(t)), \sigma)}{d\sigma} = -g(A(\boldsymbol{N}(t)), \sigma)A(\boldsymbol{N}(t)), \tag{5.4}$$

so that $g(A(\boldsymbol{N}(t)), \sigma) = \exp(-A(\boldsymbol{N}(t))\sigma)$. Setting $\sigma = s$ and substituting this expression into Equation (5.2) we have,

$$f(A(\boldsymbol{N}(t)), s)ds = A(\boldsymbol{N}(t))\exp(-A(\boldsymbol{N}(t))s)ds. \tag{5.5}$$

From Equation (5.5), we see that the if we want to compute the time τ such that the next event occurs at time $t+\tau$, then τ must be exponentially distributed with a rate $A(\boldsymbol{N}(t))$. This follows from the function $f(A(\boldsymbol{N}(t)), \tau)$ being the probability density function of an exponentially distributed random variable τ, with a rate parameter $A(\boldsymbol{N}(t))$. We now sample from these exponentially distributed waiting times.

For each lattice site i we generate a random number r_i uniformly distributed in $(0, 1)$. For a given time t we can define a nodal waiting time τ_i for $1 \leq i \leq n^2$ by

$$\tau_i = \begin{cases} \frac{1}{F_2^i} \ln\left(\frac{1}{r_i}\right), & \text{if } N_i(t) = 1, \\ \frac{1}{\sum_{j=1}^{n^2} A_{ij} F_1^i N_j} \ln\left(\frac{1}{r_i}\right), & \text{if } N_i(t) = 0, \end{cases} \tag{5.6}$$

where we define division by 0 as $\tau_i = \infty$. We then compute $\tau = \min_i\{\tau_i\}$, and then set $N_i(t+\tau) = 1 - N_i(t)$ for i such that $\tau = \tau_i$, and $N_j(t+\tau) = N_j(t)$ for all $j \neq i$. We then repeat this process again until some time T. Pseudo-code for this procedure is given in Algorithm 2. While there can be multiple minimal τ_i, in practice this will uniquely determine a single cell density to update.

Both algorithms approximate the same stochastic process, and so we anticipate that their behaviour over large regions of parameter space will be the same as long

Algorithm 2 Stochastic cell growth Algorithm with asynchronous updating.

```
$t := 0$
while $t < T$ do
    Solve (5.1) and Compute $F_1^i$ and $F_2^i$ for all $i$
    Generate $r_i \sim \mathcal{U}(0,1)$ for all $i$
    for all $1 \leq i \leq n^2$ do
        if $N_i = 1$ then
            $\tau_i := \frac{1}{F_2^i} \ln\left(\frac{1}{r_i}\right)$
        else if $N_i = 0$ then
            $\tau_i := \frac{1}{\sum_{j=1}^{n^2} A_{ij} F_1^i N_j} \ln\left(\frac{1}{r_i}\right)$
        end if
    end for
    $\tau := \min_i\{\tau_i\}$
    for all $\tau_i = \tau$ do
        $N_i := 1 - N_i$
    end for
    $t := t + \tau$
end while
```

as Δt is sufficiently small. We give numerical evidence for this in Section 5.2. Computationally, Algorithm 1 is typically much faster (and lends itself to more naive optimizations) than Algorithm 2. Specifically, the former allows cell densities at multiple nodes to change with one calculation of the pressures from Equations (5.1), which is the most computationally expensive part of either Algorithm. Additionally, if no change in cell density occurs, the pressures at the previous step can be reused. The Gillespie-type Algorithm 2 is often faster to simulate when there are rare events, but the dynamics observed in Chapters 2-4 suggest that these models typically exhibit fast transient behaviour (e.g. uniform logistic growth) followed by a period of equilibration to a steady state solution. For short time scales (e.g. growth and death time scales), there are many events occurring, and so Algorithm 2 will solve Equations (5.1) many times for each lattice site update, whereas Algorithm (1) will only solve these equations a fixed number of times for a fixed end time. Finally we note that the time scale η does not appear to play a role in the long-time behaviour as long as $\Delta t \ll \eta$, but that it can affect the timescale on which we observe transient behaviours (e.g. logistic growth).

5.2 Stochastic Simulations

Here we present numerical simulations of Algorithms 1 and 2 alongside solutions of the corresponding deterministic models for different forms of the fluid response functions F_1^i and F_2^i. We will use consistent initial conditions generated by randomly setting $N_i(0) = 1$ for a proportion of nodes $M_0 \in [0, 1]$, and $N_j(0) = 0$ for all other nodes, so that $M_0 = \sum_{i=1}^{n} N_i(0)/n^2$. For most of the simulations shown in this Chapter we set $M_0 = 0.2$ or $M_0 = 0.3$ in order to compare with small initial seeding densities used in previous Chapters. We will use the same stochastic realizations for different models or parameters by using fixed seeds for the random number generators. In other words, the uniformly distributed random numbers $r_i \sim \mathcal{U}(0, 1)$ will be the same between simulations. For each realization (e.g. seed of the random number generator), we will generate a different initial condition using the same proportion M_0 of nodes with cells for both stochastic and deterministic simulations in order to facilitate comparison between them. We then vary these seeds to generate different realizations of random initial conditions and the numbers r_i in our stochastic simulations. As mentioned before, the value of η does not appear to affect the simulation results, but only changes the timescale. As we are interested here in long-time behaviours, we set $\eta = 1$ so that the timescale of transient growth and death are both $O(1)$ in order to observe long-time behaviour within our simulation timescale, which will be $O(10)$. For Algorithm 1 we set $\Delta t = 10^{-2}$. For the deterministic simulations that we compare to, we will set $\delta = 10^{-5}$ so that nodal cell densities are close to 0 or 1 for most lattice sizes. We use the same numerical approaches for the deterministic system as in previous Chapters - see Sections 2.1.4, 3.2, and Appendix A.

Broadly these stochastic models have two kinds of long-time behaviours. They either reach a state with a cell density distribution such that the probabilities of cell death or growth at any node are extremely small (e.g. $F_1^i \approx 0$ for all i such that $N_i = 0$ and $F_2^i \approx 0$ for all i such that $N_i = 1$). This state is a pseudo-steady state, and the cell density distribution remains in it for arbitrarily long periods of time. In the limit of $g \to \infty$, these probabilities become exactly 0, and so this becomes an actual steady state of the process. Alternatively, for some of the fluid functions and for some parameter values, the cell density fluctuates for arbitrarily long periods of time. We consider these quasi-stationary distributions, although we do not show that they are necessarily unique or that they are not in fact stationary distributions. In Section 5.3 we overview our numerical results, and in particular connect them to simpler stochastic models in the literature.

5.2.1 Pressure Model

We now discuss numerical simulations of the stochastic variant of the pressure model, with deterministic counterpart discussed in Chapter 3. These simulations exhibit cell densities that have fluctuating spatial means in time about a given level of the mean cell density. These cell density distributions have a similar structure to the deterministic case (e.g. high pressure along the left side of the lattice leads to a region of low cell density, whereas low pressure on the right leads to a large region of high cell density). In Figure 5.1 we plot time series of the spatial mean cell density corresponding to averages of 400 realizations of the pressure model given by Algorithm 1 for increasing lattice sizes alongside deterministic simulations. We note that the stochastic time series in Figure 5.1 exhibit a transient growth period, followed by a state of fluctuations about a temporal mean cell density. For individual stochastic simulations, the smaller lattices exhibit large fluctuations about such a mean cell density, whereas the larger lattices have smaller fluctuations. Despite numerous realizations, the effects of these fluctuations can be seen in the local smoothness of the averages plotted in Figure 5.1. We also observe that the stochastic models over-predict the mean cell density in each case, which is similar to the result that oscillating cell density distributions in Chapter 3 had a higher mean cell density than steady state behaviours.

Plotting some of the cell density distributions for a specific realization in Figure 5.2, we see that the $n = 10$ and $n = 25$ lattices have regions of cells throughout the lattice, whereas the larger lattice ($n = 100$) has a clearer boundary between where most of the cell density is and where there are few cells (and correspondingly large pressures). These stochastic simulations do not maintain any of the vertical or reflection symmetries seen in Chapter 3, and due to fluctuations, small 'pockets' of high cell density can be found in the region of high pressure. Compare Figure 5.2 with Figures 3.2a-3.2b to see this. This lack of symmetry helps explain why the stochastic models lead to higher cell densities, as there are fluid paths through the regions of high cell density that can transport the fixed fluid flow rate without raising the pressure at the left side of the lattice as much as in the deterministic case, where the region of high cell density is more concentrated. See Figure 4.7 for a description of how this lack of symmetry can lead to smaller pressures for a given fluid flux.

The larger fluctuations in the smaller lattices is a finite-size effect that is partly due to the strong nonlocality of the pressure model (e.g. small changes in cell density at one node can have large changes in the pressure throughout the lattice). This is shown quantitatively in Figure 5.3 where we plot the number of nodes above the pressure threshold p_l over time. The sharp changes in pressure are due to the large

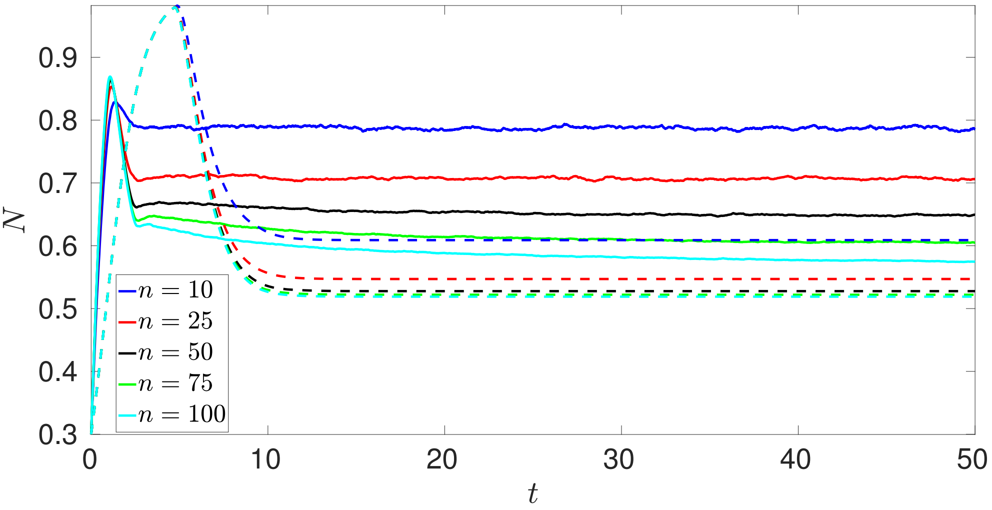

Figure 5.1: Time series of spatial mean cell densities computed via Algorithm 1 for the pressure-forced model with $p_l = 5000$, and for $n = 10, 25, 50, 75$, and 100 with the initial mean cell density as $M_0 = 0.3$. We also plot dashed lines corresponding to the spatial mean cell density for simulations of equations (3.1)-(3.4) for $n = 100$ and $\delta = 10^{-5}$. Each line corresponds to the time-dependent spatial mean averaged over 400 stochastic realizations.

changes in effective permeability that growth in a small region of the scaffold can have. In the larger lattices, cells can only diffuse into the leftmost region so far before being randomly killed by the pressure, which is frequently large enough to kill off cells diffusing into the left side of the lattice. This explains why the fluctuations decrease as the lattice size increases in this particular model. We will discuss this dependence on the lattice size n in Section 5.3.

5.2.2 Shear Stress Model

We next show simulations for both Algorithms 1 and 2 alongside numerical solutions for Equations (2.32) where cells die due to high values of shear stress. In Figure 5.4 we plot time series of spatial mean cell densities for 20 different realizations of these for lattices of sizes $n = 10, 25, 50$, and 100. Unlike the pressure model time series shown in Figure 5.1, we see that most realizations of the shear stress model shown in Figure 5.4 settle into a steady state distribution, or fluctuate only slightly about one for long times. This can be confirmed by considering the probabilities of growth in an empty lattice site which is proportional to $\Delta t F_1^i$ or death in a lattice site with cells $\Delta t F_2^i$, which are both arbitrarily small for large times t. We also note that as the size of the lattice increases, the variability between stochastic realizations (and

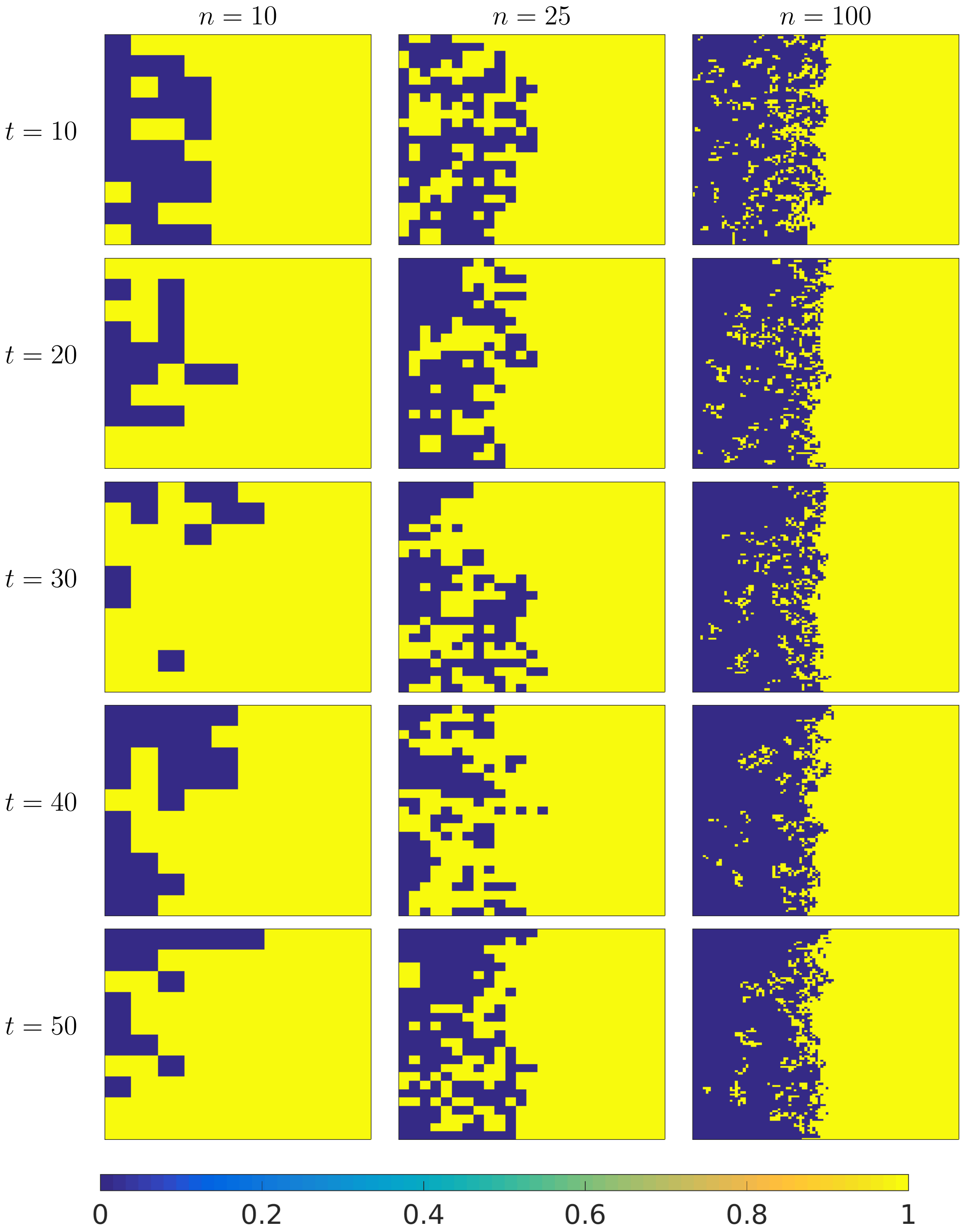

Figure 5.2: Cell density distributions for the simulations described in the caption of Figure 5.1. The yellow regions are nodes with $N_i = 1$ and the dark blue regions are nodes with $N_i = 0$.

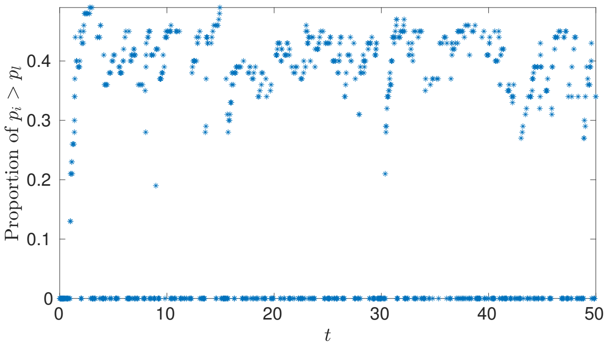
(a) $n = 10$

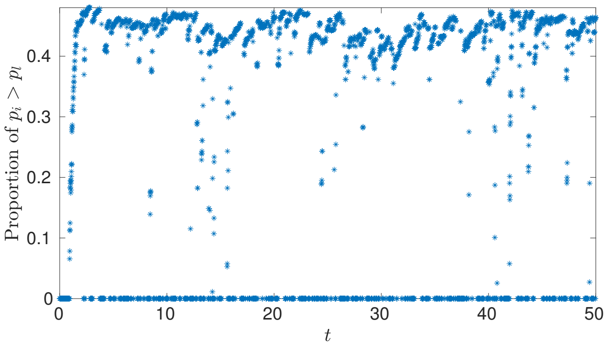
(b) $n = 25$

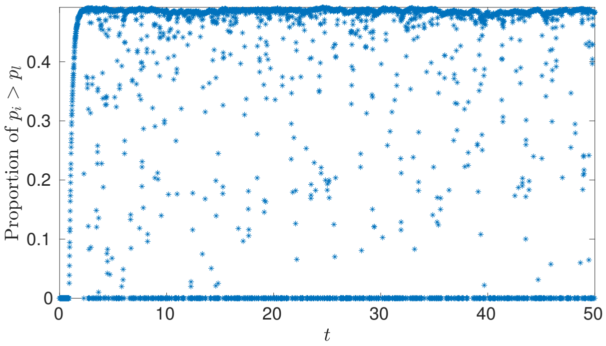
(c) $n = 100$

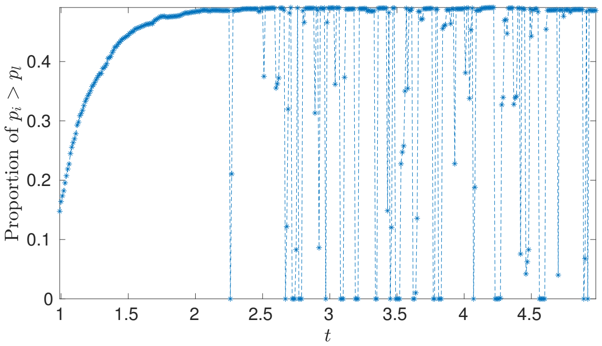
(d) $n = 100$

Figure 5.3: Plots of the proportion of nodal pressures above the threshold (equivalently, the number of nodes where $F_1^i \approx 0$ and $F_2^i \approx 1$). In (a)-(c) we increase the lattice size as $n = 10, 25$, and 100 respectively. In (d) we show a zoomed in part of (c), where we do not omit the lines showing the rapid oscillations between the data points.

deterministic simulations with random initial data) decreases substantially. We will explore this further in Section 5.3.

The two stochastic Algorithms give quantitatively and qualitatively similar behaviours, with the mean between 20 stochastic realizations less than 1% of one another for each lattice size shown in Figure 5.4. There is a transient discrepancy between the stochastic and the deterministic simulations, but as mentioned above, the timescale in the stochastic simulation is arbitrary, so changing the value of η can make the transient behaviour occur at a similar rate as the deterministic simulations, but this rate depends on initial seeding density and parameters in the deterministic model that are not present in the stochastic one (e.g. the diffusion parameter δ).

As in the pressure model, the stochastic simulations shown in Figure 5.4 predict a larger mean cell density compared to the deterministic model for the same parameters. We plot some cell density distributions for a single realization to illustrate the differences between the stochastic and deterministic simulations in Figure 5.5. In both the $n = 50$ case on the left and the $n = 100$ case on the right, the stochastic simulations have larger aggregates of high cell density and fewer small fluid channels at steady state ($t = 50$). This suggests that the stochastic process is better able to form large clusters compared to the deterministic model. The stochastic and deterministic models have a different diffusion process in that the deterministic model spreads ‘slowly’ through diffusion, whereas the stochastic model can immediately grow from no cells present at a particular node to the carrying capacity at a node within one time step. This difference is likely what biases the stochastic simulations towards having large clusters with fewer total fluid channels compared to deterministic simulations. For instance, consider times $t = 2$ and $t = 3$ for the stochastic and deterministic models for $n = 50$ in Figure 5.5. Along the middle of the right hand side in both cell density distributions there is a small channel at $t = 2$ that is closed in the stochastic simulation at $t = 3$ but remains a fluid channel (with a small cell density diffusing into it) in the deterministic case. We conjecture that this is because the stochastic model closed this channel quickly in its evolution, leading to larger cell density aggregates, whereas the deterministic model spread more slowly throughout the lattice and hence was unable to seal many such channels. Note that this is due to the nonlocal effect of the fluid flow - cell growth throughout the lattice in either simulation increases the shear stress throughout the scaffold, and hence slows growth or induces cell death elsewhere.

These qualitative differences between stochastic and deterministic models (i.e. the former having larger cell aggregates) are robust (as far as we found numerically) to the

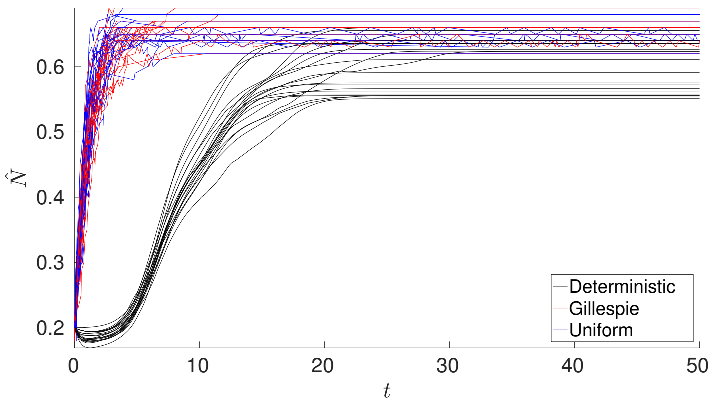

(a) $n = 10$

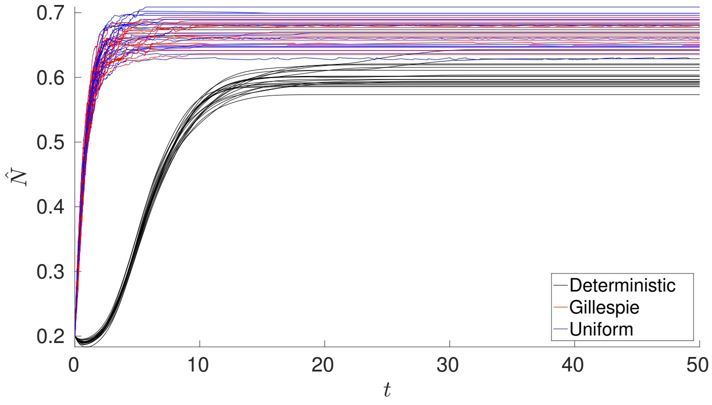

(b) $n = 25$

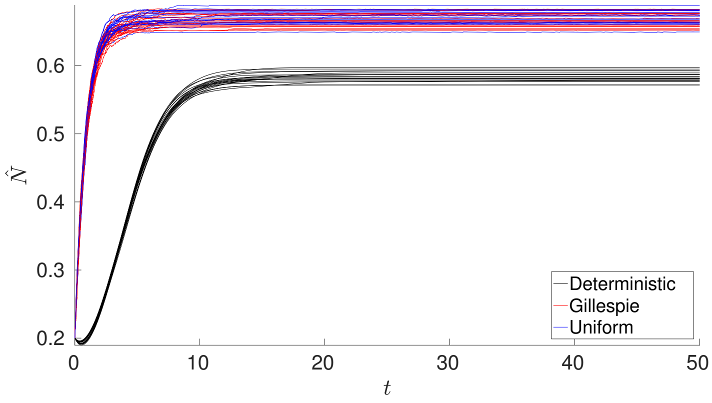

(c) $n = 50$

Figure 5.4: Time series plots of spatial mean cell density $\hat{N}$ for simulations of lattices with (a)-(c) having sizes $n = 10, 25$, and 50, with $M_0 = 0.2$ and $\sigma_l = 5$. A set of 20 initial conditions was created and then Algorithms 1 and 2 were used to construct random time series, whereas Equations (2.32) were solved to generate the deterministic time series from the same initial data.

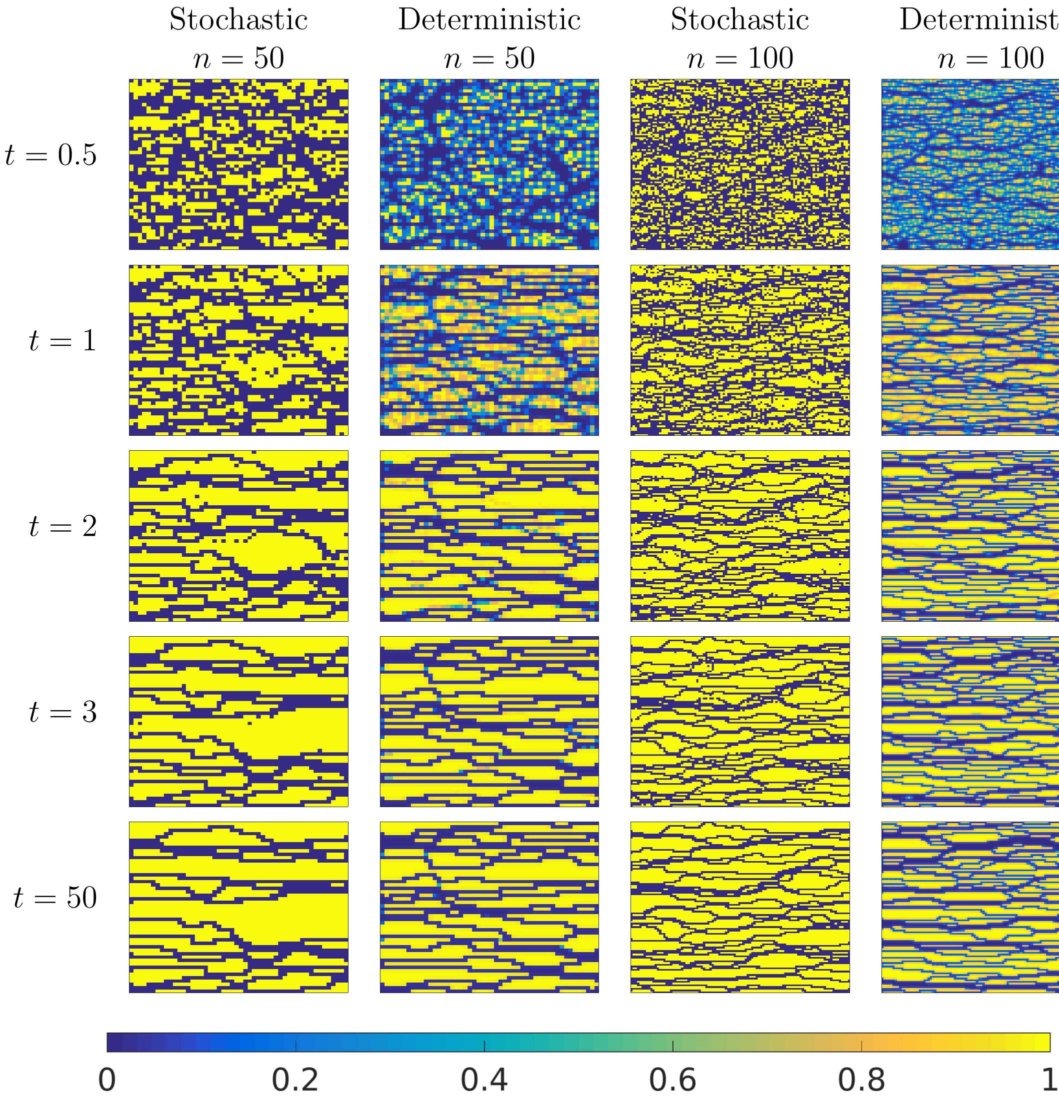

Figure 5.5: Cell density distributions for a particular realization of the simulations described in the caption of Figure 5.4. The stochastic simulations used were computed via Algorithm 1.

kinds of initial data used in the deterministic case. Smoothed initial conditions lead to quantitatively comparable mean cell densities, and qualitatively similar separation between cell and fluid phases, as in the $t = 50$ row of Figure 5.5. Special initial conditions that separate the domain into a high-shear region and a low-shear region are numerically stable in both models. For example, for an $n = 100$ lattice with $\sigma_l = 5$ as in Figure 5.5, if the upper 63% of the lattice has cells at their carrying capacity, then this cell density distribution does not change in the deterministic or stochastic models (although small diffusion in the deterministic case leads to a very small boundary layer between these regions, and hence to a mean of $\hat{N} = 62.99$). These special initial conditions suggest that the final cell density is not strictly dependent on parameters in the problem, but has a kind of hysteresis which depends on how the cell density transiently settles into an equilibrium, and hence it depends on the kind of model used.

5.2.3 Fluid Flux Model

Finally we consider the stochastic analogue of the fluid flux model of Chapter 4. We first consider the case where $Q_G \to -\infty$ and $Q_D = 5$, so that cells do not die due to low fluid flux, but only die due to high values of flux. In Figure 5.6 we plot time series of 20 realizations for both Algorithms 1 and 2, as well as deterministic solutions of Equations (2.32a-g) and (4.2), as we did for the shear stress model in Figure 5.4. We see similar behaviours as in the shear stress model, where the cell density distribution reaches a steady state value for both the deterministic and stochastic simulations, and that the mean cell density becomes less dependent on the stochastic realization and random initial conditions as n increases.

We plot cell density distributions in Figure 5.7. As in Chapter 4 we observe distinct fluid channels through the scaffold for larger values of Q_D in 5.7b and 5.7d, and smaller clumps of cells distributed throughout the lattice in Figures 5.7a and 5.7c. The deterministic model in all cases that we simulated had a higher mean cell density, which is the opposite behaviour from both the pressure and the shear stress models. This is likely due to the constitutive difference between nodal flux Q_i and shear stress σ_i, differ by a factor of the pipe radii R_{ij} towards each neighbouring node. In the deterministic setting, diffusion into fluid channels will lead to higher shear stress, but if the fluid can be forced elsewhere, then it will lead to a lower local fluid flux Q_i. In other words, cell diffusion into node i can in some cases increase σ_i but decrease Q_i. The stochastic simulation, in comparison, will never enter these fluid channels because the fluid flux is prohibitive (e.g. $F_1^i \approx 0$).

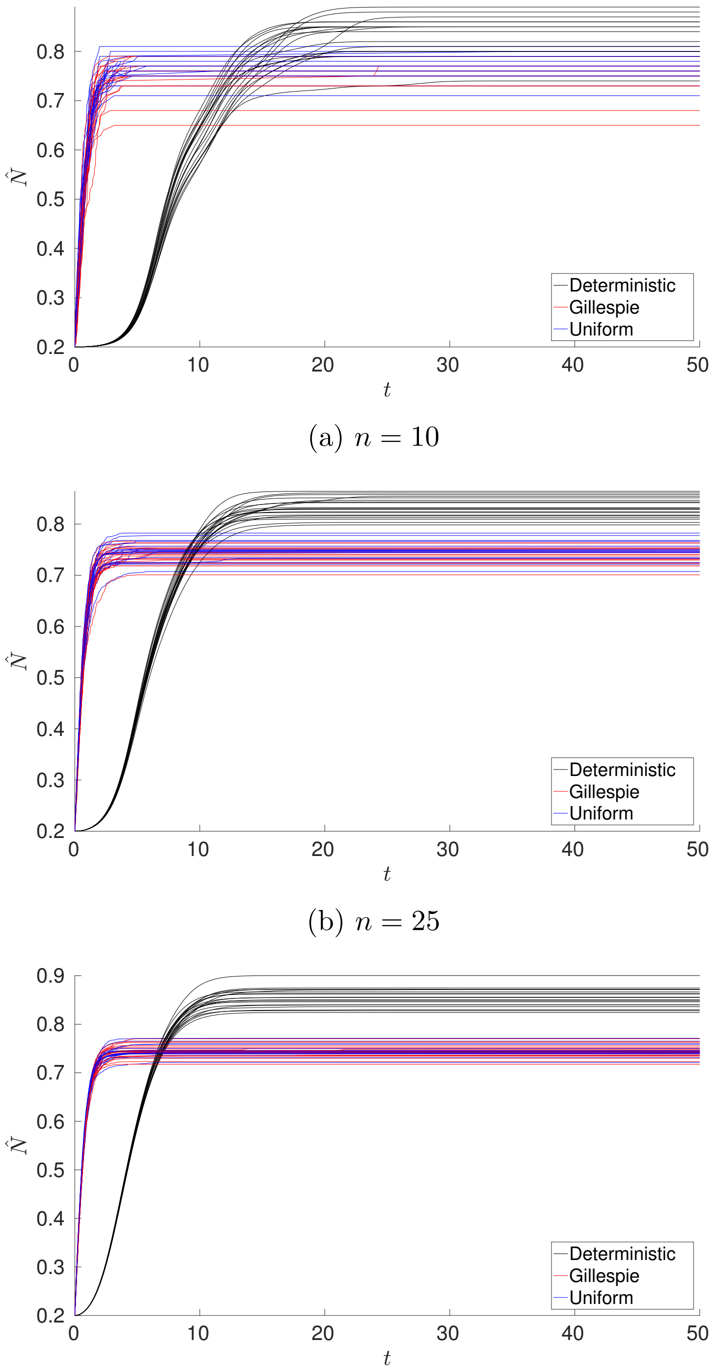

(a) $n = 10$

(b) $n = 25$

(c) $n = 50$

Figure 5.6: Time series of mean cell density $\hat{N}$ for 20 simulations of the fluid flux model with $Q_G \to -\infty$ and $Q_D = 2$ for varying n.

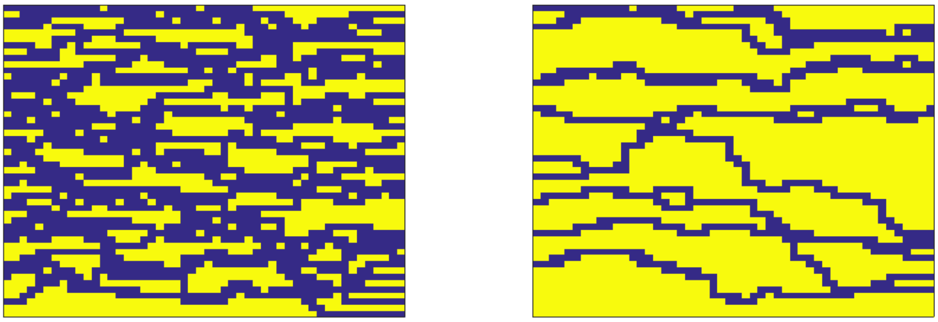

(a) Stochastic $Q_D = 2$

(b) Stochastic $Q_D = 5$

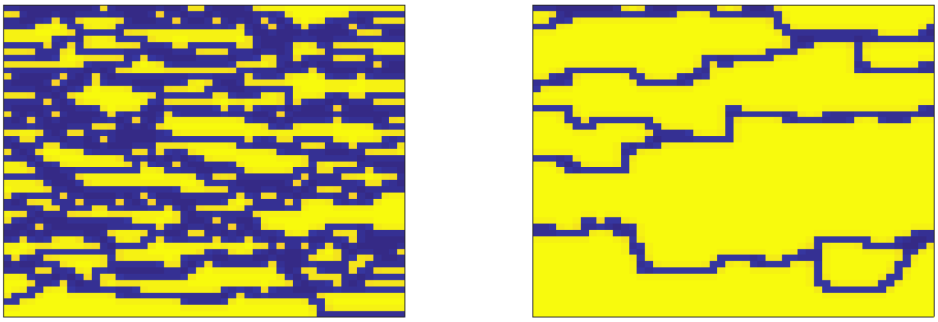

(c) Deterministic $Q_D = 2$

(d) Deterministic $Q_D = 5$

Figure 5.7: Flux cell density distributions at $t = 50$ for $Q_G \to -\infty$, $Q_D = 2$ and 5, and $n = 50$. The stochastic cell densities were computed via Algorithm 1.

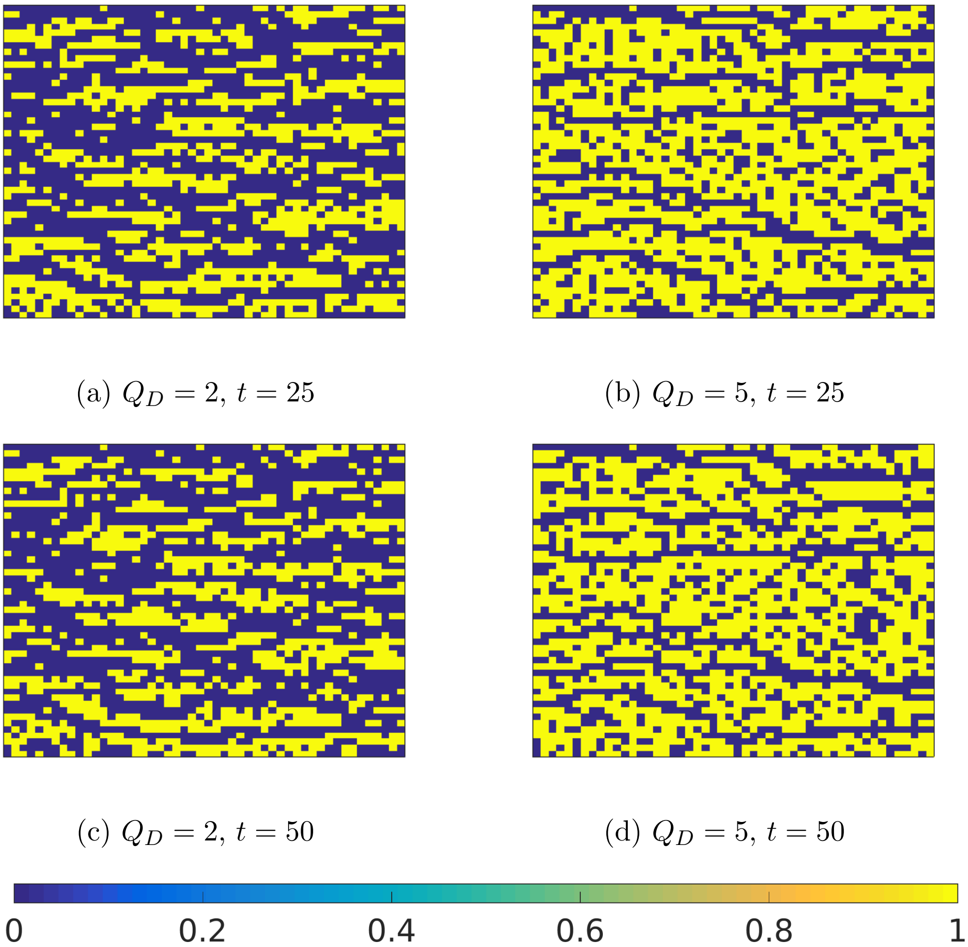

(a) $Q_D = 2$, $t = 25$

(b) $Q_D = 5$, $t = 25$

(c) $Q_D = 2$, $t = 50$

(d) $Q_D = 5$, $t = 50$

Figure 5.8: Flux cell density distributions at $t = 25$ and $t = 50$ for $Q_G = 0.1$, $Q_D = 2$ in (a) and (c) and $Q_D = 5$ in (b) and (d), with $n = 50$ in (a)-(d). These were computed via Algorithm 1.

.

Lastly we consider the effects of cell starvation. We set $Q_G = 0.1$ and plot cell density distributions at different times in Figure 5.8 corresponding to those shown in Figure 5.7. We see that some of the large-scale structure is the same, but large aggregates of high cell density have many ‘holes’ that stochastically change in time due to cell starvation. In Figure 5.9a and 5.9b, we show time series of the spatial mean cell density in this case to show how these fluctuations compare with the deterministic mean cell density. In particular we note that with $Q_G = 0.1$, the stochastic time series in 5.9 continually fluctuate, while those corresponding to $Q_G \to -\infty$ settle into a fixed distribution in finite time.

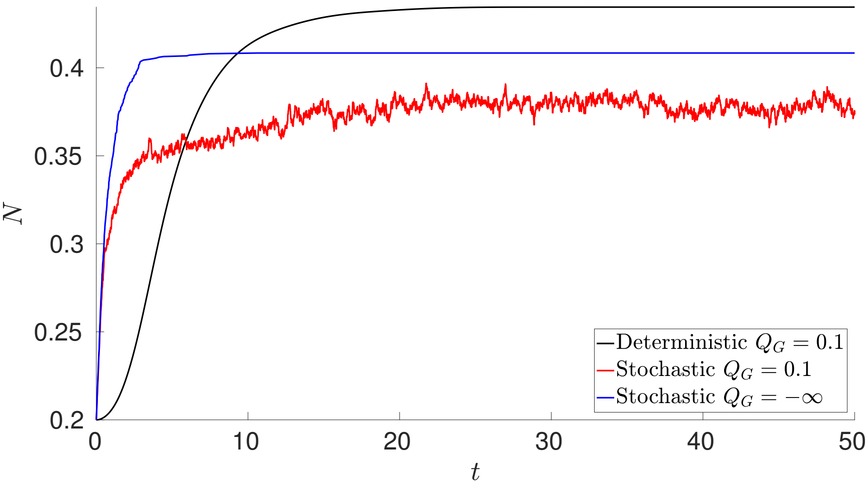

(a) $Q_D = 2$

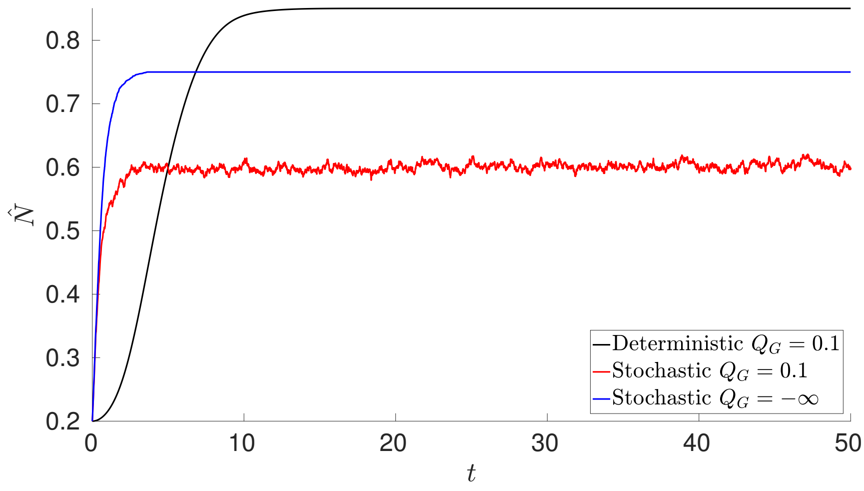

(b) $Q_D = 5$

Figure 5.9: Time series for simulations alongside deterministic simulations for the spatial mean cell density from Figures 5.7 and 5.8.

5.3 Criticality and Universality

Now that we have demonstrated some of the behaviours in our stochastic models, we discuss these behaviours in the context of their relationship to simple stochastic models from statistical physics [12]. While the behaviours we have illustrated above are quite varied and complicated, there is some evidence that there are simple aspects of these models that can be exploited to understand their behaviour by relating them to simpler models. In particular, there is a notion of critical phenomena that has recently been exploited to simplify the behaviour of models of this kind in certain regimes [3, 25, 74, 77, 88, 172].

A system is said to be at criticality if it is at a transition between two qualitatively different states, and some important properties are satisfied exactly at this transition; classically these correspond to phase transitions in simple models in statistical physics, such as the Ising model, or the Abelian Sandpile [8]. As a parameter is varied, the qualitative structure of these models changes, such that when this parameter reaches a critical threshold, some quantities become zero or diverge to infinity. As a concrete example, percolation theory studies the connectedness of nodes in infinite lattices, where a subset of the edges have been independently and randomly removed [70, 161]. A classical question is to determine for what proportion of removed edges, p, does a single 'giant cluster' of nodes exist, such that the majority of nodes are connected to this single component? For the square grid lattice, the critical proportion of connected edges needed to ensure an infinite connected cluster is $p = 1/2$. This was known soon after the question was first posed by [20], but was rigorously shown much later [86]. This transition is sharp, as the probability of being connected to this infinite connected component becomes 1 exactly as the critical threshold is crossed, and is identically 0 before this change. At criticality, several scale-invariant and fractal structures can emerge.

An important implication of these phase transitions is that they are often universal in the following sense: some behaviours of the model at criticality, and often near criticality, do not depend on the details of the process, but only on the (spatial) dimension. For instance, the value of the critical threshold in percolation depends on both the dimension of the lattice and its structure (square, hexagonal, triangular, etc). However, various other quantities of interest, such as cluster statistics (e.g. the mean size of connected components), scale in a way that does not depend on the topology of the lattice. This gives rise to the study of critical exponents and scaling laws, which are common tools of contemporary statistical physics. While we will not try and compute any of these quantities, we explore aspects of our models which exhibit similar detail-independent behaviours, and try and explain this by arguing that, for some parameters, the cell density distribution will self-organize toward some kind of criticality.

For our lattice models, one notion of criticality would be the percolation threshold, defined to be the fraction of nodes at which a flow path between the left and right sides of the lattice is connected. An alternative to this would be a self-organized criticality where the system approaches a fraction of nodes with $N_i = 1$ such that the configuration is stable (e.g. $F_1^i \approx 0$ for all i such that $N_i = 0$ and $F_2^i \approx 0$ for all i such that $N_i = 1$). In these kinds of regimes, for an asymptotically large system (for our models, $n \to \infty$), the behaviour of the model can sometimes become 'universal,' so that scaling behaviour, and other important observables of the system are independent of some details of the system (such as the structure of the network, initial configurations in dynamical models, etc). While we cannot reduce our stochastic models to one which is known to exhibit these universal behaviours, we do demonstrate some evidence of universal behaviour in both the deterministic and stochastic settings. We do not use a specific definition of critical behaviour in our models, but instead suggest that near equilibrium, they display some universal behaviours. This then suggests that some of our models may exhibit self-organized criticality, where they evolve until they reach this universal state.

5.3.1 Concentration of Measure

One of the behaviours noted in Section 5.2 is that increasing the size of the lattice leads to a corresponding decrease in the variation between the mean cell density of different stochastic simulations (and deterministic simulations with random initial data). See, for instance, Figures 5.4 and 5.6. We now consider more realizations across varying threshold parameters to determine how typical this behaviour is across different parameter regimes. For simplicity, we only consider the shear-stress model here, but find comparable behaviour in the others.

In Figures 5.10-5.11 we plot the mean cell density for various values of the threshold σ_l and for 25 stochastic realizations for each parameter. These simulations were all computed for $t = 50$ time units. As the cell density becomes larger, the variation between final mean cell densities seems to decrease; consider the values plotted in Figure 5.10 for $\sigma_l < 15$ against those for $\sigma_L > 15$. Secondly, as the size of the lattice increases, the different stochastic realizations become more concentrated in a smaller subset of $(0, 1)$ for each given σ_l; that is, the variance between the mean cell density

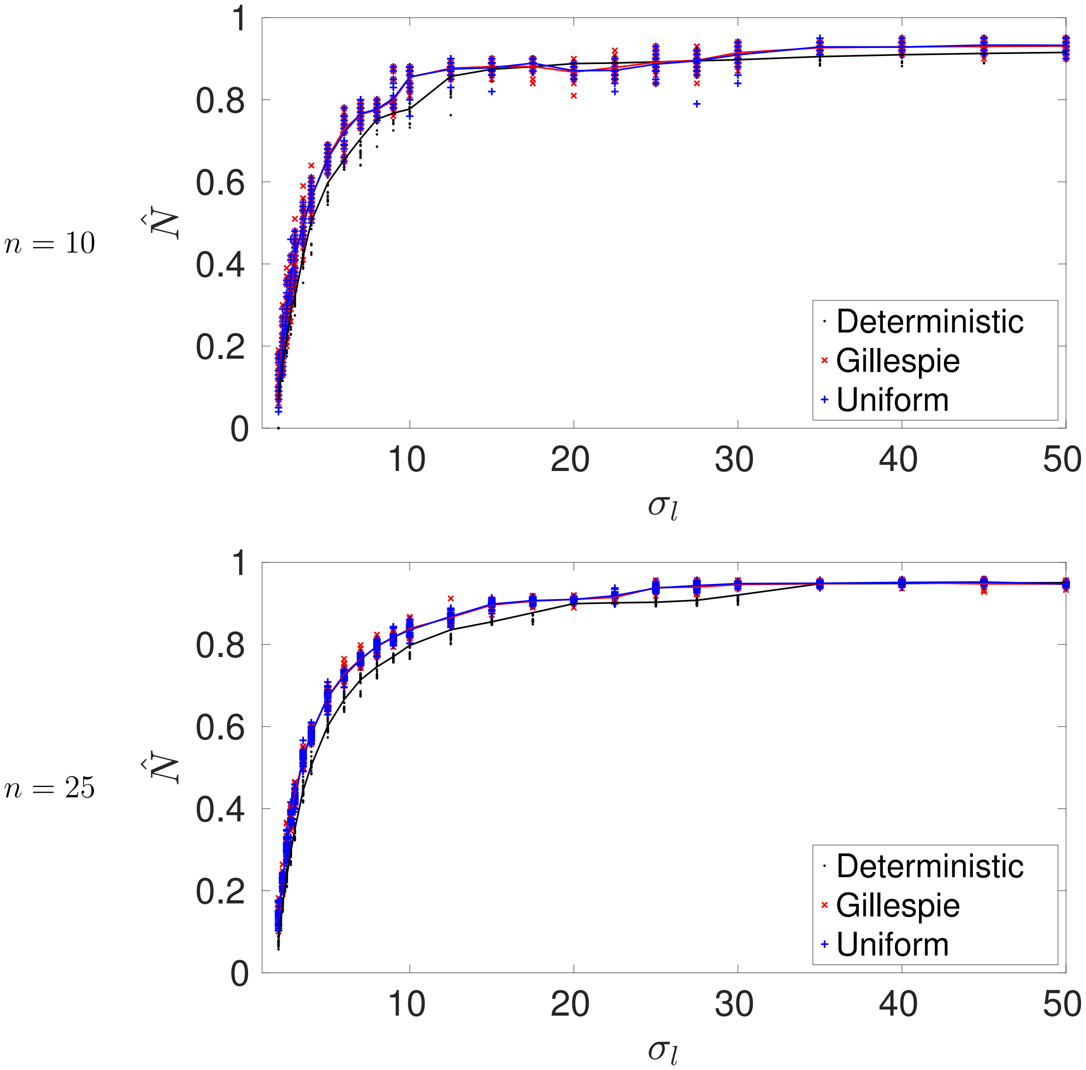

Figure 5.10: Plots of mean cell density for the shear stress models after $t = 50$ time units for 25 different values of σ_l, and different n. For each value of σ_l, 25 different stochastic realizations were sampled. The lines connect the mean computed from these realizations, as a function of σ_l.

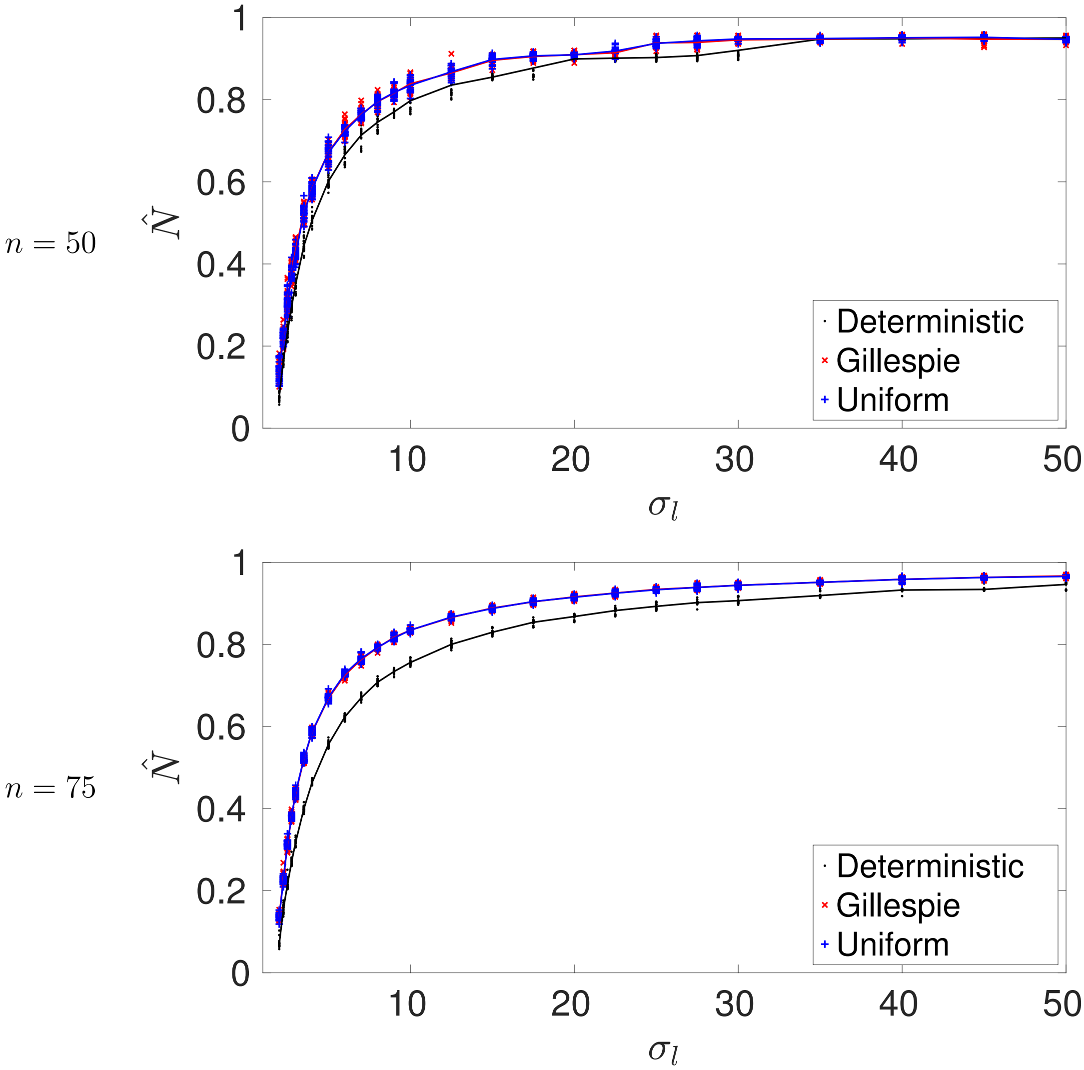

Figure 5.11: Plots of mean cell density for the shear stress models after $t = 50$ time units for 25 different values of σ_l, and different n. For each value of σ_l, 25 different stochastic realizations were sampled. The lines connect the mean computed from these realizations, as a function of σ_l.

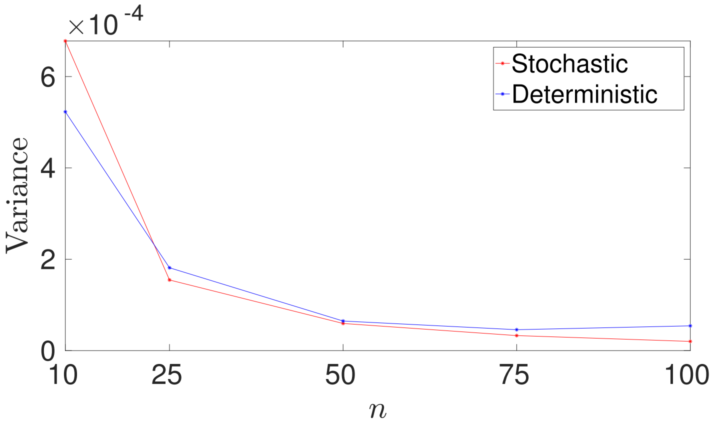

Figure 5.12: Plots of the mean (across values of σ_l) variance across realizations from Figures 5.10-5.11 in terms of the lattice size n and the model considered.

across different realizations is smaller for larger lattices. We quantify this decrease in variation in Figure 5.12, where we plot the mean value (over σ_l) of the variance from the data shown in Figures 5.10-5.11. The variance between simulations decreases as n increases except in the difference between $n = 75$ and $n = 100$ for the deterministic simulations. We note that the difference between these variances, shown as the last two blue data points in Figure 5.12, is quite small, and that the overall trend for increasing n is decreasing variance. Preliminary simulations of larger lattices, such as $n = 200$, continue to demonstrate this trend of decreasing variance, but for brevity these have been omitted.

While we are unaware of a way to prove this result, it is reminiscent of concentration of measure results for percolation and related models discussed in [70, 160, 161]. This kind of result is a generalization of the central limit Theorem, and essentially says that the variance of some observables decreases with the size of the system. In particular, Figures 5.10-5.12 show that initial seeding distributions become less important in affecting the final mean cell density. Examples of these behaviours in other models and detailed bounds on finite-size effects can be found in [25, 55]. It is interesting to note that this concentration of measure also occurs for the deterministic model with random initial data, which suggests a kind of insensitivity to initial conditions for larger lattice systems independent of the specific dynamics on the lattice.

We note that Algorithm 1 and Algorithm 2, have almost identical statistics across these parameters for the shear stress model. Similarly, the mean across realizations of the stochastic models over-predict the spatial mean cell density for all values of σ_l of the deterministic simulations. While this suggests a difference between the stochastic and deterministic models, we also see that both models appear to take the same values of mean cell density $\hat{N}$ for different values of the threshold σ_l. In other words, we suspect that both the stochastic and deterministic models have the same range of spatial mean cell densities, so that for a given 'target' spatial mean cell density there exist two different thresholds that achieve this corresponding to each kind of model. We also note by Figure 2.14 that increasing the diffusion parameter δ in the deterministic model leads to larger mean cell densities. We do not pursue this here (as we are more interested in qualitatively similar behaviours), but larger values of δ will shift these values closer together.

5.4 Computational Considerations

Finally we discuss some computational aspects of these models. For both Algorithm 1 and Algorithm 2, as well as the Runge-Kutta scheme discussed in Sections 2.1.4 and 3.2 used to solve the deterministic model, the most computationally intensive operation is solving Equations (5.1) for the pressures. This is essentially a large sparse linear system of equations where the coefficients are the weights for the graph Laplacian given by the pipe radii between nodes. All of the models we have discussed in this Chapter are typically limited by how often it is necessary to solve for the pressures, although the difficulty in solving the pressure problem itself is dependent on the cell density distribution. This can be understood in terms of the condition number C for the Laplacian matrix in Equations (5.1). The condition number C of a matrix is the ratio of the largest to the smallest singular values of the matrix. Note that the graph Laplacian is symmetric (as our lattice is undirected), and so the singular values are exactly the eigenvalues. The value of C determines the magnitude to which error propagates in solutions to the system, independent of the Algorithm used to solve it. See Chapter 3 of [178] for more details.

The condition number of the graph Laplacian affects the simulations in two ways. For the adaptive Runge-Kutta scheme, a larger condition number will correspond to a more stiff problem, and hence a smaller time-step will be taken. On the other hand, every solution of Equations (5.1) will introduce some error into the solution due to finite-precision arithmetic, and larger condition numbers will increase the size of these errors. So there is a balance between taking many very small time steps and inverting the Laplacian matrix as infrequently as possible. We will now show that these numbers change based on the mean cell density.

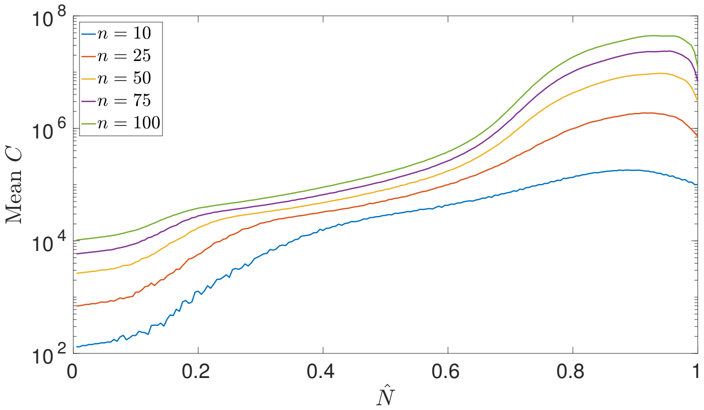

Figure 5.13: Estimate of the condition number of the weighted graph Laplacian (e.g. the left hand side of Equations (5.1)) as a function of the mean cell density $\hat{N}$ and the lattice size n. It is computed by randomly sampling from a cell density distribution with a fixed value of $\hat{N}$ 2000 times and averaging the condition number for the Laplacian matrix using the Matlab function 'condest.' We used 200 different values of $\hat{N} \in [0, 1]$. Note the logarithmic axis for the mean value of C.

In Figure 5.13 we plot an averaged condition number C as a function of the lattice size n and the mean cell density $\hat{N}$. We do this by generating 2000 random realizations of cell densities with the same number $M_0 \in [0, 1]$ of nodes i with $N_i = 1$. Note that the mean and this proportion of nodes are equivalent, so that $M_0 = \hat{N}$. We then compute the weighted graph Laplacian in the left side of Equations (5.1), and use the Matlab function 'condest' to compute a lower bound for C for each realization, and then average across different realizations. We see from Figure 5.13 that a higher mean cell density leads to a linear system with a larger condition number up to a point before dropping off slightly (as the cell density distribution becomes uniformly equal to 1). Similarly, a larger lattice size will also increase the condition number, in addition to increasing the size of the system.

Excluding small differences in this matrix due to continuous cell density, as opposed to the discrete values used here, the underlying pressure problem is the same in all models considered. The main difference between the stochastic Algorithms and the deterministic model is then how frequently Equations (5.1) have to be solved during a simulation of the system. In Figure 5.14 we plot the time taken to simulate the systems shown in Figure 5.10 for $n = 25$, where we have averaged the time over the realizations. Note that this is the clock time between calling the numerical simulation and it returning the value of nodal cell densities, using the same computer for all simulations. We note that the time for the deterministic simulation follows a

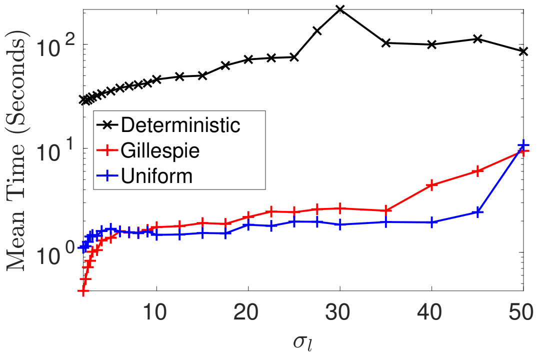

Figure 5.14: Plots of the mean (over 25 realizations) computational time T in seconds for the simulations shown in Figure 5.10 for $n = 25$. Note that the time is plotted on a logarithmic axis.

similar non-monotonic dependence on the threshold σ_l as in the plot of the condition numbers in Figure 5.13. The maximum mean time for the deterministic simulation in Figure 5.14 occurs precisely where the value of σ_l leads to a mean cell density from Figure 5.10 (for $n = 25$) such that C is maximum (in Figure 5.13) at this value of $\hat{N}$. In the simulations used to produce Figure 5.15, we note that the deterministic Algorithm in this case was relaxed so that a maximum time step of $\Delta t = 0.05$ was used, rather than the $\Delta t = 0.001$ used in previous Chapters, and the deterministic simulations still took substantially longer to simulate than the stochastic simulations. This is likely due to the condition number changing the stability of the underlying scheme, leading to the need for a reduced time step, and hence more evaluations of the pressures than in the stochastic case.

Finally we consider the total mean computational time as a function of n. We plot this in Figure 5.15 where we average over the time taken by all realizations for all values of σ_l from Figures 5.10-5.11 for each n. We note that all three approaches increase in computational time taken with n, but both the magnitude and the rate of increase are larger in the case of the deterministic model. We suspect this is due in part to additional computational overhead of an Adaptive Runge-Kutta scheme (e.g. numerically estimating the Jacobian), but also due to the small time steps needed to ensure stability of the scheme. See [21, 43, 151] for details about the Runge-Kutta scheme used, and how the adaptive time steps depend on the properties of the nonlinear system. We also note that Algorithm 2 is more computationally expensive than Algorithm 1, and this is likely due to the differences between the update rules described at the end of Section 5.1. This suggests that Algorithm 1 is a better way to simulate the desired stochastic process, at least for the kinds of mechanically-induced

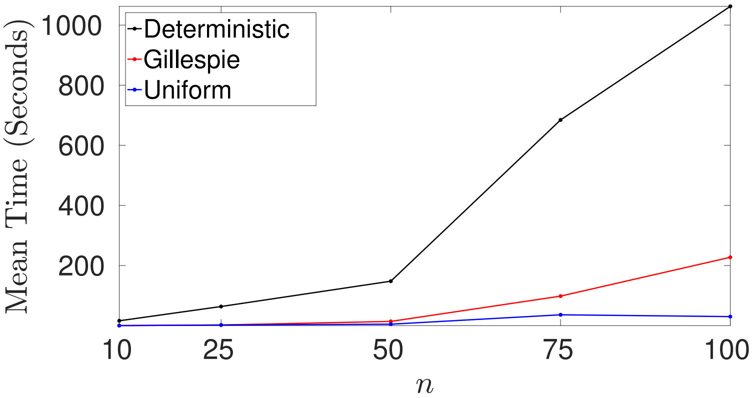

Figure 5.15: Mean clock time as a function of n for the three Algorithms across all simulations displayed in Figures 5.10-5.11.

growth mechanisms explored here. This is in contrast to other kinds of systems where Gillespie-like methods are much more efficient [47].

5.5 Discussion

These computational considerations extend similarly to the other models, but for brevity we do not explore all of them here. While the models do not give identical predictions (see, e.g. Figures 5.2, 5.6, or 5.10-5.11), the above results about concentration of measure and computational speed-up in the uniform stochastic Algorithm suggest a viable alternative paradigm within which to explore these fluid-growth interactions. Additionally, Figures 5.10-5.12 suggest that both stochastic and deterministic models will have different threshold values (in that case σ_l) such that the mean cell density predictions will be the same. As discussed, this is likely due to continuous diffusion in the deterministic models that is not captured in the stochastic setting, in addition to differences in the evolution of both models (e.g. nonlinear deterministic compared with event-driven stochastic evolution).

In addition to the computational advantages of the stochastic models, an important conclusion of this Chapter is the insensitivity to initial conditions demonstrated in Section 5.3.1. These results provide insight into comparable insensitivity discussed in our deterministic models, including in the case of the spatially continuous PDE model first presented in Chapter 2. This universality corresponds, biologically, to an insensitivity of the final cell density in the scaffold to the initial seeding strategy, as long as the lattice is sufficiently large. This contrasts with some deterministic models such as [166], where the choice of initial seeding strategy was an important factor for determining the final cell density. We anticipate that the source of this disagreement is the inclusion of a spatially-varying nutrient field, but leave further investigation as future work.

The comparable predictions for the stochastic models (with different thresholds from the deterministic equivalent) is potentially useful given how simple these stochastic simulation Algorithms are to implement and run. As with the deterministic models of Chapters 2-4, there are questions about realistic constitutive assumptions and interactions between mechanical forces and cell growth and death that should be considered before applying these models to a particular biological problem. Nevertheless, we suspect that insights from these models may be useful in informing choices made in more traditional modelling paradigms, or as alternatives for their computational advantages.

Chapter 6

Conclusion

Mathematical and computational models have been heavily explored in the context of tissue engineering to understand the multitude of processes occurring at various spatial and temporal scales [57, 73, 103, 109, 125, 157, 167, 182, 183]. Mathematical models have also been employed instead of costly and time-consuming experimental trials. These modelling efforts can help answer crucial questions about optimal parameter regimes to drive an experiment to a particular outcome, and they can also help elucidate which fundamental physical and biological interactions underlie a particular experimental protocol. Development of such models has also occurred alongside modelling in cancer biology [2, 23, 24, 147, 148, 149, 155, 158], angiogenesis [4, 27, 29, 113, 150, 155, 164, 187], and biofilms [6, 49, 89, 176], where similar processes of tissue growth modulated by biochemical and biomechanical stimuli are considered. Models of specific processes, as well as biological insights regarding tissue development, have been shared between these fields, especially in the context of understanding tissue growth as a multiscale process involving many disparate spatial and temporal phenomena.

While there is a growing literature of mathematical models addressing scientific problems that concern tissue engineering, accounting for spatial variation leads to several alternative model formulations, as described in Chapter 1. The pore and scaffold length scales in typical experiments with perfusion bioreactors can lead to scaffolds with relatively few pores [103, 182], and our results have shown that considering a discrete pore network (as opposed to a spatially continuous one) can lead to qualitatively different model behaviours. Additionally, while a method-of-lines discretization of a system of coupled PDEs will lead to an analogous discrete system, the interpretation of the model is fundamentally different. In the lattice model, the number of nodes, n^2, is a physically-relevant parameter, rather than something which controls the convergence of a discretization of PDEs. Hence, qualitative differences between these modelling paradigms can suggest that one or the other is more appropriate for a given experimental scenario.

We have developed and analyzed various models of fluid-growth interaction in bioactive porous media. This is with special emphasis on differences between spatially continuous models, and spatially discrete (lattice) models. Given the wide range of physical regimes under which tissue engineering experiments operate, and specifically perfusion bioreactors (see Table 2.1), it seems reasonable that different experimental settings would be better described by one or the other of these two different approaches. The use of discrete models in particular may be motivated by the desire to capture finite discrete effects such as those described in small lattices in Chapters 2-3 in the regime of very few pores, or for computational reasons as described in Chapter 5. All of the various models presented in this thesis have dealt with variants of the same biological problem, and the network and continuum models developed have the same components, so that the size of the network is the primary parameter that can be varied between these paradigms. We note that we have used different constitutive laws in our discrete and continuum frameworks, as described at the end of Section 2.1.2 (leading to the different uniform shear-stress predictions in Figure 2.3), but that all of the qualitative differences between these frameworks persist even if these are changed.

In Chapter 2 we described the physical idealization of a bioactive porous medium that we used throughout the thesis. We presented lattice and continuum models involving shear induced cell death at high values of the local shear stress. We numerically simulated these models, demonstrating a variety of lattice-size-dependent patterning behaviours of the cell density throughout the scaffold, and particularly contrasting the simpler behaviour of the continuum model compared to the lattice. We discussed the onset and degree of heterogeneity of patterning with respect to the nondimensional parameters of cell diffusion and the threshold for shear-stress-induced death. We also exhibited oscillations in cell density only in the lattice model, and discussed how the existence of this behaviour was dependent on the size of the lattice and these nondimensional parameters.

In Chapter 3 we considered pressure-induced cell death at high local pressure in lattice and continuum models. We numerically demonstrated a variety of solution behaviours involving vertically-symmetric and asymmetric steady states, as well as vertically-symmetric and asymmetric oscillations. Using regular asymptotic expansions in the diffusion parameter, we showed that cell density distributions in the large diffusion limit tend to a uniform spatial equilibrium. Using this result to bound the values of diffusion where non-equilibrium behaviours are present, we simulated these models in a region of parameter space in order to classify solution behaviours in terms of boundary conditions and dimensionality (e.g. 1-D or 2-D models). These results showed that the vertically-symmetric oscillations were due to the nonlocal nature of the pressure forcing, and that the asymmetric steady states and oscillations were dependent on the details of the lattice (and not present in the continuum model). While there is no experimental evidence that cell density distributions can organize themselves into vertically symmetric aggregates of cells, these solutions are valuable to understand the implications of different modelling assumptions. In particular, these symmetric solutions likely arise because of the use of a simple symmetry-preserving (e.g. left-to-right) stimulus to cell growth (pressure), and could disappear as more complicated effects are added to the model.

In Chapter 4 we presented a third variation on this framework where cells died due to values of the local fluid flow rate being too high or too low. Fluid flow was used as a proxy for nutrient transport, and low flow rates were assumed to induce cell death via starvation, whereas high flow rates were assumed to kill cells by carrying them along the flow. This model exhibited patterning of cell density similar to that discussed in Chapter 2, but also showed differences in the patterning due to starvation, especially between the lattice and continuum cases. In particular, we noted diagonal ridges of high cell density in the lattice simulations that were absent from the continuum model solutions. We also observed non-equilibrium dynamics, such as a time-varying pattern that is not a simple oscillation, as well as chaotic dynamics in some parameter regimes. While these non-equilibrium behaviours do not correspond to physically realistic experimental conditions, they are an interesting effect observed in this model, and were only present for the lattice case. In particular, these results suggest that complex spatiotemporal behaviour may be displayed by these models, despite their simplicity.

Chapter 5 presented random growth processes defined algorithmically on a lattice using the previous kinds of fluid-growth interactions. We compared simulations of these algorithms to deterministic simulations with the same random initial conditions. We found a variety of interesting behaviours including cases where the random process settled into a simple stationary distribution corresponding to a specific cell density distribution, and other cases where these simulations settled into a time and realization-dependent (quasi-)stationary distribution (e.g. fluctuating on long time scales). We demonstrated that observables such as the spatial mean cell density become less sensitive to initial conditions, for both stochastic and deterministic models, as the lattice size increases. We finally discussed these algorithms in terms of their computational efficiency compared to the systems of ordinary differential equations defining the evolution of the cell density in the deterministic lattice models. While this Chapter raised more questions that require further work, we believe the results are promising directions for future investigation.

Our results can be viewed in terms of the selection of an appropriate starting point for model development. By this we mean that we have demonstrated qualitative differences between lattice and continuum models of bioactive porous media in the context of modelling tissue engineering scaffolds, and these differences are insightful for the development of further models in tissue engineering. While a variety of spatial models for tissue engineering scaffolds exist, there are not many discussions in the literature explicitly comparing different approaches to spatial models (whereas such comparisons do exist in other areas of the broader tissue modelling literature, e.g. [22]). In this sense, our results are useful to help inform the development of models for specific tissue engineering experiments.

As we argued in Chapters 1 and 2, a substantial portion of the existing literature on bioactive porous media, and especially models applied to tissue engineering, uses spatially continuous modelling approaches. While these can be justified in various limits (see [125] for instance), there are many parameter regimes where a discrete lattice approach can be easily justified. *A fortiori*, these discrete approaches give qualitatively different results (oscillations, different kinds of heterogeneity, etc), which may call into question the validity of predictions derived from spatially continuous assumptions in some parameter regimes. Our results mirror some of the developments of alternative models within the wider tissue modelling literature relating discrete, continuum, and hybrid modelling approaches [42, 53, 142]. A key difference in our approach is that while our rigid pore network changes locally in time due to cell growth, we do not consider dynamic network effects such as pruning or expansion of the network, as is considered in the angiogenesis literature [113, 150].

Our models are simple, and do not account for many important effects in modelling growth within a tissue scaffold in a perfusion bioreactor. Extending these to include a model of nutrient transport and uptake by the cells would be a crucial next step. Many multiphase models already include nutrient transport as a component [133, 134, 135, 136, 149, 166]. Discrete and hybdrid discrete-continuum models of nutrient transport exist outside of tissue engineering [27, 29, 106, 176], and these could readily be modified to account for nutrient transport within the pore network of a tissue engineering scaffold.

In addition to modelling nutrient transport and uptake by the cells, accounting for mechanotransduction of, e.g. shear stress (as done in [126, 193]), solid mechanical effects such as deformation of the scaffold (e.g. [144, 202]), or multiple proliferating phases (e.g. cells and ECM separately) would be useful extensions to these models. Several key assumptions used to develop our mesoscopic lattice model, such as the rigidity of the scaffold, could be relaxed in order to account for degradation and deformation of the scaffold which have been studied using multiphase approaches. Such extensions would restrict the generality of these models, and so these extensions should be considered alongside experiments within appropriate operating regimes. Such experiments could validate (or, refute) the need to consider discrete pore networks, and lead to a deeper understanding of specific areas where modelling can elucidate aspects of the tissue growth process.

There are some limitations in the shared governing equations between all of the models presented, especially in terms of the mesoscopic flow problem defined between pores in the lattice models. We have only considered flow regimes in pores for which Poiseuille flow through pipes is a suitable approximation to the fluid flow. This could be replaced by a different fluid flow-pressure drop relationship for more complicated microscale geometries, obtained by solving the relevant microscale flow problem. Different fluid flow regimes (e.g. due to complicated microscale geometries) will have implications for both cell proliferation throughout the porous scaffold, as well as nutrient transport to the cells themselves. Such limitations can be addressed in an analogous way to the specification of constitutive relationships which determine, e.g., permeability in Darcy flow models; namely, alternative microscale flow relationships can be derived and applied throughout the pore network, while maintaining the same mesoscopic framework we have developed.

An important modelling question to address is the determination of which mechanical effects are important for cell death. In this thesis we have always assumed that a single scalar field (the local magnitude of the shear stress, or flow rate, or the fluid pressure) determines if cells grow or die within a region of the scaffold. In reality there may be several effects that lead to cell death. In particular, the starvation effect modelled in Chapter 4 could be a good approximation for large Péclet numbers, and certain uptake kinetics. However, it seems more realistic that cells will die due to large values of the shear stress, rather than large flow rates, and a model that couples these two effects would be informative.

In addition to these modelling considerations, our results also raise several interesting mathematical questions. The pattern formation mechanisms in Chapters

2 and 4 could be explored further in terms of local analysis of the uniform state in order to determine the dominant wavenumbers present at the onset of non-uniform patterning discussed in Section 2.2.2. This is not a trivial computation as the only stable steady states are heterogeneous. Therefore, it is insufficient to perform a local stability analysis of the uniform state, since this state is never a steady state of the system due to logistic growth. Similarly, the asymptotic analysis for large-diffusion in Section 3.3 can be extended to the shear stress and flow rate models under certain assumptions. There are also other asymptotic analyses that could be carried out for other parameter regimes, such as considering the spatial structures of small or large cell density distributions, or considering the limit $n \to \infty$ formally.

Chapter 3 raises several interesting questions about the behaviour of nonlocal lattice models, with a simple fluid-cell coupling amenable to mathematical analysis. Investigating such models further to understand the role of the discrete structure in the symmetry-breaking bifurcations could give broader insight into discretizations of comparable PDEs as well as into other lattice dynamical systems. Further mathematical analysis of small lattices, such as a rigorous understanding of the bifurcations shown in Chapter 3, could be used to fully characterize the behaviour of solutions to the continuum and discrete models by demonstrating that different bifurcations exist in small lattices which are not present for larger lattices or the continuum model. Similarly, the non-equilibrium dynamics observed in Chapter 4 could be investigated more thoroughly, especially as a model of discrete spatio-temporal chaos. These behaviours likely do not correspond to parameter regimes relevant for tissue engineering, but understanding these behaviours more thoroughly can help elucidate fundamental differences between discrete and continuous approaches to bioactive media in general.

The connections between the deterministic models and stochastic simulation algorithms made in Chapter 5 were motivated in large part by discussions of percolation theory as a modelling framework for bioactive porous media. That Chapter only scratches the surface of this approach, and there are many fruitful directions that could be pursued. Many of our simulations in the stochastic and deterministic settings suggested that the cell density increased or decreased until the spatial mean cell density reached a particular value determined by the parameters, and the resulting flow structure (in the case of shear stress and flow rate induced death) loosely resembled a kind of anisotropic percolation. Similarly, the cell density distributions in the pressure-induced death (see Figure 5.2) resemble fluctuations about a gradient percolation process [69, 70, 122, 161]. All of these would be interesting directions for further work.

We have demonstrated broad qualitative differences between spatially continuous and discrete models. These differences in the type of behaviours displayed by continuum and lattice models exist even though the network geometry studied here, a square grid lattice, is fairly simple. In addition to a more complex network geometry, there are many components that could be included in the lattice models, such as a model of nutrient transport, or a more detailed microscale relationship between cell density and fluid flow. Nevertheless, these simple models give insight into the kinds of differences one can expect from these different modelling paradigms.

For experiments involving small pore sizes or large constructs, the pore network is relatively dense [103, 182] and we expect continuum and lattice models to be comparable in terms of predicting cell proliferation and global fluid properties, such as scaffold permeability. For small scaffolds or scaffolds with large pores, however, we expect lattice models to significantly differ from continuum models in their predictions, as we have shown via the finite-size effects demonstrated in this thesis. The variations between lattices of different sizes implies that a good model of the finite network geometry of a scaffold is important in understanding the tissue growth process for such scaffolds. Given a realistic description of the evolution of cells and fluid flow at the pore scale, our approach gives an alternative to continuum approaches, such as mathematical homogenization, in upscaling these microscale processes. Numerical solution of the lattice model is no more difficult than an equivalent discretization of a continuum model, and so the only practical disadvantage of using a lattice model would be the requirement of specifying the network topology, and determining appropriate fluid and cell properties at the scale of the nodes in the network. We believe that studying these kinds of models can lead to novel insights in understanding the growth of artificial tissue, and eventually in developing clinically successful technologies.

Appendix A

Convergence of Numerical Schemes

In this appendix we will describe aspects of numerical convergence, and demonstrate that the approaches we have taken should approximate solutions of the models. We do not formally prove any convergence results or provide theoretical arguments for convergence, but instead rely on well-known techniques from numerical analysis, and practically check the convergence rate for our discretizations. We refer to [174] for a basic introduction to the formal background of the methods we use (especially Chapters 12 and 14), and to [83] and the references therein for contemporary aspects of spatial and temporal discretizations.

For the lattice equations we used a numerical scheme described in Sections 2.1.4 and 3.2. In particular we used the function ‘ode45’ in MATLAB. This uses a particular high-order adaptive Runge-Kutta method [21, 43, 151]. We constrained the maximal time step to 10^{-3} for all simulations in this Thesis. The restriction of the maximal time step was to ensure a good approximation of bifurcation phenomena [33]. As adaptive schemes can have various convergence properties, we will instead implement a fourth-order Runge-Kutta scheme and demonstrate convergence in the time step.

We will also demonstrate convergence in the space step taken by our finite difference discretization of the PDE models, although for the results found in the Thesis we used the finite element software COMSOL with a fixed mesh of 24,912 triangular elements. We will not review finite element methods here, but instead refer to [15, 18, 19] for the mathematical theory and practical details. Our finite difference discretization converges within 1% nodal error to the same solutions as the finite-element implementation for a sufficiently fine mesh, and can be thought of as a method-of-lines solution to the PDE [186].

A.1 Convergence Tests in Time

Equations (2.32a-g) are a coupled system of differential-algebraic equations. However, because the weighted graph Laplacian is invertible, and because we update the pressure variables quasi-statically (e.g. at each time step), we can think of these equations as a system of n^2 first-order ODEs. We will discuss the convergence of our numerical methods in this context. Let $\boldsymbol{u}(t) \in \mathbb{R}^n$ satisfy the autonomous equations,

$$\frac{d\boldsymbol{u}(t)}{dt} = \boldsymbol{f}(\boldsymbol{u}(t)), \quad \boldsymbol{u}(0) = \boldsymbol{u_0}, \tag{A.1}$$

with $\boldsymbol{f} : \mathbb{R}^n \to \mathbb{R}^n$ a given function, and $\boldsymbol{u_0} \in \mathbb{R}^n$ a given vector of initial conditions. We let $\boldsymbol{u}^k_{\Delta t} \approx \boldsymbol{u}(k\Delta t)$ be a discretized approximation to the solution of Equations (A.1) at the time $T = k\Delta t$ in k time steps of size Δt. These will come from the following fourth-order Runge-Kutta scheme,

$$\boldsymbol{g_1} = \Delta t \boldsymbol{f}\left(\boldsymbol{u}^k_{\Delta t}\right), \quad \boldsymbol{g_2} = \Delta t \boldsymbol{f}\left(\boldsymbol{u}^k_{\Delta t} + \frac{1}{2}\boldsymbol{g_1}\right), \quad \boldsymbol{g_3} = \Delta t \boldsymbol{f}\left(\boldsymbol{u}^k_{\Delta t} + \frac{1}{2}\boldsymbol{g_2}\right),$$

$$\boldsymbol{g_4} = \Delta t \boldsymbol{f}\left(\boldsymbol{u}^k_{\Delta t} + \boldsymbol{g_3}\right), \quad \boldsymbol{u}^{k+1}_{\Delta t} = \boldsymbol{u}^k_{\Delta t} + \frac{1}{6}\boldsymbol{g_1} + \frac{1}{3}\boldsymbol{g_2} + \frac{1}{3}\boldsymbol{g_3} + \frac{1}{6}\boldsymbol{g_4}. \tag{A.2}$$

This scheme can be readily deduced from a Taylor series expansion of the solution $\boldsymbol{u}$ at a point with $\Delta t \ll 1$ [95]. We now turn to demonstrating that our implementation of this scheme converges; that is, we want to show $\|\boldsymbol{u}^k_{\Delta t} - \boldsymbol{u}(k\Delta t)\| \to 0$ as $\Delta \to 0$, $k \to \infty$, and for every $kT = \Delta t$. This is for some norm $\| \cdot \|$. As we do not know any analytic solutions for our system, we will instead rely on showing that the sequence of values $\boldsymbol{u}^k_{\Delta t}$ is Cauchy. That is, we compute the successive differences between solutions using smaller time steps. Define these as,

$$E(\Delta t) = \|\boldsymbol{u}^k_{\Delta t} - \boldsymbol{u}^{2k}_{\frac{\Delta t}{2}}\| \equiv \max_i \left(\max_k \left(u^k_{i,\Delta t} - u^{2k}_{i,\frac{\Delta t}{2}}\right)\right), \tag{A.3}$$

where the subscript i denotes the element of the vector $\boldsymbol{u}^k_{\Delta t}$. We plot an example of these successive differences in Figure A.1 for successively smaller time steps $\Delta t = 0.052^i$ for $i = 0, 1, 2, \ldots, 14$. Comparable plots for a variety of δ, p_l, and n provide clear evidence that the scheme converges.

A.2 Convergence Tests in Space

We can analogously demonstrate convergence in the spatial step. Assuming we are in the unit square or interval (the domains considered throughout the Thesis due to the nondimensionalization of the length), we can use the lattice equations as they are as

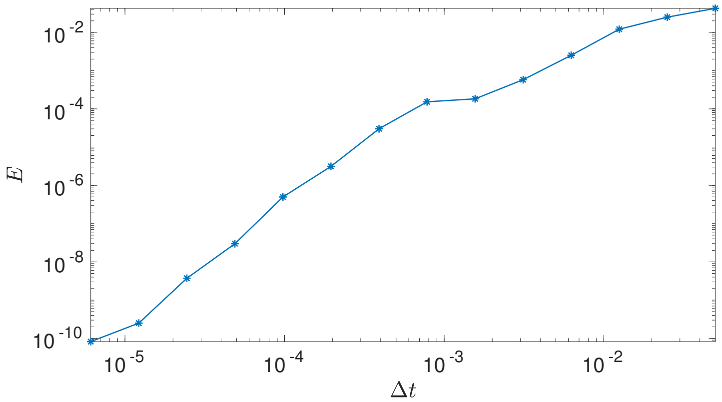

Figure A.1: Plots of the successive differences E in the numerical discretization of Equations (3.1)-(3.4) with $n = 10$, $\delta = 0.1$, and $p_l = 500$. These were computed using 15 time steps $\Delta t = 0.052^i$ for $i = 0, 1, 2, \ldots, 14$. Note the logarithmic axes.

a method of lines finite difference approximation to the PDE system, where just the spatial part of the PDE has been discretized. Note that there are subtle variations necessary to do this for the shear stress and flow rate models due to the Euclidean 2-norms in Equations (2.14f) and (4.4). We consider the following successive errors for finer discretizations of the spatial step $\Delta x = 1/n$,

$$F(\Delta t) = \left(\sum_i \left(\sum_k \left(u^i_{\Delta x}(k\Delta t) - u^{2i}_{\frac{\Delta x}{2}} \right)^2 \right) \right)^{\frac{1}{2}}, \tag{A.4}$$

where Δt a given time step and number of time steps k is given such that $T = k\Delta t$. We plot this for an sample simulation in Figure A.2. As in the temporal setting, we observe convergence here, and for other models and parameters.

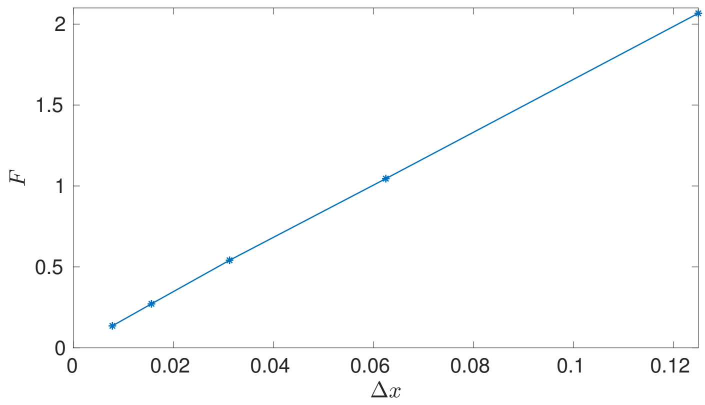

Figure A.2: Plots of the successive differences F in the numerical discretization of Equations (3.1)-(3.4) with $n = 10$, $\delta = 0.1$, and $p_l = 500$. These were computed using the adaptive Runge-Kutta method 'ode45' with lattice sizes $n = 8, 16, 32, 64, 128$, and 256.

Bibliography

[1] N. S. Abdullah and D. B. Das. Modelling Nutrient Transport in Hollow Fibre Membrane Bioreactor for Growing Bone Tissue with Consideration of Multi-Component Interactions. *Chemical Engineering Science*, 62(21):5821–5839, 2007.

[2] T. Alarcón. Modelling tumour-induced angiogenesis: A review of individual-based models and multiscale approaches. *Contemporary Mathematics*, 492:45, 2009.

[3] V. Ambegaokar, B. I. Halperin, and J. S. Langer. Hopping Conductivity in Disordered Systems. *Physical Review B*, 4(8):2612–2620, October 1971.

[4] A. R. A. Anderson and M. A. J. Chaplain. Continuous and discrete mathematical models of tumor-induced angiogenesis. *Bulletin of mathematical biology*, 60(5):857–899, 1998.

[5] P. Angele, D. Schumann, M. Angele, B. Kinner, C. Englert, R. Hente, B. Füchtmeier, M. Nerlich, C. Neumann, and R. Kujat. Cyclic, mechanical compression enhances chondrogenesis of mesenchymal progenitor cells in tissue engineering scaffolds. *Biorheology*, 41(3-4):335–346, 2004.

[6] K. Anguige, J. R. King, and J. P. Ward. A multi-phase mathematical model of quorum sensing in a maturing pseudomonas aeruginosa biofilm. *Mathematical biosciences*, 203(2):240–276, 2006.

[7] M. B. Esch, J.-M. Prot, Y. I. Wang, P. Miller, J. Ricardo Llamas-Vidales, B. A. Naughton, D. R. Applegate, and M. L. Shuler. Multi-cellular 3d Human Primary Liver Cell Culture Elevates Metabolic Activity Under Fluidic Flow. *Lab on a Chip*, 15(10):2269–2277, 2015.

[8] P. Bak, C. Tang, and K. Wiesenfeld. Self-organized criticality. *Physical review A*, 38(1):364, 1988.

[9] A. Bakker, J. Klein-Nulend, and E. Burger. Shear stress inhibits while disuse promotes osteocyte apoptosis. *Biochemical and biophysical research communications*, 320(4):1163–1168, 2004.

[10] S. S. Bale, S. Geerts, R. Jindal, and M. L. Yarmush. Isolation and Co-Culture of Rat Parenchymal and Non-Parenchymal Liver Cells to Evaluate Cellular Interactions and Response. *Scientific Reports*, 6, May 2016.

[11] Y. Barbotteau, J. L. Irigaray, and J. F. Mathiot. Modelling by Percolation Theory of the Behaviour of Natural Coral Used as Bone Substitute. *Physics in Medicine and Biology*, 48(21):3611–3623, 2003.

[12] R. J. Baxter. *Exactly Solved Models in Statistical Mechanics.* Dover Publications, Mineola, N.Y, dover ed edition, 2007. OCLC: ocn154799434.

[13] J. Bear. *Dynamics of Fluids in Porous Media.* American Elsevier, New York, 1972.

[14] T. Beard, D. Kaserman, and R. Osterkamp. *The Global Organ Shortage: Economic Causes, Human Consequences, Policy Responses.* Stanford University Press, Stanford, January 2013.

[15] P. Bettess. The Finite Element Method Vol. 1: Basic Formulation and Linear Problems. *International Journal for Numerical Methods in Engineering*, 30(3):565–567, 1990.

[16] J. Billingham. Dynamics of a Strongly Nonlocal Reaction-Diffusion Population Model. *Nonlinearity*, 17(1):313–346, 2004.

[17] M. J. Blackstock and D. C. Ray. Organ donation after circulatory death: an update. *European Journal of Emergency Medicine*, 21(5):324–329, 2014.

[18] D. Boffi, M. Fortin, and F. Brezzi. *Mixed Finite Element Methods and Applications.* Number 44 in Springer series in computational mathematics. Springer, Heidelberg ; New York, 2013. OCLC: ocn825755402.

[19] S. C. Brenner and L. R. Scott. *The Mathematical Theory of Finite Element Methods.* Number 15 in Texts in applied mathematics. Springer, New York, NY, 3rd ed edition, 2008. OCLC: ocn183259725.

[20] S. R. Broadbent and J. M. Hammersley. Percolation Processes. *Mathematical Proceedings of the Cambridge Philosophical Society*, 53(03):629, July 1957.

[21] J. C. Butcher. On Fifth Order Runge-Kutta Methods. *BIT Numerical Mathematics*, 35(2):202–209, 1995.

[22] H. Byrne and D. Drasdo. Individual-based and continuum models of growing cell populations: a comparison. *Journal of mathematical biology*, 58(4):657–687, 2009.

[23] H. Byrne and L. Preziosi. Modelling solid tumour growth using the theory of mixtures. *Mathematical Medicine and Biology*, 20(4):341–366, 2003.

[24] H. M. Byrne, J. R. King, D. L. S. McElwain, and L. Preziosi. A two-phase model of solid tumour growth. *Applied Mathematics Letters*, 16(4):567–573, 2003.

[25] J. Cardy. *Finite-Size Scaling.* Elsevier, December 2012.

[26] R. G. Casten and C. J. Holland. Instability Results for Reaction Diffusion Equations with Neumann Boundary Conditions. *Journal of Differential Equations*, 27(2):266–273, 1978.

[27] M. Chaplain and A. Anderson. Mathematical modelling of tumour-induced angiogenesis: network growth and structure. *Angiogenesis in Brain Tumors*, pages 51–75, 2004.

[28] M. Chaplain and H. Byrne. Mathematical modelling of wound healing and tumour growth-2 sides of the same coin. *Wounds*, 8:42–48, 03 1996.

[29] M. A. J. Chaplain, S. R. McDougall, and A. R. A. Anderson. Mathematical modeling of tumor-induced angiogenesis. *Annu. Rev. Biomed. Eng.*, 8:233–257, 2006.

[30] L. A. C. Chapman, R. J. Shipley, J. P. Whiteley, M. J. Ellis, H. M. Byrne, and S. L. Waters. Optimising Cell Aggregate Expansion in a Perfused Hollow Fibre Bioreactor via Mathematical Modelling. *PLoS ONE*, 9(8):e105813, August 2014.

[31] L. A. C. Chapman, J. P. Whiteley, H. M. Byrne, S. L. Waters, and R. J. Shipley. Mathematical modelling of cell layer growth in a hollow fibre bioreactor. *Journal of theoretical biology*, 418:36–56, 2017.

[32] M. J. Chen, L. S. Kimpton, J. P. Whiteley, M. Castilho, J. Malda, C. P. Please, S. L. Waters, and H. M. Byrne. Multiscale modelling and homogenisation of fibre-reinforced hydrogels for tissue engineering. 2017.

[33] N. Christodoulou. Discrete Hopf Bifurcation for Runge-Kutta Methods. *Applied Mathematics and Computation*, 206(1):346–356, 2008.

[34] N. A. Cilfone, D. E. Kirschner, and J. J. Linderman. Strategies for efficient numerical implementation of hybrid multi-scale agent-based models to describe biological systems. *Cellular and molecular bioengineering*, 8(1):119–136, 2015.

[35] E. Cimetta, M. Flaibani, M. Mella, E. Serena, L. Boldrin, P. De Coppi, and N. Elvassore. Enhancement of Viability of Muscle Precursor Cells on 3d Scaffold in a Perfusion Bioreactor. *The International Journal of Artificial Organs*, 30(5):415–428, May 2007.

[36] F. Coletti, S. Macchietto, and N. Elvassore. Mathematical Modeling of Three-Dimensional Cell Cultures in Perfusion Bioreactors. *Industrial & Engineering Chemistry Research*, 45(24):8158–8169, 2006.

[37] J. Collis, D. L. Brown, M. E. Hubbard, and R. D. ODea. Effective equations governing an active poroelastic medium. In *Proc. R. Soc. A*, volume 473, page 20160755. The Royal Society, 2017.

[38] R. B. Conolly and J. S. Kimbell. Computer Simulation of Cell Growth Governed by Stochastic Processes: Application to Clonal Growth Cancer Models. *Toxicology and Applied Pharmacology*, 124(2):284–295, 1994.

[39] S. C. Cox, J. A. Thornby, G. J. Gibbons, M. A. Williams, and K. K. Mallick. 3d Printing of Porous Hydroxyapatite Scaffolds Intended for Use in Bone Tissue Engineering Applications. *Materials Science and Engineering: C*, 47:237–247, 2015.

[40] L. J. Cummings and S. L. Waters. Tissue growth in a rotating bioreactor. part ii: fluid flow and nutrient transport problems. *Mathematical Medicine and Biology*, 24(2):169–208, 2007.

[41] Y. Davit, C.G. Bell, H.M. Byrne, L.A.C. Chapman, L.S. Kimpton, G.E. Lang, K.H. Leonard, J.M. Oliver, N.C. Pearson, R.J. Shipley, S.L. Waters, J.P. Whiteley, B.D. Wood, and M. Quintard. Homogenization via Formal Multiscale

Asymptotics and Volume Averaging: How do the Two Techniques Compare? *Advances in Water Resources*, 62, Part B:178–206, 2013.

[42] R. de la Cruz, P. Guerrero, J. Calvo, and T. Alarcón. Coarse-graining and hybrid methods for efficient simulation of stochastic multi-scale models of tumour growth. *Journal of Computational Physics*, 350:974–991, 2017.

[43] J. R. Dormand and P. J. Prince. A Family of Embedded Runge-Kutta Formulae. *Journal of Computational and Applied Mathematics*, 6(1):19–26, 1980.

[44] D. Drasdo. Center-based single-cell models: An approach to multi-cellular organization based on a conceptual analogy to colloidal particles. In *Single-Cell-Based Models in Biology and Medicine*, pages 171–196. Springer, 2007.

[45] Yi Duan, Nanami Gotoh, Qingshang Yan, Zhaopeng Du, A. M. Weinstein, T. Wang, and S. Weinbaum. Shear-induced reorganization of renal proximal tubule cell actin cytoskeleton and apical junctional complexes. *Proceedings of the National Academy of Sciences*, 105(32):11418–11423, 2008.

[46] W. M. Durham, O. Tranzer, A. Leombruni, and R. Stocker. Division by Fluid incision: Biofilm Patch Development in Porous Media. *Physics of Fluids*, 24:1107, 2012.

[47] R. Erban, J. Chapman, and P. Maini. A Practical Guide to Stochastic Simulations of Reaction-Diffusion Processes. *arXiv:0704.1908 [physics, q-bio]*, April 2007. arXiv: 0704.1908.

[48] X. F. Liu, J. Q. Yu, R. Dalan, A. Q. Liu, and K. Q. Luo. Biological Factors in Plasma from Diabetes Mellitus Patients Enhance Hyperglycaemia and Pulsatile Shear Stress-Induced Endothelial Cell Apoptosis. *Integrative Biology*, 6(5):511–522, 2014.

[49] M. G. G Fagerlind, J. S. Webb, N. Barraud, D. McDougald, A. Jansson, P. Nilsson, M. Harlén, S. Kjelleberg, and S. A. Rice. Dynamic modelling of cell death during biofilm development. *Journal of theoretical biology*, 295:23–36, 2012.

[50] G. P. Figueredo, T. V. Joshi, J. M. Osborne, H. M. Byrne, and M. R. Owen. On-lattice agent-based simulation of populations of cells within the open-source chaste framework. *Interface focus*, 3(2):20120081, 2013.

[51] J. A. Flegg, S. N. Menon, P. K. Maini, and D. L. S. McElwain. On the mathematical modeling of wound healing angiogenesis in skin as a reaction-transport process. *Frontiers in physiology*, 6, 2015.

[52] R. Flindt. *Amazing numbers in biology.* Springer Science & Business Media, 2006.

[53] J. A. Fozard, H. M. Byrne, O. E. Jensen, and J. R. King. Continuum approximations of individual-based models for epithelial monolayers. *Mathematical medicine and biology: a journal of the IMA*, 27(1):39–74, 2009.

[54] A. C. Frigo, A. Fasolo, C. Capuzzo, M. Fornea, R. Bellucci, M. Busin, G. Marchini, E. Pedrotti, D. Ponzin, CORTES Study Group, et al. Corneal transplantation activity over 7 years: changing trends for indications, patient demographics and surgical techniques from the corneal transplant epidemiological study (cortes). In *Transplantation proceedings*, volume 47, pages 528–535. Elsevier, 2015.

[55] C. Garban and J. E. Steif. Lectures on Noise Sensitivity and Percolation. *arXiv:1102.5761 [math-ph]*, February 2011. arXiv: 1102.5761.

[56] M. Garrod and D. Y. San Chau. An overview of tissue engineering as an alternative for toxicity assessment. *Journal of Pharmacy & Pharmaceutical Sciences*, 19(1):31–71, 2016.

[57] L. Geris, editor. *Computational Modeling in Tissue Engineering*, volume 10 of *Studies in Mechanobiology, Tissue Engineering and Biomaterials.* Springer Berlin Heidelberg, Berlin, Heidelberg, 2013.

[58] P. Gerlee and A. R. A. Anderson. An evolutionary hybrid cellular automaton model of solid tumour growth. *Journal of theoretical biology*, 246(4):583–603, 2007.

[59] C. L. German and S. V. Madihally. Applications of Computational Modelling and Simulation of Porous Medium in Tissue Engineering. *Computation*, 4(1):7, February 2016.

[60] M. Gharasoo, F. Centler, P. Regnier, H. Harms, and M. Thullner. A reactive transport modeling approach to simulate biogeochemical processes in pore structures with pore-scale heterogeneities. *Environmental modelling & software*, 30:102–114, 2012.

[61] D. T. Gillespie. A General Method for Numerically Simulating the Stochastic Time Evolution of Coupled Chemical Reactions. *Journal of Computational Physics*, 22(4):403–434, 1976.

[62] J. A. Glazier, A. Balter, and N. J. Poplawski. Ii. 1 magnetization to morphogenesis: A brief history of the glazier-graner-hogeweg model. *Single-Cell-Based Models in Biology and Medicine*, page 79, 2007.

[63] J. Glowacki, S. Mizuno, and J.S. Greenberger. Perfusion Enhances Functions of Bone Marrow Stromal Cells in Three-Dimensional Culture - Biochemical and ultrastructural analyses. *Cell Transplantation*, 7(3):319–326, May 1998.

[64] N. S. Goel and N. Dyn. *Stochastic Models in Biology.* Academic Press, New York, 1974.

[65] G. A. Gottwald and I. Melbourne. A New Test for Chaos in Deterministic Systems. *Proceedings of the Royal Society of London A: Mathematical, Physical and Engineering Sciences*, 460(2042):603–611, 2004.

[66] G. A. Gottwald and I. Melbourne. On the Implementation of the 01 Test for Chaos. *SIAM Journal on Applied Dynamical Systems*, 8(1):129–145, 2009.

[67] G. A. Gottwald and I. Melbourne. The 0-1 test for chaos: A review. In *Chaos Detection and Predictability*, pages 221–247. Springer, 2016.

[68] S. A. Gourley, M. A. J. Chaplain, and F. A. Davidson. Spatio-Temporal Pattern Formation in a Nonlocal Reaction-Diffusion Equation. *Dynamical Systems*, 16(2):173–192, 2001.

[69] J.-F. Gouyet and Michel Rosso. Diffusion Fronts and Gradient Percolation: A Survey. *Physica A: Statistical Mechanics and its Applications*, 357(1):86–96, 2005.

[70] G. Grimmett. *Percolation.* Number 321 in Grundlehren der mathematischen Wissenschaften. Springer, Berlin; New York, 2nd ed edition, 1999.

[71] P. Grindrod. *Patterns and Waves: Theory and Applications of Reaction-diffusion Equations.* Clarendon Press, Oxford : New York, 1991.

[72] F. Hamel and L. Ryzhik. On the Nonlocal Fisher-KPP Equation: Steady States, Spreading Speed and Global Bounds. *Nonlinearity*, 27(11):2735, 2014.

[73] R. H. Harrison, J.-P. St-Pierre, and Molly M. Stevens. Tissue Engineering and Regenerative Medicine: A Year in Review. *Tissue Engineering Part B: Reviews*, 20(1):1–16, 2014.

[74] M. Henkel. *Conformal Invariance and Critical Phenomena.* Springer Berlin Heidelberg, Berlin, Heidelberg, 1999. OCLC: 851381135.

[75] M. N. Hirt, A. Hansen, and T. Eschenhagen. Cardiac Tissue Engineering. *Circulation Research*, 114(2):354–367, January 2014.

[76] M. S. Hossain, D. J. Bergstrom, and X. B. Chen. Computational Modelling of the Scaffold-Free Chondrocyte Regeneration: A Two-Way Coupling Between the Cell Growth and Local Fluid Flow and Nutrient Concentration. *Biomechanics and Modeling in Mechanobiology*, 14(6):1217–1225, March 2015.

[77] A. G. Hunt. *Percolation Theory for Flow in Porous Media.* Number 771 in Lecture notes in physics. Springer, Berlin, 2nd ed edition, 2009.

[78] D. Hutmacher. Scaffolds in Tissue Engineering Bone and Cartilage. *Biomaterials*, 21(24):2529–2543, 2000.

[79] L. Irons, J. Collis, and R.D. O'Dea. Chapter 12 - microstructural influences on growth and transport in biological tissuea multiscale description. In Sid M. Becker, editor, *Modeling of Microscale Transport in Biological Processes*, pages 311 – 334. Academic Press, 2017.

[80] T. Iskratsch, H. Wolfenson, and M. P. Sheetz. Appreciating Force and Shape - the Rise of Mechanotransduction in Cell Biology. *Nature Reviews Molecular Cell Biology*, 15(12):825–833, December 2014.

[81] J. R. Jones, R. C. Atwood, G. Poologasundarampillai, S. Yue, and P. D. Lee. Quantifying the 3d Macrostructure of Tissue Scaffolds. *Journal of Materials Science: Materials in Medicine*, 20(2):463–471, October 2008.

[82] S. N. Jorgensen and J. R. Sanders. Mathematical models of wound healing and closure: a comprehensive review. *Medical & biological engineering & computing*, 54(9):1297–1316, 2016.

[83] B. S. Jovanovi and E. Sli. *Analysis of Finite Difference Schemes: For Linear Partial Differential Equations with Generalized Solutions.* Springer Science & Business Media, October 2013.

[84] H. Kantz. A robust method to estimate the maximal lyapunov exponent of a time series. *Physics letters A*, 185(1):77–87, 1994.

[85] J. Keener and J. Sneyd. *Mathematical Physiology, Second Edition: I: Cellular Physiology (Interdisciplinary Applied Mathematics): Cellular Physiology v. 1.* Springer, New York, NY, 2nd ed. 2009 edition edition, 2008.

[86] H. Kesten. The Critical Probability of Bond Percolation on the Square Lattice equals 1/2. *Communications in Mathematical Physics*, 74(1):41–59, February 1980.

[87] S. S. Kim, R. Penkala, and P. Abrahimi. A Perfusion Bioreactor for Intestinal Tissue Engineering. *The Journal of Surgical Research*, 142(2):327–331, 2007.

[88] S. Kirkpatrick. Classical Transport in Disordered Media: Scaling and Effective-Medium Theories. *Physical Review Letters*, 27(25):1722–1725, 1971.

[89] I. Klapper and J. Dockery. Mathematical description of microbial biofilms. *SIAM review*, 52(2):221–265, 2010.

[90] A Koponen, M Kataja, and J. V. Timonen. Tortuous flow in porous media. *Physical Review E*, 54(1):406, 1996.

[91] N. Korin, A. Bransky, U. Dinnar, and S. Levenberg. A parametric study of human fibroblasts culture in a microchannel bioreactor. *Lab on a Chip*, 7(5):611–617, 2007.

[92] J.-L. Kou, X.-M. Tang, H.-Y. Zhang, H.-J. Lu, F.-M. Wu, Y.-S. Xu, and Y.-S. Dong. Tortuosity for streamlines in porous media. *Chinese Physics B*, 21(4), 2012.

[93] A. L. Krause, D. Beliaev, R. A. Van Gorder, and S. L. Waters. Bifurcations and dynamics emergent from lattice and continuum models of bioactive porous media. *International Journal of Bifurcation and Chaos*, 2018. arXiv:1702.08345 [q-bio], In Press.

[94] A. L. Krause, D. Beliaev, R. A. Van Gorder, and S. L. Waters. Lattice and continuum modelling of a bioactive porous tissue scaffold. *IMA Mathematical Medicine and Biology*, 2018. arXiv:1702.07711 [q-bio], In Press.

[95] J. D. Lambert. *Numerical Methods for Ordinary Differential Systems: The Initial Value Problem.* Wiley, Chichester ; New York, 1991.

[96] R. P. Lanza, R. S. Langer, and Joseph Vacanti, editors. *Principles of Tissue Engineering.* Academic Press, an imprint of Elsevier, Amsterdam, fourth edition edition, 2014.

[97] D.-S. Lee, H. Rieger, and K. Bartha. Flow correlated percolation during vascular remodeling in growing tumors. *Physical review letters*, 96(5):058104, 2006.

[98] Y.-H. Lee, R.-S. Chen, N-.C. Chang, K.-R. Lee, C.-T. Huang, Y.-C. Huang, and F-.M. Ho. Synergistic Impact of Nicotine and Shear Stress Induces Cytoskeleton Collapse and Apoptosis in Endothelial Cells. *Annals of Biomedical Engineering*, 43(9):2220–2230, September 2015.

[99] G. Lemon, D. Howard, M. J. Tomlinson, L. D. Buttery, F. R. A. J. Rose, S. L. Waters, and J. R. King. Mathematical Modelling of Tissue-Engineered Angiogenesis. *Mathematical Biosciences*, 221(2):101–120, 2009.

[100] G. Lemon, J. R. King, H. M. Byrne, O. E. Jensen, and K. M. Shakesheff. Mathematical modelling of engineered tissue growth using a multiphase porous flow mixture theory. *Journal of mathematical biology*, 52(5):571–594, 2006.

[101] E. A. Levchenko, A. V. Shapovalov, and A. Yu Trifonov. Asymptotics Semiclassically Concentrated on Curves for the Nonlocal Fisher-Kolmogorov-Petrovskii-Piskunov Equation. *Journal of Physics A: Mathematical and Theoretical*, 49(30):305203, 2016.

[102] C. F. Lo. Stochastic Gompertz Model of Tumour Cell Growth. *Journal of Theoretical Biology*, 248(2):317–321, 2007.

[103] Q. L. Loh and C. Choong. Three-Dimensional Scaffolds for Tissue Engineering Applications: Role of Porosity and Pore Size. *Tissue Engineering Part B: Reviews*, 19(6):485–502, 2013.

[104] H. Lu, L. Y. Koo, W. M. Wang, D. A. Lauffenburger, L. G. Griffith, and K. F. Jensen. Microfluidic shear devices for quantitative analysis of cell adhesion. *Analytical chemistry*, 76(18):5257–5264, 2004.

[105] P. Mañas and B. M. Mackey. Morphological and Physiological Changes Induced by High Hydrostatic Pressure in Exponential- and Stationary-Phase Cells of Escherichia coli: Relationship with Cell Death. *Applied and Environmental Microbiology*, 70(3):1545–1554, March 2004.

[106] P. Macklin, S. McDougall, A. R. A. Anderson, M. A. J. Chaplain, V. Cristini, and J. Lowengrub. Multiscale modelling and nonlinear simulation of vascular tumour growth. *Journal of mathematical biology*, 58(4):765–798, 2009.

[107] I. Martin, D. Wendt, and M. Heberer. The Role of Bioreactors in Tissue Engineering. *Trends in Biotechnology*, 22(2):80–86, 2004.

[108] H. Matano. Convergence of Solutions of One-Dimensional Semilinear Parabolic Equations. *Journal of Mathematics of Kyoto University*, 18(2):221–227, 1978.

[109] R. J. McCoy, C. Jungreuthmayer, and F. J. O'Brien. Influence of Flow Rate and Scaffold Pore Size on Cell Behavior During Mechanical Stimulation in a Flow Perfusion Bioreactor. *Biotechnology and Bioengineering*, 109(6):1583–1594, 2012.

[110] S. R. McDougall, M. G. Watson, A. H. Devlin, C. A. Mitchell, and M. A. J. Chaplain. A hybrid discrete-continuum mathematical model of pattern prediction in the developing retinal vasculature. *Bulletin of mathematical biology*, 74(10):2272–2314, 2012.

[111] SR McDougall and KS Sorbie. The application of network modelling techniques to multiphase flow in porous media. *Petroleum Geoscience*, 3(2):161–169, 1997.

[112] Steven R McDougall, Alexander RA Anderson, and Mark AJ Chaplain. Mathematical modelling of dynamic adaptive tumour-induced angiogenesis: clinical implications and therapeutic targeting strategies. *Journal of theoretical biology*, 241(3):564–589, 2006.

[113] Steven R McDougall, ARA Anderson, MAJ Chaplain, and JA Sherratt. Mathematical modelling of flow through vascular networks: implications for tumour-induced angiogenesis and chemotherapy strategies. *Bulletin of mathematical biology*, 64(4):673–702, 2002.

[114] A. J. McKane and T. J. Newman. Stochastic Models in Population Biology and their Deterministic Analogs. *Physical Review E*, 70(4):041902, 2004.

[115] F. P. W. Melchels, B. Tonnarelli, A. L. Olivares, I. Martin, D. Lacroix, J. Feijen, D. J. Wendt, and D. W. Grijpma. The influence of the scaffold design on the distribution of adhering cells after perfusion cell seeding. *Biomaterials*, 32(11):2878–2884, 2011.

[116] H. Mely and J.-F. Mathiot. Double Site-Bond Percolation Model for Biomaterial Implants. *Applied Physics A*, 106(3):635–644, March 2012.

[117] A. Mikhailov and K. Showalter. Control of Waves, Patterns and Turbulence in Chemical Systems. *Physics Reports*, 425(2-3):79–194, January 2006.

[118] J. D Murray. *Mathematical Biology*. Springer-Verlag, Berlin [Germany, 2014. OCLC: 920462116.

[119] M. M. Nava, M. T. Raimondi, and R. Pietrabissa. A Multiphysics 3d Model of Tissue Growth Under Interstitial Perfusion in a Tissue-Engineering Bioreactor. *Biomechanics and Modeling in Mechanobiology*, 12(6):1169–1179, November 2013.

[120] K. H. L. Nessler, J. R. Henstock, A. J. El Haj, S. L. Waters, J. P. Whiteley, and J. M. Osborne. The Influence of Hydrostatic Pressure on Tissue Engineered Bone Development. *Journal of Theoretical Biology*, 394:149–159, 2016.

[121] M. E. J. Newman. *Networks: An Introduction*. Oxford University Press, Oxford; New York, 2010.

[122] P. Nolin. Near-Critical Percolation in Two Dimensions. *arXiv:0711.4948 [math]*, November 2007. arXiv: 0711.4948.

[123] G. V. Novakovic, T. Eschenhagen, and C. Mummery. Myocardial Tissue Engineering: In Vitro Models. *Cold Spring Harbor Perspectives in Medicine*, 4(3):a014076, March 2014.

[124] R. D. O'Dea, H. M. Byrne, and S. L. Waters. Continuum Modelling of In Vitro Tissue Engineering: A Review. In Liesbet Geris, editor, *Computational Modeling in Tissue Engineering*, number 10 in Studies in Mechanobiology, Tissue Engineering and Biomaterials, pages 229–266. Springer Berlin Heidelberg, 2012.

[125] R. D. O'Dea, M. R. Nelson, A. J. El Haj, S. L. Waters, and H. M. Byrne. A Multiscale Analysis of Nutrient Transport and Biological Tissue Growth in

Vitro. *Mathematical Medicine and Biology: A Journal of the IMA*, 32(3):345–366, September 2015.

[126] R. D. O'Dea, S. L. Waters, and H. M. Byrne. A Multiphase Model for Tissue Construct Growth in a Perfusion Bioreactor. *Mathematical Medicine and Biology: A Journal of the IMA*, 27(2):95–127, 2010.

[127] J. M. Osborne, A. G. Fletcher, J. M. Pitt-Francis, P. K. Maini, and D. J. Gavaghan. Comparing individual-based approaches to modelling the self-organization of multicellular tissues. *PLoS computational biology*, 13(2):e1005387, 2017.

[128] J. M. Osborne, R. D. ODea, J. P. Whiteley, H. M. Byrne, and S. L. Waters. The influence of bioreactor geometry and the mechanical environment on engineered tissues. *Journal of biomechanical engineering*, 132(5):051006, 2010.

[129] Z. K. Otrock, R. A. R. Mahfouz, J. A. Makarem, and A. I. Shamseddine. Understanding the biology of angiogenesis: review of the most important molecular mechanisms. *Blood Cells, Molecules, and Diseases*, 39(2):212–220, 2007.

[130] M. R. Owen, T. Alarcón, P. K. Maini, and H. M. Byrne. Angiogenesis and vascular remodelling in normal and cancerous tissues. *Journal of mathematical biology*, 58(4-5):689, 2009.

[131] T. G. Palferman. Bone and joint diseases around the world-the uk perspective. *Journal of Rheumatology-Supplements*, 30(67):33–35, 2003.

[132] A. A. Patel, E. Gawlinski, S. K. Lemieux, and R. A. Gatenby. A Cellular Automaton Model of Early Tumor Growth and Invasion: The Effects of Native Tissue Vascularity and Increased Anaerobic Tumor Metabolism. *Journal of Theoretical Biology*, 213(3):315–331, December 2001.

[133] N. C. Pearson, R. J. Shipley, S. L. Waters, and J. M. Oliver. Multiphase Modelling of the Influence of Fluid Flow and Chemical Concentration on Tissue Growth in a Hollow Fibre Membrane Bioreactor. *Mathematical Medicine and Biology: A Journal of the IMA*, 31(4):393–430, September 2013.

[134] N. C. Pearson, S.L. Waters, J.M. Oliver, and R.J. Shipley. Multiphase Modelling of the Effect of Fluid Shear Stress on Cell Yield and Distribution in a Hollow Fibre Membrane Bioreactor. *Biomechanics and Modeling in Mechanobiology*, 14(2):387–402, 2015.

[135] N.C. Pearson, J.M. Oliver, R.J. Shipley, and S.L. Waters. A Multiphase Model for Chemically- and Mechanically- Induced Cell Differentiation in a Hollow Fibre Membrane Bioreactor: Minimising Growth Factor Consumption. *Biomechanics and Modeling in Mechanobiology*, 15(3):683–700, June 2016.

[136] N.C. Pearson, R.J. Shipley, S.L. Waters, and J.M. Oliver. Dispersion-Enhanced Solute Transport in a Cell-Seeded Hollow Fibre Membrane Bioreactor. *Journal of Engineering Mathematics*, 99(1):29–63, August 2016.

[137] L. Peng, D. Trucu, P. Lin, A. Thompson, and M. A. J. Chaplain. A multiscale mathematical model of tumour invasive growth. *Bulletin of mathematical biology*, 79(3):389–429, 2017.

[138] F. Pennella, G. Cerino, D. Massai, D. Gallo, G. Falvo D'Urso Labate, A. Schiavi, M. A. Deriu, A. Audenino, and Umberto Morbiducci. A Survey of Methods for the Evaluation of Tissue Engineering Scaffold Permeability. *Annals of Biomedical Engineering*, 41(10):2027–2041, 2013.

[139] R. Penta, D. Ambrosi, and R. J. Shipley. Effective Governing Equations for Poroelastic Growing Media. *The Quarterly Journal of Mechanics and Applied Mathematics*, 67(1):69–91, February 2014.

[140] H. Perfahl, B. D. Hughes, T. Alarcón, P. K. Maini, M. C. Lloyd, M. Reuss, and H. M. Byrne. 3d hybrid modelling of vascular network formation. *Journal of theoretical biology*, 414:254–268, 2017.

[141] E. A. Phelps and A. J. Garca. Engineering More than a Cell: Vascularization Strategies in Tissue Engineering. *Current Opinion in Biotechnology*, 21(5):704–709, October 2010.

[142] S. Pillay, H. Byrne, and P. Maini. Multiscale modeling of angiogenesis and predictive capacity. *Bulletin of the American Physical Society*, 62, 2017.

[143] T. R. R. Pintelon, C. Picioreanu, M. C. N. Loosdrecht, and M. L. Johns. The Effect of Biofilm Permeability on Bio-Clogging of Porous Media. *Biotechnology and Bioengineering*, 109(4):1031–1042, 2012.

[144] J Podichetty, T. and S. V. Madihally. Modeling of Porous Scaffold Deformation Induced by Medium Perfusion. *Journal of Biomedical Materials Research. Part B, Applied Biomaterials*, 102(4):737–748, 2014.

[145] J. V. Pohlmeyer and L. J. Cummings. Cyclic Loading of Growing Tissue in a Bioreactor: Mathematical Model and Asymptotic Analysis. *Bulletin of Mathematical Biology*, 75(12):2450–2473, October 2013.

[146] J. V. Pohlmeyer, S. L. Waters, and L. J. Cummings. Mathematical Model of Growth Factor Driven Haptotaxis and Proliferation in a Tissue Engineering Scaffold. *Bulletin of Mathematical Biology*, 75(3):393–427, January 2013.

[147] G. G. Powathil, M. Swat, and M. A. J. Chaplain. Systems oncology: Towards patient-specific treatment regimes informed by multiscale mathematical modelling. In *Seminars in cancer biology*, volume 30, pages 13–20. Elsevier, 2015.

[148] L. Preziosi. *Cancer modelling and simulation.* CRC Press, 2003.

[149] L. Preziosi and G. Vitale. A multiphase model of tumor and tissue growth including cell adhesion and plastic reorganization. *Mathematical Models and Methods in Applied Sciences*, 21(09):1901–1932, 2011.

[150] A. R. Pries and T. W. Secomb. Making Microvascular Networks Work: Angiogenesis, Remodeling, and Pruning. *Physiology*, 29(6):446–455, November 2014.

[151] P. J. Prince and J. R. Dormand. High Order Embedded Runge-Kutta Formulae. *Journal of Computational and Applied Mathematics*, 7(1):67–75, 1981.

[152] R. A. Quirk, R. M. France, K. M. Shakesheff, and S. M. Howdle. Supercritical Fluid Technologies and Tissue Engineering Scaffolds. *Current Opinion in Solid State and Materials Science*, 8(34):313–321, 2004.

[153] M. Radisic, A. Marsano, R. Maidhof, Y. Wang, and G. Vunjak-Novakovic. Cardiac Tissue Engineering Using Perfusion Bioreactor Systems. *Nature Protocols*, 3(4):719–738, 2008.

[154] K. Rezwan, Q. Z. Chen, J. J. Blaker, and A. R. Boccaccini. Biodegradable and Bioactive Porous Polymer/Inorganic Composite Scaffolds for Bone Tissue Engineering. *Biomaterials*, 27(18):3413–3431, 2006.

[155] H. Rieger, Thierry Fredrich, and M. Welter. Physics of the tumor vasculature: Theory and experiment. *The European Physical Journal Plus*, 131(2):31, 2016.

[156] G. M. Riha, P. H. Lin, A. B. Lumsden, Q. Yao, and C. Chen. Roles of Hemodynamic Forces in Vascular Cell Differentiation. *Annals of Biomedical Engineering*, 33(6):772–779, June 2005.

[157] D. D. Robertson, G. B. Sharma, and B. D. Boyan. Using Mathematical Modeling to Design Effective Regenerative Medicine Strategies for Orthopaedics. *The Journal of the American Academy of Orthopaedic Surgeons*, 24(1):e18–19, 2016.

[158] T. Roose, S. J. Chapman, and P. K. Maini. Mathematical models of avascular tumor growth. *Siam Review*, 49(2):179–208, 2007.

[159] R. Rosenzweig, A. Furman, C. Dosoretz, and U. Shavit. Modeling biofilm dynamics and hydraulic properties in variably saturated soils using a channel network model. *Water Resources Research*, 50(7):5678–5697, 2014.

[160] M. Sahimi. Flow Phenomena in Rocks: From Continuum Models to Fractals, Percolation, Cellular Automata, and Simulated Annealing. *Reviews of Modern Physics*, 65(4):1393–1534, October 1993.

[161] M. Sahimi. *Applications of Percolation Theory.* Taylor & Francis, London; Bristol, PA, 1994.

[162] K. S. Sankar, B. J. Green, A. R. Crocker, J. E. Verity, S. M. Altamentova, and J. V. Rocheleau. Culturing pancreatic islets in microfluidic flow enhances morphology of the associated endothelial cells. *PLoS One*, 6(9):e24904, 2011.

[163] M. Scianna, C.G. Bell, and L. Preziosi. A Review of Mathematical Models for the Formation of Vascular Networks. *Journal of Theoretical Biology*, 333:174–209, September 2013.

[164] T. W. Secomb, J. P. Alberding, R. Hsu, M. W. Dewhirst, and A. R. Pries. Angiogenesis: An Adaptive Dynamic Biological Patterning Problem. *PLoS Computational Biology*, 9(3):e1002983, March 2013.

[165] R. Seydel. *Practical Bifurcation and Stability Analysis.* Springer Science & Business Media, New York, December 2009.

[166] M. Shakeel, P. C. Matthews, R. S. Graham, and S. L. Waters. A Continuum Model of Cell Proliferation and Nutrient Transport in a Perfusion Bioreactor. *Mathematical Medicine and Biology: A Journal of the IMA*, 30(1):21–44, 2013.

[167] R. J. Shipley, G. W. Jones, R. J. Dyson, B. G. Sengers, C. L. Bailey, C. J. Catt, C. P. Please, and J. Malda. Design Criteria for a Printed Tissue Engineering Construct: A Mathematical Homogenization Approach. *Journal of Theoretical Biology*, 259(3):489–502, 2009.

[168] S. Sircar and A. J. Roberts. Surface deformation and shear flow in ligand mediated cell adhesion. *Journal of mathematical biology*, 73(4):1035–1052, 2016.

[169] H. L. Smith. *Monotone Dynamical Systems: An Introduction to the Theory of Competitive and Cooperative Systems.* American Mathematical Soc., 2008.

[170] Josef Smolle and Haro Stettner. Computer Simulation of Tumour Cell Invasion by a Stochastic Growth Model. *Journal of Theoretical Biology*, 160(1):63–72, 1993.

[171] F. Spill, P. Guerrero, T. Alarcon, P. K. Maini, and H. M. Byrne. Mesoscopic and continuum modelling of angiogenesis. *Journal of mathematical biology*, 70(3):485–532, 2015.

[172] H. E. Stanley. *Introduction to Phase Transitions and Critical Phenomena.* Oxford University Press, New York, 1987.

[173] S. H. Strogatz. *Nonlinear dynamics and chaos: with applications to physics, biology, chemistry, and engineering.* Westview press, 2014.

[174] E. Sli and D. F. Mayers. *An Introduction to Numerical Analysis.* Cambridge University Press, August 2003.

[175] P. Thevenot, A. Nair, J. Dey, J. Yang, and L. Tang. Method to analyze three-dimensional cell distribution and infiltration in degradable scaffolds. *Tissue Engineering Part C: Methods*, 14(4):319–331, 2008.

[176] M. Thullner and P. Baveye. Computational Pore Network Modeling of the Influence of Biofilm Permeability on Bioclogging in Porous Media. *Biotechnology and Bioengineering*, 99(6):1337–1351, 2008.

[177] J. E. Till, E. A. McCulloch, and L. Siminovitch. A Stochastic Model of Stem Cell Proliferation, Based on the Growth of Spleen Colony-Forming Cells. *Proceedings of the National Academy of Sciences*, 51(1):29–36, January 1964.

[178] L. N. Trefethen and D. Bau, III. *Numerical Linear Algebra.* SIAM, 1997.

[179] S. Truscello, G. Kerckhofs, S. Van Bael, G. Pyka, J. Schrooten, and H. Van Oosterwyck. Prediction of Permeability of Regular Scaffolds for Skeletal Tissue Engineering: A Combined Computational and Experimental Study. *Acta Biomaterialia*, 8(4):1648–1658, 2012.

[180] I. N. Tsimpanogiannis and P. C. Lichtner. Fluid Displacement and Solid Formation in a Porous Medium Using Invasion Percolation in a Gradient with Pore Blocking. *Energy & Fuels*, 26(6):3935–3950, 2012.

[181] S. Turner and J. Sherrat. Intercellular Adhesion and Cancer Invasion: A Discrete Simulation Using the Extended Potts Model. *Journal of Theoretical Biology*, 216(1):85–100, 2002.

[182] K. Vafai. *Porous Media: Applications in Biological Systems and Biotechnology.* CRC Press, London, August 2010.

[183] C. A. Van Blitterswijk and P. Thomsen, editors. *Tissue Engineering.* Academic Press series in biomedical engineering. Elsevier, Acad. Press, Amsterdam, 2008.

[184] Y. van Gennip and A. L. Bertozzi. Γ-Convergence of Graph Ginzburg-Landau Functionals. *Advances in Differential Equations*, 17(11/12):1115–1180, 2012.

[185] V. Venkatasubramanian, H. Schattler, and J. Zaborszky. Local Bifurcations and Feasibility Regions in Differential-Algebraic Systems. *IEEE Transactions on Automatic Control*, 40(12):1992–2013, 1995.

[186] J. G. Verwer and J. M. Sanz-Serna. Convergence of Method of Lines Approximations to Partial Differential Equations. *Computing*, 33(3-4):297–313, September 1984.

[187] G. Vilanova, I. Colominas, and H. Gomez. A mathematical model of tumour angiogenesis: growth, regression and regrowth. *Journal of The Royal Society Interface*, 14(126):20160918, 2017.

[188] G. Vunjak-Novakovic. Biomimetic Platforms for Tissue Engineering. *Israel Journal of Chemistry*, pages n/a–n/a, September 2013.

[189] G. Vunjak-Novakovic, B. Obradovic, I. Martin, P. M. Bursac, R. Langer, and L. E. Freed. Dynamic cell seeding of polymer scaffolds for cartilage tissue engineering. *Biotechnology progress*, 14(2):193–202, 1998.

[190] M. Welter and H. Rieger. Interstitial fluid flow and drug delivery in vascularized tumors: a computational model. *PloS one*, 8(8):e70395, 2013.

[191] M. Welter and H. Rieger. Computer simulations of the tumor vasculature: Applications to interstitial fluid flow, drug delivery, and oxygen supply. In *Systems Biology of Tumor Microenvironment*, pages 31–72. Springer, 2016.

[192] B. M. Whited and M. N. Rylander. The influence of electrospun scaffold topography on endothelial cell morphology, alignment, and adhesion in response to fluid flow. *Biotechnology and bioengineering*, 111(1):184–195, 2014.

[193] R. J. Whittaker, R. Booth, R. Dyson, C. Bailey, L. P. Chini, S. Naire, S. Payvandi, Z. Rong, H. Woollard, Linda J. Cummings, S. L. Waters, L. Mawasse, J. B. Chaudhuri, M. J. Ellis, V. Michael, N. J. Kuiper, and S. Cartmell. Mathematical Modelling of Fibre-Enhanced Perfusion Inside a Tissue-Engineering Bioreactor. *Journal of Theoretical Biology*, 256(4):533–46, 2009.

[194] D. J. Wilkinson. *Stochastic Modelling for Systems Biology.* Chapman & Hall/CRC mathematical and computational biology series. CRC Press/Taylor & Francis, Boca Raton, 2nd ed edition, 2012.

[195] A. Wolf, J. B. Swift, H. L. Swinney, and J. A. Vastano. Determining lyapunov exponents from a time series. *Physica D: Nonlinear Phenomena*, 16(3):285–317, 1985.

[196] M. Wu, H. B. Frieboes, M. A. J. Chaplain, Steven R McDougall, V. Cristini, and J. S. Lowengrub. The effect of interstitial pressure on therapeutic agent transport: Coupling with the tumor blood and lymphatic vascular systems. *Journal of theoretical biology*, 355:194–207, 2014.

[197] S. Wu, X. Liu, K. W. K. Yeung, C. Liu, and X. Yang. Biomimetic Porous Scaffolds for Bone Tissue Engineering. *Materials Science and Engineering: R: Reports*, 80:1–36, 2014.

[198] L. Yadav, N. Puri, V. Rastogi, P. Satpute, and V. Sharma. Tumour angiogenesis and angiogenic inhibitors: A review. *Journal of clinical and diagnostic research: JCDR*, 9(6):XE01, 2015.

[199] H. Ye, D. B. Das, J. T. Triffitt, and Z. Cui. Modelling Nutrient Transport in Hollow Fibre Membrane Bioreactors for Growing Three-Dimensional Bone Tissue. *Journal of Membrane Science*, 272(12):169–178, 2006.

[200] X. Yin, B. E. Mead, H. Safaee, R. Langer, J. M. Karp, and O. Levy. Engineering stem cell organoids. *Cell stem cell*, 18(1):25–38, 2016.

[201] J. S. Yu and N. Bagheri. Multi-class and multi-scale models of complex biological phenomena. *Current opinion in biotechnology*, 39:167–173, 2016.

[202] A. Yun, S.-H. Lee, and J. Kim. A Phase-Field Model for Articular Cartilage Regeneration in Degradable Scaffolds. *Bulletin of Mathematical Biology*, 75(12):2389–2409, September 2013.

[203] D. Zhao, Y. Sun, X. Wei, H. Liang, L. Zhao, X. Dong, H. Chen, W. Chen, J. Yang, X. Wang, F. Gao, and W. Yi. cIAP1 Attenuates Shear Stress-Induced hBMSC Apoptosis for Tissue-Engineered Blood Vessels Through the Inhibition of the Mitochondrial Apoptosis Pathway. *Life Sciences*, 137:81–88, 2015.